Coalescence of bubbles and drops

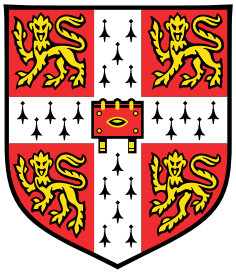

James Munro

Department of Applied Mathematics and Theoretical Physics
University of Cambridge

This dissertation is submitted for the degree of
Doctor of Philosophy

Trinity College July 2018

For my friends and family.

Declaration

I hereby declare that except where specific reference is made to the work of others, the contents of this dissertation are original and have not been submitted in whole or in part for consideration for any other degree or qualification in this, or any other university. This dissertation is my own work and contains nothing which is the outcome of work done in collaboration with others, except as specified in the text and Acknowledgements. This dissertation contains fewer than 65,000 words including appendices, bibliography, footnotes, tables and equations and has fewer than 150 figures.

James Munro
July 2018

Acknowledgements

There are lots of people I need to thank, and this is probably going to be an incomplete list; sorry to anyone I've missed out, and thank you!

Thanks to my friends and family for their endless support, help and advice; thanks to my parents for teaching me to count and encouraging me to keep going. Thanks to my brothers and sister (David, Nicholas and Caitlin) for spontaneous fun, responsible bears, party harps and terrible card games. Thanks to my friends, especially the lunchtime crew (Ben, the other Ben, Jack, the other James, Jo, Lawrence, Nicholas, Nigel and Tom) for giving me insight into pure mathematics, teaching me the difference between analytic functions and functional analysis, and explaining why the answer is not always to take a Mayer–Vietoris sequence. Thanks in particular to Ben for all the hexagons, for being a great housemate in three houses, and for eventually giving me my pencils back. I've been part of a great community of mathematicians from the minute I arrived at Cambridge; in particular I'd like to thank all the fantastic Trinity mathematicians I've met over the years (too many to list here, but you know who you are).

Thanks to everyone at the Institute for Theoretical Geophysics and everyone in Pavilion H for discussions over coffee, for useful conversations about fluid dynamics and for general motivation. Thanks in particular to past and present occupants of H1.04, especially long-term residents Megan and Frederick, for giving me a perspective on other areas of fluid dynamics, and for patiently listening to me going on and on about asymptotic expansions. Special thanks must go to my supervisor and my DoS, John, for insight, supervision, guidance, help and advice over three degrees and eight years. My PhD has been generously funded by EPSRC, and I'm very grateful to Trinity College and DAMTP at Cambridge for support for travel.

Finally, and most importantly, thanks to Fiona. You've brought a lot of happiness, houseplants, tea and owls into my life. Thanks for all the brewing, party planning and adventurous food over the years. And thanks for encouraging me to actually finish writing this thesis. You're the best.

James Munro, Cambridge, July 2018

Abstract

When two fluid drops come close enough together to touch, surface tension quickly pulls the drops together into one larger drop. This is an example of a singular fluid flow, as the topology of the interface changes at the moment of contact. Similarly, when a pair of bubbles touch, the surface topology changes and a singular flow begins. Since the stress from surface tension depends on the surface curvature, these singularities are often characterised by divergent fluid velocities. Experimental observation or numerical simulation of these flows is therefore difficult due to the high velocities and small lengthscales.

In this thesis, I will find multi-scale theoretical solutions for the singular flows during the initial stages of the coalescence of bubbles and drops, solving for the velocity field in the fluid and the rate of coalescence. Each solution has several lengthscales, and on each lengthscale, we must solve some form of the Navier–Stokes equations. I will employ a variety of analytical and numerical techniques to solve for the flow on each scale. These asymptotic solutions are valid at early times; future numerical simulations of the subsequent flow could be initialised with these solutions, rather than the actual singularity.

In the course of solving for these singular flows, I will also describe the solution for the motion of a stretched fluid edge, the retraction of a narrow fluid wedge, the capillary flow around a parabola, and the effect of a time-dependent force on a fluid half-space. These fundamental flows have applications outside of coalescence, which I will outline throughout the thesis.

Table of contents

Chapter 1

Introduction

1.1 Motivation

Drops and bubbles are found everywhere in nature, in industry and in everyday life. Just while doing the washing up, I can see droplets fall from a dripping tap and splash into the washing-up bowl, while soap bubbles clump together to form a foam which gradually breaks down as the walls of soap film between the bubbles burst. With a slow enough flow rate from the tap, or by dribbling a stream of water off the edge of a plate, I can send a tiny droplet bouncing across the surface of the water. Suddenly, it disappears, coalescing with the 'sea' of water in the bowl. This coalescence event sometimes produces an underwater bubble, which may rest at the surface before suddenly bursting. Why are these events so fast? What would happen with a different liquid than water, or a different size of drop or bubble? I will try to answer these questions in this thesis.

In nature, drop coalescence occurs in clouds, where droplets aggregate before falling as rain. As these raindrops run down a window, they merge together to form larger drops. The drops gather with others, running downhill to form streams and rivers until they reach the sea. When a wave breaks out in the ocean, spray and foam are formed. This is captured beautifully in Hokusai's *The Great Wave off Kanagawa*, in which the artist shows the white foam on the breaking wave and the spray of droplets formed (see figure 1.1). A moment later, when the wave hits the ocean, it will mix air into the water in the form of underwater bubbles. Some of these will merge and rise, and some will dissolve into the ocean, taking with them any atmospheric gases. The fate of the carbon dioxide transferred to the water column in this way is an important factor in climate models (see [8] for a review of drops and bubbles in the environment).

Fig. 1.1 *The Great Wave off Kanagawa*, by Hokusai. Reproduced from Wikimedia Commons.

In ink-jet printing, tiny drops of ink are formed by a 'pinch-off' instability. These are deposited onto a page to form the printed image. The break-up and coalescence of these drops determines the clarity of the final printed image (for a review, see [32]).

A key feature of these small drops and bubbles is their surface tension. This force tends to pull fluid masses into rounded shapes; a small rain droplet is not a cartoon tear-drop shape but closer to a sphere [e.g. 4]. This happens because a sphere minimises the surface area between the fluid and its surroundings for a given volume of fluid. For a falling drop, the shape is deformed by the pressure of the airflow around the drop. Similarly, an underwater bubble of air will also tend to be spherical unless deformed by gravity or by some shear flow in the fluid (see [53] for a review of sheared drops and bubbles).

When the surfaces of two fluid masses meet, the shape often changes quickly. There is a change in topology as a new surface is formed, and surface tension acts to minimise the area of this new surface. For example, rain droplets which touch will quickly merge to form a larger fluid mass. A soap bubble, a fluid mass with an inner surface and an outer surface, will burst if those two surfaces touch. Water from a dripping tap will pinch off into droplets. The gas in a bubble resting at the surface of beer or champagne is separated from the atmosphere by a thin film of fluid; if this drains enough for the

film to burst at a point, then surface tension will quickly pull back on the remainder of the film.

The motion may be resisted by viscosity or by inertia. The viscosity of a fluid measures its 'stickiness'; honey, molasses and magma are examples of very viscous fluids, while water and air are much less viscous, and are sometimes even thought of as 'inviscid', that is, lacking viscosity. The dynamics of a very viscous 'inertialess' fluid are likely to be very different from the dynamics of an inviscid fluid.

The size of the system is also important for determining the resistance to motion. The mass of a droplet of radius a scales with its volume proportional to a^3, while the viscous stress on the surface scale proportional to a^2. Inertia is therefore more likely than viscosity to determine the dynamics for a larger fluid droplet.

We therefore expect a wide range of possible flows for different fluids and different coalescence settings. Indeed, there has been much previous work on various problems associated with coalescence and rupture, which we will now review.

1.2 Literature review

In 1891, Lord Rayleigh gave a lecture at the Royal Institution on the use of a new technique called 'instantaneous photography' [55]. This process involves taking photographs with very short exposure times. During the lecture, Lord Rayleigh generated an electrical spark in a Leyden jar, and illuminated various experiments for a fraction of a second. He produced some amazingly sharp images of a rising column of bubbles, of the break-up of a liquid jet and of the bursting of a soap film. In each case, the photographs reveal the true nature of the flow; the rising bubble column is made of several individual pancake-shaped bubbles, the undulations on the surface of the liquid jet are visible even before it breaks into a string of droplets, and the edge of the retracting soap film is thickened when compared with the undisturbed sheet ahead.

At around the same time, Worthington used instantaneous photography to take amazing photographs of the splash formed by a drop impacting on a liquid surface [74], capturing the 'crown' of the splash, the jet that forms in the middle of the impact crater, and the subsequent break-up of that jet. Worthington used a 'timing-sphere' released at the same time as the drop, which hit a metal plate and triggered the flash. By adjusting the height of the plate, Worthington could precisely control when the photograph was taken relative to the moment of impact.

Ranz employed a similar method to find the speed of the edge of a retracting soap film [54]. He used a 'timing guillotine'; a system of switches activated by a sliding block,

to take two separate images separated by about $1/2750^{th}$ of a second. Comparing the position of the edge in the two images, gives the velocity (about 7ms^{-1} for Ranz's experiments).

Theoretical work on bursting soap films has tried to predict this velocity, and tried to explain the dependence on the fluid parameters. Rayleigh's lecture is sometimes cited for the historical calculation; in fact, he briefly refers to the existence of some work by Dupré [21]. Dupré calculated the velocity of the edge based on conservation of energy, with the kinetic energy of the edge supplied by the surface energy of the removed film. This calculation was later corrected by Culick, who reasoned that energy is not conserved since there is viscous dissipation in the sheet [16]. Instead, the momentum of the sheet should be conserved. Culick's prediction for the velocity of the edge is

$$v = \left(\frac{2\gamma}{\rho h}\right)^{1/2} \tag{1.1}$$

where ρ and h are the density and thickness of the fluid sheet, and γ is the coefficient of surface tension. At about the same time and working independently, Taylor arrived at the same conclusion for the velocity, as part of a series of papers on the dynamics of thin sheets [66–68]. The velocity (1.1) is sometimes referred to as the Taylor-Culick velocity.

This approach was generalised by Keller [33], who conserved mass and momentum for a sheet with some general initial power-law shape. A later paper by Keller *et al.* [34] resolved the potential flow in the growing blob at the edge of the sheet as fluid enters from the sheet ahead. Sünderhauf *et al.* [62] show that, although the Taylor–Culick velocity is independent of the viscosity, the approach to this velocity from rest does depend on the dynamic viscosity μ.

We define the Ohnesorge number to be $\text{Oh} = \mu/\sqrt{\rho a \gamma}$ where μ is the dynamic viscosity, ρ is the density, a is a typical lengthscale of the flow and γ is the coefficient surface tension. This compares the importance of inertia and viscosity for a particular fluid. The experiments of Rayleigh and Ranz on bursting fluid sheets used relatively inviscid fluids with $\text{Oh} \ll 1$. In contrast, Debrégeas *et al.* [19] investigate the bursting of very viscous sheets and very viscous bubbles [18], that is, sheets with $\text{Oh} \gg 1$. The dynamics is very different; rather than moving with a constant velocity, the edge accelerates exponentially.

Numerical computation has been used to model these flows. Brenner and Gueyffier consider the retraction of a two-dimensional fluid edge for a range of fluid parameters [9]. They simplify the Navier–Stokes equations to a one-dimensional approximation

in the sheet, and integrate numerically to find the evolution of the shape of the sheet edge, identifying three cases; the sheet may thicken uniformly, may form an elongated blob at the edge, or may form capillary waves away from the edge. Savva and Bush adapt this method to an axisymmetric geometry with some additional assumptions on the shape [57].

When two bubbles touch, a hole is formed in the sheet between them, and this hole is quickly pulled wider by surface tension. Bubble coalescence is therefore related to the sheet-bursting problem, as both involve the rupture of a thin sheet of fluid. The hole joining two coalescing bubbles was imaged by Stover *et al.* [65]. Later experiments by Paulsen *et al.* [50] focus on the initial stage of coalescence and vary the material properties of the fluid. They find a dependence on the viscosity not present in the previous experiments with $\mathrm{Oh} \ll 1$. A variation of this problem in which a rising bubble coalesces with the underside of an air-coated hydrophobic slide is described by de Maleprade *et al.* [17].

There has also been work on the motion of a fluid wedge, a sheet of linearly-growing thickness. Keller and Miksis give a similarity solution for the retraction of an inviscid wedge [35], and asymptotic results for the retraction of slender inviscid wedges were found by Ting and Keller [73]. The corresponding similarity solution for inertialess wedges was found by Miksis and Vanden-Broeck [39]. Billingham has worked on the retraction of fluid wedges and cones for a fluid with both viscosity and inertia [5, 6]. Billingham's solution has similarity scalings on two separate lengthscales, and the flow is different from both the inviscid solution and the inertialess solution. We will review Billingham's work on the retraction of two-dimensional wedges of fluid in detail in chapter 4 below.

Billingham's solutions neglect the effect of an outer fluid. This effect was studied by Sierou and Lister, who describe the break-up of an inertialess fluid thread surrounded by a second fluid [59]. They identify a similarity solution for the shape and velocity as the thread pinches off, for various values of the viscosity ratio between the two fluids.

Sierou and Lister were also able to include the effect of an outer fluid in a solution for the retraction of inviscid cones [60]. Here, the outer fluid and the inner fluid are both inviscid, with different densities. Sierou and Lister vary the density ratio, and find the effect on the capillary waves on the surface of the retracting cones.

Related work on the post-rupture retraction of a liquid thread has been carried out by Eggers [22]. Here, any effect of the outer fluid is neglected, but the effects of both viscosity and inertia in the inner fluid are taken into account. There are two scales to the solution; a large scale where viscosity and inertia balance, and a small local scale

proportional to the radius of the thread where viscosity dominates and the tip of the thread is rounded off.

The experimental technique of taking multiple photographs to reveal the motion during a fluid flow has developed further with the new technology available in the digital age. Experiments by Aarts *et al.* [1], studying the coalescence of water droplets, use a digital camera to achieve a frame rate of 1.2×10^5 frames per second. Experiments by Thoroddsen *et al.* [70, 71] use a specialised high-speed digital camera developed by Etoh *et al.* [24, 25], capable of a frame rate of a million frames per second. This is used to capture the early stages of bubble coalescence [70] and drop coalescence [71]. These high frame rates are necessary for coalescence problems, since the flow begins suddenly and happens quickly. Even with these frame rates, it is difficult to see the flow, since the disturbed region is very small at early times.

To study drop coalescence and related phenomena in more detail, a new technique was developed by Burton *et al.* [10]. The experiment investigates the pinch-off of a thread of liquid mercury; during this flow, the thread narrows very quickly. Burton *et al.* applied a direct current over the mercury thread and measured the electrical resistance during pinch-off. By comparing this with a theoretical model for the resistance of a thin wire, they could infer the thickness of the mercury thread. A similar method was later used to infer the width of the bridge joining two coalescing oil lenses floating on water [11] and for the coalescence of two water drops [12]. The results from the electrical technique have been compared with the results from high-speed imaging to check that the methods agree [47, 48, 50]. Experiments by Paulsen *et al.* vary the fluid parameters of the drops, searching for the different stages or regimes of drop coalescence [49].

For drop coalescence, the theoretical work aims to predict the rate of growth of the fluid bridge joining the drops. We will call the radius of the bridge r_b. An exact solution for the coalescence of two-dimensional inertialess drops was found independently by Hopper and Richardson [28–30, 56]. This remarkable solution resolves the full motion of the fluid from the moment of contact to the eventual relaxation towards a single circular drop. During the initial stage, while the fluid bridge between the drops is small, the fluid bridge grows as $r_b \propto (\gamma t/\mu) \log 1/t$, where t is the time since contact.

Later work has included the effect of an outer fluid of comparable viscosity; no exact solution has been found, but Eggers *et al.* [23] have solved numerically for the initial stage. Their solution describes a fluid bridge which grows as $r_b \propto (\gamma t/\mu) \log 1/t$ again, with a toroidal blob of the outer fluid trapped at the edge of the fluid bridge.

Eggers *et al.* also make the claim that inertia is negligible at early times for a general fluid. They argue that the Reynolds number, based the radius of the fluid bridge, the capillary velocity and the kinematic viscosity, is initially small, since

$$Re = \frac{r_b \dot{r}_b}{\nu} \tag{1.2}$$

is small while r_b is small. They therefore conclude that inertia is initially negligible during drop coalescence at early times. This argument can be adapted to predict a cross-over time after which inertia may enter the problem, and there has been much work on the coalescence of inviscid drops. A scaling law for inviscid coalescence is given by Eggers *et al.* [23], and a numerical simulation was later carried out by Duchemin *et al.* [20]. Thompson and Billingham [69] include the effect of an outer fluid, and show that the surface does not reconnect. In the inviscid version of the problem, the fluid bridge grows as $r_b \propto t^{1/2}$.

These two coalescence laws were previously thought to be a full description of the initial stages of drop coalescence [48]. By the argument of Eggers *et al.*, viscosity would dominate at early times, and then after some cross-over time, inertia would dominate, and coalescence would proceed as $r_b \propto t^{1/2}$. However, recent experiments by Paulsen *et al.* show that this is not the case [49].

Paulsen *et al.* study coalescence experimentally and numerically, varying the fluid viscosity to explore the different stages of coalescence at different Ohnesorge numbers $\mathrm{Oh} = \mu/\sqrt{\rho a \gamma}$, with a the radius of each drop. In the experiments, the drops are held from two nozzles, and slowly brought together until coalescence takes place (see figure 1.2). The prediction from Hopper and Richardson's theory is that the inertialess solution should describe the initial stage of coalescence. For Hopper and Richardson's solution, this involves some motion in the bulk of each drop at early times. But the experiments showed that, for a fluid with moderate Oh, there is no such motion; the bulk of each drop is held stationary by its inertia. However, the fluid bridge does not grow as $r_b \propto t^{1/2}$ during this initial stage, so the inviscid theory does not describe the experimental observations either.

The flow with both inertia and viscosity is therefore very different from the solution neglecting either effect. We will explore this idea in this thesis, and find a new solution including both inertia and viscosity.

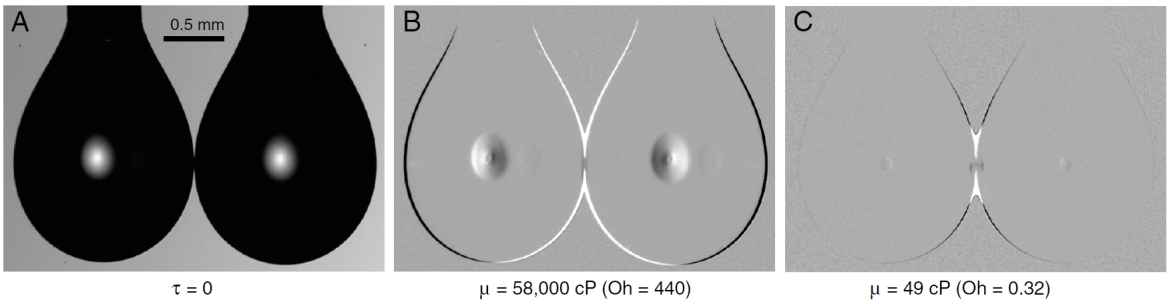

Fig. 1.2 Reproduced from Paulsen *et al.* (2014) [50]. Photos of coalescence with two different fluids. (*a*) Two pendant drops before coalescence. (*b*) During coalescence with Oh = 440, with the initial image subtracted. The bulk of each drop moves as predicted by Hopper and Richardson. (*c*) During coalescence with Oh = 0.32. The bulk of each drop is stationary.

1.3 Aims and outline of this thesis

This thesis will address two separate fluid flows; the coalescence of bubbles and drops. In each case, we will include the effects of both inertia and viscosity. Our solutions will describe any real fluid with finite, non-zero Ohnesorge number.

1.3.1 Bubble coalescence

Experiments by Paulsen *et al.* [50] show that the radius of the hole between two coalescing bubbles always grows proportional to $t^{1/2}$ during the initial stage of coalescence. The prefactor of $t^{1/2}$ depends on the fluid viscosity in a way that is not explained by a previous model of bubble coalescence by Keller [33]. Key questions are:

- What is the initial growth rate of the hole between two coalescing bubbles?
- How does the growth rate depend on the viscosity?
- Is Keller's model valid in the limit of low viscosity?
- What is the flow in the sheet ahead of the edge?

In chapter 2, we will find a family of similarity solutions for bubble coalescence with inertia and viscosity. These solutions predict the velocity in the fluid sheet between the bubbles, the thickness of the sheet and the rate of retraction of the edge of the hole. We will compare this rate of retraction with experiments, with asymptotic models and with numerical simulations of the full Navier–Stokes equations.

The edge of the fluid sheet in this solution is rounded over some small radius proportional to the thickness of the sheet. In chapter 3, we will solve for the detailed shape of this retracting edge, and show that the shape is independent of any lateral stretching along the edge. As an example, we will solve for the growth of a hole in a bursting suspended sheet of viscous fluid. This will explain the observations of Debrégeas *et al.* [19].

1.3.2 Drop coalescence

Previous theoretical solutions for drop coalescence have either neglected inertia [e.g. 23, 28, 56] or neglected viscosity [e.g. 20, 69]. Experiments by Paulsen *et al.* [49] show that the initial dynamics do not agree with either approximation. Key questions are:

- What is the initial growth rate of the fluid bridge between two coalescing drops?
- How does the initial stage depend on viscosity and inertia?
- Are the previous models valid in any limit?
- When does the initial stage cross over to a different, later stage?

In chapter 4, we will review related work by Billingham on the retraction of fluid wedges with both inertia and viscosity [6]. In particular, we will discuss Billingham's asymptotic solution for wide wedges (the case with a narrow crack of air). We will make some modifications, showing how an exact Stokes solution [31] can be applied to the problem.

Then in the following two chapters, we will adapt Billingham's solutions for wedges to drop coalescence. In chapter 5, we will find a similarity solution for the initial stage of inertialess drop coalescence in two and three dimensions. The asymptotic solution in two dimensions can be compared with Hopper and Richardson's exact solution [28, 56], and the solution in three dimensions can explain some of the dynamics seen in the experiments. In chapter 6, we will introduce inertia, combining the ideas of Billingham's wedge solution and the asymptotic analysis from chapter 5. We will derive a new asymptotic description for drop coalescence with inertia and viscosity.

1.4 Publications

An abridged version of the work in chapter 2 was published as [41]. I also contributed to the paper on the numerical simulations by Anthony *et al.* [2]. My explanation of

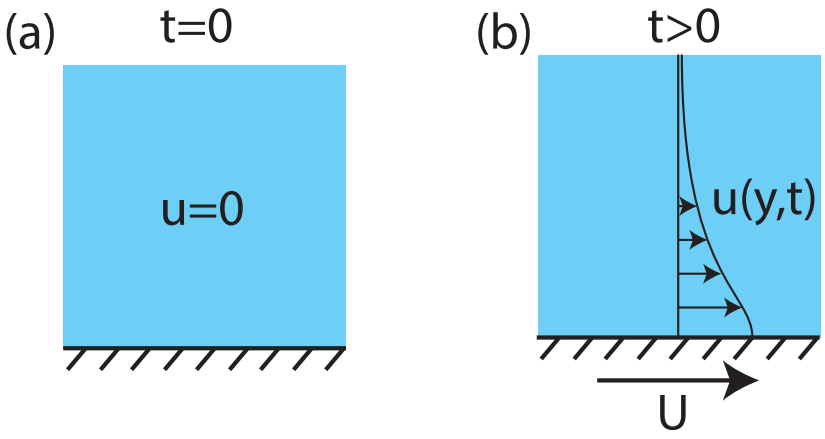

Fig. 1.3 (a) The fluid is initially stationary. (b) The plate begins to move at speed U at time $t = 0$, and causes a flow $u(y, t)\mathbf{e}_x$ in the fluid above the plate.

the transient motion was not included in the paper, but is presented below as section 2.7. The work in chapter 3 was published as [42]. Two papers are in preparation, based on some of the work in chapters 5 and 6.

1.5 An example of a flow with inertia and viscosity

Since the flows in this thesis involve both inertia and viscosity, we will first review a famous example of a flow where inertia and viscosity are both important. Insight from this example will help us to identify the structure and the flow in more complicated problems.

We consider the rectilinear fluid flow above a plate moving with speed U, with the fluid initially at rest, and the plate set in motion instantaneously at time $t = 0$. The initial condition and the subsequent flow are sketched in figure 1.3.

The no-slip boundary condition is $\mathbf{u} = U\mathbf{e}_x$ at $y = 0$, and the initial condition is $\mathbf{u} = \mathbf{0}$ at $t = 0$. The Navier–Stokes equations for the rectilinear velocity field $u(y, t)\mathbf{e}_x$ reduce to

$$\rho\frac{\partial u}{\partial t} = \mu\frac{\partial^2 u}{\partial y^2}. \tag{1.3}$$

This is the heat equation for the velocity, and so we expect the velocity to 'diffuse' out from $y = 0$. Before we solve this differential equation, it will be instructive to consider the inertialess and inviscid versions of the problem. We will see that neither of these has a satisfactory solution.

Without inertia, the equation of motion (1.3) is

$$0 = \mu \frac{\partial^2 u}{\partial y^2}, \tag{1.4}$$

with solution $u = A + By$ where A and B are independent of y. If we apply the boundary condition $u = U$ at $y = 0$, this sets $A = U$. We are left with a family of flows $u = U + By$, and none of these solutions satisfies the initial condition.

On the other hand, without viscosity, the equation of motion (1.3) is

$$\rho \frac{\partial u}{\partial t} = 0. \tag{1.5}$$

Together with our initial condition, this gives $u = 0$ for all time; the inviscid fluid is unaffected by the moving boundary. We are unable to apply the boundary condition $u = U$ on the plate.

So neither the inertialess nor the inviscid model can properly explain the fluid motion above a moving plate in a way that satisfies our boundary condition and initial condition. To find a proper solution, we must include both the effects of inertia and viscosity in our model, and return to the equation of motion (1.3).

We make progress by introducing the similarity variable $\eta = y/\sqrt{\nu t}$, and we will look for a similarity solution $u = f(\eta)$. With this new variable, the equation of motion becomes

$$-\frac{\eta}{2}\frac{\partial f}{\partial \eta} = \frac{\partial^2 f}{\partial \eta^2}. \tag{1.6}$$

This second-order ordinary differential equation has the solution

$$u = A + B \operatorname{erf}\left(\sqrt{\frac{y^2}{4\nu t}}\right), \tag{1.7}$$

where erf is the error function and A and B are unknown constants.

The boundary condition on $y = 0$ gives $A = U$. Then for any fixed $y > 0$, the limit $t \to 0$ gives the initial velocity as $A - B$. By the initial condition, this is zero, and so

$$u = U \operatorname{erfc}\left(\sqrt{\frac{y^2}{4\nu t}}\right). \tag{1.8}$$

where erfc is the complementary error function. This solution is shown at various times (with $\nu = 1$ and $U = 1$) in figure 1.4. At early times, the motion is limited to a region near the moving plate, while at late times the velocity at any given point tends to U.

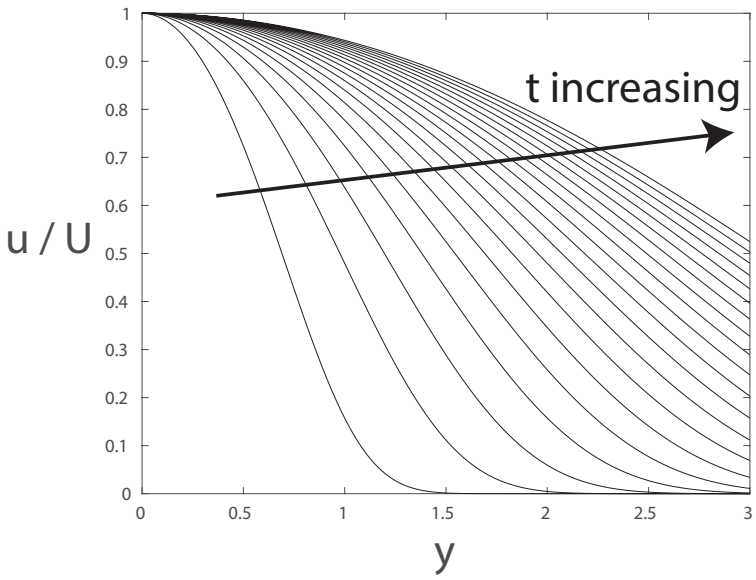

Fig. 1.4 Solution for the rectilinear flow above a moving plate, given by (1.8) at equally-spaced times from $t = 1$ to $t = 20$ with $\nu = 1$.

We can also consider the spatial dependence of the flow at a fixed time. At any particular time, the solution sufficiently near the plate is $u \approx U$, which is comparable with the inertialess 'solution' found above. For y sufficiently large, the velocity decays exponentially to zero, and the half-life for this decay is proportional to the length $(\nu t)^{1/2}$. This is the natural lengthscale for the problem, which we could have constructed just by balancing the terms of (1.3), scaling time derivatives with $1/T$ and spatial derivatives with $1/L$. We note that the far-field solution $u = 0$ is comparable with the inviscid 'solution' found above.

This same structure will re-occur throughout this thesis, with viscosity and inertia balancing on a lengthscale proportional to $(\nu t)^{1/2}$, and with far-field decay to an inviscid flow, and with a inertialess solution on a smaller lengthscale.

Chapter 2

Bubble coalescence

2.1 Introduction

2.1.1 Context

Bubbles are found in a wide variety of geophysical, industrial and biological settings. In a magma chamber, bubbles may form, grow and rise through the magma. When they burst at the surface, the violent motion disrupts the magmatic froth [64]. In the ocean, bubbles are mixed into the water column by breaking waves. These bubbles may subsequently burst at the surface, throwing droplets up to form marine aerosol [7]. Similarly, bursting bubbles at the surface of a glass champagne produce tiny droplets which give the drink its characteristic smell.

The bubbles may instead come close enough together to touch. When the surfaces meet, a hole is formed in the fluid sheet between the bubbles, and surface tension acting on the tightly-curved edge of this hole pulls the hole wider. This process of bubble coalescence affects the distribution of bubble sizes in a bubbly suspension, which will in turn affect the rate of gas transfer between the bubbles and the fluid. This is important for bubbles in the ocean, which contain carbon dioxide from the atmosphere, and may transfer this gas to the ocean.

There has been much previous work on the related problem of a bursting fluid sheet. Taylor and Culick describe the retraction of the edge of a fluid sheet under surface tension [16, 67]. They model the retracting rim as a growing mass of fluid swept up by the edge, moving at a uniform speed. Balancing the force of surface tension with the

rate of change of momentum gives the simple differential equation

$$2\gamma = \rho \frac{\mathrm{d}}{\mathrm{d}t}\left(\frac{\mathrm{d}x}{\mathrm{d}t} x h\right), \tag{2.1}$$

with solution

$$x = \sqrt{\frac{2\gamma}{\rho h}}\, t. \tag{2.2}$$

More recently, Keller extended these ideas to the retraction of a inviscid mass of fluid with an initial power-law shape [33]. For a sheet of fluid with thickness growing as r^2/a, Keller predicts that the radius of the edge of the hole, $r_{\scriptscriptstyle E}$, grows as

$$r_{\scriptscriptstyle E} \propto \left(\frac{\rho a}{\gamma}\right)^{1/4} t^{1/2}. \tag{2.3}$$

These simple scaling laws all neglect viscosity. Recent experiments by Paulsen *et al.* [50] observe bubble coalescence with at a range of viscosities. The radius of the hole joining the bubbles grows as $r_{\scriptscriptstyle E} \propto t^{1/2}$ in all of the experiments. There are distinct scaling laws for very viscous and very inviscid fluids.

We could also consider the coalescence of a spherical bubble with a half-space. This would model the coalescence of a small bubble undeformed by gravity, coalescing with a planar interface. Experiments by de Maleprade *et al.* [17] image the coalescence of a bubble with a thin flat layer of air on a hydrophobic slide, which is analogous to the special case of a planar interface. As with two bubbles, the hole joining the bubble to the air on the slide grows as $r_{\scriptscriptstyle E} \propto t^{1/2}$.

2.1.2 Overview

Inspired by the experiments of Paulsen *et al.* [50], we will look for a similarity solution for bubble coalescence that includes viscosity and inertia.

First, we will consider the coalescence of two spherical bubbles of equal radius. We will neglect any effect of a fluid in the bubbles, and solve for the flow in the thin sheet of fluid between the bubbles. Let the fluid density be ρ, the dynamic viscosity be μ, the surface tension coefficient be γ.

We will see that $r_{\scriptscriptstyle E} \propto (\nu t)^{1/2} \ll a$ at early times, and that the typical thickness of the sheet is much less than $r_{\scriptscriptstyle E}$. This justifies the use of the extensional flow equations to describe the flow in the thin fluid sheet. This long-wavelength approximation reduces the dimension of the domain in the bulk of the sheet, but this fails near the edge of the

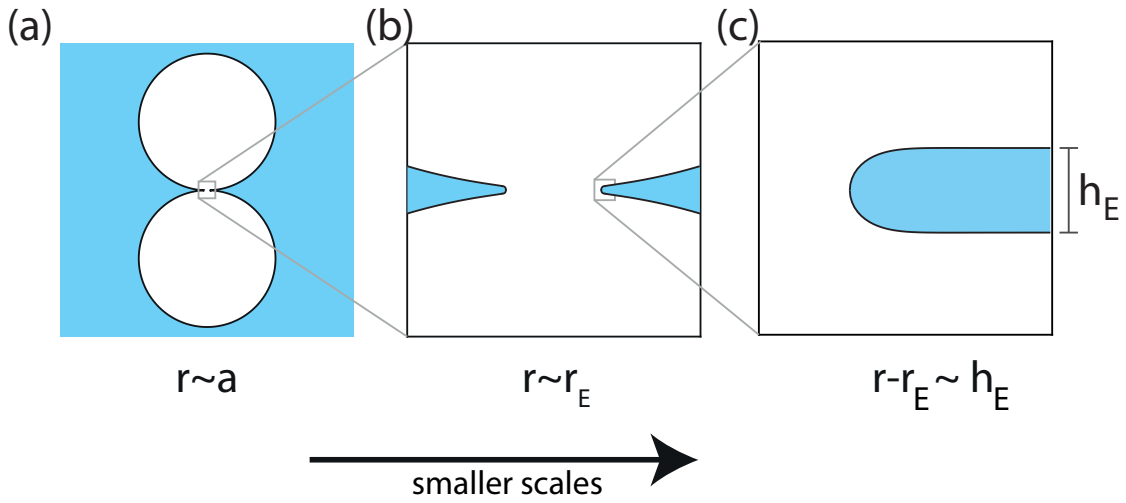

Fig. 2.1 Scales for bubble coalescence. (a) On the scale of the bubble radius, there is little flow. (b) The hole joining the bubbles grows as $r_E \propto (\nu t)^{1/2}$. ($c$) The edge is curved on a scale proportional to the thickness h_E.

sheet, over some lengthscale proportional to the thickness of the sheet. We will define h_E to be the sheet thickness on intermediate scales between the long lengthscale of the sheet and the short lengthscale of the thickness of the sheet. As part of our solution, we will show that such a thickness h_E is well-defined and consistent between the scales.

On the small lengthscale h_E near the edge, the surface is tightly curved, and a free-surface Stokes flow driven by surface tension sets the shape. We will show that the net force from surface tension can be inferred from intermediate scales without resolving the detailed shape of the curved edge. The scales of the problem are shown in figure 2.1.

We will therefore solve for the flow and sheet thickness over a radial lengthscale proportional to r_E, neglecting the tightly-curved edge and modelling the force from surface tension with a stress applied at the edge of the sheet.

In §2.2, we will derive equations for the velocity and the sheet thickness over a radial lengthscale proportional to r_E, and we will show that $r_E \propto t^{1/2}$. We expand the equations of motion in the far-field in §2.3 and near the edge in §2.4, before solving numerically in §2.5. We will find asymptotic solutions for $\mathrm{Oh} \ll 1$ and $\mathrm{Oh} \gg 1$ in §2.6, and compare the results of this simple model with a full Navier–Stokes simulation in §2.7. We compare our asymptotic solution for $\mathrm{Oh} \ll 1$ with Keller's model in §2.8, and discuss the applicability of the solution as a whole in §2.9. Finally, in §2.10, we repeat the analysis in two dimensions, for comparison with the two-dimensional theory.

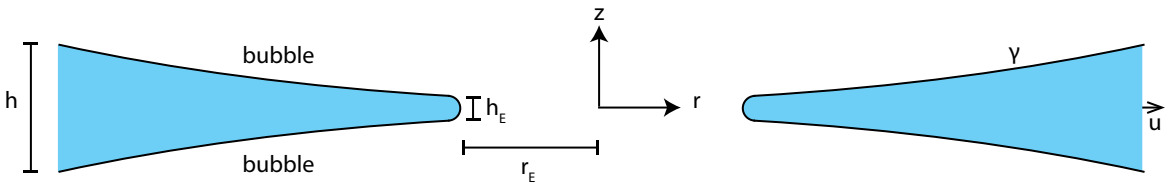

Fig. 2.2 Cross-section of the axisymmetric fluid sheet.

2.2 Equations of motion

Since the initial condition and the forcing are axisymmetric, we expect the flow to be axisymmetric. We define cylindrical co-ordinates (r, θ, z) with r radial, θ azimuthal and z axial along the line joining the bubble centres, as shown in figure 2.2. We write the velocity as $\mathbf{u} = u(r, z, t)\mathbf{e}_r + w(r, z, t)\mathbf{e}_z$ and the thickness of the sheet as $h(r, t)$. Local mass conservation gives

$$\frac{1}{r}\frac{\partial(ru)}{\partial r} + \frac{\partial w}{\partial z} = 0. \tag{2.4}$$

The initial shape of the free surface is a pair of spheres of radius a touching at a single point. During the initial stage of coalescence, while the radius of the hole is much less than a, we will approximate the initial shape with a power of r. We expand the initial sheet thickness for $r \ll a$ as

$$h = 2\left(a - \sqrt{a^2 - r^2}\right) = \frac{r^2}{a} + \mathrm{O}\left(\frac{r^4}{a^3}\right). \tag{2.5}$$

We will work with this parabolically-curved sheet for the similarity solution. Using r_E, the radius of the edge of the hole, as a typical lengthscale for the radial extent of the flow, the typical thickness of the sheet is r_E^2/a. Since this typical thickness is much less than the radial lengthscale, the sheet is long and thin. By the local mass conservation equation (2.4), we expect the radial velocity to be much larger than the vertical velocity, with

$$\frac{u}{r_E} \sim \frac{w}{r_E^2/a}. \tag{2.6}$$

Since, in addition, the fluid sheet is bounded by free surfaces, there is little shear in the sheet, and we can take the radial velocity to be constant across the sheet thickness, writing $u = u(r, t)$ for the radial velocity. We write $h(r, t)$ for the thickness of the sheet

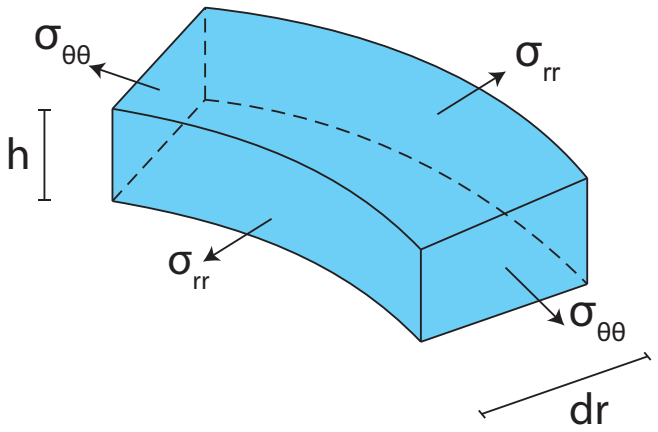

Fig. 2.3 Schematic of the forces on a section of the sheet, of radial extent dr and azimuthal extent dθ.

and integrate (2.4) over the thickness of the sheet for

$$\frac{\partial h}{\partial t} + \frac{1}{r}\frac{\partial (ruh)}{\partial r} = 0. \tag{2.7}$$

We can now solve for the pressure in the sheet. We will neglect any effect of the fluid in the bubbles, such as any stress from any flow in the bubbles. Also, since the curvature of the surface away from the edge is low, we neglect any normal stress from surface tension. The normal stress condition is

$$-p + 2\mu\frac{\partial w}{\partial z} = 0. \tag{2.8}$$

Now local mass conservation lets us eliminate w in favour of u in (2.8), which becomes

$$p = -\frac{2\mu}{r}\frac{\partial (ru)}{\partial r}. \tag{2.9}$$

Now consider the forces on a section of the sheet, as shown in figure 2.3. We take a section of the fluid at with radial extent dr and azimuthal extent dθ. The acceleration of the fluid in this section of the sheet is $\frac{\mathrm{D}u}{\mathrm{D}t}$, and the mass is $\rho hr\mathrm{d}\theta$. The radial forces are $hr\mathrm{d}\theta\sigma_{rr}|_r^{r+\mathrm{d}r}$, and the forces from the hoop stresses are $h\mathrm{d}r\sigma_{\theta\theta}|_{\theta-\mathrm{d}\theta/2}^{\theta+\mathrm{d}\theta/2}$. Balancing the forces on a sector of fluid with the acceleration and taking the limit for small dθ and dr gives

$$\rho hr\frac{\mathrm{D}u}{\mathrm{D}t} = \frac{\partial}{\partial r}\left(hr\sigma_{rr}\right) - \sigma_{\theta\theta}h, \tag{2.10}$$

where the radial and azimuthal components of the stress tensor in cylindrical coordinates are

$$\sigma_{rr} = -p + 2\mu\left(\frac{\partial u}{\partial r}\right) = 2\mu\left(2\frac{\partial u}{\partial r} + \frac{u}{r}\right), \tag{2.11}$$

$$\sigma_{\theta\theta} = -p + 2\mu\left(\frac{u}{r}\right) = 2\mu\left(\frac{\partial u}{\partial r} + \frac{2u}{r}\right). \tag{2.12}$$

following, for example, Batchelor [3]. Substituting these into (2.10) gives

$$\rho h r\frac{\mathrm{D}u}{\mathrm{D}t} = 2\mu\frac{\partial}{\partial r}\left(hr\left(2\frac{\partial u}{\partial r} + \frac{u}{r}\right)\right) - 2\mu h\left(\frac{\partial u}{\partial r} + \frac{2u}{r}\right), \tag{2.13}$$

which is the standard momentum equation for axisymmetric extensional flow in agreement with e.g. [51, 57].

The velocity at the edge of the sheet gives the speed of the edge of the hole, so

$$u(r_E, t) = \frac{\mathrm{d}r_E}{\mathrm{d}t}. \tag{2.14}$$

The thin-sheet approximation fails near the edge of sheet on a scale proportional to the thickness of the sheet. Our solution must match to the flow on this smaller scale. The detailed shape of the curved edge on the smaller scale depends on a coupling between the force from surface tension and the kinematic boundary condition, and solving for this flow would involve solving the full Stokes equations (without a thin-sheet approximation). The far-field of this small-scale flow would then give the net force from surface tension.

Here, we will show that the net force from surface tension is independent of the actual shape of the curved edge, and is 2γ. Crucially, this means that we do not need to solve for the detailed shape of the edge, or the flow on the inner scale. Instead, we will derive a stress boundary condition for the flow on the outer scale without resolving the full solution on the inner scale.

To prove this fact about the effect of surface tension, we must integrate the force distribution $-\gamma\kappa\mathbf{n}$ around the edge. We parametrise the two-dimensional edge shape with the arc-length s as $(X(s), Y(s))$, so that the tangent is (X', Y'), the normal is

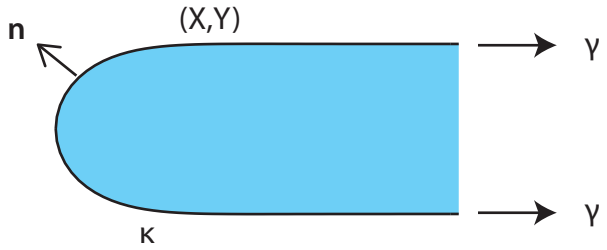

Fig. 2.4 The net force from surface tension acting on any tightly-curved edge is 2γ.

$(-Y', X')$ and the curvature is $X''Y' - X'Y''$. This gives

$$-\int \gamma\kappa\mathbf{n}\,\mathrm{d}s = \gamma\int (X'Y'' - X''Y')\,(-Y', X')\,\mathrm{d}s \tag{2.15}$$

$$= \gamma\int (X'', Y'')\,\mathrm{d}s \tag{2.16}$$

$$= \gamma\left[(X', Y')\right]_{s_1}^{s_2}, \tag{2.17}$$

and so for a curved edge such as that shown in figure 2.4, the net force is $2\gamma\mathbf{e}_r$. This force applied to the bulk of the sheet gives the stress condition at the edge;

$$2\gamma = -2\mu h\left(2\frac{\partial u}{\partial r} + \frac{u}{r}\right)\bigg|_{r_E}. \tag{2.18}$$

We also have initial conditions; the fluid is stationary, and the sheet thickness is given by (2.5). We write these in the form

$$h(r,t) \to \frac{r^2}{a}, \quad u(r,t) \to 0 \quad \text{as } t \to 0. \tag{2.19}$$

Now we will seek a similarity solution. The boundary conditions and the momentum equation motivate balances for the velocity scale $U(t)$, the thickness scale $H(t)$ and the radial lengthscale $L(t)$ as

$$U \sim \frac{L}{t}, \quad \gamma \sim \frac{H\mu U}{L}, \quad \frac{\rho}{t} \sim \frac{\mu}{L^2}. \tag{2.20}$$

Now we solve these for L, U and H;

$$L \sim (\nu t)^{1/2}, \quad U \sim \left(\frac{\nu}{t}\right)^{1/2}, \quad H \sim \frac{\gamma t}{\mu}. \tag{2.21}$$

We note that this scaling predicts that the hole will grow as $t^{1/2}$, which is the time-dependence law seen in the experiments.

We define similarity variables

$$r = (\nu t)^{1/2}\eta, \quad u = \left(\frac{\nu}{t}\right)^{1/2} U(\eta), \quad h = \frac{\gamma t}{\mu} H(\eta). \tag{2.22}$$

Note that this choice of scaling is not unique since there is a dimensionless number $\mathrm{Oh} = \mu/\sqrt{\rho a \gamma}$. To find the dependence of r_E on Oh, we must solve the momentum equation (2.13).

The equation of mass conservation (2.7) becomes

$$\left(H - \frac{\eta}{2}H'\right) + \frac{(\eta H U)'}{\eta} = 0, \tag{2.23}$$

and we separate variables for

$$\frac{H'}{H} = \frac{U' + \frac{U}{\eta} + 1}{\frac{\eta}{2} - U}. \tag{2.24}$$

The momentum equation (2.13) becomes

$$H\eta\left(-\frac{1}{2}U - \frac{\eta}{2}\frac{\partial U}{\partial \eta} + U\frac{\partial U}{\partial \eta}\right) = 2\frac{\partial}{\partial \eta}\left(H\eta\left(2\frac{\partial U}{\partial \eta} + \frac{U}{\eta}\right)\right) - 2H\left(\frac{\partial U}{\partial \eta} + \frac{2U}{\eta}\right), \tag{2.25}$$

which is independent of Oh. We simplify this to

$$\frac{1}{4}\left(-\frac{1}{2}U - \frac{\eta}{2}U' + UU'\right) = U'' + \frac{U'}{\eta} - \frac{U}{\eta^2} + \frac{H'}{H}\left(U' + \frac{U}{2\eta}\right), \tag{2.26}$$

and then eliminate H with the mass equation (2.23) to find

$$\frac{1}{4}\left(-\frac{1}{2}U - \frac{\eta}{2}U' + UU'\right) = U'' + \frac{U'}{\eta} - \frac{U}{\eta^2} + \left(\frac{U' + \frac{U}{\eta} + 1}{\frac{\eta}{2} - U}\right)\left(U' + \frac{U}{2\eta}\right), \tag{2.27}$$

which gives a non-linear differential equation for U alone.

The boundary conditions at the edge become

$$U = \frac{\eta}{2}, \quad 1 = -H\left(2\frac{\partial U}{\partial \eta} + \frac{U}{\eta}\right) \quad \text{at } \eta = \eta_E. \tag{2.28}$$

The initial velocity condition is more subtle; we want $u \to 0$ as $t \to 0$, so

$$\left(\frac{\nu}{t}\right)^{1/2} U\left(\frac{r}{(\nu t)^{1/2}}\right) \to 0. \tag{2.29}$$

It is not sufficient just to have $U \to 0$ as $\eta \to \infty$ because the prefactor is proportional to $t^{-1/2}$. Instead we note that at fixed r, we must have

$$\frac{r}{(\nu t)^{1/2}} U\left(\frac{r}{(\nu t)^{1/2}}\right) \to 0, \tag{2.30}$$

and so we can write the initial condition as

$$\eta U(\eta) \to 0 \quad \text{as } \eta \to \infty. \tag{2.31}$$

This condition applies for early times at fixed r, or equivalently at large r for fixed t.

The initial shape condition simply becomes

$$H \sim \mathrm{Oh}^2 \eta^2 \quad \text{as } \eta \to \infty, \tag{2.32}$$

which includes the Ohnesorge number.

We can integrate the mass equation (2.23) for H in terms of U;

$$\log\left(\frac{H(\eta)}{H(\eta_E)}\right) = \int_{\eta_E}^{\eta} \frac{U'(\hat{\eta}) + U(\hat{\eta})/\hat{\eta} + 1}{\hat{\eta}/2 - U(\hat{\eta})} \, \mathrm{d}\hat{\eta}. \tag{2.33}$$

This gives the thickness of the sheet in terms of the thickness at the edge and the velocity profile.

In summary, we have a second-order non-linear ordinary differential equation for U given by (2.27). The far-field velocity condition (2.31) and the edge velocity condition (2.28) give solutions to this differential equation with varying η_E. We expect a one-parameter family of solutions parametrised by the edge position η_E. With the integral (2.33), we can deduce the thickness for each solution and then, from the far-field growth of H, we can deduce the corresponding value of Oh.

2.3 Far-field solution

To solve the momentum equation (2.27), we must find the solutions which decay properly in the far-field, satisfying the far-field condition (2.31). First, we will find the rate at which such a solution decays in the far-field.

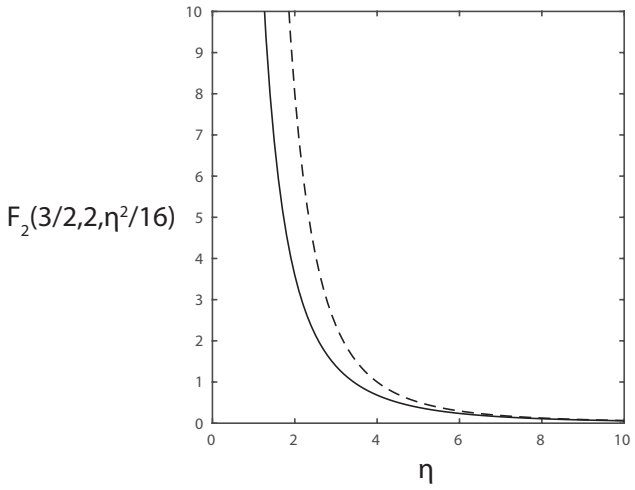

Fig. 2.5 Solid line; the hypergeometric function $F_2(3/2, 2, \eta^2/16)$. Dashed line; its far-field asymptotic behaviour, $64\eta^{-3}$.

In the far-field, we know that U decays. So we will have $U \ll \eta$ and $U' \ll 1$ for sufficiently large η. We can then approximate the momentum equation as

$$U'' + \left(\frac{3}{\eta} + \frac{\eta}{8}\right) U' + \frac{U}{8} = 0, \tag{2.34}$$

which is a simple second-order differential equation for U. The solutions to this differential equation are

$$U = A\mathrm{e}^{-\eta^2/16} F_2\left(\frac{3}{2}, 2, \frac{\eta^2}{16}\right) + B\mathrm{e}^{-\eta^2/32}\left(I_0\left(\frac{\eta^2}{32}\right) + I_1\left(\frac{\eta^2}{32}\right)\right), \tag{2.35}$$

where F_2 is the confluent hypergeometric function of the second kind[1] and I_ν are the modified Bessel functions of the first kind. The far-field condition (2.31) sets $B = 0$, leaving a one-parameter family of solutions parametrised by A. The function $F_2(3/2, 2, \eta^2/16)$ is shown in figure 2.5 and decays as $64\eta^{-3}$ for large η. So the velocity decays in the far-field as

$$U \sim \frac{64A}{\eta^3}\mathrm{e}^{-\eta^2/16}. \tag{2.36}$$

We note that, in physical variables, this is exponential decay over the lengthscale $(\nu t)^{1/2}$; the solution describes the diffusion of momentum from the edge of the sheet outwards. This exponential decay is also seen for solutions to the heat equation, as in the introduction.

[1] HypergeometricU in Mathematica

2.4 Expansion near the edge

The integral (2.33) diverges unless $1 + U/\eta + U' = 0$ at η_E, and since $U(\eta_E) = \eta_E/2$ at the edge, we must therefore have $U'(\eta_E) = -3/2$. Now the stress boundary condition (2.28) with $U' = -3/2$ gives $H(\eta_E) = 2/5$ for the non-dimensional thickness at the edge. We will see in chapter 3 that this is consistent with the detailed solution on the small scale of the edge. In dimensional terms, this corresponds to $h_E = 2\gamma t/5\mu$.

We can expand further with

$$H = \frac{2}{5} + H_1(\eta - \eta_E)^\alpha + \mathrm{O}((\eta - \eta_E)^{\alpha+1}, (\eta - \eta_E)), \tag{2.37}$$

$$U = \frac{\eta_E}{2} - \frac{3(\eta - \eta_E)}{2} + U_1(\eta - \eta_E)^\beta + \mathrm{O}((\eta - \eta_E)^{\beta+1}, (\eta - \eta_E)^2), \tag{2.38}$$

where H_1 and U_1 are constants and where α and β are exponents with $\alpha > 0$ and $\beta > 1$. In addition, we suppose that $\beta < 2$. Now we consider the leading-order terms of the conservation of mass equation (2.24). If $\beta < 2$, the leading-order balance is

$$\frac{5H_1\alpha(\eta - \eta_E)^{\alpha-1}}{2} = \frac{U_1\beta(\eta - \eta_E)^{\beta-2}}{2}, \tag{2.39}$$

and so we conclude that $5H_1\alpha = B\beta$ and $\beta = \alpha + 1$. Then the momentum equation (2.27) has leading-order terms

$$0 = U_1\beta(\beta - 1)(\eta - \eta_E)^{\beta-2} - \frac{25H_1\alpha(\eta - \eta_E)^{\alpha-1}}{8}, \tag{2.40}$$

and so we have $U_1\beta(\beta - 1) = 25H_1\alpha/8$. These simultaneous equations for H_1 and U_1 only have a non-zero solution if $\beta = 13/8$. This gives a consistent expansion near the edge:

$$H = \frac{2}{5} + H_1(\eta - \eta_E)^{5/8} + \mathrm{O}((\eta - \eta_E)), \tag{2.41}$$

$$U = \frac{\eta_E}{2} - \frac{3(\eta - \eta_E)}{2} + \frac{25H_1}{13}(\eta - \eta_E)^{13/8} + \mathrm{O}((\eta - \eta_E)^2). \tag{2.42}$$

The remaining constant H_1 is set by the solution away from the edge, and will depend on Oh.

2.5 Numerical solution

2.5.1 Similarity solutions

We intend to integrate (2.27) inwards from large η, but there is a numerical difficulty; we have seen that the velocity decays exponentially in the far-field. A naive approach to initialise with the far-field behaviour (2.36) would fail, as the exponentially small velocity is likely to be rounded to zero. Instead, we will take a logarithm, and solve for the function V such that $U = \exp(V)$. Then O(1) variations in the function V will capture the exponential variations in the velocity U. We make this substitution in the momentum equation (2.27) to find a second-order non-linear ordinary differential equation for V;

$$\frac{1}{4}\left(-\frac{1}{2}V' - \frac{\eta}{2}V' + \mathrm{e}^V V'\right) = V'' + \frac{V'}{\eta} - \frac{1}{\eta^2} + \frac{V'\mathrm{e}^V + \mathrm{e}^V/\eta + 1}{\eta/2 - \mathrm{e}^V}\left(V' + \frac{1}{2\eta}\right). \quad (2.43)$$

We integrate this differential equation inwards with the MATLAB routine `ode45`. The velocity is initialised with the far-field behaviour (2.36). We run the integration multiple times, varying the parameter A to explore the family of solutions. We integrate inwards through decreasing values of η until we reach a point with $U = \eta/2$, where we stop the integration. This gives a solution that satisfies the edge velocity boundary condition at some η_E.

With this velocity profile, we can calculate the sheet thickness. We integrate (2.33) numerically with our solution for U and U'. In the far-field, we know that H must grow as $\mathrm{Oh}^2\eta^2$, so we can infer the numerical value of Oh for a particular solution from the far-field growth of H. This gives the relationship between the edge position η_E and the Ohnesorge number Oh. By varying A, we find solutions with various Oh, and the corresponding solutions for the velocity and sheet thickness.

To find the solution for a particular value of Oh, we could perform a binary search on A, varying the parameter in the far-field in search of a solution with the correct far-field shape. With this method, we can find the sheet thickness and velocity for any value of Oh. Some representative solutions are shown in figure 2.6.

The dimensionless position of the sheet edge, η_E, is shown in figure 2.7 with a solid line. There are two clear asymptotic limits for $\mathrm{Oh} \ll 1$ or $\mathrm{Oh} \gg 1$. In each limit, there is some power-law for the dependence of η_E on Oh. We will find asymptotic solutions in each limit in §2.6 below.

Now we investigate the lengthscales in the solution. In figure 2.8, we plot the similarity solutions again, with the η-axis rescaled by a factor of η_E, and the velocity

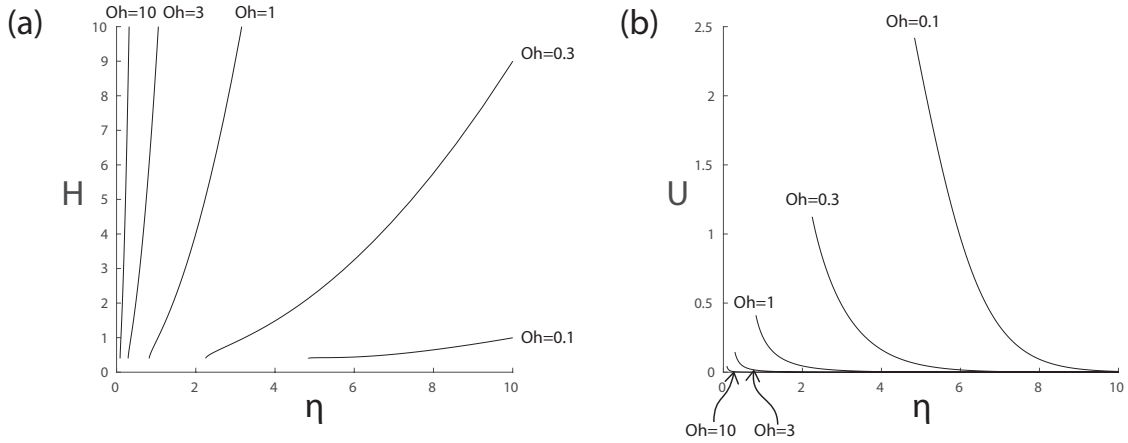

Fig. 2.6 (*a*) Shape and (*b*) velocity for the numerically-calculated similarity solutions with Oh = 0.1, 0.3, 1, 3 and 10.

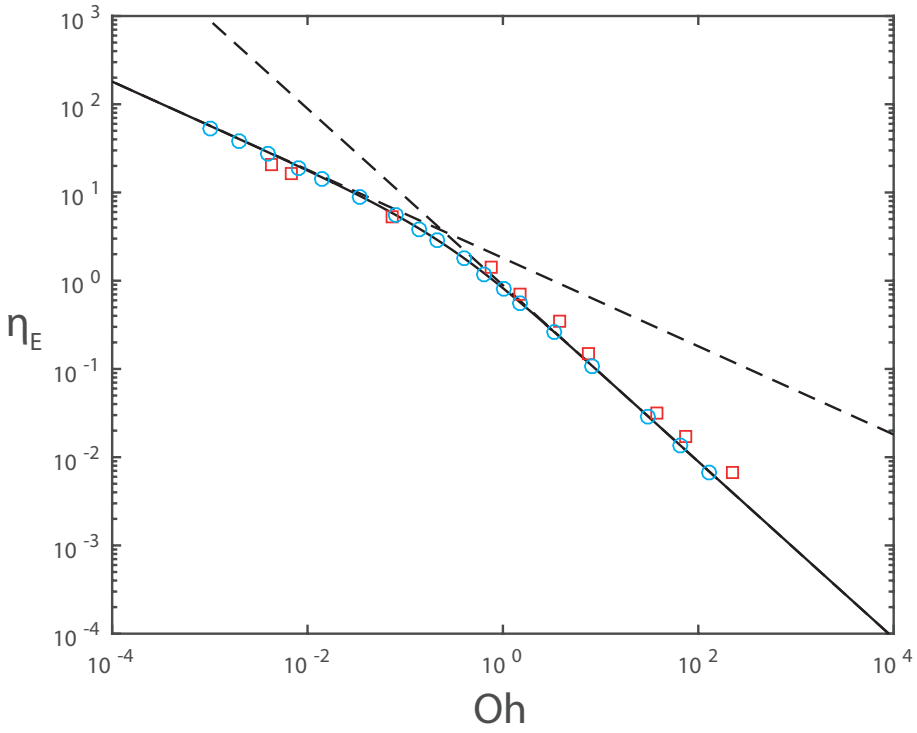

Fig. 2.7 Solid line; numerically-calculated similarity solutions for $\eta_E = r_E/(\nu t)^{1/2}$ over a range of Oh. Dashed lines; asymptotic expressions for small and large Oh given by (2.61) and (2.72). Squares; η_E inferred from the experiments of Paulsen *et al.* described in §2.5.2. Circles; η_E from the full Navier–Stokes solutions described in §2.7.

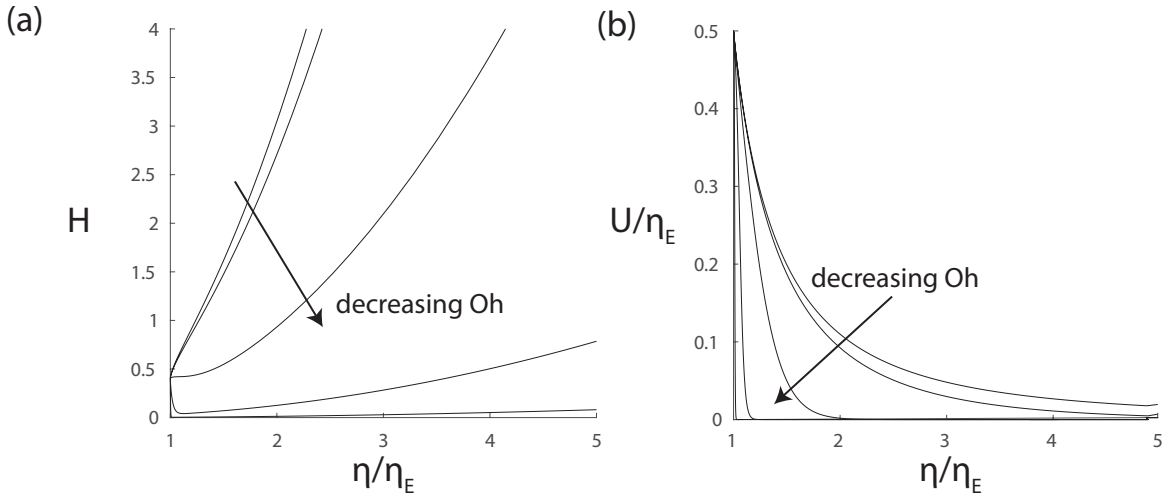

Fig. 2.8 (*a*) Shape and (*b*) velocity for the similarity solutions, with the velocity rescaled by a factor of η_E, each plotted a function of η/η_E, for Oh $= 10^{-3}$, 10^{-2}, 10^{-1}, 10^{0} and 10^{1}.

also rescaled so that all the solution curves pass through $\left(1, \frac{1}{2}\right)$. We note that η_E is a representative lengthscale of the solution for Oh > 1, but for Oh $\ll 1$, the solutions in figure 2.8 develop a new lengthscale which is shorter than η_E. This will be explored in more detail below, when we find an asymptotic solution for Oh $\ll 1$ in §2.6.1. Here, we note that although the lengthscale in the solution is shorter than expected in dimensionless terms, the sheet is still long and thin at early times; the argument that justified the use of the extensional flow equations was based on a separation of dimensional lengthscales by their growth with time, and holds even for sheets that appear to be short or thick in the dimensionless variables. This will be discussed further below.

2.5.2 Comparison with experiment

We can compare these results with the experiments by Paulsen *et al.* [50]. The squares in figure (2.7) show the experimental retraction rates from [50], converted to non-dimensional edge positions η_E, with the value of Oh calculated from the experimental values of μ, ρ, a and γ. There is good agreement between the experiments and the similarity solutions, which is remarkable for such a simple model. There is perhaps a slightly different gradient to the trend for each asymptotic limit. This is discussed below.

2.6 Asymptotic solutions

We've seen that the there is some power-law dependence of η_E on Oh for small and for large Oh. In this section, we will find the structure of the solution and solve reduced forms of the momentum equation in each limit.

2.6.1 Oh $\ll 1$

The solutions with Oh $\ll 1$ have a short lengthscale ahead of the edge at $\eta_E \gg 1$, indicating the presence of a boundary layer ahead of the moving edge. We therefore look for an asymptotic solution with a boundary-layer structure.

In this limit, the edge of the sheet is moving quickly into fluid with a low viscosity that is initially at rest. The boundary layer forms as momentum diffuses out from the fast-moving edge. We expect the dominant balance to be between the convective term and the diffusive term of the Navier–Stokes equations, which occurs if $\eta U' \sim U''$. taking $\eta \sim \eta_E$ but $U' \sim U/L$, we derive the lengthscale $L = \eta_E^{-1}$. On this scale, we expect $U \sim \eta_E$ since the boundary condition at η_E requires that $U = \eta_E/2$. We must solve the momentum equation to find the variation in velocity through the boundary layer. This will describe the acceleration of a fluid from rest to the speed of the edge over the short length of the boundary layer.

We rescale with $U = \eta_E V(x)$, where $\eta = \eta_E + x\eta_E^{-1}$. This gives the reduced equation

$$\frac{1}{4}\left(-\frac{1}{2}V_x + VV_x\right) = V_{xx} + \frac{V_x^2}{\frac{1}{2} - V}. \tag{2.44}$$

This is a non-linear second-order differential equation which can be solved exactly for

$$V = \frac{1 + (1 - 8\alpha)\mathrm{e}^{\alpha(x - x_0)}}{2\left(1 + \mathrm{e}^{\alpha(x - x_0)}\right)}, \tag{2.45}$$

where α and x_0 are arbitrary constants. The constant x_0 represents a change of origin, and is present because the differential equation is autonomous. The constant α represents the decay rate as we leave the boundary layer, and we will solve for that constant now.

We want the solution which decays to zero as $x \to \infty$. If $\alpha < 0$ then $V \to \frac{1}{2}$ as $x \to \infty$, so we must instead have $\alpha > 0$. But then $V \to (1 - 8\alpha)/2$ as $x \to \infty$, so we

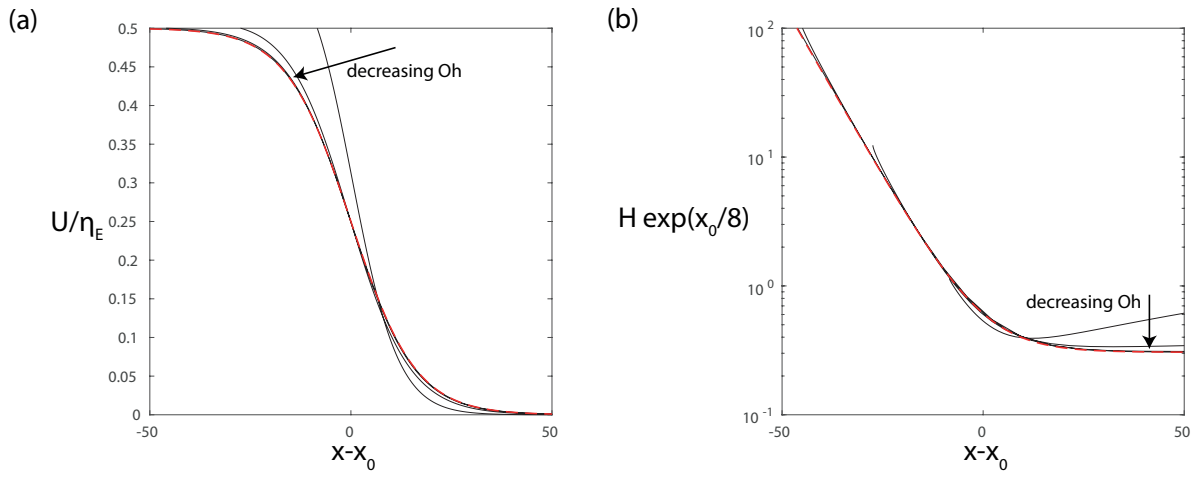

Fig. 2.9 Solid lines; the (a) rescaled velocity and (b) sheet thickness in the boundary layer, for the similarity solutions with Oh $= 3 \times 10^{-5}$, 3×10^{-4}, 3×10^{-3} and 3×10^{-2}. The boundary-layer co-ordinate x is defined by $\eta = \eta_E + x\eta_E^{-1}$, and the constant x_0 is calculated with (2.55). Dashed lines; the asymptotic solution for the velocity in the boundary layer (2.46) and the corresponding sheet thickness (2.58).

must have $\alpha = 1/8$. The velocity is therefore the sigmoid

$$V = \frac{1}{2\left(1 + \mathrm{e}^{(x-x_0)/8}\right)}, \tag{2.46}$$

which is shown in figure 2.9(a) with a red dashed line.

But now there is a problem: as $x \to -\infty$,

$$V \sim \frac{1}{2}(1 - \mathrm{e}^{(x-x_0)/8}), \tag{2.47}$$

which never reaches $\frac{1}{2}$. So we cannot apply our edge condition $V = \frac{1}{2}$. We might have anticipated this, as we know that at the edge $U'(\eta_E) = -3/2 = \mathrm{O}(1)$, whereas our boundary-layer solution with the scalings $U = \mathrm{O}(\eta_E)$, $L = 1/\eta_E$ can only have $U' = \mathrm{O}(\eta_E^2)$. We must instead match to an 'inner-inner' region near the edge, in which $U' = \mathrm{O}(1)$. The solution on this inner-inner scale will set the remaining constant x_0.

We rescale with the new scaling $U = \frac{1}{2}\eta + \omega(x)/\eta_E$ so that $\omega'(x) = \mathrm{O}(1)$ at the edge. The momentum equation (2.27) becomes

$$-\frac{1}{16} = \omega_{xx} - \frac{(\omega_x + 2)\left(\omega_x + \frac{3}{4}\right)}{\omega}. \tag{2.48}$$

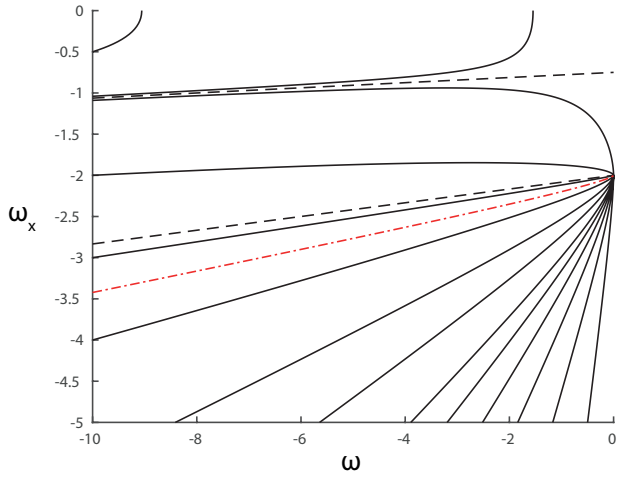

Fig. 2.10 Phase portrait for the dynamical system (2.49). Black dashed lines; exact solutions (2.51) Red dash-dotted line; the solution with $\omega_x = \omega/8$ for large negative ω.

This is a dynamical system for (ω, ω_x) if we write

$$\begin{pmatrix} \omega \\ \omega_x \end{pmatrix}_x = \begin{pmatrix} \omega_x \\ -\frac{1}{16} + (\omega_x + 2)(\omega_x + \frac{3}{4})/\omega \end{pmatrix}. \tag{2.49}$$

The phase portrait in (ω, ω_x)-space is shown in figure 2.10. Two exact solutions are shown with dashed lines; they satisfy

$$\omega_x = \frac{\omega}{12} - 2 \quad \text{or} \quad \omega_x = \frac{\omega}{32} - \frac{3}{4}. \tag{2.50}$$

with corresponding solutions

$$\omega = 6 + \mathrm{e}^{(x-x_1)/12} \quad \text{or} \quad \omega = 24 + \mathrm{e}^{(x-x_2)/32}, \tag{2.51}$$

where x_1 and x_2 are constants. The system is autonomous, so there is an arbitrary choice of origin for x.

There is a node at $(\omega, \omega_x) = (0, -3/2)$ and a saddle at $(0, -1/4)$; one of the exact solutions is the separatrix for the saddle point. There is a one-parameter family of solution curves that satisfy the boundary condition $(\omega, \omega_x) = (0, -3/2)$ at $x = 0$.

In order to match to the sigmoidal solution, we must find the solution which has $\omega_x \sim \omega/8$ when ω is large and negative and has $(\omega, \omega_x) = (0, -3/2)$ at $x = 0$. We note that this is neither of the exact solutions above in (2.51). We can find a solution with the correct far-field behaviour by integrating inwards from a point with large negative

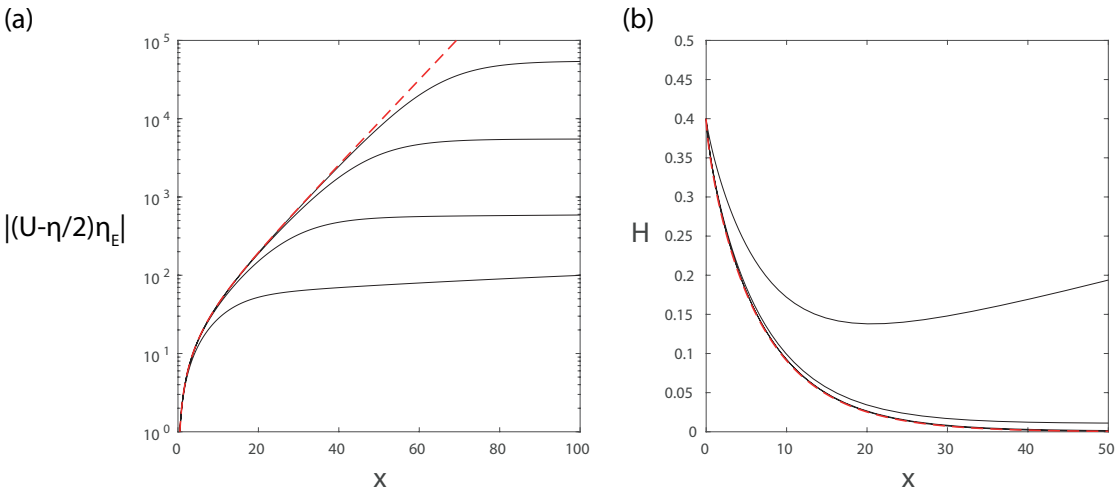

Fig. 2.11 Solid lines; the (a) velocity and (b) shape, for the similarity solutions with $\mathrm{Oh} = 3\times10^{-5}$, 3×10^{-4}, 3×10^{-3}, 3×10^{-2}. Dashed lines; the solution to the dynamical system (2.49) and the corresponding expression for the sheet thickness (2.56).

(ω, ω_x) and $\omega_x = \omega/8$. The phase portrait shows that we should start with $\omega < -8$ so that our initial condition is on the correct side of the separatrix. In fact, we shoot from $\omega = -10^{12}$, starting with an arbitrary value of $x = 300$. We shoot inwards until $\omega = 0$, and then choose the origin for x so that $x = 0$ at the edge. The solution for the velocity is shown in figure 2.11(a) with a red dashed line.

We can now infer the constant x_0 from the far-field behaviour of $\omega(x)$. The numerical solution has $\omega \sim -17.44\mathrm{e}^{x/8}$ for large x, and so

$$U = \frac{\eta}{2} + \frac{\omega}{\eta_E} \sim \frac{\eta_E}{2} - \frac{17.44}{\eta_E}\mathrm{e}^{x/8}. \tag{2.52}$$

On intermediate scales, the sigmoidal velocity (2.46) has

$$U = \eta_E V \sim \frac{\eta_E}{2}\left(1 - \mathrm{e}^{(x-x_0)/8}\right). \tag{2.53}$$

Matching these velocities gives

$$\frac{\eta_E}{2}\mathrm{e}^{(x-x_0)/8} = \frac{17.44}{\eta_E}\mathrm{e}^{x/8}, \tag{2.54}$$

and so

$$x_0 = -\,28.4 + 16\log\eta_E. \tag{2.55}$$

We have therefore determined the constants for the sigmoidal solution.

To check the boundary-layer solution, we can compare the similarity solutions found above with the asymptotic solution for the velocity. In figure 2.9(a), we plot the asymptotic solution for the sigmoidal velocity in the boundary layer with a red dashed line, and compare this with the similarity solutions for Oh $= 3 \times 10^{-5}$, 3×10^{-4}, 3×10^{-3} and 3×10^{-2}. For the similarity solutions, we have calculated x_0 with the equation (2.55). There is very good agreement between the numerically-calculated velocity profiles and the asymptotic sigmoid.

We can also compare the velocities on the inner-inner scale, rescaling the numerically-calculated similarity solutions according to $\omega = (U - \eta/2)\eta_E$. The rescaled solutions are shown in figure 2.11, and compared with the solution to the dynamical system, shown with a dashed red line. There is excellent agreement again, over a range of x. As Oh decreases, the agreement improves over a larger range of x. This corresponds to the slow change in x_0; for decreasing Oh, η_E increases according to some power-law, and so x_0 grows logarithmically with Oh according to (2.55). There is therefore a wider range of $0 < x \ll x_0$ and a wider range of applicability of the inner-inner region.

We can now calculate an asymptotic expression for the sheet thickness and hence the relationship between η_E and Oh. Integrating (2.33) in the inner-inner region for $x \ll x_0$ gives

$$\log\left(\frac{H}{2/5}\right) \sim \int_0^x \frac{\omega' + 2}{-\omega}\,\mathrm{d}x, \tag{2.56}$$

and we integrate this numerically to find the thickness in this region. This is shown in figure 2.11(b) with a red dashed line.

In the region where $x \sim x_0$, we must include the contribution to (2.33) from the sigmoidal V. A divide-and-conquer approach gives

$$\log\left(\frac{H}{2/5}\right) = \int_0^\delta \frac{\omega' + 2}{-\omega}\,\mathrm{d}x + \int_\delta^x \frac{V'}{\frac{1}{2} - V}\,\mathrm{d}x, \tag{2.57}$$

where we have chosen δ such that $1 \ll \delta \ll x_0$. Then with the sigmoid solution for V as above (2.46), the integral becomes

$$H = \frac{2}{5}\exp\left(\int_0^\infty \left\{\frac{\omega' + 2}{-\omega} + \frac{1}{8}\right\}\,\mathrm{d}x\right)\mathrm{e}^{-x_0/8}\left(1 + \mathrm{e}^{-(x-x_0)/8}\right). \tag{2.58}$$

The numerical value of the remaining integral in (2.58) is

$$\int_0^\infty \frac{\omega' + 2}{-\omega} + \frac{1}{8}\,\mathrm{d}x \approx -0.2688, \tag{2.59}$$

and the resulting sheet thickness is shown with a red dashed line in figure 2.9(b). In both figures, there is excellent agreement between the asymptotic solutions and the similarity solutions.

The sheet thickness therefore decays to the constant $(2/5)\exp(-0.2688 - x_0/8)$. Outside this region, the fluid is stationary, and the sheet is undisturbed with its initial thickness $\mathrm{Oh}^2\eta^2$, which we can approximate with $\mathrm{Oh}^2\eta_E^2$. Matching the sheet thickness (2.58) to this far-field value gives

$$\frac{2}{5}\mathrm{e}^{-0.2688-x_0/8} = \mathrm{Oh}^2\eta_E^2, \tag{2.60}$$

and using the expression for x_0 above reduces this to

$$\eta_E = 1.807\mathrm{Oh}^{-1/2}, \tag{2.61}$$

which is, as expected, a power-law relationship between the Ohnesorge number and the retraction rate of the sheet edge. This asymptotic expression is shown with a dashed line in figure 2.7, and agrees very well with the numerically-calculated similarity solutions in the limit $\mathrm{Oh} \ll 1$.

We note that, in dimensional terms, this asymptotic result for the growth of the hole is

$$r_E = 1.807\left(\frac{a\gamma}{\rho}\right)^{1/4} t^{1/2}, \tag{2.62}$$

which is independent of the viscosity. We will compare this below to other asymptotic results from the literature.

2.6.2 Oh $\gg 1$

When $\mathrm{Oh} \gg 1$, we expect viscous stresses to dominate and inertia to play no role. The similarity scalings above (2.22) are unwieldy for this problem as they depend explicitly on the kinematic viscosity. In this section, we will define new scalings based on the stress condition, the velocity boundary condition and the far-field sheet thickness;

$$\gamma \sim \frac{\mu U H}{L}, \quad U \sim \frac{L}{t}, \quad H \sim \frac{L^2}{a}. \tag{2.63}$$

These give

$$H \sim \frac{\gamma t}{\mu}, \quad L \sim \left(\frac{\gamma a t}{\mu}\right)^{1/2}, \quad U \sim \left(\frac{\gamma a}{\mu t}\right)^{1/2}. \tag{2.64}$$

We define the change of variables

$$r = \left(\frac{\gamma a t}{\mu}\right)^{1/2} \tilde{\eta}, \quad u = \left(\frac{\gamma a}{\mu t}\right)^{1/2} U(\tilde{\eta}), \quad h = \frac{\gamma t}{\mu} H(\tilde{\eta}), \tag{2.65}$$

which are different from the scalings above by a factor of Oh, and are independent of the density. Without inertia, we have the Stokes equations

$$U'' + \frac{U'}{\tilde{\eta}} - \frac{U}{\tilde{\eta}^2} + \left(\frac{U' + U/\tilde{\eta} + 1}{\tilde{\eta}/2 - U}\right)\left(U' + \frac{U}{2\tilde{\eta}}\right) = 0 \tag{2.66}$$

and

$$\frac{H'}{H} = \frac{U' + U/\tilde{\eta} + 1}{\tilde{\eta}/2 - U}. \tag{2.67}$$

The boundary conditions at the edge are

$$U(\tilde{\eta}_E) = \frac{\tilde{\eta}_E}{2} \quad \text{and} \quad 1 = -H(\tilde{\eta}_E)\left(2U' + \frac{U}{\tilde{\eta}}\right)\Bigg|_{\tilde{\eta}_E}, \tag{2.68}$$

and the far-field conditions are

$$\tilde{\eta} U \to 0, \quad H \sim \tilde{\eta}^2 \quad \text{as } \tilde{\eta} \to \infty. \tag{2.69}$$

In the far-field, the momentum equation becomes

$$U'' + \frac{3U'}{\tilde{\eta}} = 0, \tag{2.70}$$

with solutions $U = A\tilde{\eta}^{-2} + B$. We have $\tilde{\eta}U \to 0$, so $B = 0$. The velocity therefore decays algebraically as $U = A\tilde{\eta}^{-2}$ for $\tilde{\eta} \to \infty$.

As above, we can solve for the velocity numerically, integrating from the far-field to a point with $U = \tilde{\eta}/2$. Rather than varying A to search for the correct far-field decay as above, we can instead exploit a symmetry of the Stokes equations not present in the full non-linear problem. If we find the solution with $A = 1$ say, then we can rescale

$$\tilde{\eta} = k\bar{\eta}, \quad U = k\bar{U}, \quad \tilde{\eta}_E = k\bar{\eta}_E, \tag{2.71}$$

and this gives a new solution to the Stokes equations. We choose k so that the far-field shape $H \sim \tilde{\eta}^2$ is satisfied. The resulting shape and velocity profile are shown in figure 2.12. For comparison, we also show some of the similarity solutions found above

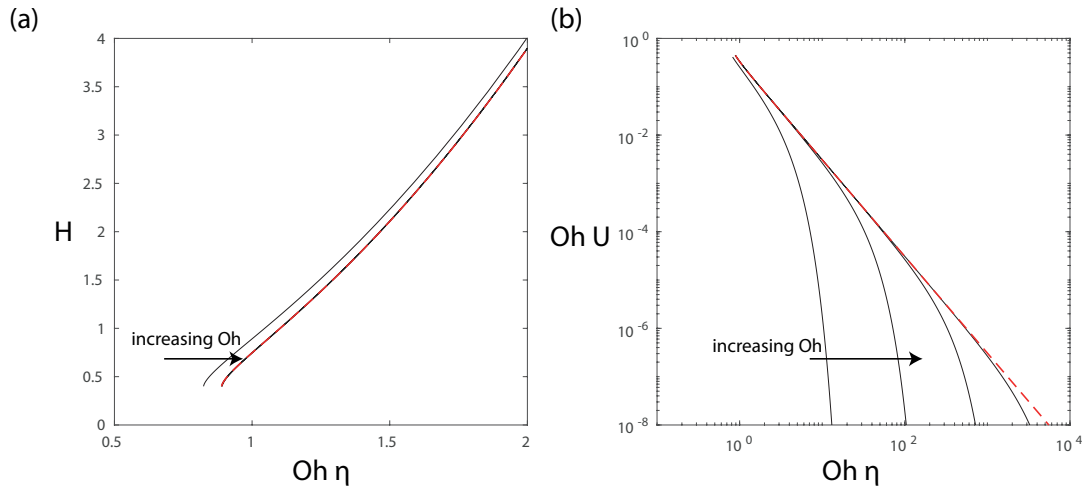

Fig. 2.12 Solid lines; the (a) shape and (b) velocity for the similarity solutions with Oh = 1, 10, 10^2, 10^3, rescaled to the viscous similarity solution variables. Dashed lines; the solution to the Stokes equations.

with large Ohnesorge number. There is very good agreement between the solutions, justifying the approximation that inertia could be neglected everywhere.

The edge position is $\tilde{\eta}_E = 0.8895$, which corresponds to

$$\eta_E = 0.8895\mathrm{Oh}^{-1}, \tag{2.72}$$

which is shown in figure 2.7 with a dashed line. There is very good agreement between the similarity solutions and the asymptotic expression.

In terms of dimensional variables, we have

$$r_E = 0.8895 \left(\frac{a\gamma}{\mu}\right)^{1/2} t^{1/2} \tag{2.73}$$

for Oh $\gg 1$. This asymptotic result is independent of the density.

2.7 Comparison with full Navier–Stokes solution

A group at Purdue University has also solved for the dynamics of bubble coalescence numerically [2]. Their approach makes fewer simplifying approximations, and attempts to solve the full Navier–Stokes equations without approximation, coupled to the full curvature for the surface. This approach has some advantages and disadvantages over our similarity solution approach, which we outline here before discussing their solution.

Firstly, the full Navier–Stokes model does not make any form of thin-sheet or long-wavelength approximation. Both the radial and axial components of the flow are calculated, and the full dependence of these velocity components on the radial and axial co-ordinates is accounted for. This could allow the full numerical solution to include the effects of higher-order terms in the flow, which we neglected above. To this end, the full numerical solution uses the full curvature across the surface everywhere, rather than neglecting the surface curvature away from the edge. This is computationally expensive.

The full numerical solution can in theory describe coalescence beyond the initial stage, including the full relaxation towards a single spherical bubble of radius $\sqrt[3]{2}a$.

There are some challenges associated with the full numerical approach. Our asymptotic model shows that there are many separate lengthscales for the initial stage of coalescence, and this requires a grid which resolves small scales near the edge of the sheet, while also resolving the large radial lengthscale of the bubbles. This is difficult for early times, and impossible for the initial condition since a pair of touching spheres is a geometrically singular configuration. The full numerical solution must be initialised from some 'nearby' configuration, and there will be some transient behaviour as the solution adjusts to the true dynamics.

The model used by Anthony *et al.* [2] uses advanced computational techniques to solve the Navier–Stokes equations. The code was developed by Christodoulou et al. [14] and has previously been used for drop breakup and coalescence [43, 44, 49]; the full details are beyond the scope of this discussion, and can be found in [2].

The surface shape is initialised with some small hole of radius r_E joining the bubbles with $r_E \ll a$. A natural choice would be for the sphere centres to be separated by a distance $2a$, as for two touching spheres. However, the initial condition used by Anthony *et al.* has the sphere centres separated by $2a + r_E^2/a$. The thickness of the fluid sheet has been arbitrarily increased by a constant r_E^2/a when compared with the distance between two spheres (2.5). This will cause some transient behaviour while the added thickness is comparable with the sheet thickness.

Anthony *et al.* extract the growth rate of the hole; neglecting the initial transients and the late-time relaxation to a single sphere, they fit a power-law to the growth. With a fixed exponent of $\frac{1}{2}$ (that is, fitting $r_E \propto t^{1/2}$), they find a growth rate for the initial stage. Their results are shown with circles in figure 2.7. There is very good agreement across the range of Oh between the similarity solutions and the full solutions, where the latter exists.

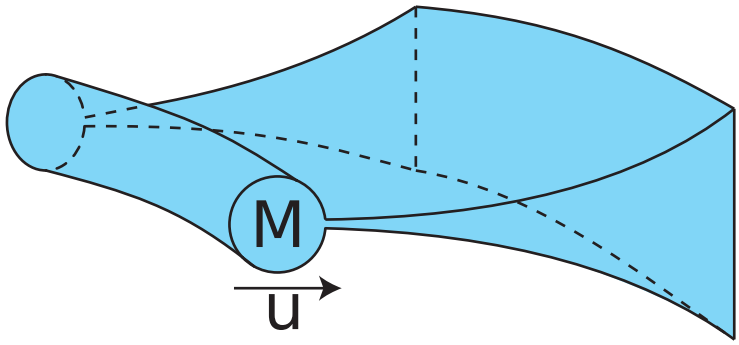

Fig. 2.13 Keller's model; fluid is swept up into a blob of mass M moving at uniform speed u.

2.8 Comparison with Keller's model

Previous work by Keller [33] gives an alternative solution for bubble coalescence when $\mathrm{Oh} \ll 1$. Neglecting viscosity entirely, Keller assumes that the fluid is collected into an expanding 'blob' or 'rim' of fluid, sketched in figure 2.13. Keller also assumes that the velocity in the rim has a uniform radial velocity $u\mathbf{e}_r$. If the fluid ahead of the rim is undisturbed, then the volume of fluid swept up by the expanding rim is simply given by the initial volume of the sheet in $r < r_E$. Working with a sector $\mathrm{d}\theta$ of the axisymmetric sheet, we have a mass

$$\mathrm{d}M = \rho \mathrm{d}\theta \int_0^{r_E} \frac{r^2}{a}\, r\, \mathrm{d}r = \rho \frac{r_E^4}{4a}\, \mathrm{d}\theta, \tag{2.74}$$

which has been swept up into the rim. The force from surface tension gives the rate of change of momentum

$$\rho \frac{\mathrm{d}}{\mathrm{d}t}\left(\frac{r_E^4}{4a}\frac{\mathrm{d}r_E}{\mathrm{d}t}\right) = 2\gamma r_E. \tag{2.75}$$

This equation has solution

$$r_E = \left(\frac{32a\gamma}{3\rho}\right)^{1/4} t^{1/2}. \tag{2.76}$$

Since $(32/3)^{1/4} \approx 1.807$, this is in agreement with the asymptotic solution above.

Our asymptotic solution above shows that, even with a small amount of viscosity, Keller's assumptions still hold. Our asymptotic structure shows that the sheet thins rapidly in the inner-inner region, while the velocity remains almost constant. This gives a boundary layer in which the majority of the mass is moving at the same speed. Our model also describes the convection-diffusion balance which smooths the velocity profile ahead of the edge, where the sheet is thinned.

We can even extend Keller's model to describe the transient effect of the unusual initial shape used for the full Navier–Stokes simulations by Anthony *et al.* [2]. Approximating the spheres with parabolas, the sheet has initial thickness

$$h \sim \frac{r^2}{a} + h_0 \tag{2.77}$$

for some constant h_0, which Anthony *et al.* vary before choosing $h_0 = r_E^2/a$. Once again, we recall that $h_0 = 0$ for two touching spheres, as in our model above. With this modified thickness (2.77), a balance of forces gives

$$\rho \frac{\mathrm{d}}{\mathrm{d}t}\left(\left(\frac{r_E^4}{4a} + \frac{h_0 r_E^2}{2}\right)\frac{\mathrm{d}r_E}{\mathrm{d}t}\right) = 2\gamma r_E. \tag{2.78}$$

We can non-dimensionalise r_E in this model with the bubble radius a, and the times with $t_\rho = (\rho a^3/\gamma)^{1/2}$. This choice removes all the fluid parameters from (2.78), leaving only the dimensionless number h_0/a. We integrate the differential equation numerically for various values of h_0/a, starting from rest with no accumulated mass. The resulting growth of the hole is shown in figure 2.14(a) for $h_0/a \in \{0, 10^{-6}, 9\times10^{-6}, 1.9\times10^{-5}, 9.9\times10^{-5}, 1.99\times10^{-4}\}$, for comparison with [2]. We note that the larger the value of h_0/a, the longer the transient before the solution approaches the similarity scaling $r_E/a \propto (t/t_\rho)^{1/2}$. The more extra fluid there is, the longer it takes before that volume of fluid is negligible compared with the mass accumulated. We may also note that even the solution with the 'correct' value for a pair of touching spheres, $h_0/a = 0$, has some transient behaviour. This is due to the fact that the numerical solution has been initialised from rest with no accumulated mass.

This transient behaviour can be qualitatively compared with the output of the full Navier-Stokes simulations from [2]. The curves shown in figure 2.14(b), adapted from [2], are the simulations with Oh = 0.1. We see that there is some qualitative agreement, indicating that the full numerical simulations suffer from the transient effects discussed here.

In summary, the full numerical simulations of bubble coalescence carried out by Anthony *et al.* have been initialised with more mass and less velocity than the similarity solution has at a corresponding value of the bridge radius. The transient behaviour observed in [2] for moderately small Oh can be understood in terms of a sheet of fluid accelerated by a force 2γ per unit azimuthal length, and a simple one-dimensional model can explain the behaviour observed.

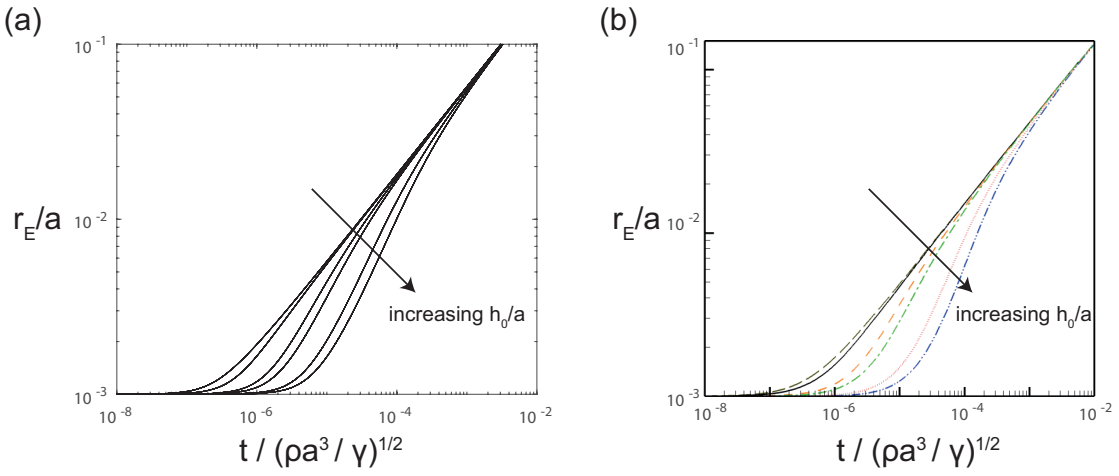

Fig. 2.14 (*a*) The result of integrating (2.78) numerically for various values of h_0/a given in the text. (*b*) The corresponding full Navier-Stokes simulations with Oh = 0.1 (reproduced from [2], figure 2).

2.9 Discussion

We have seen that

$$r_E \sim 0.8895 \left(\frac{a\gamma}{\mu}\right)^{1/2} t^{1/2} \text{ if Oh} \gg 1, \quad \text{and} \quad r_E \sim 1.807 \left(\frac{a\gamma}{\rho}\right)^{1/4} t^{1/2} \text{ if Oh} \ll 1. \tag{2.79}$$

The result in the limit Oh $\ll 1$ is in slight disagreement with the experimental observations of Paulsen *et al.* [50], in which the prefactor is closer to 1.4. This may be due to surfactant on the interface, which is likely to be accumulated at the edge of the expanding hole, where it will tend to decrease the coefficient of surface tension. We note that the diffusion of a surfactant could be easily included in the model presented above, since it would also involve a lengthscale proportional to $t^{1/2}$. Whether or not this could accurately model the actual surfactant dynamics is a question for future work.

The initial stage of coalescence described here requires $r_E \ll a$. For Oh $\gg 1$, the asymptotic expression for r_E shows that we need $t \ll a\mu/\gamma$ for this to be the case.

For Oh $\ll 1$ the question of asymptoticity is more complicated. Our asymptotic solution in §2.6.1 shows that the solution develops a new, short lengthscale near the edge. In dimensionless terms, this new lengthscale is proportional to η_E^{-1}. For the solution to be asymptotic, we need the thickness to be less than this lengthscale, and

so we need

$$\frac{\gamma t}{\mu} \ll \frac{(\nu t)^{1/2}}{\eta_E} \tag{2.80}$$

which is only true while $t \ll \mathrm{Oh}^3 \mu a/\gamma$. The corresponding condition on the edge position is $r_E \ll \mathrm{Oh}^2 a$, and since $\mathrm{Oh} \ll 1$, this is a much stricter inequality than $r_E \ll a$ (which is also necessary).

We can now critically evaluate some of the experiments and numerical simulations that have been done for the initial stage of bubble coalescence. Many of the numerical simulations carried out by the Purdue group [2] are initialised with $r_E > \mathrm{Oh}^2 a$, and as such cannot capture the initial stage of coalescence. Experimental observations with $r_E \ll \mathrm{Oh}^2 a$ are very difficult for even moderately small Oh.

After the initial stage, coalescence will continue as the surface tends to a single sphere. For viscous fluids with $\mathrm{Oh} \gg 1$, the initial stage ends when the fluid bridge is comparable in size to the radius of the bubbles. The surface will then relax to a sphere of radius $\sqrt[3]{2}a$ over a timescale proportional to $\mu a/\gamma$.

For more inviscid fluids with $\mathrm{Oh} \ll 1$, the initial stage ends when the 'blob' of accumulated fluid is no longer slender. The asymptotic solution in §2.6.1 above describes the initial retraction of a long, thin mass of fluid. At the cross-over time, this mass of fluid is no longer slender, and in the subsequent motion, we expect surface tension to round off this mass of fluid towards a round rim. We expect this round rim of fluid to move at a uniform speed, and so by the argument of Keller, the growth of the hole will be given by $r_E = (32/3)(a\gamma/\rho)^{1/2} t^{1/2}$. This is the same speed as before; the only difference is the geometry of the blob of fluid. As a result, the cross-over from the initial stage to the non-slender stage would be hard to observe from the time-dependence of r_E alone. The numerical simulations by Anthony *et al.* for $r_E \gg \mathrm{Oh}^2 a$ show a non-slender blob of fluid accumulating at the edge [2]. It would, be interesting to see a numerical simulation initialised with the slender shape described in §2.6.1, to confirm the change in geometry at a cross-over time proportional to $\mathrm{Oh}^3 \mu a/\gamma$.

For bubbles with unequal radii, our solution can easily be adapted by simply changing the value of a. For bubbles of radius a_1 and a_2, first we note that the thickness of the sheet is

$$h \sim \frac{r^2}{2a_1} + \frac{r^2}{2a_2} = \frac{r^2}{\bar{a}}, \quad \text{where} \quad \bar{a} = \frac{2a_1 a_2}{a_1 + a_2}. \tag{2.81}$$

In this expression, $\bar{a}$ is the harmonic mean of a_1 and a_2. Since we can neglect the curvature of the sheet while $r_E \ll a_1, a_2$, the initial stage of coalescence proceeds as

that of a pair of bubbles each with radius $\bar{a}$. To find the dynamics for a particular pair of bubbles, we would calculate the corresponding Ohnesorge number $\mu/\sqrt{\rho\bar{a}\gamma}$ and read off the rate of coalescence from figure 2.7.

In the special case of one bubble coalescing with a flat surface, we consider the limit $a_2 \to \infty$. In this limit, $\bar{a} \to 2a_1$. This case is relevant to the experiments of de Maleprade *et al.* [17]. They observe the spreading of a bubble on a super-hydrophobic slide coated with a thin layer of air. The Ohnesorge number is low, and the experimental observation is that the hole joining the bubble to the air on the slide grows as

$$r_{\scriptscriptstyle E} \sim (2.5 \pm 0.1)\left(\frac{\gamma a}{\rho}\right)^{1/4} t^{1/2}, \tag{2.82}$$

where a is the radius of the bubble. This is close to the prefactor $(64/3)^{1/4} \approx 2.15$ predicted by our theory.

2.10 Two-dimensional bubble coalescence

We can also consider coalescence of bubbles in two dimensions. The equations are simplified by the absence of a hoop stress, and we carry out the same analysis as the three-dimensional case above. This simplifies matters for the asymptotic solution for $\mathrm{Oh} \ll 1$ in two dimensions to the extent that we are able to solve the dynamical system on the inner-inner scale exactly. This gives an analytical expression for the asymptotic dependence of $\eta_{\scriptscriptstyle E}$ on Oh, which agrees precisely with a Keller-like argument. This is somewhat more satisfactory than the argument above, where the constant is precisely $(32/3)^{1/4}$ by the argument of Keller, but is only found numerically by the argument of §2.6.1. The two-dimensional case therefore shows more clearly the relationship between $\mathrm{Oh} \ll 1$ and $\mathrm{Oh} = 0$.

2.10.1 Equations of motion

With the scalings

$$r = (\nu t)^{1/2}\eta, \quad u = \left(\frac{\nu}{t}\right)^{1/2} U(\eta), \quad h = \frac{\gamma t}{\mu} H(\eta) \tag{2.83}$$

as above, the equations of motion are now

$$H' = H\left(\frac{1+U'}{\frac{\eta}{2}-U}\right), \quad \text{and} \quad \frac{1}{4}\left(-\frac{1}{2}U - \frac{1}{2}\eta U' + UU'\right) = U'' + \frac{H'}{H}U', \tag{2.84}$$

with boundary conditions

$$U = \frac{\eta_E}{2}, \quad HU' = -\frac{1}{2} \quad \text{at } \eta = \eta_E, \tag{2.85}$$

and far-field conditions

$$H \sim \mathrm{Oh}^2\eta^2, \quad \eta U \to 0 \quad \text{as } \eta \to \infty. \tag{2.86}$$

as above.

We eliminate H from the momentum equation to find

$$\frac{1}{4}\left(-\frac{1}{2}U - \frac{1}{2}\eta U' + UU'\right) = U'' + \left(\frac{1+U'}{\frac{\eta}{2} - U}\right)U', \tag{2.87}$$

and we will recover the thickness H with the integral

$$\log\left(\frac{H}{H(\eta_E)}\right) = \int_{\eta_E}^{\eta} \frac{1+U'}{\eta/2 - U}\,\mathrm{d}\eta. \tag{2.88}$$

This integral diverges unless $U' = -1$ at the edge. If this is the case, then we must have $H = 1/2$ at the edge by the stress boundary condition.

2.10.2 Far-field solution

In the far-field, where $U \ll \eta$ and $U' \ll 1$, the equation of motion becomes

$$U'' + \left(\frac{2}{\eta} + \frac{\eta}{8}\right)U' + \frac{U}{8} = 0, \tag{2.89}$$

with solutions $U = (A + B\mathrm{erf}(\eta/4))\eta^{-1}$. Since $\eta U \to 0$, the solution is

$$U = \frac{A}{\eta}\mathrm{erfc}\left(\frac{\eta}{4}\right), \tag{2.90}$$

where erfc is the complementary error function. This decays in the far-field as

$$U \sim \frac{4}{\sqrt{\pi}\eta^2}\mathrm{e}^{-\eta^2/16}. \tag{2.91}$$

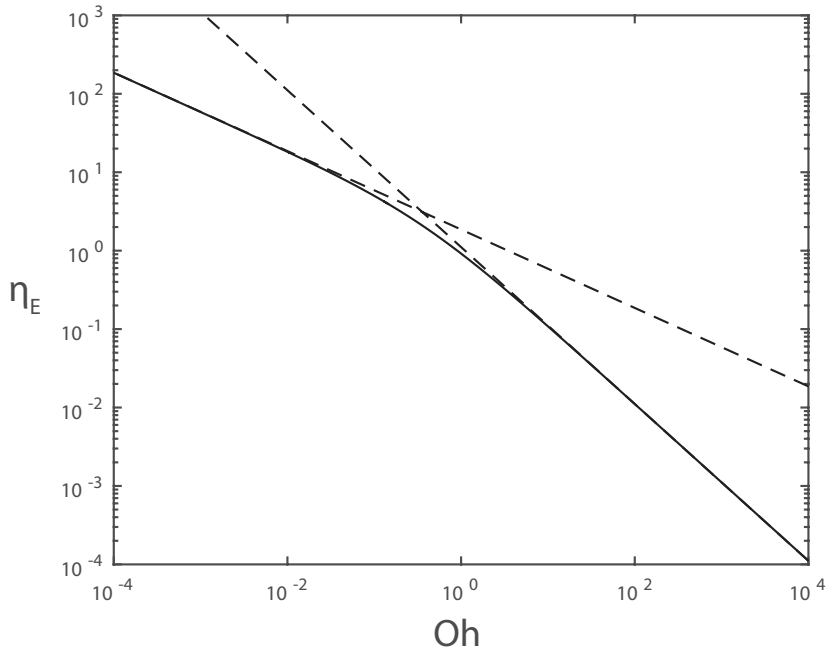

Fig. 2.15 Numerically-calculated η_E for coalescence of two-dimensional bubbles

2.10.3 Numerical solution

As above, we shoot inwards from the far-field behaviour, varying A to find the one-parameter family of solutions to the momentum equation (2.87), then we integrate (2.88) numerically to find the thickness and the value of Oh. The results for η_E as a function of Oh are shown in figure 2.15.

2.10.4 Asymptotic solution for Oh $\ll 1$

When Oh $\ll 1$, we expect a similar boundary layer structure to that described above for coalescence in three dimensions. Where $U \sim \eta_E$, we write $U = \eta_E V(x)$, with $\eta = \eta_E + x/\eta_E$. The momentum equation becomes

$$\frac{1}{4}\left(-\frac{1}{2}V_x + VV_x\right) = V_{xx} + \frac{V'}{\frac{1}{2} - V}V' \tag{2.92}$$

as above, with solution

$$V = \frac{1}{2(1 + \mathrm{e}^{(x-x_0)/8})}. \tag{2.93}$$

Once again, this fails near the edge, where $U' = \mathrm{O}(1)$. Near the edge, we rescale with $U = \frac{1}{2}\eta + \omega(x)/\eta_E$. The momentum equation (2.87) becomes

$$-\frac{1}{16} = \omega_{xx} - \frac{\left(\omega_x + \frac{3}{2}\right)\left(\omega_x + \frac{1}{2}\right)}{\omega}, \tag{2.94}$$

which is autonomous and can be converted to a dynamical system as before. More directly, there is an exact family of solutions

$$\omega = 12 + A\mathrm{e}^{x/8} \tag{2.95}$$

for any A. We want $\omega(0) = 0$, so $A = -12$. Then on this scale, the integral for the sheet thickness gives

$$\log\left(\frac{H}{1/2}\right) = \int_0^x \frac{3/2 + \omega_x}{-\omega}\,\mathrm{d}x' = -\frac{x}{8}, \tag{2.96}$$

so $H = \frac{1}{2}\mathrm{e}^{-x/8}$.

We match the inner solution to the sigmoid with $12/\eta_E = (\eta_E/2)\mathrm{e}^{-x_0/8}$. In the sigmoidal region, we have

$$\log\left(\frac{H}{1/2}\right) = \int_0^\delta \frac{\omega' + \frac{3}{2}}{-\omega}\,\mathrm{d}x' + \int_0^x \frac{V_x}{\frac{1}{2} - V}\,\mathrm{d}x'. \tag{2.97}$$

Rearranging this gives

$$\log\left(\frac{H}{1/2}\right) = \log\left(\frac{1 + e^{(x-x_0)/8}}{e^{(x-x_0)/8}}\right) - \frac{x_0}{8}, \tag{2.98}$$

and finally

$$H = \frac{12}{\eta_E^2}\frac{(1 + e^{(x-x_0)/8})}{e^{(x-x_0)/8}}. \tag{2.99}$$

In the far-field, the sheet thickness tends to $12/\eta_E^2$. We know that the far-field thickness is $\mathrm{Oh}^2\eta_E^2$, so we must have

$$\eta_E = 12^{1/4}\mathrm{Oh}^{-1/2}, \tag{2.100}$$

which gives the dashed line in figure 2.15.

2.10.5 Asymptotic solution for Oh $\gg 1$

When Oh $\gg 1$, we neglect inertia everywhere, and scale the momentum equation as above for the three-dimensional viscous asymptotic solution. This gives $\eta_E \sim 1.11/\mathrm{Oh}$, shown with a dashed line in figure 2.15.

2.10.6 Comparison with Keller's model

We can construct a simple 'blob' model for the retraction of an initially parabolic sheet in the manner of Culick or Keller [16, 33], as above in section 2.8. In two dimensions, we have

$$\rho \frac{\mathrm{d}}{\mathrm{d}t}\left(\frac{\mathrm{d}r_E}{\mathrm{d}t}\frac{r_E^3}{3a}\right) = 2\gamma, \tag{2.101}$$

with solution

$$r_E = \left(\frac{12a\gamma}{\rho}\right)^{1/4} t^{1/2}, \tag{2.102}$$

which agrees exactly with the asymptotic expression above.

2.10.7 Discussion

We have seen

$$r_E \sim 1.11\left(\frac{a\gamma}{\mu}\right)^{1/2} t^{1/2} \text{ if } \mathrm{Oh} \gg 1, \quad \text{and} \quad r_E \sim 12^{1/4}\left(\frac{a\gamma}{\rho}\right)^{1/4} t^{1/2} \text{ if } \mathrm{Oh} \ll 1 \tag{2.103}$$

for bubble coalescence in two dimensions.

In both the three-dimensional and the two-dimensional cases, the edge is rounded over the small scale of the thickness of the sheet at the edge, which is proportional to $\gamma t/\mu$. In the three-dimensional case, this edge is stretched by the hoop stress as it moves, with some time-dependent rate of stretching. For a ring of fluid of expanding radius $r_E(t)$, the stretching rate is

$$E = \frac{1}{r_E}\frac{\mathrm{d}r_E}{\mathrm{d}t}, \tag{2.104}$$

which is $1/(2t)$ for the three-dimensional case. There is no such stretching for the two-dimensional case.

In order to resolve the shape of the curved edge in each case, we might expect that it would be necessary to solve for each edge shape separately, either with or without stretching. In fact, we will find in chapter 3 that there is a universal similarity solution

for the retraction of stretched curved edges, and so the shape of these edges is the same in the two-dimensional and three-dimensional cases.

Chapter 3

Edge retraction

3.1 Introduction

3.1.1 Motivation

In chapter 2, we used a force balance argument to neglect the shape of the curved edge. The asymptotic separation of lengthscales allowed us to solve for the flow in the bulk of the sheet, modelling the force from surface tension with a stress condition at the edge of the sheet. Near the edge, the thin-sheet approximation used in the bulk of the sheet must fail, and the dominant lengthscale will be the thickness of the sheet. In this chapter, we will solve for the flow on the scale of the thickness of the sheet, and the shape of the curved edge. We will not be able to use the thin-sheet approximation, and we must solve the full Stokes equations, driven by the stress on the surface due to surface tension. This flow, coupled with the shape through the kinematic boundary condition, will give the evolution of the shape of the retracting edge. For bubble coalescence, this will give the shape of the edge of the sheet, on the scale of the thickness, as shown in figure 3.1.

We could solve for the particular problem of the sheet edge in three-dimensional bubble coalescence, for which there is a stretching rate $E = 1/(2t)$ along the sheet edge as discussed above. Instead, we will solve for an arbitrary time-dependent stretching rate $E(t)$. This solution will then be applicable not only to bubble coalescence in three dimensions, but also to any other stretched edge.

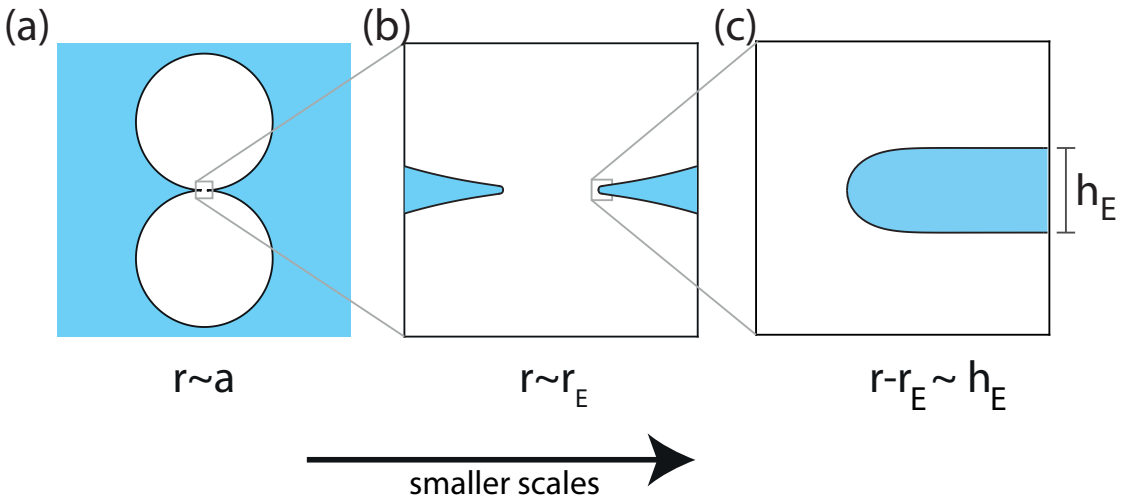

Fig. 3.1 Scales for bubble coalescence. In the previous chapter, we solved for the shape on the $(\nu t)^{1/2}$ scale. Here, we will solve for the shape on the scale proportional to h_E near the edge.

3.1.2 Context

A previous attempt by Brenner and Gueyffier [9] to describe the shape of a retracting edge used a thin-sheet approximation to resolve the shape. Their method is to keep the full curvature in the thin-sheet equations, without the corresponding terms of the velocity or pressure. There is no reason for this asymptotically inconsistent approach to give the right shape for the edge. The proper thin-sheet approximation would be to apply a stress condition at the edge of the sheet, with a finite thickness at the edge, as above with our solution for bubble coalescence.

Stretched fluid edges appear in industrial settings. Whenever a fluid sheet falls, or is pulled, through air, surface tension tends to round the edges of the sheet. The glass redrawing process involves a sheet of molten glass which is pulled through rollers in order to stretch it thinner. If the sheet is thin, then progress can be made by solving for the flow in the bulk of the sheet [e.g. 45, 46]. Our edge solution will describe the curved edges that invariably develop due to surface tension along the free edges of the sheet.

Our edge solution will also be applicable to a range problems with bursting sheets. Debrégeas *et al.* [19] report experiments on bursting with suspended sheets of very viscous polydimethylsiloxane (PDMS). The experiment begins with a thin sheet of PDMS held in a circular ring, which is burst at the centre of the sheet with a sharp needle. The hole grows and the sheet retracts. Debrégeas *et al.* present experimental evidence that the initial growth of the hole is exponential in the elapsed time, and give

an argument based on dissipation to support this exponential growth rate. We will use our edge solution to solve for the shape of the bursting sheet and the rate of growth of the hole, explaining the initial exponential growth.

3.1.3 Overview

We will solve for the Stokes flow in a retracting fluid edge, driven by surface tension and with constant stretching along the edge. Later, we will justify neglecting inertia in sufficiently thin sheets, and show how to adapt this solution to time-dependent stretching and fluid parameters.

By subtracting a particular solution associated with the stretching, we will reduce the problem to a two-dimensional Stokes flow driven by surface tension. We will solve this numerically with a boundary integral method, and advect the surface towards the similarity solution with the kinematic boundary condition.

In §3.2, we derive equations of motion for the problem. We expand these in the far-field in §3.3, and we solve the problem numerically in §3.4. The consistency of the solution and the range of possible applications are discussed in §3.5. In §3.6, we apply the edge solution to a problem with a bursting sheet.

3.2 Equations of motion

Let the dimensional pressure and velocity be $\hat{p}$ and $\hat{\mathbf{u}}$. The Stokes equations are

$$\mathbf{0} = -\hat{\boldsymbol{\nabla}}\hat{p} + \mu\hat{\nabla}^2\hat{\mathbf{u}}, \quad \hat{\boldsymbol{\nabla}}\cdot\hat{\mathbf{u}} = 0, \tag{3.1}$$

where μ is the dynamic viscosity. We will use a Cartesian co-ordinate system with the $\hat{z}$-axis along the edge of the sheet, the $\hat{y}$-axis across the thickness of the sheet and the mid-plane of the sheet in the $(\hat{x},\hat{z})$-plane, as shown in figure 3.2.

We write $\hat{\mathbf{X}}(\hat{s},\hat{t})$ for the position of the surface, where $\hat{s}$ is the arc-length and $\hat{t}$ is time, and then the kinematic boundary condition is

$$\frac{\partial\hat{\mathbf{X}}}{\partial\hat{t}}\cdot\hat{\mathbf{n}} = \hat{\mathbf{u}}\cdot\hat{\mathbf{n}}, \tag{3.2}$$

where $\hat{\mathbf{n}}$ is the outward normal to the surface, as shown in figure 3.2.

The dynamic boundary condition is

$$\hat{\boldsymbol{\sigma}}\cdot\hat{\mathbf{n}} = -\gamma\hat{\kappa}\hat{\mathbf{n}}, \tag{3.3}$$

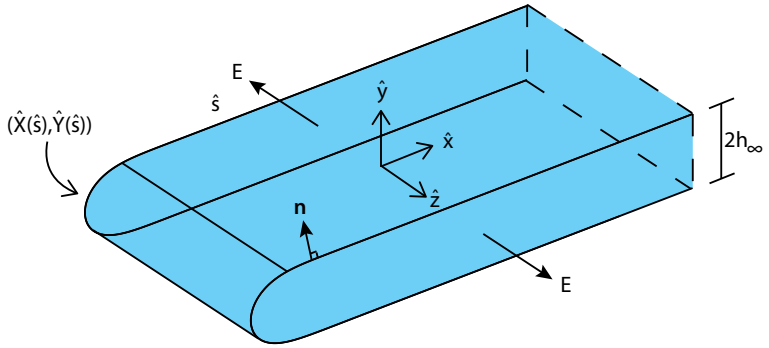

Fig. 3.2 The sheet is stretched along the edge with rate E. The mid-plane of the sheet is the $(\hat{x}, \hat{z})$-plane, with $\hat{z}$ along the edge. The $\hat{y}$-axis is normal to the mid-plane. The shape is given by $(\hat{X}, \hat{Y})$ and the far-field thickness is $2h_\infty$.

where $\hat{\kappa} = \hat{\boldsymbol{\nabla}} \cdot \hat{\mathbf{n}}$ is the surface curvature and γ is the coefficient of surface tension.

We will consider the retraction of a sheet with uniform thickness in the far-field $2h_\infty(\hat{t})$, as shown in figure 3.2, so that $Y \to h_\infty$ as $s \to \infty$. We will take the sheet to be uniform along the edge, so that h_∞ is independent of $\hat{z}$. As part of our solution, we will determine $h_\infty(\hat{t})$. Our sheet is stretched along its length, so that $\frac{\partial \hat{w}}{\partial \hat{z}} = E$ say. Then up to choice of origin in the $\hat{z}$-direction, we have $\hat{w} = E\hat{z}$.

Since the motion in the $\hat{z}$-direction is accounted for by the stretching, we are left with a two-dimensional problem for the components in the $(\hat{x}, \hat{y})$-plane. We write $\hat{\mathbf{u}}_H = (\hat{u}, \hat{v})$ for this cross-sectional velocity, for which the Stokes equations are

$$\hat{\boldsymbol{\nabla}}_H \cdot \hat{\mathbf{u}}_H = -E, \quad \mathbf{0} = -\hat{\boldsymbol{\nabla}}_H \hat{p} + \mu \hat{\nabla}_H^2 \hat{\mathbf{u}}_H, \tag{3.4}$$

where ∇_H^2 is the two-dimensional Laplace operator $\frac{\partial^2}{\partial \hat{x}^2} + \frac{\partial^2}{\partial \hat{y}^2}$. The dynamic boundary condition is

$$\hat{\boldsymbol{\sigma}} \cdot \hat{\mathbf{n}} = -\gamma \hat{\kappa} \hat{\mathbf{n}}, \tag{3.5}$$

as the normal lies in the $(\hat{x}, \hat{y})$-plane. The kinematic boundary condition is

$$\frac{\partial \hat{\mathbf{X}}}{\partial \hat{t}} \cdot \hat{\mathbf{n}} = \hat{\mathbf{u}}_H \cdot \hat{\mathbf{n}}. \tag{3.6}$$

Now we consider the far-field of the edge. Since the forces must balance for a Stokes flow, the far-field stress must balance the net force from surface tension. So $2h_\infty \hat{\sigma}_{xx} = 2\gamma$. Together with mass conservation and the lateral stretching rate E, this

gives the far-field velocity and pressure

$$\hat{\mathbf{u}}_H \sim \frac{\gamma}{4\mu h_\infty}(-\hat{x},\hat{y}) - \frac{E}{2}(\hat{x},\hat{y}), \quad \hat{p} \sim \frac{\gamma}{2h_\infty} - \mu E \quad \text{as } \hat{x} \to \infty, \tag{3.7}$$

up to a solid-body motion, which we have chosen to be zero.

This far-field velocity, with the kinematic boundary condition, gives the differential equation for the thickness

$$\frac{\mathrm{d}h_\infty}{\mathrm{d}\hat{t}} = \frac{\gamma}{4\mu} - \frac{Eh_\infty}{2}. \tag{3.8}$$

This describes the rate that the sheet thickens as a result of surface tension and the stretching. We see that surface tension compresses the sheet in the $\hat{x}$-direction and tends to thicken the sheet. Meanwhile, if the sheet is stretched with $E > 0$, then this tends to pull the sheet thinner. The general solution is

$$h_\infty = h_0 \exp\left(-\int_0^t \frac{E}{2}\,\mathrm{d}t'\right) + \frac{\gamma}{4\mu}\exp\left(-\int_0^t \frac{E}{2}\,\mathrm{d}t'\right)\int_0^{\hat{t}} \exp\left(\int_0^\tau \frac{E(t')}{2}\,\mathrm{d}t'\right)\mathrm{d}\tau. \tag{3.9}$$

If $E(\hat{t}) \equiv E_0$ is constant in time, then this simplifies to

$$h_\infty = h_0 \mathrm{e}^{-E_0 t/2} + \frac{\gamma}{2\mu E_0}\left(1 - \mathrm{e}^{-E_0 t/2}\right), \tag{3.10}$$

and so, if $E_0 > 0$, then $h_\infty \to \gamma/(2\mu E_0)$ as $t \to \infty$. This is the minimum thickness that the sheet can be stretched to by the stretching rate E_0, while it retracts under surface tension.

With $E_0 = 0$, the solution is $h_\infty = \gamma\hat{t}/4\mu$. This agrees with the edge thickness for two-dimensional bubble coalescence above (we recall that the thickness is $2h_\infty = \gamma t/2\mu$ in §2.10).

If instead $E = 1/(2\hat{t})$, which is the time-dependent stretching rate for three-dimensional bubble coalescence, then the differential equation (3.8) has solution

$$h_\infty = \frac{\gamma\hat{t}}{5\mu} + C\hat{t}^{-1/4}. \tag{3.11}$$

With the additional condition that $h_\infty \to 0$ as $t \to 0$, this gives $h_\infty = \gamma\hat{t}/5\mu$, which agrees with the thickness above in §2.4.

Now we return to the problem of determining the shape of the edge and the associated velocity field. The velocity $\hat{\mathbf{u}}_H$ does not satisfy the Stokes equations for

$E \neq 0$, as $\hat{\boldsymbol{\nabla}}_H \cdot \hat{\mathbf{u}}_H = -E$. But if we write

$$(\bar{u}, \bar{v}) = (\hat{u}, \hat{v}) + \frac{E}{2}(\hat{x}, \hat{y}), \quad \bar{p} = \hat{p} + \mu E, \tag{3.12}$$

then the velocity $\bar{\mathbf{u}} = (\bar{u}, \bar{v})$ does satisfy the Stokes equations. Moreover, the dynamic boundary condition becomes

$$\bar{\boldsymbol{\sigma}} \cdot \bar{\mathbf{n}} = -\gamma \hat{\kappa} \bar{\mathbf{n}}, \tag{3.13}$$

where $\bar{n} = \hat{n}$ is the normal, and the stretching E has been removed from the problem for the velocity at any instant. Now consider the kinematic boundary condition;

$$\frac{\partial \hat{\mathbf{X}}}{\partial \hat{t}} = \bar{\mathbf{u}} \cdot \bar{\mathbf{n}} - \frac{E}{2} \hat{\mathbf{X}} \cdot \bar{\mathbf{n}}. \tag{3.14}$$

We can also remove the stretching rate from this boundary condition by rescaling lengths and times. Let

$$\hat{\mathbf{x}} = h_\infty \mathbf{x}, \quad \hat{\mathbf{X}} = h_\infty \mathbf{X}, \quad \frac{\mathrm{d}t}{\mathrm{d}\hat{t}} = \frac{\gamma}{\mu h_\infty}, \tag{3.15}$$

and then

$$\frac{\gamma}{4\mu} \mathbf{X} \cdot \bar{\mathbf{n}} + \frac{\gamma}{\mu} \frac{\partial \mathbf{X}}{\partial t} = \bar{\mathbf{u}} \cdot \bar{\mathbf{n}}, \tag{3.16}$$

which removes E and h_∞ from the problem entirely. With the stretching rate prescribed, we can solve for h_∞ and then integrate $\gamma / \mu h_\infty$ to find the time rescaling. For three-dimensional bubble coalescence, as an example, we have seen above that $h_\infty = \gamma \hat{t} / 5\mu$. Integrating (3.15) gives $t = 5 \log \hat{t}$ up to a choice of constant. As another example, with $E \equiv E_0 > 0$ constant, h_∞ is given by (3.10), and the time rescaling is

$$t = 4 \log \left(1 + \frac{\gamma}{2\mu E_0 h_0} \left(\mathrm{e}^{E_0 t/2} - 1 \right) \right), \tag{3.17}$$

up to a constant.

With these scales, we need only solve a single problem independent of h_∞ and E, and then this single solution will apply to the surface-tension–driven retraction of any stretched edge, for any stretching rate $E(\hat{t})$.

We can non-dimensionalise the problem, and subtract the far-field linear velocity with

$$\bar{\mathbf{u}} = \frac{\gamma}{\mu} \mathbf{u} + \frac{\gamma}{4\mu h_\infty} (-\hat{x}, \hat{y}), \quad \bar{p} = \frac{\gamma}{2h_\infty} + \frac{\gamma}{h_\infty} p, \tag{3.18}$$

so that in the far-field, $\mathbf{u} \to \mathbf{0}$. This introduces some stress into the dynamic boundary condition:

$$\boldsymbol{\sigma} \cdot \boldsymbol{n} = -\kappa \boldsymbol{n} + \begin{pmatrix} -1 & 0 \\ 0 & 0 \end{pmatrix} \cdot \mathbf{n}, \tag{3.19}$$

and the kinematic boundary condition becomes

$$\frac{\partial \mathbf{X}}{\partial t} \cdot \mathbf{n} = \mathbf{u} \cdot \mathbf{n} - \frac{1}{2}(x, 0) \cdot \mathbf{n}. \tag{3.20}$$

We now have a non-dimensional problem to solve, with the velocity decaying in the far-field.

In summary, we take the physical variables $\hat{\mathbf{x}}$, $\hat{\mathbf{u}}$, $\hat{p}$ and $\hat{t}$ and non-dimensionalise by

$$(\hat{u}, \hat{v}) = \frac{\gamma}{\mu}\mathbf{u} + \frac{\gamma}{4\mu h_\infty}(-\hat{x}, \hat{y}) - \frac{E}{2}(\hat{x}, \hat{y}), \quad \hat{p} = \frac{\gamma}{h_\infty}p + \frac{\gamma}{2h_\infty} - \mu E, \tag{3.21}$$

$$\hat{\mathbf{x}} = h_\infty \mathbf{x}, \quad \hat{\mathbf{X}} = h_\infty \mathbf{X}, \quad t = \int^t \frac{\gamma}{\mu h_\infty(\hat{t})}\,\mathrm{d}\hat{t}, \tag{3.22}$$

where h_∞ is given by the solution to

$$\frac{\mathrm{d}h_\infty}{\mathrm{d}\hat{t}} = \frac{\gamma}{4\mu} - \frac{E h_\infty}{2}. \tag{3.23}$$

With these variables, we must solve

$$-\boldsymbol{\nabla} p + \nabla^2 \mathbf{u} = \mathbf{0}, \quad \boldsymbol{\nabla} \cdot \mathbf{u} = 0, \tag{3.24}$$

with dynamic boundary condition

$$-p\mathbf{n} + \left(\nabla \mathbf{u} + (\nabla \mathbf{u})^T\right) \cdot \mathbf{n} = -\kappa \mathbf{n} + \begin{pmatrix} -1 & 0 \\ 0 & 0 \end{pmatrix} \cdot \mathbf{n}, \tag{3.25}$$

and kinematic boundary condition

$$\frac{\partial \mathbf{X}}{\partial t} \cdot \mathbf{n} = \mathbf{u} \cdot \mathbf{n} - \frac{1}{2}(x, 0) \cdot \mathbf{n}, \tag{3.26}$$

with far-field conditions

$$\mathbf{u} \to \mathbf{0}, \quad p \to 0 \quad \text{as } x \to \infty, \text{ and} \quad Y \to 1 \quad \text{as } s \to \infty. \tag{3.27}$$

3.3 Far-field asymptotic solution

In the far-field, we can expand further by considering the variation in the sheet thickness as $Y \to 1$. We write

$$u = \frac{\partial \psi}{\partial y} \quad \text{and} \quad v = -\frac{\partial \psi}{\partial x}, \tag{3.28}$$

where ψ is the streamfunction. By the Stokes equations (3.24), this must satisfy the biharmonic equation $\nabla^4 \psi = 0$. On the surface, $Y(x) \approx 1$ and the normal is $\mathbf{n} \sim (-Y_x, 1)$ since $|Y_x| \ll 1$.

Now we linearise the kinematic boundary condition to $y = 1$. Since the velocity decays, we assume $|\psi| \ll 1$, and we keep the first-order terms in Y_x and ψ. The kinematic boundary condition becomes

$$\frac{\partial \psi}{\partial x} = \frac{x}{2}\frac{\mathrm{d}Y}{\mathrm{d}x} \quad \text{on } y = 1. \tag{3.29}$$

Similarly, the dynamic boundary condition becomes

$$-p - 2\frac{\partial^2 \psi}{\partial x \partial y} = \frac{\mathrm{d}^2 Y}{\mathrm{d}x^2} \quad \text{and} \quad \frac{\partial^2 \psi}{\partial x^2} - \frac{\partial^2 \psi}{\partial y^2} = \frac{\mathrm{d}Y}{\mathrm{d}x} \quad \text{on } y = 1. \tag{3.30}$$

where the normal stress is driven by the small curvature of the surface, and the tangential stress balances the small stress from the leading-order linear flow in the far-field. Recall that although the leading-order flow is large, the tangential stress is small since the normal is almost in the y-direction.

Now we take an x-derivative of the normal stress condition so that we can eliminate p with the Stokes equations. Also, we can use the kinematic boundary condition to eliminate Y_x. This gives boundary conditions on $y = 1$ in terms of ψ alone:

$$-\frac{\partial^3 \psi}{\partial y^3} - 3\frac{\partial^3 \psi}{\partial x^2 \partial y} = 2\frac{\partial^2}{\partial x^2}\left(\frac{1}{x}\frac{\partial \psi}{\partial x}\right) \quad \text{and} \quad \frac{\partial^2 \psi}{\partial x^2} - \frac{\partial^2 \psi}{\partial y^2} = \frac{2}{x}\frac{\partial \psi}{\partial x} \quad \text{on } y = 1. \tag{3.31}$$

We must solve $\nabla^4 \psi = 0$ with these boundary conditions. Without the surface stress, we would expect exponentially decaying solutions to the biharmonic equation. The boundary conditions suggest that we might make progress by expanding for large x with algebraically small terms to allow for the imposed stress. We consider a series of the form

$$\psi = \mathrm{Re}\left\{\sum_{i=1}^{\infty}\sum_{j=0}^{\infty} \phi_{i,j}(y)\mathrm{e}^{-\lambda_i x} x^{\sigma_i - j}\right\}, \tag{3.32}$$

where we will show that the λ_i are complex eigenvalues of the free-surface problem, and the functions $\phi_{i,0}(y)$ are the eigenfunctions. Then the terms $j \geq 1$ are the corrections due to the surface stress. We will show that the offset constants σ_i are necessary as the forcing of the correction is resonant, with the same spatial structure as the eigensolutions of the free-surface problem. By symmetry in the mid-plane of the sheet, we expect $\phi_{i,j}(y)$ to be odd in y.

We consider the leading-order term, $j = 0$, for the i^{th} mode, and find the biharmonic equation at leading order in x is

$$\left(\frac{\partial^2}{\partial y^2} + \lambda_i^2\right)^2 \phi_{i,0} = 0. \tag{3.33}$$

There are four solutions, of which only two are odd functions of y, and so we write

$$\phi_{i,0}(y) = A_{i,0} y \cos \lambda_i y + B_{i,0} \sin \lambda_i y, \tag{3.34}$$

for some constants $A_{i,0}$ and $B_{i,0}$. The boundary conditions (3.31) become a system of linear equations at leading order in x:

$$L_i \begin{pmatrix} A_{i,0} \\ B_{i,0} \end{pmatrix} = \mathbf{0}, \quad \text{where} \quad L_i = \begin{pmatrix} \sin \lambda_i & -\cos \lambda_i \\ \sin \lambda_i + \lambda_i \cos \lambda_i & \lambda_i \sin \lambda_i \end{pmatrix}. \tag{3.35}$$

The surface stresses will enter at further algebraic factors of x. At leading-order, we have free-surface eigenvalue problem for λ_i. There are non-trivial solutions only if $\det L_i = 0$, which requires

$$\sin 2\lambda_i + 2\lambda_i = 0. \tag{3.36}$$

We number the roots of (3.36) in order of increasing real part, with $\lambda_1 \approx 2.106 + 1.125\text{i}$, $\lambda_2 \approx 5.356 + 1.552\text{i}$ and so on. With these eigenvalues,

$$\phi_{i,0}(y) = A_{i,0} \left(y \cos \lambda_i y + \tan \lambda_i \sin \lambda_i y\right). \tag{3.37}$$

At the next algebraic order, $j = 1$, and the next order of the biharmonic equation gives

$$\phi_{i,1}(y) = A_{i,0} \sigma_i y^2 \sin \lambda_i y + A_{i,1} y \cos \lambda_i y + B_{i,1} \sin \lambda_i y. \tag{3.38}$$

The first term is driven by the leading-order flow through the Stokes equations and the other terms are the complementary solutions of the biharmonic equation. The

boundary conditions at this order become

$$L_i \begin{pmatrix} A_{i,1} \\ B_{i,1} \end{pmatrix} = A_{i,0} \begin{pmatrix} \sigma_i \cos\lambda_i - \sec\lambda_i \\ \sigma_i(2\cos\lambda_i - \lambda_i \sin\lambda_i) - \sec\lambda_i \end{pmatrix}, \tag{3.39}$$

which is a singular matrix problem for $A_{i,1}$ and $B_{i,1}$. The matrix L_i is the same as the leading-order free-surface problem. The right-hand side lies in the image of L_i only if $\sigma_i = \frac{1}{2}$. So the surface forcing is resonant. With this value for σ_i, we have

$$\phi_{i,1} = A_{i,0}\left(\frac{1}{2}(1+y^2) + \tan^2\lambda_i\right)\sin\lambda y + A_{i,1}(y\cos\lambda_i y + \tan\lambda_i \sin\lambda_i y). \tag{3.40}$$

This solution includes a multiple of the stress-free eigensolution at this order. The magnitude $A_{i,1}$ of this stress-free function cannot be determined by the imposed stress, and will be set at the next algebraic order.

We now proceed through algebraic orders by induction. For $j \geq 2$, suppose that we know $B_{i,k}$ in terms of $A_{i,0}$ for all $k < j$ and that we know $A_{i,k}$ in terms of $A_{i,0}$ for all $k < j-1$. Then the boundary conditions at the j^{th} order give

$$L_i(A_{i,j}, B_{i,j}) = A_{i,0}\mathbf{e}_1 + A_{i,j-1}\mathbf{e}_2, \tag{3.41}$$

where $\mathbf{e}_1$ and $\mathbf{e}_2$ are vectors depending on λ_i. There is a solution only if the right-hand side lies in the image of L_i, and this requirement gives an expression for $A_{i,j-1}$ in terms of $A_{i,0}$. The corresponding solution to the matrix problem (3.41) gives $B_{i,j}$. We can therefore induct to arbitrary algebraic order for each λ_i.

The leading-order expressions for the displacement and the velocity on the surface are the real parts of

$$(u, v) \sim A_{1,0}\mathrm{e}^{-\lambda_1 x}x^{1/2}(\cos\lambda_1, \lambda_1 \sec\lambda_1), \quad Y \sim 1 + 2A_{1,0}\sec\lambda_1 \mathrm{e}^{-\lambda_1 x}x^{-1/2}. \tag{3.42}$$

This corresponds to a series of counter-rotating eddies with wavelength $2\pi/\mathrm{Im}(\lambda_1) \approx 5.59$ times the sheet half-thickness, while the magnitude of the flow decays exponentially over the lengthscale $1/\mathrm{Re}(\lambda_1) \approx 0.475$ times the sheet half-thickness. This is similar to Moffatt's solution for eddies in a zero-angle wedge [40]. Here there is an additional factor of $x^{1/2}$ from the resonant free-surface forcing, and a series of further algebraic corrections.

With the first ten terms of the asymptotic expansion, the streamfunction is shown in figure 3.3. Numerically, the series seems to converge for $x \gtrsim 2$.

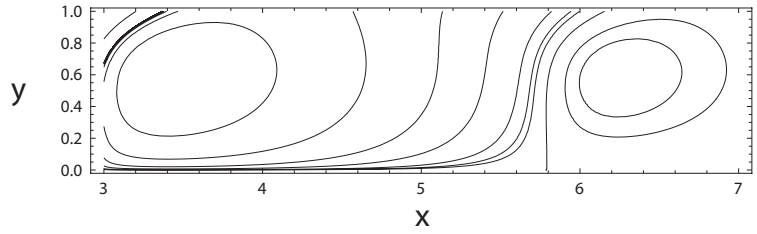

Fig. 3.3 Streamlines for the ten-term asymptotic expansion, showing the counter-rotating eddies. The contours shown here are not equally spaced.

3.4 Numerical solution

Armed with the far-field behaviour, we can now solve for the detailed shape of the edge numerically. We will use the boundary integral equation for a Stokes flow [e.g. 52], which gives the relationship between the velocity and stress on the surface. The boundary integral equation requires us to integrate over a surface enclosing the fluid. We will use the far-field asymptotic behaviour derived above for the far-field of the boundary integral. This allows us to include the effect of the far-field, while only solving numerically for the velocity in some finite region.

We divide the sheet into two regions: a local region $S_1 = \{(X, Y) : X - X(0, t) \leq 4\}$ and a far-field region $S_2 = \{(X, Y) : X - X(0, t) > 4\}$. In S_1, we solve for the velocity $\mathbf{u}$ by numerically inverting the boundary integral equation. The boundary integral equation for a point $\mathbf{y}$ on the surface is

$$\int_S \mathcal{J}(\mathbf{y} - \mathbf{x}) \cdot \boldsymbol{\sigma} \cdot \mathbf{n} \, \mathrm{d}s_{\mathbf{x}} + \int_S \mathbf{u} \cdot \mathcal{K}(\mathbf{y} - \mathbf{x}) \cdot \mathbf{n} \, \mathrm{d}s_{\mathbf{x}} = \frac{1}{2}\mathbf{u}(\mathbf{y}), , \tag{3.43}$$

where the tensors $\mathcal{J}$ and $\mathcal{K}$ are defined by

$$\mathcal{J}(\mathbf{x}) = \frac{1}{4\pi}\left(-I \log|\mathbf{x}| + \frac{\mathbf{xx}}{|\mathbf{x}|^2}\right), \quad \mathcal{K}(\mathbf{x}) = -\frac{\mathbf{xxx}}{\pi|\mathbf{x}|^4}, \tag{3.44}$$

and $\boldsymbol{\sigma} \cdot \mathbf{n}$ is given by the dynamic boundary condition. The integral is over points $\mathbf{x}$ on the surface, with respect to the arc-length s.

We discretise S_1 with grid points at points with co-ordinates $(X(s_i), Y(s_i))$ for $1 \leq i \leq n$. By the reflectional symmetry, we only need to paramterise the half of the surface with $Y > 0$, and we choose s to be zero at the nose; $Y(s_1) = 0$. Between the grid points, we interpolate $X(s)$ and $Y(s)$ with quintic splines over the arc-length s. Here, we use splines for X and Y separately, rather than fitting splines to Y as a function of X, since we expect $Y \sim X^{1/2}$ at the nose, which is difficult to capture with

splines (we cannot spline X as a function of Y since the far-field shape is not invertible near $Y = 1$; the asymptotic expressions above show that the shape oscillates around $Y = 1$ in the far-field).

The splines for the initial shape are calculated iteratively; starting with an initial guess for the splined shape and the values of s_i at each grid point, we calculate the arc-length along the spline and update the s_i values. Repeating this process a few times gives a quintic spline with the correct arc-length at each point. We have symmetry conditions on the splines at $s = 0$, and we set $Y'(s_n)$ and $Y''(s_n)$ to match to the asymptotic form for the far-field shape derived above, using the first ten terms of the series.

In S_2, we know the asymptotic form of the shape and the velocity field. We use this asymptotic form to integrate the boundary integral equation (3.43) numerically over $\mathbf{x}$ in S_2. This gives the far-field contribution to the integral.

For the local contribution, we must integrate over x in S_1. There is an issue of convergence; for any given $\mathbf{y}$ on the surface, the first integrand in (3.43) diverges at $s_\mathbf{x} = s_\mathbf{y}$, where $J(\mathbf{y} - \mathbf{x}) \cdot \boldsymbol{\sigma} \cdot \mathbf{n} \sim \log|s_\mathbf{y} - s_\mathbf{x}|\, \boldsymbol{\sigma}(\mathbf{y}) \cdot \mathbf{n}$. This singularity is in fact integrable, but is difficult to calculate numerically, as the integrand has large cancelling terms. To avoid this issue, we subtract the function $\log|s_\mathbf{y} - s_\mathbf{x}|\, \boldsymbol{\sigma}(\mathbf{y}) \cdot \mathbf{n}$ from the integrand on panels where the integrand diverges. This subtracted term can be integrated analytically, and the well-behaved remainder can be found with seven-point Gaussian quadrature.

The second integral in (3.43) depends on the unknown velocity $\mathbf{u}$; the contribution is linear in the velocity components, and we must find the linear map from the velocity components to the integral contributions at each point on the surface. We discretise the integral by considering a set of test functions for the velocity. For each component of the velocity at each grid point in S_1, we set a test function to one at that point and zero on the other points. We interpolate the velocity with quintic splines and again use Gaussian integration to find the contribution to the integral. The result of this discretisation is a matrix problem for the velocity components in S_1. We invert this matrix for the velocity in S_1.

We advect the surface with the kinematic boundary condition (3.26), using a time step of order 10^{-2}. After each advection step, we rescale the shape so that $Y(s_n) - 1$ matches the asymptotic expression derived above. We repeat and step forward in time up to $t = 30$ to allow any transients from the initial shape to decay.

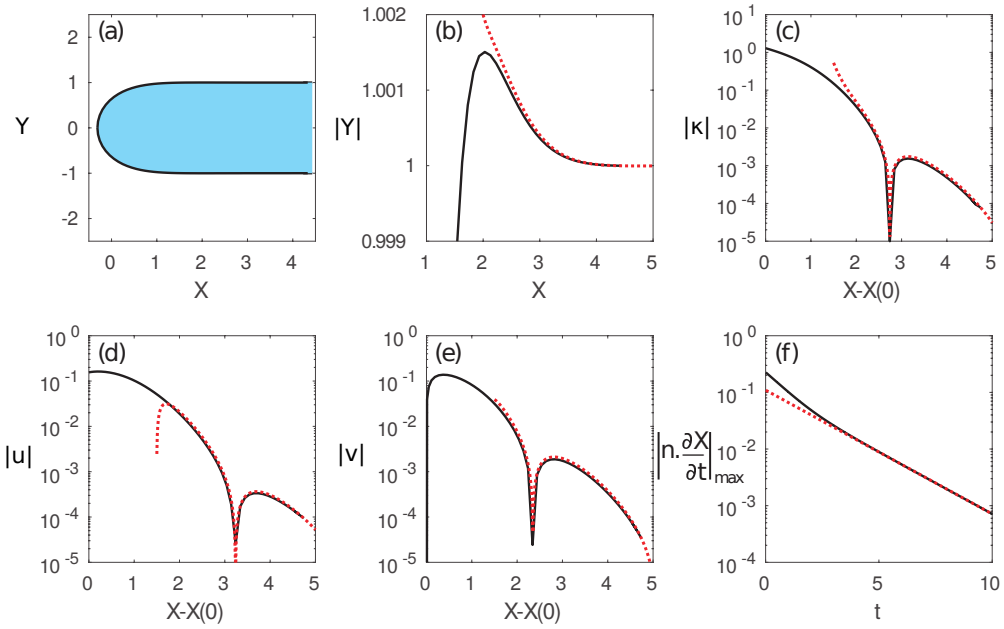

Fig. 3.4 The numerically calculated steady-state solution to (3.24)–(3.27) (solid lines) and its far-field behaviour (dashed lines). (a) The self-similar shape of the retracting edge. (b) The decay of the shape to its far-field thickness $Y = 1$. (c) The full curvature κ of the surface. (d)–(e) The velocity components $\mathbf{u} = (u, v)$, defined by (3.21). (f) The maximum of the normal velocity at each time step. In (b)–(e), the asymptotic solution found in section 3.3 is shown for comparison.

We initialise the shape with a rectangle of fluid rounded by a semicircular cap. With 51 points spaced so that $\Delta s \approx 0.1$, the far end of the rectangle is initially at $X(s_n) \approx 4.4$.

The shape relaxes to the steady-state solution shown in figure 3.4(a). The edge of the sheet is at $X(0) = -0.312$, and we recall that the origin of X (the frame of reference) was chosen such that the far-field velocity is given by (3.7). This choice implies that the steady-state shape must have the same area as a rectangle of height 2 with its end at $X = 0$. The sheet thickness does not monotonically decay to the far-field thickness; the maximum half-thickness is $Y = 1 + 1.5 \times 10^{-3}$ at $X = 2.03$, as shown in figure 3.4(b). Changing the number of points used to discretise the surface does not affect these constants, so we can be confident that we have resolved the shape accurately.

We can compare the shape and velocity with the far-field asymptotic series given above, calculating the amplitude $A_{1,0}$ of the series from the final velocity components $(u(s_n), v(s_n))$. Figure 3.4(b) shows the asymptotic decay of the surface shape to its far-field thickness, and there is good agreement between the numerically calculated

similarity solution and the asymptotic series. We compare the full curvature with Y_{XX} in figure 3.4(c), showing that the approximation $\kappa \sim Y_{XX}$ holds far from the edge. The velocity components are shown in figure 3.4(d)–(e). The numerically calculated values agree well with the far-field asymptotic series not only at s_n, where the series is set to match the velocity components, but also in some overlap region where $X - X(0) \gtrsim 2$. This verifies the accuracy of the solution.

The similarity solution is stable; changing the initial shape of the sheet does not affect the resultant steady state. Moreover, our numerical solution shows the decay rate of the slowest-decaying mode. Figure 3.4(f) shows the maximum absolute value of the normal component of the velocity at each time step. After some shorter-lived transients, the residual normal velocity decays exponentially with time. We fit an exponential to the data between $t = 5$ and $t = 10$ and find that the slowest mode decays proportional to $\mathrm{e}^{-0.50t}$ (shown as a dashed line in figure 3.4(f)). We can therefore be sure that the solution has converged to the required accuracy by time $t = 30$.

3.5 Discussion

This universal solution valid for all stretching rates E. We have confirmed that the far-field is the linear flow predicted from force balance, and shown that the next correction to this velocity decays exponentially. It would presumably be difficult to observe this exponentially decaying flow experimentally, or to see the eddies in the flow associated with the oscillatory decay of the velocity.

We have shown that surface tension causes a variation in thickness of just 0.15% near the edge, and moreover that this perturbation to the sheet thickness decays exponentially over the lengthscale of the sheet thickness. The sheet is therefore extremely flat in the far-field of this edge solution. This thickening of the edge is distinct from effects in the bulk of the sheet, such as the bubble coalescence solutions in the previous chapter. In that problem, for small Oh, the sheet thickness varied over a lengthscale proportional to $t^{1/2}$ as the fluid ahead of the edge was held at rest by inertia. O'Kiely *et al.* [45] describe edge thickening in a retracting edge, where the retraction is limited not by inertia, but by conditions on the flow impeding motion normal to the edge. In their study, the lateral extent of the edge is much larger than the thickness, so the edge solution above will describe the solution on the scale of the sheet thickness. Over the longer lengthscale of the lateral extent of the sheet, the boundary conditions on the ends of the sheet act to hold back the sheet, causing fluid to accumulate into a thickened rim.

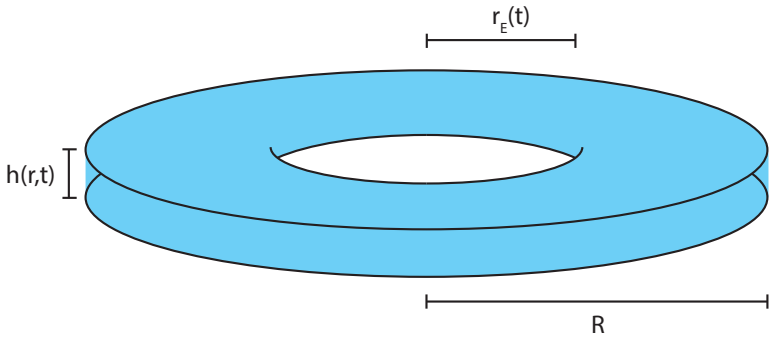

Fig. 3.5 Notation for a bursting film confined to a circle of radius R, with r_E the radius of the hole and $h(r,t)$ the thickness of the sheet.

The solution above neglects inertia. The lengthscale of the flow is h_∞, and the time scale is $\mu h_\infty/\gamma$. Comparing terms of the Navier–Stokes equations, we see that inertia is negligible if $\rho/T \ll \mu/L^2$, which is the case if $\mathrm{Oh}^2 \gg 1$, where $\mathrm{Oh} = \mu/\sqrt{\rho h_\infty \gamma}$ is the Ohnesorge number. This can be alternatively posed as a condition on the thickness of the sheet; if $h_\infty \ll \mu^2/\rho\gamma$ then inertia can be neglected.

In the work above, we neglected any variation of the sheet along the edge, and took the fluid parameters μ and γ to be constant. If μ and γ vary with time, the solution above still holds at any instant in time. The differential equation (3.8) for h_∞ will still hold with time-dependent μ and γ. If the sheet varies slowly along the edge (with typical lengthscale of the variation much larger than h_∞), then we can adapt the solution above, using material derivatives $\frac{\partial}{\partial t} + w\frac{\partial}{\partial z}$ in place of the time derivatives $\frac{\partial}{\partial t}$ to track the fluid parameters seen by a fluid parcel moving along the sheet edge.

3.6 Application to bursting

Because the edge solution is valid for all stretching rates, we can apply it to other problems with curved edges, even with an unknown stretching rate. For example, consider the bursting of a viscous axisymmetric liquid sheet with uniform initial thickness h_0, contained within a circular ring of radius R. If the sheet is burst at the centre of the circle, then we could consider the axisymmetric evolution of the hole in the sheet. Surface tension acting on the tightly curved edge of the hole will quickly pull the hole wider. We write $r_E(t)$ for the radius of the hole (using a subscript E since this is the position of the edge). We write $u(r,t)$ and $h(r,t)$ for the radial velocity and the thickness of the sheet.

Experiments by Debrégeas *et al.* [19] on this problem with a very viscous PDMS solution show that the radial velocity $u \propto 1/r$ at early times, while the hole grew exponentially; $r_E \propto \exp(\alpha t)$, with the growth rate α observed to be proportional to $\gamma/\mu h_0$. Debrégeas *et al.* attribute this exponential behaviour to viscoelasticity. However, later work has suggested that a viscous sheet would behave in this way. Savva and Bush [57] adapted Brenner and Gueyffier's model for a two-dimensional edge [9] to the axisymmetric case. As with Brenner and Gueyffier's model, this work attempts to use a thin-sheet approximation even where it is not valid (near the edge). In addition, Savva and Bush neglect variation in the film thickness outside of some curved cap of prescribed shape. Their solutions also include inertia, which will be negligible for a sufficiently viscous sheet by the argument above.

We will neglect inertia and solve the Stokes equations in the thin film, driven by surface tension at the edge, the shape of which is given by the similarity solution above. We will find the velocity, and show that $u \propto 1/r$ at early times. Then we will show that the film remains of uniform thickness, and solve exactly for the growth of the hole, confirming the initial exponential growth seen in the experiments, and predicting the subsequent growth of the hole confined by the circular ring.

The Stokes equations for a thin film are given above for bubble coalescence. The thickness h and radial velocity u of the sheet satisfy

$$\frac{\partial h}{\partial t} + \frac{1}{r}\frac{\partial (ruh)}{\partial r} = 0, \tag{3.45}$$

$$2\mu \frac{\partial}{\partial r}\left(hr\left(2\frac{\partial u}{\partial r} + \frac{u}{r}\right)\right) - 2\mu h\left(\frac{\partial u}{\partial r} + \frac{2u}{r}\right) = 0, \tag{3.46}$$

where we have neglected inertia, and neglected the pressure due to curvature in favour of the larger pressure driving the flow.

If, at some time, h is constant in space, then the momentum equation at that instant becomes

$$r\frac{\partial^2 u}{\partial r^2} + \frac{\partial u}{\partial r} - \frac{u}{r} = 0. \tag{3.47}$$

This has two solutions, so at that instant

$$u = Ar + \frac{B}{r} \tag{3.48}$$

for some A and B, independent of r.

Now conservation of mass (3.45), with h uniform, gives

$$\frac{\partial h}{\partial t} = -\frac{h}{r}\frac{\partial}{\partial r}\left(Ar^2 + B\right) \tag{3.49}$$

$$= -2Ah, \tag{3.50}$$

which is constant in space at the particular instant under consideration. So remarkably, any solution to the Stokes equations in this geometry with a flat film will keep the film flat, since the change in thickness is the same everywhere. Since the film is initially flat, we conclude that it remains flat for all time, and that the velocity has the form (3.48), where A and B may depend on time.

Debrégeas et al. consider an infinite sheet, and if we require the velocity to decay in the far-field, then we would have $u \propto 1/r$. Here, we will include the effect of confinement. The confining circular ring imposes $u(R) = 0$ and so $B = -AR^2$. The remaining constant will be set by the force applied from the curved edge; the stress at the edge is

$$2\frac{\partial u}{\partial r} + \frac{u}{r} = -\frac{\gamma}{\mu h}, \tag{3.51}$$

where h is the thickness of the sheet. So we have

$$A = -\frac{\gamma}{\mu h(3 + R^2/r_E^2)}. \tag{3.52}$$

and the velocity is

$$u = -\frac{\gamma}{\mu h(3 + R^2/r_E^2)}\left(r - \frac{R^2}{r}\right). \tag{3.53}$$

Now the velocity at the edge gives the rate of the growth of the hole

$$\frac{\mathrm{d}r_E}{\mathrm{d}t} = -\frac{\gamma}{\mu h(3 + \frac{R^2}{r_E^2})}\left(r_E - \frac{R^2}{r_E}\right). \tag{3.54}$$

We can find the growth of the thickness of the sheet from (3.50) or from the edge solution above (3.8), with $E = \dot{r_E}/r_E$ and recalling that h_∞ is half the thickness of the sheet. Either way, we have

$$\frac{1}{2}\frac{\mathrm{d}h}{\mathrm{d}t} = \frac{\gamma}{4\mu} - \frac{h}{4r_E}\frac{\mathrm{d}r_E}{\mathrm{d}t}. \tag{3.55}$$

We therefore have the system of equations

$$\frac{\mathrm{d}r_E}{\mathrm{d}t} = -\frac{\gamma r_E\,(1 - R^2/r_E^2)}{\mu h(3 + R^2/r_E^2)} \tag{3.56}$$

$$\frac{\mathrm{d}h}{\mathrm{d}t} = \frac{2\gamma}{\mu\,(3 + R^2/r_E^2)}. \tag{3.57}$$

These can be combined to form

$$(R^2 - r_E^2)\frac{\mathrm{d}h}{\mathrm{d}t} - 2r_E\frac{\mathrm{d}r_E}{\mathrm{d}t}h = 0, \tag{3.58}$$

so the volume $(R^2 - r_E^2)h$ is a constant; since the initial thickness is h_0 while the hole is much smaller than R, we must have $(R^2 - r_E^2)h = R^2h_0$. We are left with one ordinary differential equation for the motion

$$\frac{\mathrm{d}r_E}{\mathrm{d}t} = \frac{\gamma}{\mu h_0 R^2}\frac{(R^2 - r_E^2)^2}{r_E(3 + R^2/r_E^2)}. \tag{3.59}$$

Now we non-dimensionalise with $r_E = R\eta$ and $t = (\mu h_0/\gamma)\tau$:

$$\frac{\mathrm{d}\eta}{\mathrm{d}\tau} = \frac{\eta(1 - \eta^2)^2}{3\eta^2 + 1}. \tag{3.60}$$

This can be integrated exactly for

$$\tau - \tau_0 = \frac{2\eta^2}{1 - \eta^2} + \frac{1}{2}\log\left(\frac{\eta^2}{1 - \eta^2}\right), \tag{3.61}$$

and inverted for $\eta(\tau)$;

$$\eta = \sqrt{1 - \frac{4}{4 + W(4\exp(2(\tau - \tau_0)))}}, \tag{3.62}$$

where $W(z)$ is the Lambert-W function which satisfies $W(z)\exp W(z) = z$. This solution is shown in figure 3.6; at early times the hole grows slowly, and then it quickly rips open, before slowing as the confining circle begins to have an effect.

At early times, the hole grows as

$$r_E \sim R\exp\left(\frac{\gamma}{\mu h_0}(t - t_0)\right). \tag{3.63}$$

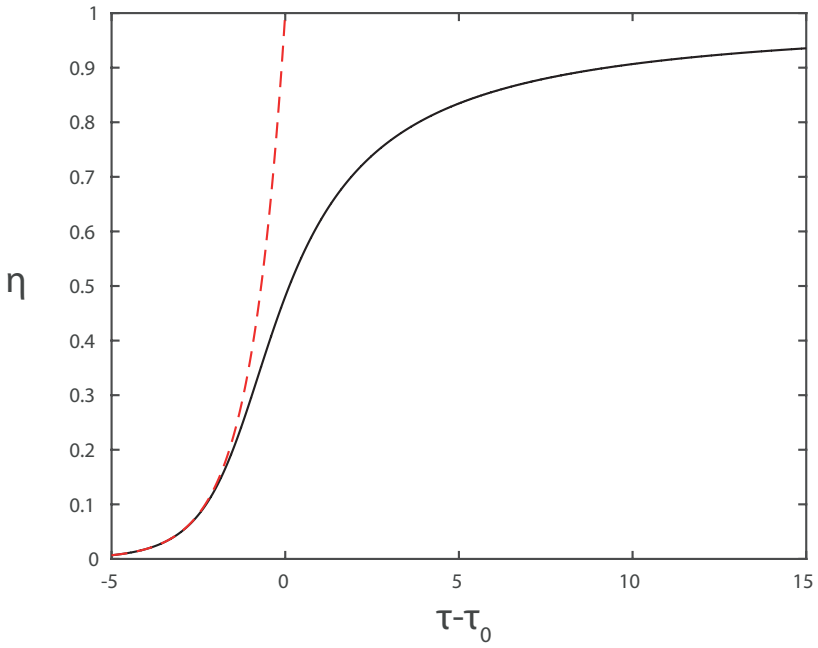

Fig. 3.6 Solid line; The growing radius r_E of a bursting hole, confined within a circular ring of radius R. The non-dimensionalised radius is $\eta(\tau) = r_E/R$, and the non-dimensionalised times $\tau = \gamma t/\mu h_0$. Red dashed line; the asymptotic behaviour (3.63).

This simple model agrees with the behaviour seen in the experiments, and continues the solution to times when the size of the hole is comparable to R. The Stokes equations explain the exponential growth, without the need for viscoelasticity. In addition, we have explained why the film remains flat, even with a confining ring. This solution is valid while the sheet thickness is smaller than the radius of the hole and the radial extent of the film, and therefore requires $h_E \ll r_E$ and $h_E \ll (R - r_E)$.

Chapter 4

Wedge retraction

4.1 Introduction

4.1.1 Context

In chapter 2, we solved for the thin-sheet flow between coalescing bubbles. For that problem, the fluid motion was limited to a thin sheet, and the Navier–Stokes equations reduced to the extensional flow equations for the thin sheet. For drop coalescence, we will need to solve for fluid flows that are three-dimensional in nature and not restricted to a thin sheet. Before we attempt the solution for drop coalescence, it will be useful to review some related work on the retraction of fluid wedges by Billingham [5, 6]. Billingham solves for the motion of a fluid mass which is initially in a wedge with half-angle α. The wedge retracts under the influence of surface tension.

When $\alpha \approx 0$, the fluid is limited to a thin sheet and when $\alpha \approx \pi$, the fluid fills almost all of the space. Billingham's asymptotic theory for the solution for wide wedges will be useful for our work on drop coalescence in chapters 5 and 6. In particular, we will see that some of the flows in this chapter can be applied directly to parts of the drop coalescence problem.

Here, we will review the structure of Billingham's solution and the asymptotic solutions for narrow and wide wedges. There are a few places where we can make technical improvements to Billingham's solution; in particular, we will replace a complicated numerical solution for a free-boundary Stokes flow with an analytical solution from the literature [31].

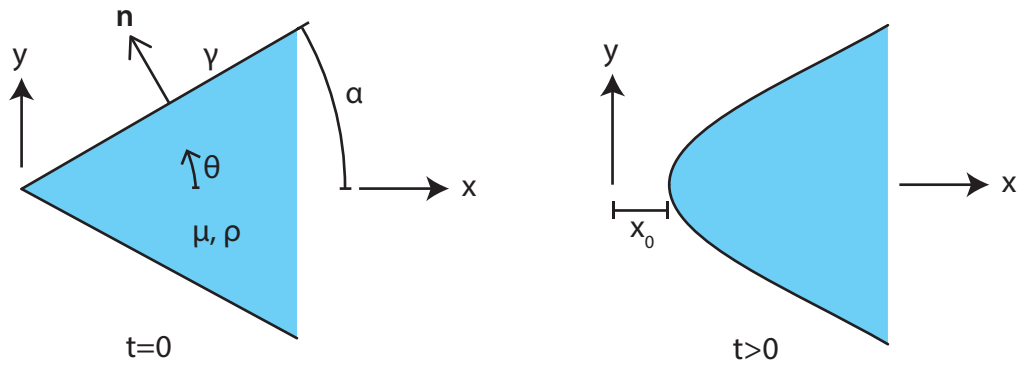

Fig. 4.1 Co-ordinates for the initial wedge shape. The x-axis is along the centreline of the wedge, and the y-axis is normal.

4.2 Overview

Billingham considers the early-time motion of a fluid mass initially at rest in some region $-\alpha < \theta < \alpha$, where θ is the polar angle [6]. We will focus on the two-dimensional version of the problem, with the fluid initially in a wedge (rather than the three-dimensional version, where $|\theta| < \alpha$ defines a cone). Let ρ be the density of the fluid, μ be the dynamic viscosity and γ be the coefficient of surface tension.

We define Cartesian axes with the x-axis along the centreline of the wedge, and the y-axis normal, as shown in figure 4.1. Note that our co-ordinate system is different from that of [6], where the y-axis is along the centreline of the wedge. We write $Y(x,t)$ for the surface position, and the initial wedge is at $Y = x\tan\alpha$. During the subsequent motion, we write the position of the tip of the wedge as $x_0(t)$ (Billingham writes $Y(0,t)$).

Surface tension drives a flow which is opposed by the viscosity and the inertia of the fluid. We have seen above that a balance of the unsteady term of the Navier–Stokes equations with the viscous term gives the lengthscale L, where $\rho/t \sim \mu/L^2$, that is, $L \sim (\nu t)^{1/2}$.

On smaller scales, we expect the viscous stress to dominate and the Stokes equations to hold. This suggests that the velocity near the tip will be proportional to γ/μ, the capillary velocity.

With this reasoning, we define an outer region with $x, y = \mathrm{O}((\nu t)^{1/2})$ where inertia and viscosity will both play a role, and an inner region $x \sim x_0 + \mathrm{O}(\gamma t/\mu)$, $y \sim \mathrm{O}(\gamma t/\mu)$ where the Stokes equations will hold. The scales are shown in figure 4.2. We note that $(\nu t)^{1/2} \gg \gamma t/\mu$ for sufficiently early times, so this structure is an asymptotic description of the initial stage of wedge retraction.

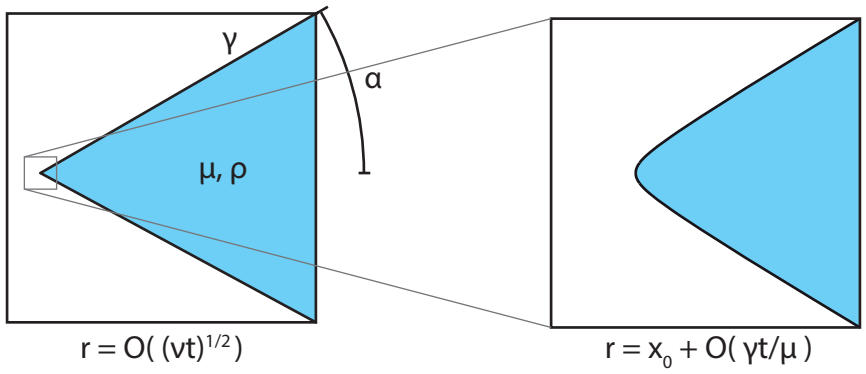

Fig. 4.2 Scales of the solution for the initial stage of wedge retraction. On the outer scale, inertia balances viscosity. On the inner scale, a Stokes flow sets the shape of the tip of the retracting wedge.

The outer diffusive scale will describe how inertia limits the motion of the wedge; since the wedge has mass, it cannot be easily accelerated by the force from surface tension. We review Billingham's solution on the outer scale in §4.3.

The inner scale describes the shape of the curved tip of the wedge. In the previous chapter, we solved for the shape of an edge with a constant far-field thickness. Here, the curved surface must tend to the right far-field shape set by the outer scale. Surface tension acting on the curved surface on this inner scale drives the flow, and the solution on this scale gives the distribution of that stress as well as the net effect on the larger scale.

We must solve for the unsteady Stokes flow on the outer scale to find the flow which decays to zero in the far-field, and we must solve for the Stokes flow on the inner scale to resolve the detailed shape. These flows match together to determine the rate of coalescence; in particular, the tip position x_0 is set by the matching.

We note that, inspired by slender-body theory, Billingham chooses to write $x_0 = K(\gamma t/\mu)\log(1/t) + \mathrm{O}(\gamma t/\mu)$ for some initially unknown K. Here, to show how the matching works that determines this leading-order position, we will not assume a particular form for x_0, but we will instead derive the leading-order solution for x_0 by asymptotic matching.

4.3 Solution on the outer scale

The problem on this scale is shown in figure 4.3. The flow is driven by surface tension from the curved tip, so the velocity is proportional to γ/μ. We non-dimensionalise

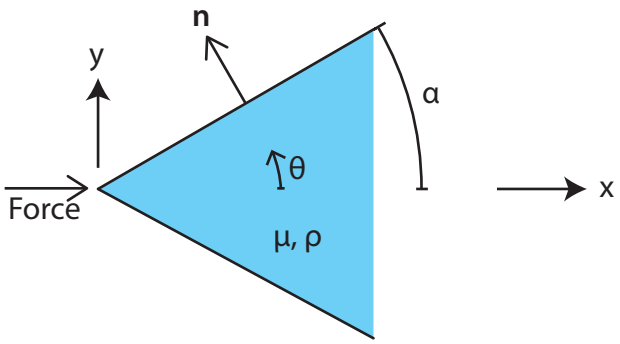

Fig. 4.3 Co-ordinates for the outer problem. The surface is near the initial wedge.

with

$$x = (\nu t)^{1/2}\tilde{x}, \quad y = (\nu t)^{1/2}\tilde{y}, \quad Y = x\tan\alpha + \frac{\gamma t}{\mu}\tilde{Y}, \quad p = \frac{\gamma}{(\nu t)^{1/2}}\tilde{p}, \quad \mathbf{u} = \frac{\gamma}{\mu}\tilde{\mathbf{u}}. \tag{4.1}$$

Now consider the terms of the Navier–Stokes equations. Since the lengthscale on the outer scale is $(\nu t)^{1/2} \gg \gamma t/\mu$, while the velocity is only proportional to γ/μ, we can neglect the non-linear term $\mathbf{u}\cdot\boldsymbol{\nabla}\mathbf{u}$ of the Navier–Stokes equations, and this gives the unsteady Stokes equations;

$$\rho\frac{\partial \mathbf{u}}{\partial t} = -\boldsymbol{\nabla}p + \mu\nabla^2\mathbf{u}, \quad \boldsymbol{\nabla}\cdot\mathbf{u} = 0. \tag{4.2}$$

With the non-dimensionalisation above, the unsteady Stokes equations become

$$-\frac{1}{2}\tilde{\mathbf{x}}\cdot\tilde{\boldsymbol{\nabla}}\tilde{\mathbf{u}} = -\tilde{\boldsymbol{\nabla}}p + \tilde{\nabla}^2\tilde{\mathbf{u}}, \quad \tilde{\boldsymbol{\nabla}}\cdot\tilde{\mathbf{u}} = 0. \tag{4.3}$$

The deviation from the initial wedge shape is small on this scale as $\gamma t/\mu \ll (\nu t)^{1/2}$. So we can linearise the boundary conditions to the initial wedge, and solve for the flow in the wedge $-\alpha < \theta < \alpha$ with boundary conditions on $\theta = \pm\alpha$.

The normal to the surface, $\boldsymbol{n}$, is therefore approximately $(-\sin\alpha, \cos\alpha)$. With this approximation, the kinematic boundary condition is

$$\frac{\partial Y}{\partial t} = u_y - u_x\tan\alpha, \tag{4.4}$$

where (u_x, u_y) are the velocity components. In terms of the non-dimensional variables, this is

$$\tilde{Y} - \frac{1}{2}\tilde{x}\frac{\mathrm{d}\tilde{Y}}{\mathrm{d}\tilde{x}} = \tilde{u}_y - \tilde{u}_x\tan\alpha. \tag{4.5}$$

Since the surface is almost flat, we can neglect the stress from surface tension away from the tip, as in chapter 2 for our thin-sheet solution for bubble coalescence. The stress boundary condition is

$$\begin{pmatrix} \tilde{\sigma}_{xx} & \tilde{\sigma}_{xy} \\ \tilde{\sigma}_{yx} & \tilde{\sigma}_{yy} \end{pmatrix} \cdot \begin{pmatrix} -\sin\alpha \\ \cos\alpha \end{pmatrix} = \mathbf{0}, \tag{4.6}$$

where $\tilde{\sigma} = -\tilde{p}\boldsymbol{I} + \mu(\tilde{\boldsymbol{\nabla}}\tilde{\mathbf{u}} + (\tilde{\boldsymbol{\nabla}}\tilde{\mathbf{u}})^T)$. The normal and tangential components are

$$-\cos\alpha\,\sin\alpha\,\tilde{\sigma}_{xx} + \cos\alpha\,\sin\alpha\,\tilde{\sigma}_{yy} + (\cos^2\alpha - \sin^2\alpha)\tilde{\sigma}_{xy} = 0, \tag{4.7}$$

$$\sin^2\alpha\tilde{\sigma}_{xx} + \cos^2\alpha\tilde{\sigma}_{yy} - 2\cos\alpha\,\sin\alpha\,\tilde{\sigma}_{xy} = 0, \tag{4.8}$$

and in terms of the pressure and velocity, these are

$$\begin{aligned} -\tilde{p} + 2\cos 2\alpha\frac{\partial\tilde{u}_y}{\partial y} - \sin 2\alpha\left(\frac{\partial\tilde{u}_x}{\partial y} + \frac{\partial\tilde{u}_y}{\partial x}\right) &= 0, \\ 2\sin 2\alpha\frac{\partial\tilde{u}_y}{\partial y} + \cos 2\alpha\left(\frac{\partial\tilde{u}_x}{\partial y} + \frac{\partial\tilde{u}_y}{\partial x}\right) &= 0. \end{aligned} \tag{4.9}$$

We define a streamfunction $\tilde{\psi}$ such that

$$\tilde{u}_x = \frac{\partial\tilde{\psi}}{\partial y}, \quad \tilde{u}_y = -\frac{\partial\tilde{\psi}}{\partial x}. \tag{4.10}$$

The problem so far is homogeneous; there is no flow unless we specify the conditions at the origin. Formally, we should solve for the generic solution on the inner scale and find its far-field behaviour. However, without solving for the details of the inner shape, we can employ the argument that we used before in §2.2 to deduce the net force from surface tension. In that section, we showed that the net effect of surface tension is a Stokeslet in the far-field. In two dimensions, the Stokeslet flow is

$$\mathbf{u} = \frac{\mathbf{F}}{4\pi\mu} \cdot \left(-\mathbf{I}\log r + \frac{\mathbf{xx}}{r^2}\right), \tag{4.11}$$

and the stress tensor is

$$\boldsymbol{\sigma} = -\frac{\mathbf{F}\cdot\mathbf{x}\,\mathbf{x}\,\mathbf{x}}{\pi r^4}. \tag{4.12}$$

Importantly, we note that if $\mathbf{x}\cdot\mathbf{n} = 0$ then $\boldsymbol{\sigma}\cdot\mathbf{n} = \mathbf{0}$. So the Stokeslet velocity satisfies the stress boundary condition on the initial wedge.

This Stokeslet flow from the inner scale sets conditions which apply at the origin for the outer scale flow. In addition to the Stokeslet, there could be a solid-body motion on intermediate scales, since this also satisfies the Stokes equations with stress-free boundary conditions on the wedge surfaces. This solid-body motion will be set by the solution on the outer diffusive scale.

Billingham imposes a Stokeslet of unknown strength at the origin, and names the unknown solid-body motion Kb_∞. With our choice of θ, the corresponding streamfunction is

$$\tilde{\psi} = -2K\tilde{r}\sin\theta\log\tilde{r} + Kb_\infty\tilde{r}\sin\theta, \tag{4.13}$$

for constants K and b_∞. K is set by the solution on the inner scale, while b_∞ is set by the response on the outer scale. In dimensional terms, the velocity components are

$$u_x = -2K\frac{\gamma}{\mu}\log\frac{r}{(\nu t)^{1/2}} + \frac{2\gamma K x^2}{\mu(x^2+y^2)} - \frac{2\gamma K}{\mu} + \frac{\gamma K b_\infty}{\mu} \tag{4.14}$$

$$u_y = \frac{2\gamma K x y}{\mu(x^2+y^2)}. \tag{4.15}$$

Billingham now solves numerically for the response b_∞ in terms of the wedge angle α and the Stokeslet strength K. This requires the solution of the unsteady Stokes equations (4.3) with the stress boundary conditions (4.9). Billingham converts the problem for velocity components and the pressure to an equivalent problem for the streamfunction and the vorticity $\tilde{\omega}$, defined by

$$\tilde{\nabla}^2\tilde{\psi} + \tilde{\omega} = 0. \tag{4.16}$$

The unsteady Stokes equations become

$$\tilde{\nabla}^2\tilde{\omega} + \frac{1}{2}\frac{\partial}{\partial\tilde{r}}(\tilde{r}\tilde{\omega}) = 0, \tag{4.17}$$

and the boundary conditions become

$$\begin{aligned} \tilde{\omega} + 2\frac{\partial\tilde{\psi}}{\partial\tilde{r}} &= 0, \\ \frac{2}{\tilde{r}}\frac{\partial^3\tilde{\psi}}{\partial\tilde{r}^2\partial\tilde{\theta}} + \left(\frac{1}{2} - \frac{4}{\tilde{r}^2}\right)\left(\frac{\partial^2\tilde{\psi}}{\partial\tilde{r}\partial\theta} - \frac{1}{\tilde{r}}\frac{\partial\tilde{\psi}}{\partial\theta}\right) - \frac{1}{\tilde{r}}\frac{\partial\tilde{\omega}}{\partial\theta} &= 0, \end{aligned} \tag{4.18}$$

and they apply on $\theta = \pm\alpha$.

In the far-field, we want

$$\psi \to 0, \quad \text{and} \quad \omega \to 0 \quad \text{as } r \to \infty. \tag{4.19}$$

At the origin, the streamfunction and vorticity are

$$\psi \sim -2K\tilde{r}\sin\theta\log\tilde{r} + Kb_\infty\tilde{r}\sin\theta, \quad \omega \sim \frac{4\sin\theta}{r} \quad \text{as } r \to 0. \tag{4.20}$$

Billingham rescales the solution by a factor of K to remove that constant from the numerical solution and, since it is numerically difficult to solve for a divergent streamfunction, subtracts the driving Stokeslet from ψ and ω. The problem is then to find the streamfunction which grows in the correct manner in the far-field. Billingham solves this numerically with a finite-differences method, and extracts the value of b_∞ from the solution near the origin.

This solid-body motion affects the matching, since is describes the 'extra' velocity at the tip. A Stokes flow without this outer scale would be free to include any solid-body motion, but here, inertia on the outer scale describes the distance that the tip can actually retract, while the bulk of the wedge remains stationary. We will solve for the tip position x_0 below, but first we review Billingham's numerical solution on the inner scale.

4.4 Solution on the inner scale

On the inner scale, there is a surface-tension–driven free-boundary flow. Billingham solves for this flow numerically with a boundary integral method similar to that used above for the retracting edge in §3.4.

In a frame moving with the edge, we write

$$x = x_0 + \frac{\gamma t}{\mu}\bar{x}, \quad y = \frac{\gamma t}{\mu}\bar{y}, \quad Y = \frac{\gamma t}{\mu}\bar{Y}(\bar{x}), \quad p = \frac{\mu}{t}\bar{p}, \quad \mathbf{u} = \dot{x}_0\mathbf{e}_x + \frac{\gamma}{\mu}\bar{\mathbf{u}}. \tag{4.21}$$

In this moving frame, we expect a similarity solution for the shape of the tip of the wedge, with $\bar{\mathbf{u}} = \mathrm{O}(1)$ velocity, driven by surface tension acting around the tip.

We now deviate from Billingham's solution; rather than inferring the Stokeslet strength K from the numerical solution on the inner scale, we will make a theoretical argument for the exact value of K.

We argued above that the flow in the far-field of this scale is a Stokeslet together with some solid-body motion. But we can go further; we know that the force from

surface tension is given precisely by the change in tangent vector around the surface. From the wedge geometry, the net force from surface tension is $2\gamma\cos\alpha\mathbf{e}_x$ in dimensional variables. Now the forces on a Stokes flow must balance, so the integral of the Stokeslet stress (4.12) must balance the force from surface tension. The x-component of the force balance is

$$\frac{F}{\pi}\int_{-\alpha}^{\alpha}\cos^2\theta\,\mathrm{d}\theta = 2\cos\alpha \tag{4.22}$$

in non-dimensional variables. We deduce that

$$F = \frac{2\pi\cos\alpha}{\alpha+\sin\alpha\cos\alpha}. \tag{4.23}$$

Now from the streamfunction for a Stokeslet, we infer $K = F/8\pi$, so

$$K = \frac{\cos\alpha}{4\left(\alpha+\sin\alpha\cos\alpha\right)}. \tag{4.24}$$

Figure 4.4 shows this solution for $K(\alpha)$, and reproduces Billingham's numerical solution. These curves agree very well. Billingham also gives three asymptotics for K, based on asymptotic solutions for α close to zero, $\pi/2$ and π. For $0<\epsilon\ll 1$, these are

$$K(\epsilon) = \frac{1}{8\epsilon}+\mathrm{O}(\epsilon),\quad K\left(\frac{\pi}{2}+\epsilon\right) = -\frac{\epsilon}{2\pi}+\mathrm{O}(\epsilon^3),\quad K(\pi-\epsilon) = -\frac{1}{4\pi}+\mathrm{O}(\epsilon), \tag{4.25}$$

which all agree with (4.24).

The actual velocity of the tip of the wedge is given by matching the solution on the inner scale to the outer velocity. Here, we will match at leading order in time. On intermediate scales, we have seen that the velocity is a Stokeslet plus a solid-body motion, and we have two expressions for that velocity from the inner and the outer scales. Neglecting $\mathrm{O}(\gamma/\mu)$ contributions, we have

$$\dot{x}_0 - \frac{2\gamma K}{\mu}\log\frac{r}{\gamma t/\mu}+\mathrm{O}\left(\frac{\gamma}{\mu}\right) = -\frac{2\gamma K}{\mu}\log\frac{r}{(\nu t)^{1/2}}+\mathrm{O}\left(\frac{\gamma}{\mu}\right). \tag{4.26}$$

The expression on the left is the far-field velocity on the inner scale, including the term $\dot{x}_0$ due to the moving frame, and where K is given by (4.24). The expression on the right is the velocity on the outer scale near the origin, and the $\mathrm{O}(\gamma/\mu)$ corrections include the velocity Kb_∞. We can solve (4.26) for $\dot{x}_0$ to find

$$\dot{x}_0 = \frac{\gamma K}{\mu}\log\left(\frac{\mu^3}{\rho\gamma^2 t}\right)+\mathrm{O}\left(\frac{\gamma}{\mu}\right), \tag{4.27}$$

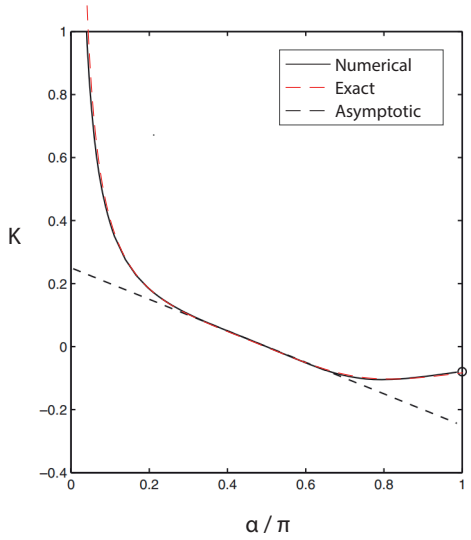

Fig. 4.4 Adapted from figure 5.3 of [6]. We compare Billingham's numerical solution for K (solid black line) with the exact solution (red dashed line; (4.24)). The asymptotic expression for $K \approx \pi/2$ is shown with a black dashed line.

where K is given by (4.24). Integrating up for the leading-order solution gives

$$x_0 = \frac{\gamma K t}{\mu} \log\left(\frac{\mu^3}{\rho\gamma^2 t}\right) + \mathrm{O}\left(\frac{\gamma t}{\mu}\right). \tag{4.28}$$

This agrees with the asymptotic form $x_0 \sim -Kt \log t$ used by Billingham. The $\mathrm{O}(\gamma/\mu)$ constant depends on b_∞ and also on the numerical solution on the inner scale, and is given by Billingham in [6].

We recall that the asymptotic structure requires $\gamma t/\mu \ll (\nu t)^{1/2}$. This holds for early times, while $t \ll \mu^3/\rho\gamma^2$. For those times, the logarithmic term of (4.27) dominates and the neglected terms are small. The solution is therefore asymptotically consistent.

4.5 Billingham's solution for narrow wedges

We will now review the asymptotic expressions that Billingham gives for narrow and for wide wedges. In these cases, the proximity of the free surface to the x-axis can be exploited to simplify the geometry of the problem.

For narrow wedges with $\alpha \ll 1$, Billingham splits the inner scale in two. We will write $\alpha = \epsilon \ll 1$ as reminder that α is small. Near the tip of the wedge, the flow is driven by the surface stress distribution from surface tension. This causes the tip to thicken as $\gamma t/\mu$. On that scale, the Stokes equations hold and the tip of the wedge

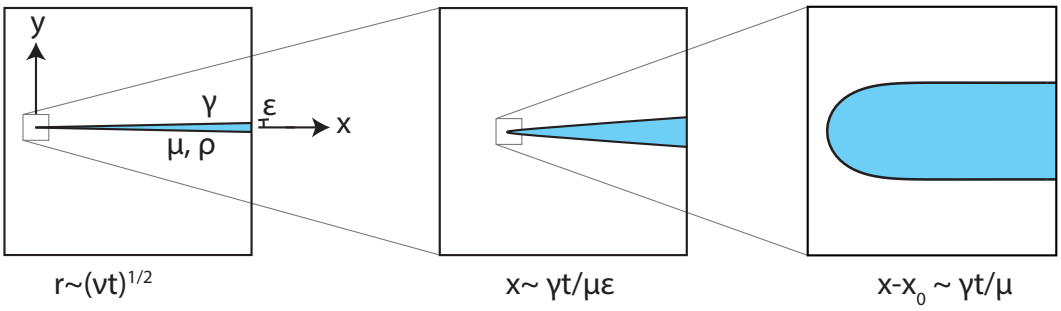

Fig. 4.5 Scales for narrow wedges

thickens. This is comparable with the inner scale that Billingham considers for a general wedge. On a larger scale, the wedge must match to its initial shape $Y = \epsilon x$. This happens over the lengthscale $x \sim \gamma t/\mu\epsilon$, while the thickness of the wedge is proportional to $\gamma t/\mu$.

There is therefore an 'inner' scale with $x \sim \gamma t/\mu\epsilon$, and an 'inner-inner' scale with $x - x_0 \sim \gamma t/\mu$. These scales are shown in figure 4.5.

On the outer scale, the unsteady Stokes equations describe the effect of inertia and set the solid-body motion b_∞. On the inner scale, the Stokes equations describe the thickening of the sheet and the matching from the curved tip to the far-field wedge. On the inner-inner scale, a Stokes flow driven by surface tension gives the detailed shape of the curved tip, and gives the net force which drives the flow on larger scales. We will now review Billingham's solution on each of these scales.

4.5.1 Outer scale

On the outer scale, since $0 < \epsilon \ll 1$, Billingham can expand the streamfunction and the vorticity in terms of θ as

$$\tilde{\psi} = A_0(\tilde{r})\theta + \mathrm{O}(\theta^3), \quad \tilde{\omega} = B_0(\tilde{r})\theta + \mathrm{O}(\theta^3), \tag{4.29}$$

although we note that the expansion in [6] is in terms of $\bar{\theta}$, which is related to our choice of θ by $\bar{\theta} = -\theta/\epsilon$.

The stress boundary conditions (4.18) are satisfied if

$$B_0 + 2\frac{\mathrm{d}^2 A_0}{\mathrm{d}\tilde{r}^2} = 0 \quad \text{and} \quad \frac{2}{\tilde{r}}\frac{\mathrm{d}^2 A_0}{\mathrm{d}\tilde{r}^2} + \left(\frac{1}{2} - \frac{4}{\tilde{r}^2}\right)\left(\frac{\mathrm{d}A_0}{\mathrm{d}\tilde{r}} - \frac{A_0}{\tilde{r}}\right) - \frac{B_0}{\tilde{r}} = 0. \tag{4.30}$$

We can eliminate B_0 with the first of these equations, and then the second becomes a second-order ordinary differential equation for A_0 with solution

$$A_0 = k_1\tilde{r}\int_{1/16}^{\tilde{r}^2/16}\frac{\mathrm{e}^{-u}}{u}\,\mathrm{d}u + k_2\tilde{r}, \tag{4.31}$$

for constants k_1 and k_2, following Billingham's notation (up to a sign and a factor of ϵ). The far-field condition $\psi \to 0$ as $r \to \infty$ then gives

$$k_1\int_{1/16}^{\infty}\frac{\mathrm{e}^{-u}}{u}\,\mathrm{d}u + k_2 = 0. \tag{4.32}$$

We expand the integral (4.31) for small r, and match to the forcing condition at the origin, $\psi \sim -(2\tilde{r}\log\tilde{r} - b_\infty\tilde{r})\sin\theta$. This gives

$$-(2\log\tilde{r} - b_\infty)\epsilon = k_1\left(E_\gamma + \int_{1/16}^{\infty}\frac{\mathrm{e}^{-u}}{u}\,\mathrm{d}u - 2\log 4 + 2\log\tilde{r}\right) + k_2, \tag{4.33}$$

where E_γ is the Euler–Mascheroni constant $0.5772\ldots$. The coefficient of $\log\tilde{r}$ gives $k_1 = -\epsilon$ in agreement with Billingham's result. However, we do not recover Billingham's result for k_2. We have instead

$$k_2 = \alpha b_\infty + \epsilon\left(E_\gamma + \int_{1/16}^{\infty}\frac{\mathrm{e}^{-u}}{u}\,\mathrm{d}u - 2\log 4\right). \tag{4.34}$$

This sets

$$b_\infty = 2\log 4 - E_\gamma \approx 2.19537, \tag{4.35}$$

where Billingham has $b_\infty = \int_{1/16}^{\infty}\mathrm{e}^{-u}/u\,\mathrm{d}u - 1/16 \approx 2.194$. Despite this, Billingham's value for b_∞ is correct to within 0.1%, and the difference is not noticeable in the numerically calculated values of b_∞ shown in Billingham's figure 4.2.

4.5.2 Inner scale

On the inner scale, Billingham models the velocity with a uni-directional plug flow $u_x(x)$. The Stokes flow is driven by a force on the edge from the tightly curved surface on the inner-inner scale. Billingham solves for the velocity and the slender shape analytically in terms of K and α.

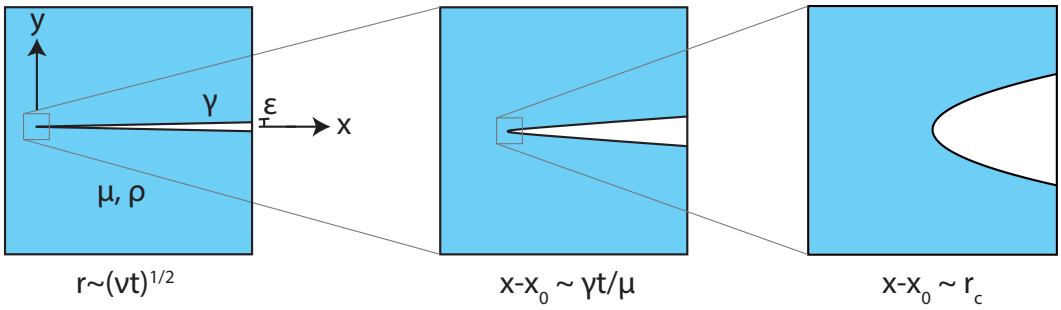

Fig. 4.6 Scales for the retraction of wide wedges with $\alpha \lesssim \pi$.

4.5.3 Inner-inner scale

On the inner-inner scale, Billingham solves for a free-surface Stokes flow driven by surface tension. Since the variation of thickness of the wedge happens over the longer lengthscale of the inner scale, the appropriate far-field condition is for the thickness to be constant. The flow is coupled to the shape through the normal stress on the surface, which depends on the curvature, and through the kinematic boundary condition.

This problem is satisfied by the universal edge solution found in chapter 3, with zero lateral stretching. The far-field velocity of the edge solution shows that $K = 1/(8\alpha)$, in agreement with the solution for K above.

Billingham solves for the edge shape numerically, approaching the edge with a continuation parameter through a series of wedges. The final shape agrees well with the similarity solution found in chapter 3.

4.6 Billingham's solution for wide wedges

Now we consider the retraction of very wide wedges, with half-angle $\alpha \lesssim \pi$. We will redefine $\epsilon = \pi - \alpha \ll 1$ as a reminder that α is close to π. In this case, the fluid occupies nearly the whole space, with a thin crack between the free surfaces.

We will define new co-ordinates for this asymptotic problem, rotating the axes so that the free surfaces are near the positive x-axis, as in figure 4.6. Note that this is different from Billingham's choice of co-ordinates where the free surfaces lie near the negative y-axis. We have chosen co-ordinates for consistency with the work on drop coalescence below in chapter 6.

Since $\epsilon \ll 1$, we can linearise the free surface to the x-axis, except for some small region near the tightly curved tip. This suggests that we should split the Stokes region into two regions; an inner region where we linearise the free-surface to the x-axis, and

a small inner-inner region where the surface is tightly curved. This inner-inner scale will be proportional to the radius of curvature of the surface, which we must solve for. The structure of the solution is shown in figure 4.6.

Billingham solves for the unsteady flow on the outer diffusive scale as before. This will set the solid-body motion Kb_∞ which applies in the far-field for the flow on smaller scales. On the inner scale, the Stokes equations govern the flow, with the free surface linearised to the x-axis. Finally, a Stokes flow on the inner-inner scale of the tightly-curved tip of the wedge gives the detailed shape of the tip and the resulting flow. Surface tension acting on the tightly-curved surface drives the flow on that scale, and gives the force which is applied to larger scales.

4.6.1 Outer scale

On the outer diffusive scale, Billingham's numerical solutions show that $b_\infty \to 1.82$ as $\alpha \to \pi$. It might be possible to solve for this flow analytically with some transform, but since the matching only requires the single constant b_∞, we will not attempt an analytical solution here.

4.6.2 Inner scale

On the inner scale, we rescale the co-ordinates with

$$x_0 = \frac{\gamma t}{4\pi\mu}\log\frac{\mu^3}{\rho\gamma^2 t} + \frac{\gamma t}{\mu}\bar{x}_0, \quad x = \frac{\gamma t}{4\pi\mu}\log\frac{\mu^3}{\rho\gamma^2 t} + \frac{\gamma t}{\mu}\bar{x}, \quad y = \frac{\gamma t}{\mu}\bar{y}, \quad \mathbf{u} = \frac{\gamma}{\mu}\bar{\mathbf{u}}. \tag{4.36}$$

Here, we have included in x_0 the leading-order term as a function of time. In this section, we will find the leading-order dependence of $\bar{x}_0$ on ϵ.

Since we will linearise the boundary conditions to the x-axis, the far-field Stokeslet and solid-body motion will satisfy the stress boundary conditions not only in the far-field but throughout this scale. We know that the solution on the inner-inner scale gives a Stokeslet with $K = -1/4\pi$ and some solid-body motion, and the leading-order solution on the inner scale is therefore a Stokeslet with $K = -1/4\pi$ at $\bar{x}_0$, together with a solid-body motion that matches to the far-field velocity from the outer scale.

In order to find the effect on the surface shape, we must expand further. Following Billingham, we expand the velocity and the pressure in terms of the streamfunction $\bar{\psi}$

as

$$\bar{u}_x = -\frac{1}{2\pi}\log\bar{r} + \frac{1}{2\pi}\frac{\bar{x}^2}{\bar{r}^2} - \frac{1}{2\pi} + \frac{1}{4\pi}b_\infty + \epsilon\frac{\partial\bar{\psi}}{\partial\bar{y}} + \mathrm{O}(\epsilon^2), \tag{4.37}$$

$$\bar{u}_y = \frac{1}{2\pi}\frac{(\bar{x}-\bar{x}_0)\bar{y}}{\bar{r}^2} - \epsilon\frac{\partial\bar{\psi}}{\partial\bar{x}} + \mathrm{O}(\epsilon^2), \tag{4.38}$$

$$\bar{p} = -\frac{\bar{x}-\bar{x}_0}{\pi\bar{r}^2} + \epsilon\bar{p}_1 + \mathrm{O}(\epsilon^2), \tag{4.39}$$

where $\bar{r}^2 = (\bar{x}-\bar{x_0})^2+\bar{y}_0^2$ and ψ is the streamfunction for the next-order flow. Billingham notes that the numerical solutions have $\bar{x}_0 \gg 1$ (in Billingham's notation, $-\bar{y}_0 \gg 1$); we will see that $\bar{x}_0 \sim \log\frac{1}{\epsilon}$. We let $\delta = (\bar{x}_0)^{-1}$ and expand in $\delta \ll 1$:

$$\bar{x} = \bar{x}_0 + \delta^{-1}\tilde{x}, \quad \bar{y} = \delta^{-1}\tilde{y}, \quad \bar{r} = \delta^{-1}\tilde{r}, \quad \psi = \delta^{-2}\left(\tilde{\psi_0} + \delta\log\delta\tilde{\psi_1} + \delta\tilde{\psi_2} + \dots\right). \tag{4.40}$$

The streamfunction must satisfy the biharmonic equation, so at leading order we have $\tilde{\nabla}^4\tilde{\psi_0} = 0$, where $\tilde{\nabla}$ is the gradient operator taken with respect to $\tilde{r}$

Now Billingham shows that the surface stress from the leading-order Stokeslet and the linearisation are both smaller than the stress associated with $\tilde{\psi_0}$ by a factor of δ. We can therefore neglect the surface stress at this order, and we have stress-free boundary conditions for $\tilde{\psi_0}$. In terms of polar co-ordinates, with θ the angle above the x-axis, the stress-free boundary conditions for $\tilde{\psi_0}$ on $\tilde{y} = 0$ are

$$\begin{aligned} \frac{\partial^2\tilde{\psi_0}}{\partial\tilde{r}^2} - \frac{1}{\tilde{r}}\frac{\partial\tilde{\psi_0}}{\partial\tilde{r}} - \frac{1}{\tilde{r}^2}\frac{\partial^2\tilde{\psi_0}}{\partial\theta^2} &= 0, \\ -\frac{3}{\tilde{r}}\frac{\partial^3\tilde{\psi_0}}{\partial\tilde{r}^2\partial\theta} + \frac{3}{\tilde{r}^2}\frac{\partial^2\tilde{\psi_0}}{\partial\tilde{r}\partial\theta} - \frac{4}{\tilde{r}^3}\frac{\partial\tilde{\psi_0}}{\partial\theta} - \frac{1}{\tilde{r}^3}\frac{\partial^3\tilde{\psi_0}}{\partial\theta^3} &= 0. \end{aligned} \tag{4.41}$$

The kinematic boundary condition is

$$-(1+\tilde{x})\frac{\mathrm{d}\chi}{\mathrm{d}\tilde{x}} + \chi = \frac{\partial\tilde{\psi_0}}{\partial\tilde{x}}, \tag{4.42}$$

where the free surface is at $Y(x) = \epsilon\delta^{-1}\chi(\tilde{x})$. In the far-field, we want $Y \sim \epsilon x$ so we must have $\chi \sim \tilde{x}$ as $x \to \infty$. We have symmetry conditions on $y = 0$:

$$\frac{\partial\tilde{\psi_0}}{\partial x} = 0, \quad \text{and} \quad \frac{\partial^3\tilde{\psi_0}}{\partial x^3} = 0. \tag{4.43}$$

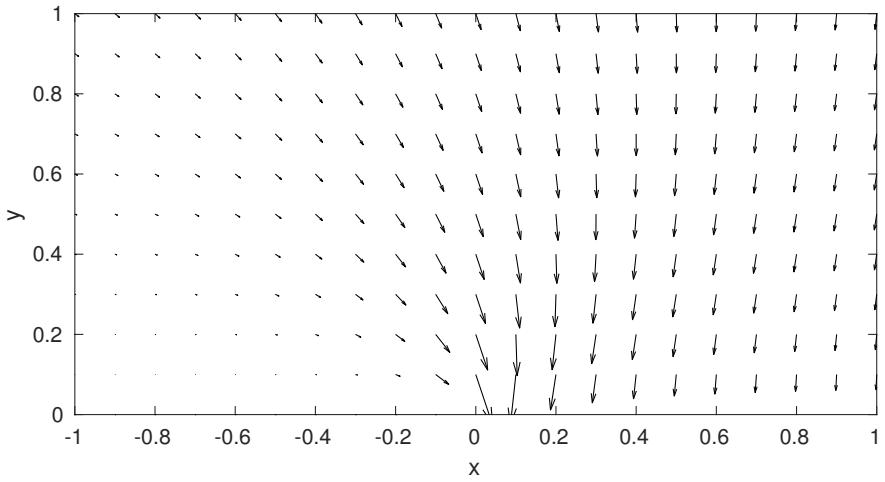

Fig. 4.7 The Stokes solution satisfying stress-free boundary conditions on the x-axis for $x > 0$, and symmetry conditions on $x < 0$, with streamfunction given by 4.44.

The stress-free solution to $\tilde{\nabla}^4\tilde{\psi}_0 = 0$ satisfying the symmetry conditions is the streamfunction

$$\left(3\cos\frac{\theta}{2} + \cos\frac{3\theta}{2}\right)\tilde{r}^{1/2}, \tag{4.44}$$

and the corresponding velocity field is shown in figure 4.7. For $\tilde{\psi}_0$, we take a multiple k_1, say, of this solution. Now we integrate the kinematic boundary condition for

$$\chi = -2k_1\left(\tilde{x}^{1/2} + (1+\tilde{x})\arctan\tilde{x}^{1/2}\right) + k_2(1+\tilde{x}), \tag{4.45}$$

where k_2 is the constant of integration. Since we want $\chi(0) = 0$, we must have $k_2 = 0$. Matching the shape to the far-field wedge $\chi \sim \tilde{x}$ then gives $k_1 = -1/\pi$, closing the problem. So the shape on this scale is

$$Y(x) = \frac{2\epsilon\delta^{-1}}{\pi}\left((\delta x)^{1/2} + (1+\delta x)\arctan(\delta x)^{1/2}\right). \tag{4.46}$$

This shape is shown in figure 4.8. Near $x = 0$, the surface is curved as $Y \sim 4\epsilon\delta^{-1/2}x^{1/2}/\pi$. As a result, the radius of curvature of the surface is proportional to $\epsilon^2\delta^{-1}$.

In order to understand the matching to the inner-inner scale, we should first consider the solution on intermediate scales, where the surface is curved into the parabolic shape $Y = 4\epsilon\delta^{-1/2}x^{1/2}/\pi$. The solution should be simpler on this scale, since we can approximate the shape with the parabola, while still linearising the boundary conditions to the x-axis.

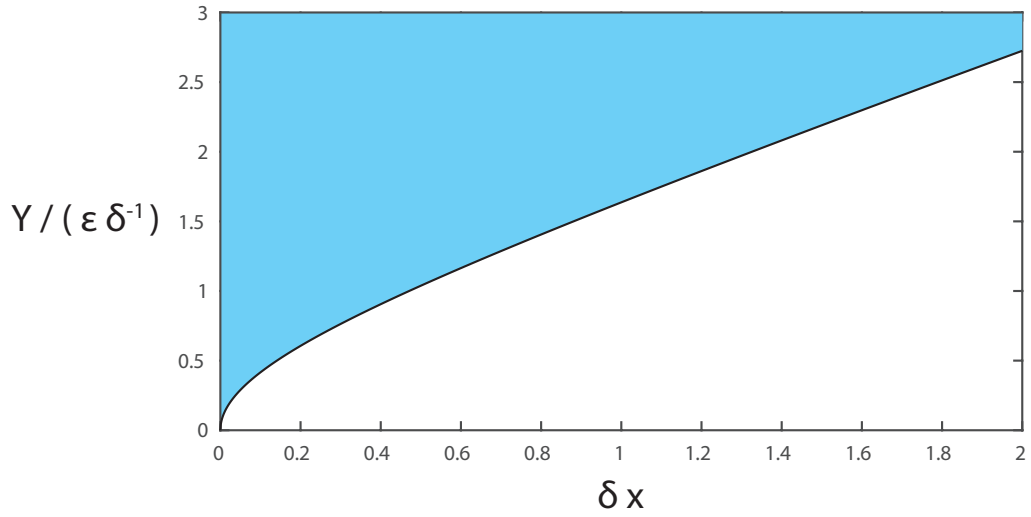

Fig. 4.8 Billingham's solution for the surface shape on the inner scale for a wide retracting wedge.

4.7 Single-cut Stokes solutions

In this section, we will consider the retraction of a slender parabolic cut. This solution will apply on intermediate scales for the retraction of wide wedges between the inner and the inner-inner scale. In later chapters, we will see that this flow is useful for a range of drop coalescence problems. This work is a review of Billingham's work on the problem, presented in §7 of [6]; Billingham derives this solution for $\alpha \gg 1$, but neglects some parts of the solution for the application to wide wedges. We will discuss this below.

In a frame moving with the parabola, we suppose that the free surface is at $Y(x) = (r_c x)^{1/2}$ for some constant r_c. This constant is proportional to the curvature of the parabola at the tip, and we will call it the 'radius-of-curvature lengthscale'. For the retraction of wide wedges, r_c is the inner-inner scale on which we cannot linearise the free surface to the x-axis.

For the problem with general r_c, we note that on scales with $r \gg r_c$, we have $Y \ll x$ and so the free surface is near the x-axis. We can therefore linearise the free-surface boundary conditions to the axis. We will model the effect of the tightly curved tip with a Stokeslet, so that near $r = 0$

$$\psi \sim -\frac{r \sin\theta \log r}{2\pi} + u_\infty r \sin\theta, \tag{4.47}$$

where u_∞ is some solid-body motion in the x-direction.

As we have seen above, this Stokeslet and solid-body motion satisfy stress-free boundary conditions on the x-axis. Now we will consider the corrections due to the actual position of the surface. There are two sources of small terms in the stress boundary conditions; firstly from the linearisation, since the Stokeslet has some stress on the actual surface, and secondly from surface tension acting on the curved parabolic shape. We expect both of these correction terms to scale with $\sqrt{r_c}$, since both the first term of the linearisation and the stress from surface tension are linear in the surface position.

The normal stress boundary condition is given by surface tension;

$$\frac{\partial^2\psi}{\partial r^2} - \frac{1}{r}\frac{\partial\psi}{\partial r} - \frac{1}{r^2}\frac{\partial^2\psi}{\partial\theta^2} = -\frac{\gamma\sqrt{r_c}}{\pi\mu r^{3/2}}. \tag{4.48}$$

The tangential stress condition is given by the Stokeslet stress;

$$-\frac{3}{r}\frac{\partial^3\psi}{\partial r^2\partial\theta} + \frac{3}{r^2}\frac{\partial^3\psi}{\partial r\partial\theta^2} - \frac{4}{r^3}\frac{\partial\psi}{\partial\theta} - \frac{1}{r^3}\frac{\partial^3\psi}{\partial\theta^3} = -\frac{3\sqrt{r_c}}{8r^{5/2}}. \tag{4.49}$$

The kinematic boundary condition contains the leading-order velocity

$$\sqrt{r_c}r^{-1/2}\left(-\frac{1}{4\pi}\log r - \frac{1}{2\pi} + \frac{1}{2}u_\infty\right) = -\frac{\partial\psi}{\partial r}. \tag{4.50}$$

In order to satisfy the Stokes equations, we need $\nabla^4\psi = 0$. Inspired by functions of r in the boundary conditions, we look for solutions proportional to $r^{1/2}\log r$ or $r^{1/2}$. Four such solutions are

$$\begin{aligned}\psi = \frac{\gamma\sqrt{r_c}}{\mu}\Bigg\{\ & Ar^{1/2}\left(\log r\cos\frac{3\theta}{2} - (\pi-\theta)\sin\frac{3\theta}{2}\right)\\ & +Br^{1/2}\left(\log r\cos\frac{\theta}{2} + (\pi-\theta)\sin\frac{\theta}{2}\right)\\ & +Cr^{1/2}\left(3\cos\frac{\theta}{2} - \cos\frac{3\theta}{2}\right)\\ & +Dr^{1/2}\left(3\cos\frac{\theta}{2} + \cos\frac{3\theta}{2}\right)\ \Bigg\},\end{aligned} \tag{4.51}$$

where A, B, C and D are arbitrary constants. The solution proportional to D is the stress-free solution found above (4.44), and the other three velocity fields are shown in figure 4.9.

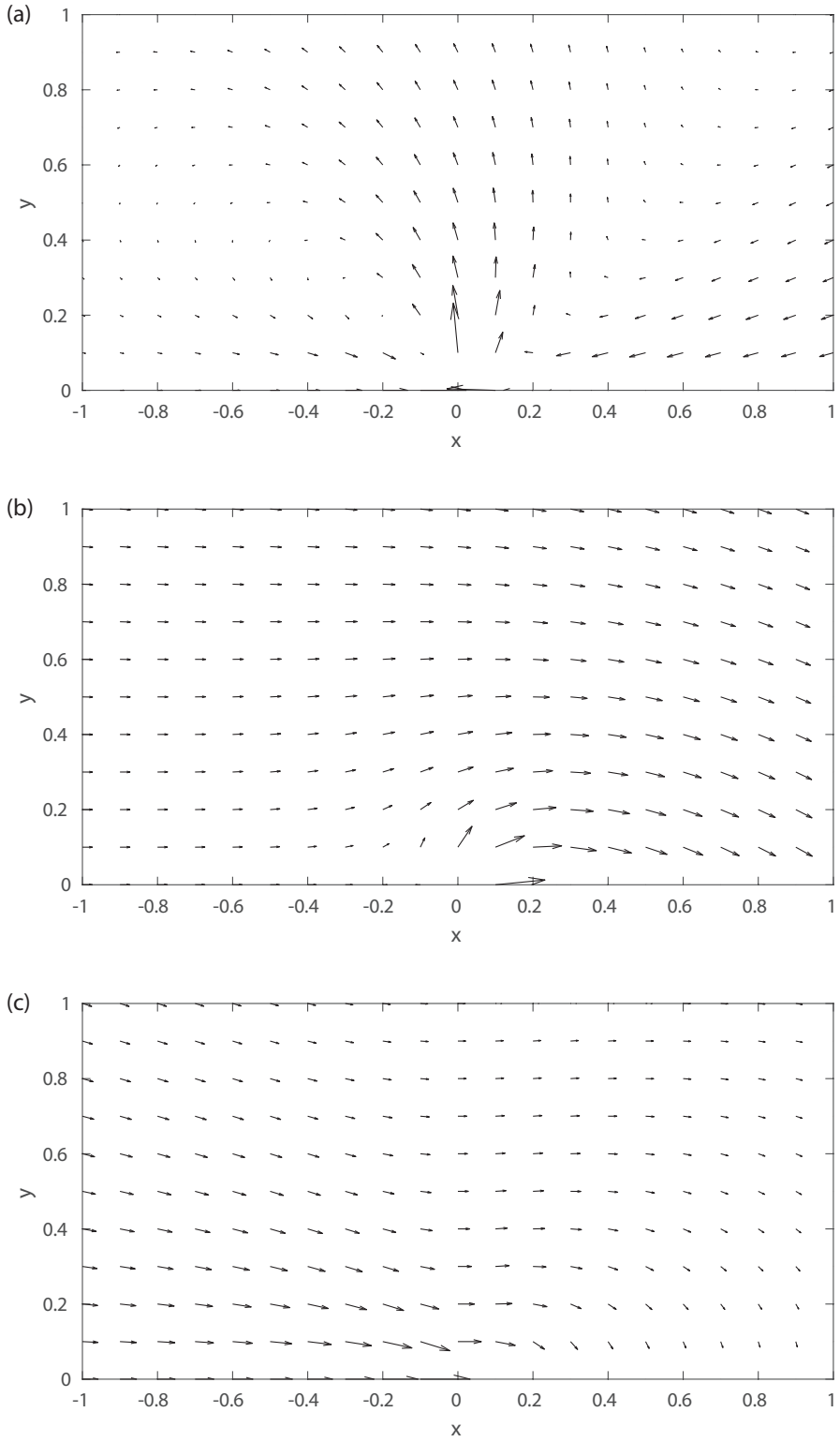

Fig. 4.9 The Stokes flows given by the streamfunction (4.51) corresponding to each of the coefficients A, B and C. The flow given by the term proportional to D is the stress-free solution shown in figure 4.7.

Now we can compare coefficients in the boundary conditions with this combination of solutions (4.51). We find

$$-4A - 3C = -\frac{1}{\pi}, \quad 3A - B = 0, \tag{4.52}$$

$$-\frac{3(A+B)\pi}{4} = -\frac{3}{8}, \tag{4.53}$$

$$-\frac{1}{2}A - \frac{1}{2}B = -\frac{1}{4\pi}, \quad -(A+B+C+2D) = -\frac{1}{2\pi} + \frac{1}{2}u_\infty. \tag{4.54}$$

We see that the solutions with coefficients A and B have some normal stress, while the term with coefficient C has no normal stress, but some tangential stress. All the terms appear in the kinematic boundary condition, including the free-surface solution with coefficient D.

We can solve these equations for

$$A = \frac{1}{8\pi}, \quad B = \frac{3}{8\pi}, \quad C = \frac{1}{6\pi}, \quad D = -\frac{1}{12\pi} - \frac{u_\infty}{4}. \tag{4.55}$$

and so

$$\begin{aligned}\psi =& \frac{\gamma\sqrt{r_c}}{\mu}\left\{\frac{r^{1/2}}{8\pi}\left(\log r\cos\frac{3\theta}{2} - (\pi-\theta)\sin\frac{3\theta}{2}\right) + \frac{3r^{1/2}}{8\pi}\left(\log r\cos\frac{\theta}{2} + (\pi-\theta)\sin\frac{\theta}{2}\right)\right.\\ &\left. + \frac{r^{1/2}}{6\pi}\left(3\cos\frac{\theta}{2} - \cos\frac{3\theta}{2}\right) + r^{1/2}\left(-\frac{1}{12\pi} - \frac{u_\infty}{4}\right)\left(3\cos\frac{\theta}{2} + \cos\frac{3\theta}{2}\right)\right\}.\end{aligned} \tag{4.56}$$

This solution on intermediate scales should be ubiquitous for parabolically-curved surfaces, in cases where the radius of curvature is asymptotically separated from the outer flow. In particular, for Billingham's wide wedges, we have seen that the surface is tightly curved into a parabola near the tip on the inner scale. The solution presented here will hold on intermediate scales smaller than x_0 but larger than $\epsilon^2\delta^{-1}$.

This slender parabola solution should therefore be the far-field flow for the smaller scales. But Billingham imposes the far-field

$$\tilde{\psi} \sim \frac{1}{2\pi}\tilde{r}\log\tilde{r}\sin\theta - \frac{b_\infty}{4\pi}\tilde{r}\sin\theta - \frac{\tilde{r}^{1/2}}{\pi}\left(3\sin\frac{\theta}{2} - \sin\frac{3\theta}{2}\right), \tag{4.57}$$

which is missing some of the terms of the intermediate solution. Billingham has kept the stress-free eigenfunction, but neglected the surface-stress–driven terms. On the larger scale these are smaller by a factor of $\log\delta$, but they grow as $\log r$ and so they

change order on intermediate scales. This is a problem for Billingham's inner-inner numerical solution, where the incorrect far-field flow (4.57) is imposed on the numerical solution.

Instead of solving the inner-inner problem numerically, we will use an exact Stokes flow to describe the solution on the radius-of-curvature lengthscale.

4.8 Capillary retraction of a parabola

In the previous section, we solved for the flow around a slender parabola, linearising the surface to the x-axis. We will now improve on this result by solving for the flow around an arbitrary parabola, without linearisation.

Remarkably, there is an exact similarity solution in which the surface is a streamline, so that the parabola remains parabolic as it retracts. This is the inner-inner solution for Billingham's wedge retraction problem, and we will see in a later chapter that it is also applicable to drop coalescence. We will show that the far-field flow includes a Stokeslet, a solid-body motion and the flows proportional to $r^{1/2}\log r$ and $r^{1/2}$ found above (4.56).

This exact solution was first given by Hopper [31]. Hopper solves for a more general flow, with the parabola opening at some rate as it moves. Here, since the parabolic tip moves at speed proportional to γ/μ but only opens at a rate proportional to $\dot{r}_c \ll \gamma/\mu$, we can neglect the opening motion. We therefore only need the 'steady' solution so that, in the frame moving with the tip, the parabolic shape does not change. We note that even with a stationary shape, there is some flow driven by surface tension, which slips past the stress-free surface. The solution presented here will closely follow Hopper's solution, with some simplifications for the steady case.

For a given parabolic free surface $Y = (r_c x)^{1/2}$, we first non-dimensionalise the problem by scaling the velocity with γ/μ and the lengths by r_c;

$$\mathbf{u} = \frac{\gamma}{\mu}\bar{\mathbf{u}}, \quad p = \frac{\gamma}{r_c}\bar{p}, \quad x = r_c\bar{x}, \quad y = r_c\bar{y}, \quad Y = r_c\bar{Y}, \tag{4.58}$$

and we will immediately drop the bars. The parabolic free-surface is now at $Y^2 = x$.

Now we define $z = x + iy$ where $i = \sqrt{-1}$, and we will show that the fluid domain is the image of the upper half-plane $\Im(\zeta) > 0$ under the conformal map

$$z = w(\zeta) := \zeta^2 + i\zeta. \tag{4.59}$$

The effect of this conformal map is illustrated in figure 4.10. To show that the image

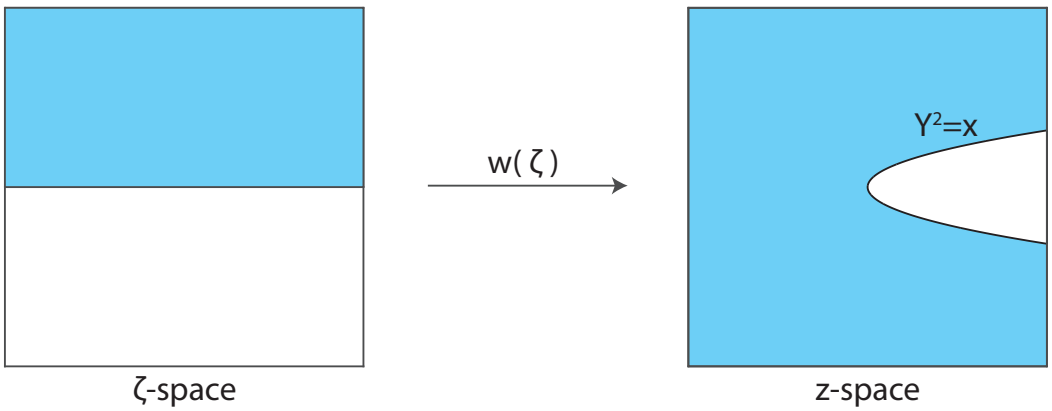

Fig. 4.10 The conformal map $z = w(\zeta)$ maps the upper half plane in ζ-space to the fluid domain in z-space.

of the upper half space is the region exterior to the parabola, we take a point in the upper-half plane $\zeta = \xi + i\eta$ such that $\eta > 0$, with image

$$w(\zeta) = (\xi^2 - \eta^2 - \eta) + i(2\xi\eta + \xi). \tag{4.60}$$

Now

$$\Im(w(\zeta))^2 - \Re(w(\zeta)) = \eta(\eta + 1)(4\xi^2 + 1) > 0, \tag{4.61}$$

and so the image of any point in the upper half-plane is outside the parabola. Now suppose that two such points ζ_1 and ζ_2 are both mapped to the same point. Then

$$\zeta_1^2 + i\zeta_1 = \zeta_2^2 + i\zeta_2, \tag{4.62}$$

and so

$$(\zeta_1 - \zeta_2)\,(\zeta_1 + \zeta_2 + i) = 0. \tag{4.63}$$

Since both ζ_1 and ζ_2 lie in the upper-half plane, we cannot have $\zeta_1 + \zeta_2 = -i$. So $\zeta_1 = \zeta_2$ and the pre-image is unique.

With this map, we transform the problem from z-space to ζ-space. Following the general theory of Hopper [29, 30], we write the velocity components (u, v) in terms of the Kolosov-Muskhelishvili potentials ϕ and ψ with

$$u + iv = \frac{1}{2}(\phi(z) - z\overline{\phi'(z)} - \overline{\psi(z)}), \tag{4.64}$$

where z is given by $w(\zeta)$.

Now we transform the boundary conditions to the ζ-plane, where they will apply at $\eta = 0$. The kinematic boundary condition is, for a general map w,

$$\phi(\xi) - \frac{w(\xi)}{\overline{w'(\xi)}}\overline{\phi'(\xi)} - \overline{\psi(\xi)} = 2\left(w'\frac{\partial \xi}{\partial t} + \frac{\partial w}{\partial t}\right), \tag{4.65}$$

where $\frac{\partial \xi}{\partial t}$ is the change in ξ following a physical parcel of fluid along the surface. For our problem, $\frac{\partial \xi}{\partial t}$ is unknown as the fluid can slip along the surface, but we know that $\frac{\partial w}{\partial t} = 0$ for the steady solution. The stress conditions are given by surface tension as

$$\phi(\xi) + \frac{w(\xi)}{\overline{w'(\xi)}}\overline{\phi'(\xi)} + \overline{\psi(\xi)} = i\frac{w'(\xi)}{|w'(\xi)|}. \tag{4.66}$$

These two boundary conditions combine to give

$$\phi(\xi) = iw'(\xi)\left(\frac{1}{2|w'(\xi)|} - i\frac{\partial \xi}{\partial t}\right), \tag{4.67}$$

where $\frac{\partial \xi}{\partial t}$ is still unknown. We write $G(\xi)$ for the function $\frac{1}{2|w'(\xi)|} - i\frac{\partial \xi}{\partial t}$. Following Hopper's work [30], this can be analytically continued into $\Im(\zeta) > 0$ as

$$G(\zeta) = \frac{1}{2\pi i}\int_{-\infty}^{\infty} \frac{\mathrm{d}u}{(u-\zeta)|w'(u)|} \quad \text{for } \Im(\zeta) > 0. \tag{4.68}$$

For the parabola, we have $w = \zeta^2 + i\zeta$, and so we can compute the integral for G exactly;

$$G(\zeta) = \frac{1}{2\pi i\sqrt{1+4\zeta^2}} \log\left(\frac{2\zeta - \sqrt{1+4\zeta^2}}{2\zeta + \sqrt{1+4\zeta^2}}\right). \tag{4.69}$$

Then the boundary conditions give the potentials $\phi(\zeta)$ and $\psi(\zeta)$ in terms of $G(\zeta)$;

$$\phi(\zeta) = iw'(\zeta)G(\zeta), \tag{4.70}$$

$$\psi(\zeta) = -i\overline{w(\bar{\zeta})}\left(\frac{w''(\zeta)G(\zeta)}{w'(\zeta)} + G'(\zeta)\right) - i\overline{w'(\bar{\zeta})}G(\zeta), \tag{4.71}$$

and so the velocity is

$$u + iv = \frac{1}{2}i\left(w'(\zeta)G(\zeta) - w'(\bar{\zeta})\overline{G(\zeta)} + (w(\zeta) - w(\bar{\zeta}))\left(\frac{\overline{w''(\zeta)G(\zeta)}}{\overline{w'(\zeta)}} + \overline{G'(\zeta)}\right)\right). \tag{4.72}$$

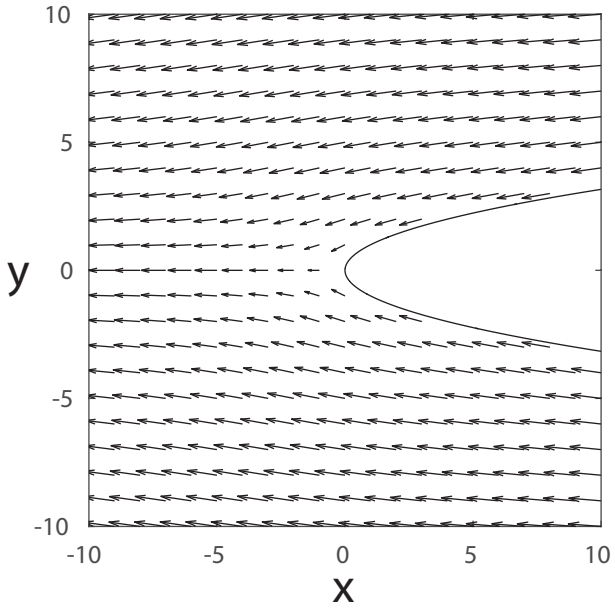

Fig. 4.11 Velocity field for Hopper's parabola solution.

The streamfunction is $\Re\left\{\frac{1}{2}w'(\zeta)G(\zeta)(\overline{w(\bar{\zeta})}-\overline{w(\zeta)})\right\}$, and the velocity field is shown in figure 4.11. We can check that on $\eta=0$, we have $\zeta=\bar{\zeta}$ so $w(\bar{\zeta})=w(\zeta)$ and the streamfunction is constant. So the free surface is a streamline, as we wanted for our steady solution.

To check that this solution agrees with the outer single-cut solution in section §4.7, we need to find the far-field of this exact flow around a parabola. We will expand the streamfunction in terms of z, keeping both the leading order term, and the terms smaller by a factor of $z^{-1/2}$ or $z^{-1/2}\log z$. We have

$$\begin{aligned} w'(\zeta) =& 2\zeta + i \\ \sim& 2\sqrt{z} + \mathrm{O}(z^{-1/2}), \end{aligned} \tag{4.73}$$

$$\begin{aligned} \overline{w(\bar{\zeta})} - \overline{w(\zeta)} =& \zeta^2 - \bar{\zeta}^2 + i\bar{\zeta} - i\zeta \\ \sim& z - \bar{z} - 2i\sqrt{z} + \mathrm{O}(1), \end{aligned} \tag{4.74}$$

and so

$$G(\zeta) \sim \frac{1}{4\pi i\zeta}\log\left(\frac{-1}{16\zeta^2}\right) + \mathrm{O}(\zeta\log\zeta) \tag{4.75}$$

$$\sim \frac{1}{2\pi i}\left(\frac{1}{2\sqrt{z}}+\frac{i}{4z}\right)\left(\log\left(\frac{-1}{16z}\right)+\frac{i}{\sqrt{z}}\right) + \mathrm{O}(z^{-3/2}\log z), \tag{4.76}$$

where we have made used the inverse map

$$\zeta = -\frac{i}{2} + \frac{\sqrt{4z-1}}{2} \sim \sqrt{z} - \frac{i}{2}. \tag{4.77}$$

Combining these results, we find that the far-field streamfunction grows as

$$\psi \sim \Re\left\{\frac{1}{4\pi i}(z-\bar{z})\log\left(\frac{-1}{16z}\right) + \frac{\sqrt{z}}{4\pi} - \frac{\bar{z}}{4\pi\sqrt{z}} - \frac{1}{8\pi}\left(3\sqrt{z} + \frac{\bar{z}}{\sqrt{z}}\right)\log\left(\frac{-1}{16z}\right)\right\} \tag{4.78}$$

$$\begin{aligned}\sim &\frac{-r\sin\theta\log(16r)}{2\pi} \\ &+ \frac{r^{1/2}}{8\pi}\left(\log r\cos\frac{3\theta}{2} - (\pi-\theta)\sin\frac{3\theta}{2}\right) + \frac{3r^{1/2}}{8\pi}\left(\log r\cos\frac{\theta}{2} + (\pi-\theta)\sin\frac{\theta}{2}\right) \\ &+ \frac{r^{1/2}}{6\pi}\left(3\cos\frac{\theta}{2} - \cos\frac{3\theta}{2}\right) + r^{1/2}\left(-\frac{1}{12\pi} + \frac{\log 4}{4\pi}\right)\left(3\cos\frac{\theta}{2} + \cos\frac{3\theta}{2}\right).\end{aligned} \tag{4.79}$$

At leading order, we recover the streamfunction for a Stokeslet and a particular solid-body motion:

$$u_x \sim -\frac{1}{2\pi}\log r + \frac{x^2}{2\pi r^2} - \frac{1}{2\pi} - \frac{\log 4}{\pi} + \mathrm{O}(r^{-1/2}\log r), \tag{4.80}$$

$$u_y \sim \frac{xy}{2\pi(x^2+y^2)} + \mathrm{O}(r^{-1/2}\log r). \tag{4.81}$$

With the notation of section 4.7 above, this solid body motion corresponds to $u_\infty = -(\log 4)/\pi$. This will be important when matching the velocity to the solution on larger scales, both for wide wedges and then later for drop coalescence.

The remaining terms in the streamfunction proportional to $r^{1/2}$ and $r^{1/2}\log r$ agree with the solution for a slender single cut found above (4.56), with $u_\infty = -(\log 4)/\pi$. This is therefore the correct inner-inner solution that matches to the far-field solution on larger scales.

4.9 Updated solution for wide wedges

Returning to the problem of the retraction of a wide wedge, we will now match the solution on the radius-of-curvature lengthscale to the solution on the inner scale. We recall that the solution in 4.8 was rescaled, and was found in a frame moving with the tip of the parabola. We can compare the x-component of the velocity between

Hopper's parabola solution and the velocity on the inner scale, with

$$\dot{x}_0 - \frac{\gamma}{2\pi\mu}\log\frac{r}{\gamma t/\mu\,(4\epsilon\delta^{-1/2}/\pi)^2} + \frac{\gamma x^2}{2\pi\mu r^2} - \frac{\gamma\log 4}{\pi\mu} = -\frac{\gamma}{2\pi\mu}\log\frac{r}{(\nu t)^{1/2}} + \frac{\gamma x^2}{2\pi\mu r^2} + \frac{\gamma}{4\pi\mu}b_\infty, \tag{4.82}$$

where the left-hand side is the velocity from Hopper's parabola solution, and the right-hand side is a Stokeslet with a solid-body motion set by inertia on the outer scale. We solve this equation for $\dot{x}_0$ as

$$\dot{x}_0 = -\frac{\gamma}{2\pi\mu}\log\left(\frac{\gamma t}{\mu(\nu t)^{1/2}}\frac{16\epsilon^2\delta^{-1}}{\pi^2}\right) + \frac{\gamma\log 4}{\pi\mu} + \frac{\gamma b_\infty}{4\pi\mu}. \tag{4.83}$$

Now we recall that $\delta = (\bar{x}_0)^{-1}$ and $x_0 = (\gamma t/4\pi\mu)\log(\mu^3/\rho\gamma^2 t) + \gamma t\bar{x}_0/\mu$, so substituting gives

$$-\frac{\gamma}{4\pi\mu} + \frac{\gamma}{\mu}\bar{x}_0 = -\frac{\gamma}{2\pi\mu}\log\left(\frac{16\epsilon^2\bar{x}_0}{\pi^2}\right) + \frac{\gamma\log 4}{\pi\mu} + \frac{\gamma b_\infty}{4\pi\mu} \tag{4.84}$$

and so

$$\bar{x}_0 = \frac{1}{\pi}\log\left(\frac{\pi}{4\epsilon(\bar{x}_0)^{1/2}}\right) + \frac{\log 4}{\pi} + \frac{b_\infty}{4\pi} + \frac{1}{4\pi}, \tag{4.85}$$

where $b_\infty \approx 1.82$ from the outer solution. We invert this for $\bar{x}_0$, either numerically, or with a Lambert-W function as

$$\bar{x}_0 = \frac{1}{2\pi}W\left(2\pi^3\epsilon^{-2}\exp\left(\frac{b_\infty}{2} + \frac{1}{2}\right)\right), \tag{4.86}$$

where the Lambert-W function satisfies $W(z)\exp(W(z)) = z$. We can compare this final result for the rate of retraction with Billingham's numerical solutions for small ϵ. For this comparison, we recall that our choice of coordinates was different from that in [6], so that Billingham's $\bar{y}_0$ is equivalent to our $-\bar{x}_0$. We reproduce Billingham's plot of $\bar{y}_0$ as figure 4.12(a). Billingham's caption for the figure indicates that the dashed line is the asymptotic expression

$$\bar{y}_0 \sim \frac{1}{\pi}\log\epsilon + \frac{1}{2\pi}\log\left(-\frac{1}{2\pi}\log\epsilon\right) + \tilde{y}_0, \tag{4.87}$$

where $\tilde{y}_0$ is an O(1) constant from the inner-inner solution. Billingham's discussion of the inner-inner region gives the value "$\bar{y}_0 \approx -0.381$". This may be a typographical error

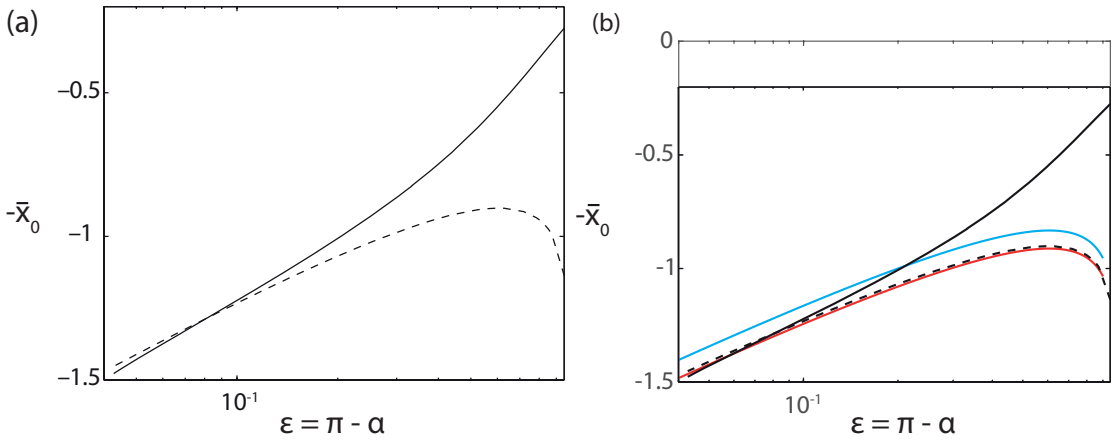

Fig. 4.12 (a) Billingham's solution for the retraction rate, reproduced from figure 7.1 of [6]. Numerical solutions (solid line) and Billingham's asymptotic (dashed line). The label on the y-axis has been changed from $Y(0)$ to $-\bar{x}_0$ here. (b) Attempts to re-create Billingham's asymptotic in figure 7.1. Blue line: (4.87) with $\tilde{y}_0 = -0.381$. Red line: (4.87) with $\tilde{y}_0 = -0.461$.

for $\tilde{y}_0$, but the value $\tilde{y}_0 = -0.381$ in (4.87) does not give the asymptotic expression plotted in figure Billingham's figure 7.1; it gives an asymptotic expression shown with a blue line in figure 4.12(b). Billingham has clearly plotted the asymptotic expression with a different constant.

If we subtract a factor of $1/4\pi$ from -0.381, we get something closer to the dashed line in figure 4.12(a). It is possible that, while working on the inner-inner problem, Billingham made a substitution for the constant $\tilde{y}_0 - K_0$, and intended to report that constant as -0.381. This would explain the extra factor of $1/4\pi$, and imply a real numerical value for $\tilde{y}_0 \approx -0.461$ for Billingham's inner-inner problem. This gives the red line in figure 4.12(b), which is much closer to the dashed line plotted by Billingham.

We plot our asymptotic expression (4.86) in figure 4.13b with a red dashed line. While the updated asymptotic line is further from the numerical results than Billingham's asymptotic prediction for this range of ϵ, it seems possible that the trend in the numerical results is towards the updated asymptotic line for small ϵ. The smallest value of ϵ in the numerical solutions is about 0.04, and it would be interesting to see if the numerical results continue to approach the new asymptotic expression for smaller ϵ.

We can also make a prediction for the curvature at the tip of the wedge from the exact parabola solution on the radius-of-curvature scale. We have seen that the surface is curved on the smallest scale as $Y = (r_c x)^{1/2}$ with $\sqrt{r_c} = 4\epsilon\delta^{-1/2}/\pi$. The curvature at

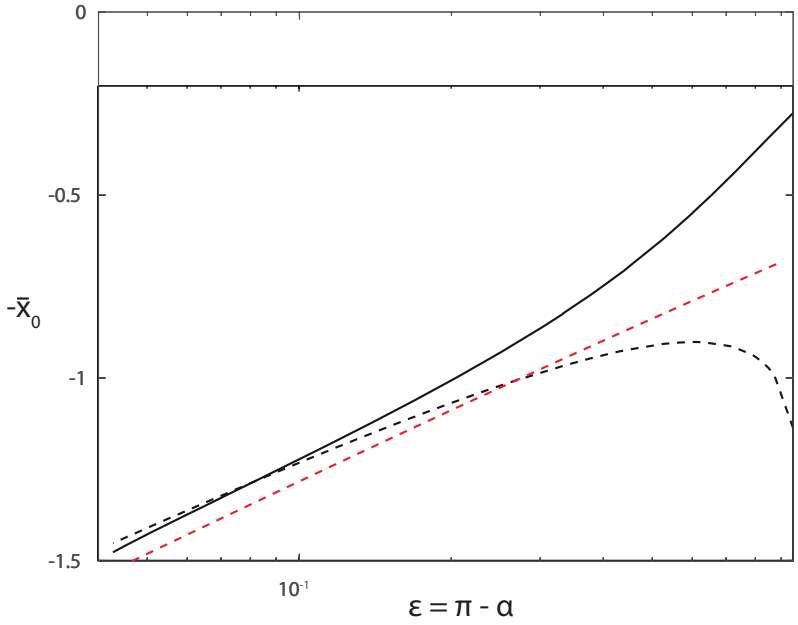

Fig. 4.13 Solid black line; Billingham's numerical solution for $-\bar{x}_0$. Black dashed line; Billingham's asymptotic expression. Red dashed line; the updated asymptotic expression (4.86).

the tip is therefore

$$\kappa \sim \frac{2}{r_c} \sim \frac{\pi^2 \delta}{8\epsilon^2}, \tag{4.88}$$

which is shown in figure 4.14 with a red dashed line. Once again, the difference between the numerical results and the asymptotic expression is larger than with Billingham's asymptotic expression for this range of ϵ. However, the updated asymptotic expression does not cross the numerical solution line, and the numerical results could still tend to the new asymptotic expression for smaller ϵ.

4.10 Discussion

Billingham solves for the initial stage of retraction of wedges with viscosity and inertia. The solution involves an outer scale on which inertia balances viscosity, and an inner scale where the Stokes equations hold. Matching the velocity between the two scales determines the rate of retraction of the wedge tip. Billingham also gives asymptotic results for very narrow and very wide wedges, each of which uses a linearisation of the boundary conditions to the axis.

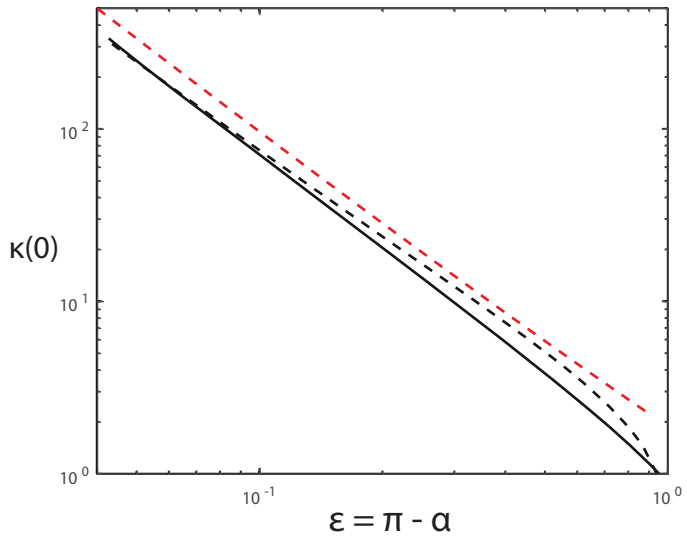

Fig. 4.14 Reproduced from figure 7.3 of [6]. Black solid line; Billingham's numerical solution for the curvature at the tip. Black dashed line; Billingham's asymptotic expression. Red dashed line; the asymptotic (4.88)

In this chapter, we reviewed the solution and the asymptotic limits, and made some technical improvements to the solution. We solved for the constant K with a force balance argument rather than numerically, and we applied Hopper's exact solution for the retraction of a parabola to the radius-of-curvature scale for the asymptotic solution for wide wedges.

The use of this exact solution gives neat expressions for the position of the wedge (4.86) and the curvature at the tip (4.88). The updated solution also gives an exact expression for the flow on the smallest scale, and clarifies the matching between the parabola solution and the Stokes solution on the inner scale. We have shown that the solution on intermediate scales is a combination of four Stokes solutions proportional to $r^{1/2}$ or $r^{1/2}\log r$. These were in fact identified by Billingham, but the asymptotic solution for wide wedges in [6] neglects some parts of the solution. We have shown that all of these four solutions appear on intermediate scales, rather than just the stress-free solution.

Billingham's paper [6] ends with an appendix describing difficulties applying the asymptotic solutions for narrow and wide wedge retraction to the coalescence of bubbles and drops. We have seen that the asymptotic solution for narrow wedges involves the universal solution for a retracting edge, which was also relevant for bubble coalescence in chapter 2. We will now show how the asymptotic solution for wide wedges is relevant for drop coalescence.

Chapter 5

Drop coalescence without inertia

5.1 Introduction

5.1.1 Context

Just after two drops touch, they are in contact over some 'fluid bridge' of radius r_b say, as sketched in figure 5.1. The surface at the edge of this fluid bridge is tightly curved at early times. Surface tension acts on this tightly-curved surface, driving a flow that quickly pulls the fluid bridge wider. At later times, the surface will relax towards one spherical drop.

The initial stage of coalescence, just after contact, has attracted significant interest in recent years [e.g. 1, 23, 28, 47, 49, 56]. This is an example of a fluid singularity, as the topology of the surface changes at the moment of contact between the drops. The curvature is initially very large and so the resulting flow driven by surface tension is also large. This motion is difficult to resolve with experimental imaging techniques or with numerical simulations [49]. We will therefore look for theoretical descriptions of drop coalescence.

In two dimensions, there is an exact solution for the fluid flow and the shape of the surface during coalescence for two inertialess drops. This solution was independently found by Hopper and Richardson [28, 56]. The flow is driven by surface tension and resisted by viscosity, and during the initial stage the fluid bridge grows as $r_b \sim (\gamma t/\pi\mu)\log(1/t)$, where γ is the coefficient of surface tension, μ is the dynamic viscosity and t is the time elapsed since contact.

Eggers *et al.* [23] present an argument to suggest that inertia should be negligible for drop coalescence with any fluid at sufficiently early times. The Reynolds number

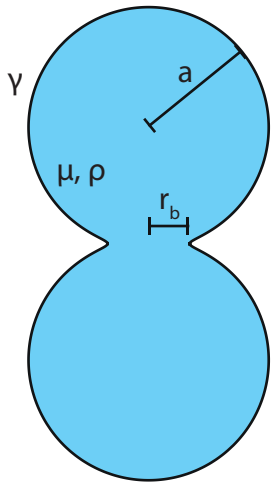

Fig. 5.1 Sketch of two coalescing drops, in contact over some fluid bridge of radius r_b. The density is ρ, the dynamic viscosity is μ, the initial drop radius is a and the coefficient of surface tension is γ.

based on the radius of the fluid bridge r_b, the velocity $\dot{r}_b$ and the kinematic viscosity ν is $r_b\dot{r}_b/\nu$. At early times, if $r_b\dot{r}_b$ is small, then the Reynolds number is small.

However, experiments by Paulsen *et al.* [49] show that the bulk of each drop is initially stationary. This is contrary to the exact two-dimensional Stokes solution, which has some motion in the bulk of each drop. Moreover, Paulsen *et al.* argue that inertia cannot be neglected; suppose that the mass of each drop, $4\pi\rho a^3/3$, were to accelerate. By Newton's second law, this would require a force, which must come from the fluid-bridge scale. Paulsen *et al.* argue that the force is bounded by $2\pi\gamma r_b$, and that this force is not sufficient to cause the acceleration in the two-dimensional Stokes solution.

We will show that both of these arguments are flawed. The Reynolds number constructed by Eggers *et al.* is appropriate on the scale of the fluid bridge, but there is a larger scale on which inertia matters. The force considered by Paulsen *et al.* is not a bound on the force over the fluid bridge, and is in fact balanced locally by viscous stresses in all the cases we consider below.

We will eventually seek an asymptotic solution for drop coalescence in three dimensions with inertia and viscosity. But first, to demonstrate the method, we will find an asymptotic solution for inertialess drop coalescence. A comparison with the exact solution [28, 56] will justify the use of the asymptotic method in the more complicated case of coalescence with inertia, for which no exact solution is known.

As an added bonus, we will find a simple closed-form expression for the velocity during the initial stage of inertialess drop coalescence. Although Hopper and Richard-

son's exact solution [28, 56] does determine the velocity, it is given implicitly in terms of integrals which must be calculated numerically.

Our analysis of the inertialess problem will also identify several solutions of the Stokes equations. A linear combination of these solutions gives the flow for inertialess drop coalescence, and we will see later that a different linear combination will give the flow for drop coalescence with inertia.

5.1.2 Overview

In §5.2 we will describe the lengthscales of the solution for coalescence in two dimensions without inertia. We will solve for the similarity solution on the scales of the fluid bridge in §5.3, and solve for the flow near the edge in §5.4. The calculation on the fluid-bridge scale neglects certain stresses on the free surface, which we address in §5.6. We match the two flows together in §5.5 and extract the growth of the fluid bridge $r_b(t)$.

For two-dimensional inertialess coalescence, there is an exact solution. We compare the asymptotic solution with the exact solution in §5.7, and discuss the agreement between the two in §5.8.

The advantage of the asymptotic solution is that we can adapt it to three dimensions. We find the appropriate three-dimensional asymptotic solution for inertialess coalescence in §5.9.

5.2 Structure of the asymptotic solution

We will consider the early-time behaviour for the coalescence of two inertialess drops, with equal initial radius a. The solution will be asymptotic in the small parameter t, the time elapsed since contact.

At early times, there is separation of lengthscales between the fluid bridge and the radius of each drop. We will therefore seek a similarity solution on the fluid-bridge scale. This will match to some flow in the bulk of each drop. Since the surfaces of the two drops are initially close together, the surface is tightly curved at the edge of the fluid bridge.

We must therefore match our similarity solution on the fluid-bridge scale to a Stokes flow on the inner scale where the surface is tightly curved. We will show that, on this inner scale, Hopper's solution for the retraction of a parabola describes the flow, as in section §4.9 for wide wedges. Then matching the velocities will give the rate of retraction. The scales of the problem are shown in figure 5.2.

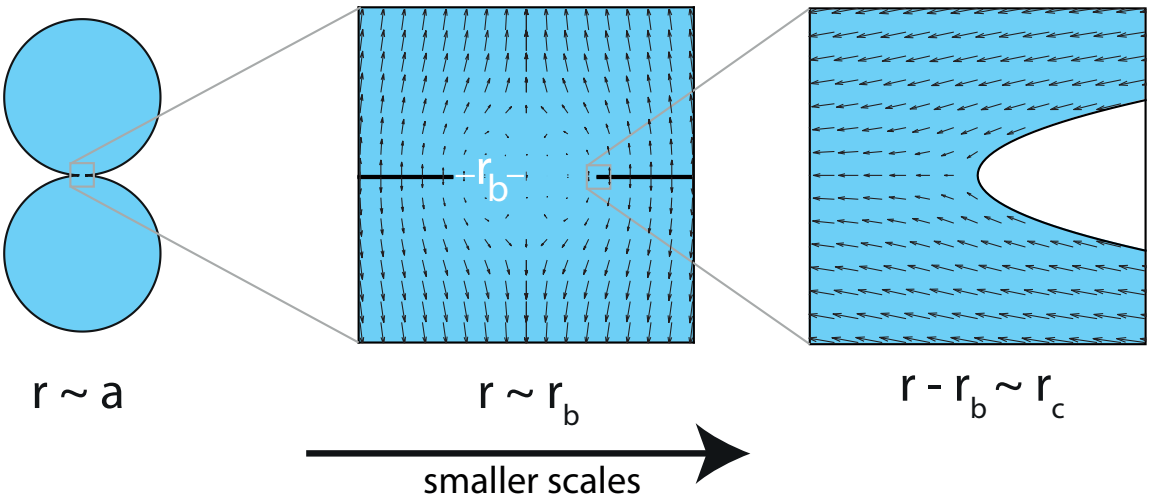

Fig. 5.2 Scales for the coalescence of viscous drops. The flow in the bulk of each drop matches to the similarity solution on the fluid-bridge scale, which is driven by the free-surface Stokes flow on the radius of curvature scale.

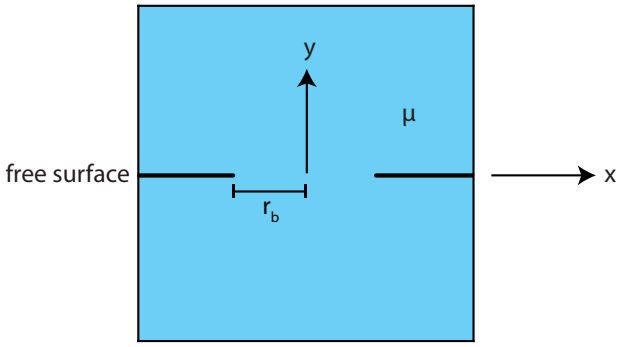

Fig. 5.3 Co-ordinates for the similarity solution on the fluid-bridge scale. The fluid bridge lies in $-r_b < x < r_b$. The free surfaces of the drops are near $y = 0$ for $|x| > r_b$.

For wedge retraction, we have seen that the tip retracts a distance proportional to $(\gamma t/\mu)\log(1/t)$. Inspired by this result, we will assume that $r_b \gg \gamma t/\mu$ for the initial stage of drop coalescence (to be checked from the actual solution).

5.3 Similarity solution on the fluid-bridge scale

We take co-ordinates (x, y) with the x-axis along the fluid bridge and the y-axis along the centreline of the drops, as shown in figure 5.3. The free surface is at $\pm h(x)$ for $x > r_b$. On scales smaller than the radius of the drops, the initial circular shape of the drops is approximately $h \sim x^2/2a$. On the fluid-bridge scale $x \sim r_b$, so $h \sim r_b^2/a$. Since $r_b^2/a \ll r_b$, we can linearise the boundary conditions on to the line $y = 0$.

As a result, the surface is tightly curved at $x = \pm r_b$, with a radius of curvature much smaller than r_b. We can estimate the radius of curvature as $r_c \sim h^2/r_b \sim r_b^3/a^2$. Since this lengthscale is much smaller than r_b at early times, we have asymptotic separation between the fluid-bridge scale and the radius of curvature scale.

In analogy with Billingham's asymptotic solution for wide wedges, the fluid-bridge scale plays the role of the inner scale, while the radius-of-curvature scale plays the role of the inner-inner solution. As with the wide wedge asymptotic solution, we model the force from the tightly-curved surface with a point force on the larger scale. Here, the surface is tightly curved in two places, at $x = \pm r_b$ on the x-axis. We model the force from surface tension with a pair of Stokeslets. The velocity is

$$\begin{aligned} u_x =& \frac{\gamma}{2\pi\mu}\left(-\log\left(\sqrt{\frac{(x-r_b)^2+y^2}{(x+r_b)^2+y^2}}\right) + \frac{(x-r_b)(x-r_b)}{(x-r_b)^2+y^2} - \frac{(x+r_b)(x+r_b)}{(x+r_b)^2+y^2}\right), \\ u_y =& \frac{\gamma}{2\pi\mu}\left(\frac{(x-r_b)y}{(x-r_b)^2+y^2} - \frac{(x+r_b)y}{(x+r_b)^2+y^2}\right). \end{aligned} \tag{5.1}$$

We have shown before that a Stokeslet has no stress on a plane through its point of application. Here, both parts of the free surface lie on the plane $y = 0$, so each Stokeslet satisfies the no-stress conditions on the free surface.

Also, this pair of Stokeslets has no normal velocity on the free surface at leading order, since $u_y = 0$ when $y = 0$. At the next order, our similarity solution must have some normal velocity on the surface, since the free surface must vary from its far-field shape $h \sim x^2/2a$ down to $h = 0$ at $x = r_b$. The correction velocity $\mathbf{u}_c$ that gives this motion must scale with $r_b\dot{r}_b/a$. We note that, at early times, this velocity is smaller than the Stokeslet velocity, so this really is an asymptotically small correction. We will now find the similarity solution for $\mathbf{u}_c$ to find the surface shape on the fluid-bridge scale. This will give the curvature at the edge of the fluid bridge. This is analogous to the inner Stokes flow for the wide wedge asymptotic solution in section 4.6.2.

The Stokes equations for $\mathbf{u}_c$ are

$$-\boldsymbol{\nabla} p + \mu\nabla^2\mathbf{u}_c = \mathbf{0}, \quad \boldsymbol{\nabla}\cdot\mathbf{u} = 0, \tag{5.2}$$

and the kinematic boundary condition, neglecting terms that are quadratically small in $\mathbf{u}_c$ and h, is

$$\frac{\partial h}{\partial t} = u_y. \tag{5.3}$$

We can non-dimensionalise the co-ordinates and the velocities with

$$\mathbf{x} = r_b\bar{\mathbf{x}}, \quad h = \frac{r_b^2}{2a}\bar{h}(\bar{x}), \quad \mathbf{u}_c = \frac{r_b\dot{r}_b}{a}\bar{\mathbf{u}}, \quad p = \frac{\mu\dot{r}_b}{a}\bar{p}, \tag{5.4}$$

The pressure has been scaled to balance the stress in the Stokes equations, which become

$$-\bar{\boldsymbol{\nabla}}\bar{p} + \bar{\nabla}^2\bar{\mathbf{u}} = \mathbf{0}, \quad \bar{\boldsymbol{\nabla}}\cdot\bar{\mathbf{u}} = 0. \tag{5.5}$$

For the leading-order solution, we linearised the free-surface to $y = 0$. We might expect that the next-order correction from the linearisation would enter the problem for $\bar{\mathbf{u}}$. But in fact, we will show that the surface stress from the linearisation is small, and only enters the problem at the next order. Expanding the stress for the pair of Stokeslets, the stress at (x, h) is

$$\boldsymbol{\sigma}\cdot\mathbf{n} = \frac{2\gamma}{\pi}\frac{(xh_x - h)}{(x-1)^2}\mathbf{e}_x - \frac{2\gamma}{\pi}\frac{(xh_x - h)}{(x+1)^2}\mathbf{e}_x + \mathrm{O}\left(\frac{\gamma h^2}{r_b^3}\right), \tag{5.6}$$

where $\boldsymbol{n} \approx (h_x, -1)$ is the normal pointing out of the fluid. The stress is therefore of order $\mathrm{O}(\gamma/a)$. But the pressures we are considering, scaling as in (5.4), are of size $\mu\dot{r}_b/a$. Since we expect $\dot{r}_b \gg \gamma/\mu$ at early times, the stresses proportional to $\mu\dot{r}_b/a$ are much larger than γ/a. So at this order, we have stress-free boundary conditions; at further orders there will be corrections due to the surface stresses, with the associated velocity proportional to $\gamma r_b/\mu a$. We will discuss this additional correction further in §5.6 and appendix A.

The stress-free boundary conditions for the non-dimensionalised problem are

$$-\bar{p} + 2\frac{\partial\bar{u}_y}{\partial\bar{y}} = 0 \quad \text{on } \bar{y} = 0,\ |\bar{x}| > 1, \tag{5.7}$$

$$\left(\frac{\partial\bar{u}_x}{\partial\bar{y}} + \frac{\partial\bar{u}_y}{\partial\bar{x}}\right) = 0 \quad \text{on } \bar{y} = 0,\ |\bar{x}| > 1. \tag{5.8}$$

By symmetry between the drops, we must have no tangential stress or normal velocity on the fluid bridge, so

$$\frac{\partial\bar{u}_x}{\partial\bar{y}} + \frac{\partial\bar{u}_y}{\partial\bar{x}} = 0 \quad \text{on } \bar{y} = 0,\ |\bar{x}| < 1, \tag{5.9}$$

$$\bar{u}_y = 0 \quad \text{on } \bar{y} = 0,\ |\bar{x}| < 1. \tag{5.10}$$

We could, if we wanted, replace the boundary conditions on $\bar{x} < 0$ with symmetry conditions on the centre-line $\bar{x} = 0$:

$$\bar{u}_x = 0, \quad \text{and} \quad \frac{\partial \bar{u}_y}{\partial \bar{x}} = 0 \quad \text{on } \bar{x} = 0. \tag{5.11}$$

The kinematic boundary condition with the scalings (5.4) becomes

$$\bar{h} - \frac{\bar{x}}{2}\frac{\partial \bar{h}}{\partial \bar{x}} = \bar{u}_y \quad \text{on } \bar{y} = 0,\ \bar{x} > 1. \tag{5.12}$$

We will write the correction velocity components in terms of a streamfunction,

$$\bar{u}_x = \frac{\partial \psi}{\partial \bar{y}}, \quad \bar{u}_y = -\frac{\partial \psi}{\partial \bar{x}}, \tag{5.13}$$

and then if we take the curl of the Stokes equations (5.5) with this streamfunction then we have the biharmonic equation

$$\nabla^4 \psi = 0. \tag{5.14}$$

The boundary conditions in terms of p and ψ are

$$-p - 2\frac{\partial^2 \psi}{\partial \bar{x} \partial \bar{y}} = 0 \quad \text{on } \bar{y} = 0,\ |\bar{x}| > 1, \tag{5.15}$$

$$\frac{\partial^2 \psi}{\partial \bar{y}^2} - \frac{\partial^2 \psi}{\partial \bar{x}^2} = 0 \quad \text{on } \bar{y} = 0, \tag{5.16}$$

$$\frac{\partial \psi}{\partial \bar{x}} = 0 \quad \text{on } \bar{y} = 0,\ |\bar{x}| < 1, \tag{5.17}$$

and the symmetry conditions become

$$\frac{\partial \psi}{\partial \bar{y}} = 0, \quad \frac{\partial^2 \psi}{\partial \bar{x}^2} = 0, \quad \text{on } \bar{x} = 0. \tag{5.18}$$

We will solve for ψ using elliptic cylindrical co-ordinates, defined by

$$\bar{x} + i\bar{y} = \cosh(\xi + i\eta), \tag{5.19}$$

where we restrict $-\infty < \xi < \infty$, $0 < \eta < \pi$. We will write $\zeta = \xi + i\eta$. The contours of ξ are confocal ellipses, and contours of η are the hyperbolas orthogonal to these ellipses, sketched in figure 5.4. The advantage of this co-ordinate system is that it maps the fluid bridge to $\xi = 0$ and the free surface to $\eta = 0$. So rather than a problem

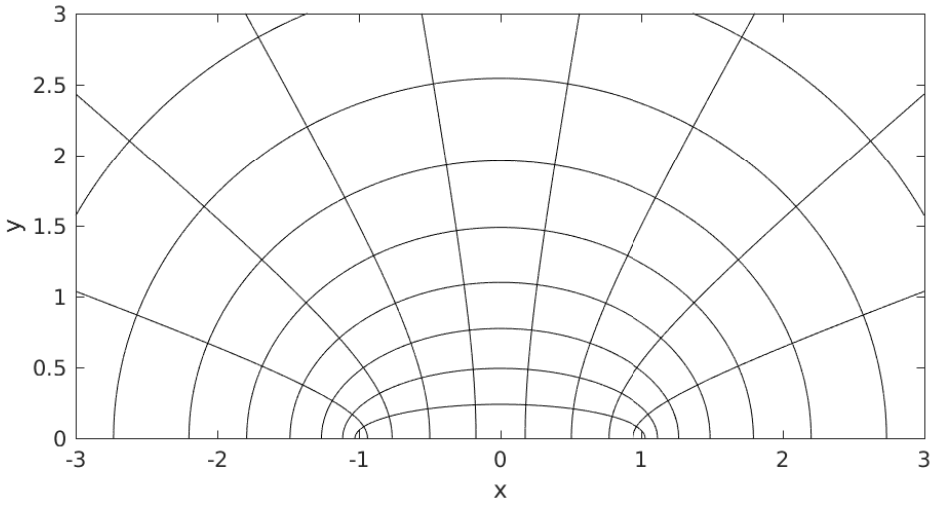

Fig. 5.4 Contours of the elliptic cylindrical co-ordinate system defined by (5.19).

with different boundary conditions on different parts of the axis, we have separate boundary conditions on separate axes in ζ-space.

The Laplacian in these co-ordinates is

$$\nabla^2 = \frac{1}{\sinh^2\xi + \sin^2\eta}\left(\frac{\partial^2}{\partial\xi^2} + \frac{\partial^2}{\partial\eta^2}\right), \tag{5.20}$$

and we must solve the biharmonic equation $\nabla^4\psi = 0$. The boundary conditions in these co-ordinates are

$$-\frac{\partial^3\psi}{\partial\eta^3} - 3\frac{\partial^3\psi}{\partial\xi^2\partial\eta} + 2\left(1 - 3\coth^2\xi\right)\frac{\partial\psi}{\partial\eta} + 6\coth\xi\frac{\partial^2\psi}{\partial\xi\partial\eta} = 0 \quad \text{on } \eta = 0, \tag{5.21}$$

$$\frac{\partial^2\psi}{\partial\eta^2} + 2\coth\xi\frac{\partial\psi}{\partial\xi} - \frac{\partial^2\psi}{\partial\xi^2} = 0 \quad \text{on } \eta = 0, \tag{5.22}$$

$$\cot\eta\frac{\partial\psi}{\partial\eta} + \frac{\partial^2\psi}{\partial\xi^2} - \cot\eta\frac{\partial\psi}{\partial\xi} + \frac{\partial^2\psi}{\partial\xi\partial\eta} = 0 \quad \text{on } \xi = 0, \tag{5.23}$$

$$\frac{\partial\psi}{\partial\eta} = 0 \quad \text{on } \xi = 0, \tag{5.24}$$

where we have taken the x-derivative of the normal stress condition and eliminated the pressure with the Stokes equations. This removes the arbitrary constant from the pressure, and gives a problem in terms of the streamfunction alone.

A large family of solutions to the biharmonic equation can be found by taking the real and imaginary parts of certain complex functions. First, we note that if $f(z)$ is an

analytic function of $z = x + iy$, then f satisfies the Cauchy-Riemann equations

$$\frac{\partial \Re f}{\partial x} = \frac{\partial \Im f}{\partial y}, \quad \text{and} \quad \frac{\partial \Re f}{\partial y} = -\frac{\partial \Im f}{\partial x}, \tag{5.25}$$

and so f satisfies

$$\left(\frac{\partial^2}{\partial x^2} + \frac{\partial^2}{\partial y^2}\right) f = 0. \tag{5.26}$$

So the real and imaginary parts of f satisfy Laplace's equation $\nabla^2 \psi = 0$.

Now we write $g(z) = \bar{z} f(z)$ and note that

$$\left(\frac{\partial^2}{\partial x^2} + \frac{\partial^2}{\partial y^2}\right) g = 4\frac{\partial f}{\partial z}, \tag{5.27}$$

and so $\nabla^4 g = 0$, so the real and imaginary parts of $g(z)$ satisfy the biharmonic equation. By choosing suitable analytic functions $f(z)$ and taking the real and imaginary parts of $f(z)$ and $\bar{z} f(z)$, we can find a large family of solutions.

Working with functions from this family, and with some trial and error, we can find two solutions to the biharmonic equation which satisfy all the boundary conditions (5.21)–(5.24). They are

$$\psi_1 = \frac{\sinh^3 \xi \cos \eta}{\sinh^2 \xi + \sin^2 \eta} \quad \text{and} \quad \psi_2 = \cos \eta \left(\xi \cosh \xi - \sinh \xi\right). \tag{5.28}$$

The velocity fields corresponding to ψ_1 and ψ_2 are shown in figure 5.5. The velocity field corresponding to ψ_1 tends to a constant solid-body motion in the far-field. We can find this constant by expanding the streamfunction;

$$\psi_1 \sim \cosh \xi \cos \eta \quad \text{as } \xi \to \infty, \tag{5.29}$$

and since $x = \cosh \xi \cos \eta$, this corresponds to the velocity $\bar{u}_x = 0$, $\bar{u}_y = -1$.

The velocity field corresponding to ψ_2 grows in the far-field. We can expand ψ_2 as

$$\psi_2 \sim \cos \eta \left(\xi \cosh \xi - \cosh \xi\right) \quad \text{as } \xi \to \infty, \tag{5.30}$$

and since $\xi \sim \log(2\sqrt{x^2 + y^2})$ in the far-field, this is

$$\psi_2 \sim x \log \sqrt{x^2 + y^2} - x \quad \text{as } x^2 + y^2 \to \infty, \tag{5.31}$$

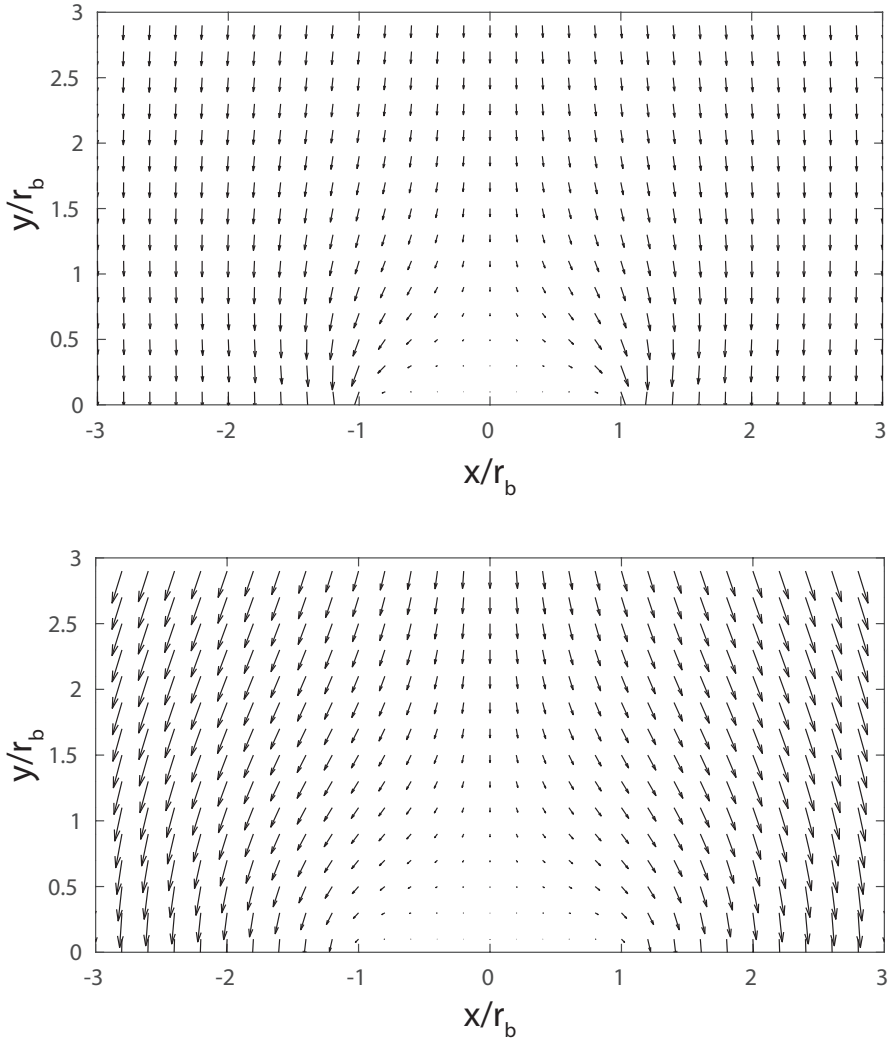

Fig. 5.5 The Stokes flows given by streamfunctions ψ_1 and ψ_2 (5.28).

which corresponds to the velocity

$$u_x \sim \frac{xy}{x^2+y^2}, \quad u_y \sim -\log\sqrt{x^2+y^2} + \frac{y^2}{x^2+y^2} \quad \text{as } x^2+y^2 \to \infty. \tag{5.32}$$

This is the two-dimensional Stokeslet velocity. There must be some normal stress distribution over the fluid bridge for this flow to balance this Stokeslet.

The streamfunction ψ_2 corresponds to the solution given by Timoshenko and Goodier for the displacement of a stretched elastic hyperbola with a specified force across the neck [72, pp. 204–206]. By analogy, we could think of the streamfunction ψ_1 as the solution for a specified strain with no stress over the neck.

For drop coalescence without inertia, the solution on the outer drop scale must satisfy the Stokes equations. Since the forces on the outer Stokes flow must balance, we cannot have any force on the outer flow from the fluid bridge. So there must be no Stokeslet in the far-field of the fluid-bridge scale, and so we cannot have any multiple of ψ_2 on the fluid-bridge scale. We therefore take a multiple of ψ_1 alone as the streamfunction on this scale. With $\psi = A\psi_1$, the kinematic boundary condition becomes

$$\bar{h} - \frac{1}{2}\coth\xi\frac{\partial\bar{h}}{\partial\xi} = -A\coth\xi, \tag{5.33}$$

which we integrate for

$$\bar{h}(\xi) = 2A\cosh\xi\sinh\xi, \tag{5.34}$$

where we have applied $\bar{h} = 0$ at $\xi = 0$. In order for the shape to match to the far-field shape $h \sim x^2/2a$, we must have $A = \frac{1}{4}$, and so

$$h(x) = \frac{x}{2a}\sqrt{x^2 - r_b^2}. \tag{5.35}$$

This is the shape of the surface on the scale of the fluid bridge. We note that there is some displacement in the far-field; we have

$$h \sim \frac{x^2}{2a} - \frac{r_b^2}{4a} + \mathrm{O}\left(\frac{r_b^4}{ax^2}\right). \tag{5.36}$$

This displacement corresponds to the velocity in the far-field, which is a solid-body motion with magnitude $r_b\dot{r}_b/2a$.

On the drop scale, we must technically solve for the free-surface Stokes flow in a circular drop which matches to this solid-body motion. But this is trivially satisfied by a solid-body motion throughout the drop; the bulk of each drop moves with spatially-

uniform velocity at leading order. Further corrections, smaller than the flows considered here, will drive smaller flows in the bulk of each drop.

Now to close the problem for $r_b(t)$, we must consider the flow on smaller scales. The linearisation which we applied to the boundary conditions fails near the edge of the fluid bridge, where the surface is curved as $h^2 \sim r_c(x - r_b)$ with $r_c = r_b^3/2a^2$. In order to find the rate of coalescence, we must solve for the Stokes flow on an inner-inner scale with $(x - r_b) \sim r_c$ and $y \sim r_c$. Asymptotic matching between this smaller scale and the fluid-bridge scale will give a matching condition for $\dot{r}_b$.

5.4 Inner-inner scale

On the inner-inner scale, we rescale with

$$x = r_b + r_c\tilde{x}, \quad y = r_c\tilde{y}, \quad Y = r_c\tilde{Y}, \quad u_x = \dot{r}_b + \frac{\gamma}{\mu}\tilde{u}_x, \quad u_y = \frac{\gamma}{\mu}\tilde{u}_y. \tag{5.37}$$

The velocity scale here has been chosen so that the stress balances the imposed stress from surface tension. With this rescaling, the far-field shape is now $\tilde{Y}^2 = \tilde{x}$. Since the velocity γ/μ is much larger than $\dot{r}_c$, the kinematic boundary condition is

$$\tilde{\mathbf{u}} \cdot \tilde{\mathbf{n}} = 0, \tag{5.38}$$

and the shape is steady at this order. This is precisely the problem solved by Hopper [31] for the surface-tension–driven retraction of a parabola, which we reviewed above in §4.8. We can therefore simply quote the solution above for the velocity on the inner-inner scale. The far-field velocity is

$$\tilde{u}_x \sim -\frac{1}{2\pi}\log\tilde{r} + \frac{\tilde{x}^2}{2\pi\tilde{r}^2} - \frac{1}{2\pi} - \frac{\log 4}{\pi} + \mathrm{O}(\tilde{r}^{-1/2}\log\tilde{r}) \tag{5.39}$$

$$\tilde{u}_y \sim \frac{\tilde{x}\tilde{y}}{2\pi(\tilde{x}^2 + \tilde{y}^2)} + \mathrm{O}(\tilde{r}^{-1/2}\log\tilde{r}). \tag{5.40}$$

We will now match the velocities between the inner-inner scale and the fluid-bridge scale to close the problem.

5.5 Matching

We have two expressions for the velocity on scales between r_c and r_b; the velocity on intermediate scales can be described either with the Stokeslet flow near the edge, or

with the far-field velocity of the retracting parabola. From the parabola solution, we have

$$u_x \sim \dot{r}_b + \frac{\gamma}{2\pi\mu}\left(-\log\frac{\sqrt{(x-r_b)^2+y^2}}{r_c} + \frac{(x-r_b)(x-r_b)}{(x-r_b)^2+y^2}\right) - \frac{\gamma}{\pi\mu}\left(\log 4 + \frac{1}{2}\right), \quad (5.41)$$

which must agree with the Stokeslet flow

$$u_x \sim \frac{\gamma}{2\pi\mu}\left(-\log\sqrt{(x-r_b)^2+y^2} + \frac{(x-r_b)(x-r_b)}{(x-r_b)^2+y^2}\right) + \frac{\gamma}{2\pi\mu}\left(\log 2r_b - 1\right). \quad (5.42)$$

So we must have

$$\dot{r}_b \sim \frac{\gamma}{\pi\mu}\log\frac{8a}{r_b} \quad (5.43)$$

for the velocity at the edge of the fluid bridge, which we integrate at leading-order for

$$r_b \sim \frac{\gamma t}{\pi\mu}\log\frac{8\pi a\mu}{\gamma t}. \quad (5.44)$$

This gives the growth of the fluid bridge during the initial stage.

5.6 Next-order corrections due to surface stress

In the similarity solution above, we neglected the surface stresses. There are two sources of these surface stress terms. Firstly, the surface is not flat, so surface tension acts on the curved interface to produce some stress. Also, the surface is not quite on $y = 0$, and so the leading-order Stokeslet has some stress on the actual surface.

These surface stresses will drive a smaller flow; the velocity we considered above was proportional to $r_b\dot{r}_b/a$, whereas the velocity driven by these surface stresses is proportional to $\gamma r_b/\mu a$, which is smaller by a factor of $\log(1/t)$ using the solution for r_b above. We know the leading-order surface displacement, so we know the form of the stress on the x-axis.

We have different boundary conditions inside and outside the fluid bridge, and we can solve for the flow with Tranter's method. Appendix A gives the details of the calculation. Near the edge, the solution matches to the $r^{1/2}$ and $r^{1/2}\log r$ terms in the far-field of the parabola solution, in agreement with the single-cut solution in §4.7.

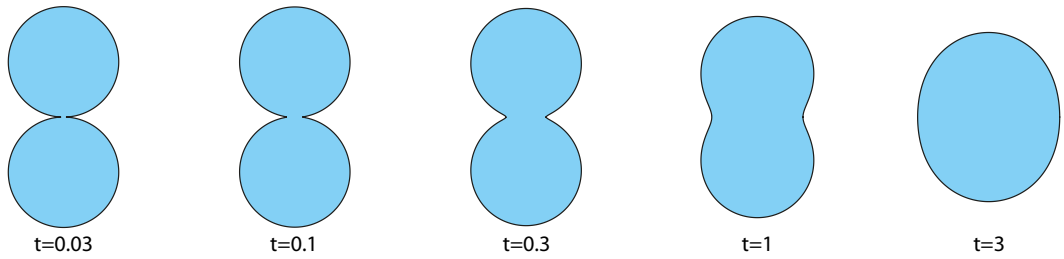

Fig. 5.6 Shapes during Hopper and Richardson's exact solution for inertialess drop coalescence in two dimensions. Times have been non-dimensionalised with respect to $\mu a/\gamma$.

5.7 Comparison with exact solution

We will now compare this asymptotic solution with the exact solution found by Hopper and Richardson [28, 56]. If the asymptotic solution compares well with the exact solution at early times, this will justify the use of similar asymptotic methods to describe three-dimensional coalescence or coalescence with inertia.

5.7.1 Hopper and Richardson's solution

Working with complex co-ordinates $z = x + iy$, Hopper and Richardson write the fluid domain as the image of the unit disc $|\zeta| < 1$ under the conformal map $z = w(\zeta)$, where the map $w(\zeta)$ is given by

$$w(\zeta) = 2a\frac{1-n^2}{\sqrt{2(1+n^2)}}\left(\frac{\zeta}{1+n\zeta^2}\right) \quad \text{for } |\zeta| \leq 1, \tag{5.45}$$

where $0 \leq n \leq 1$ is a function of time given implicitly by

$$t = \frac{\pi\mu a}{2\sqrt{2}\gamma}\int_{n(t)}^{1}\frac{\mathrm{d}k}{K(k)k\sqrt{1+k^2}}, \tag{5.46}$$

and where $K(k) = \int_0^{\pi/2}(1-k^2\sin^2\theta)^{-1/2}\,\mathrm{d}\theta$. Some representative shapes during coalescence are shown in figure 5.6. The corresponding times have been inferred by numerically inverting the implicit equation (5.46).

It will be useful in the following to briefly review the solution method. Here, we will follow the notation of Richardson [56]. An equivalent derivation can be found in the papers on drop coalescence by Hopper [26–29]. Much of theory is shared with the solution for the retraction of a parabola above in §4.8, in which we reviewed work by Hopper [30, 31].

We write the velocity as

$$u + iv = \phi(z) - z\overline{\phi'(z)} - \overline{\chi'(z)}. \tag{5.47}$$

The surface stress boundary condition is

$$\phi(z) + z\overline{\phi'(z)} + \overline{\chi'(z)} = \frac{\gamma i}{2\mu}\frac{\mathrm{d}z}{\mathrm{d}s}, \tag{5.48}$$

where s is the arc-length around the surface. Now we write $z = w(\zeta)$ to map the unit circle to the fluid domain, for some analytic function $w(\zeta)$, and we define

$$\Phi(\zeta) = \phi(w(\zeta)), \quad \text{and} \quad X(\zeta) = \chi'(\phi(\zeta)). \tag{5.49}$$

In terms of these new variables, the boundary condition becomes

$$\Phi(\zeta) + w(\zeta)\frac{\bar{\Phi}'(1/\zeta)}{\bar{w}'(1/\zeta)} + \bar{X}(1/\zeta) = -\frac{\gamma\zeta}{2\mu}\left(\frac{w'(\zeta)}{\bar{w}'(1/\zeta)}\right)^{1/2}, \tag{5.50}$$

where the notation $\bar{f}(z)$ means $\overline{f(\bar{z})}$, which is analytic if $f(z)$ is analytic. Now we split the right-hand side into analytic parts with

$$\frac{1}{(w'(\zeta)\bar{w}'(1/\zeta))^{1/2}} = F_+(\zeta) - F_-(\zeta), \tag{5.51}$$

where $F_+(\zeta)$ and $F_-(\zeta)$ are analytic inside and outside the unit circle respectively, and are defined by

$$F_\pm(\zeta) = \frac{1}{2\pi i}\int \frac{1}{(\tau-\zeta)(w'(\tau)\bar{w}'(1/\tau))^{1/2}}\,\mathrm{d}\tau, \tag{5.52}$$

integrating around the unit circle anti-clockwise. The boundary condition becomes

$$\Phi(\zeta) + \frac{\gamma}{2\mu}F_+(\zeta)\zeta w'(\zeta) = -w(\zeta)\frac{\bar{\Phi}'(1/\zeta)}{\bar{w}'(1/\zeta)} - \bar{X}(1/\zeta) + \frac{\gamma}{2\mu}F_-(\zeta)\zeta w'(\zeta) \quad \text{on } |\zeta| = 1. \tag{5.53}$$

The expression on the left-hand side is analytic inside the unit circle, and the right-hand side is the analytic continuation into $|\zeta| > 1$. The kinematic boundary condition is

$$\frac{\partial w}{\partial t} = 2\Phi(\zeta) + \frac{\gamma}{2\mu}\left(2F_+(\zeta) - F_+(0)\right)\zeta w'(\zeta). \tag{5.54}$$

Now for the map

$$w(\zeta) = Cb\zeta\left(\frac{1}{1-b\zeta} + \frac{1}{1+b\zeta}\right), \tag{5.55}$$

with b and C unknown functions of time, we can use the analytic continuation to solve for the coefficients. This map is relevant to drop coalescence, because for $b \approx 1$, the unit circle is mapped to a pair of circles in contact over a small region. Richardson considers the function

$$G(\zeta) = \Phi(\zeta) + \frac{\gamma}{2\mu}F_+(\zeta)\zeta w'(\zeta), \tag{5.56}$$

which appears in both the boundary condition (5.53) and in the kinematic boundary condition (5.54). Comparing the principal parts at $\zeta = 1/b$ and at $\zeta = -1/b$ gives the analytic function $G(\zeta)$. Finally, the kinematic boundary condition gives the time-dependence of b and C. This gives the solution for $w(\zeta)$ above, where $n = b^2$.

5.7.2 Comparison

The free surface is given by the image of the unit circle. In particular, $\zeta = 1$ maps to the edge of the fluid bridge. So expanding $w(e^{i\theta})$ for small θ gives the free-surface shape near the edge of the fluid bridge. We have

$$w(e^{i\theta}) \sim r_b\left(1 + ir_b\theta/2a + \frac{1}{2}\theta^2\right), \tag{5.57}$$

so the surface nearby has

$$h^2 \sim \frac{r_b^3(x - r_b)}{2a^2}. \tag{5.58}$$

This agrees with the parabola shape at the edge found in the asymptotic solution above.

Hopper and Richardson do not calculate the velocity directly, giving the potentials implicitly. We can calculate the potentials ϕ and χ numerically by first integrating for $F_\pm(\zeta)$. Since we know $G(\zeta)$, we can then solve for $\Phi(\zeta)$ and then $X(\zeta)$. This lets us calculate the velocity at any point in the fluid domain in z-space, at any time t.

As a comparison, we calculate the velocity on the fluid-bridge scale. To check the similarity solution above, we subtract the Stokeslet velocity from the numerically-calculated velocity, and we plot the remainder in figure 5.7(a). For this calculation, we set $n = 1 - \epsilon$ with $\epsilon = 10^{-3}$. The velocity is qualitatively similar to the velocity field associated with ψ_1 that we found above.

More precisely, we can compare u_x along the y-axis. As we decrease ϵ, we expect to see the velocity collapse to the similarity solution found above. Figure 5.7(b) shows

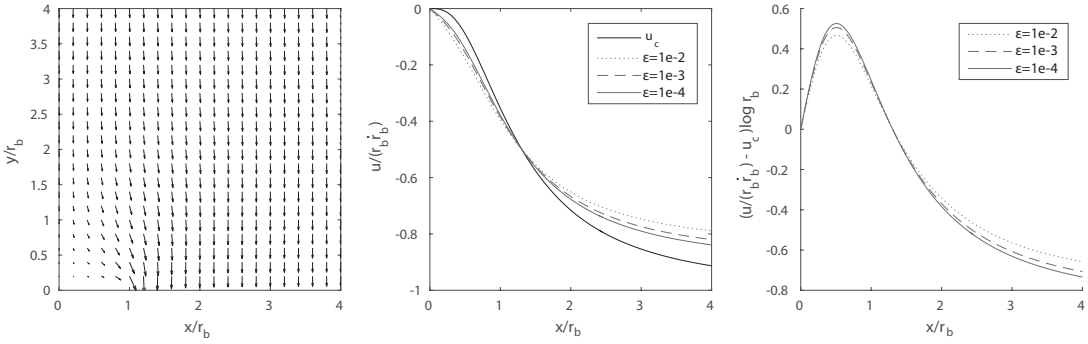

Fig. 5.7 (*a*) Hopper and Richardson's solution when $\epsilon = 10^{-3}$ on the fluid-bridge scale, with the Stokeslets subtracted. (*b*) The velocity u_x along the y-axis for $\epsilon = 10^{-2}$, 10^{-3} and 10^{-4} (dashed lines), rescaled by $r_b\dot{r}_b$ and compared with $\boldsymbol{u}_c$ calculated above (solid line). (*c*) The difference between the rescaled exact solution and u_c at each value of ϵ, multiplied by $\log r_b$ to collapse the next correction.

the numerically-calculated values of the velocity for $\epsilon = 10^{-2}$, 10^{-3} and 10^{-4}. There is some collapse, but the next correction term decays slowly with ϵ.

As a check of the size of the next term, we can subtract the similarity solution from the numerically-calculated solution, and we multiply the remainder by $\log r_b$. The plot in figure 5.7(*c*) shows that the next correction does indeed collapse with such a rescaling. This justifies our claim above that the next correction is smaller by a factor of $\log r_b$. The corresponding asymptotic solution for the velocity is found in appendix A.

We can also compare our final result for r_b with the exact solution. To do this, we must approximate the integral (5.46) for small t. This gives the early-time relationship between t and n. Then using $r_b = w(1)$, we can recover the asymptotic expression for r_b;

$$r_b \sim \frac{\gamma t}{\pi\mu} \log \frac{8\pi a\mu}{\gamma t}, \tag{5.59}$$

in agreement with the similarity solution above.

5.8 Discussion

We have found an asymptotic solution for the coalescence of inertialess drops in two dimensions. This solution involves multiple lengthscales, and is only valid for early times. We find that during the initial stage, the fluid bridge joining the drops grows as

$$r_b \sim \frac{\gamma t}{\pi\mu} \log\left(\frac{8\pi a\mu}{\gamma t}\right). \tag{5.60}$$

Inspired by retracting wedges, we assumed that during the initial stage, $\dot{r_b} \gg \gamma/\mu$. The solution for r_b justifies this approximation. As a result, the neglected surface stresses on the fluid-bridge scale are asymptotically small.

The solution neglects inertia. For a general fluid with inertia and viscosity, Eggers *et al.* argue that, since the fluid bridge is initially small, the viscous stress dominates on the fluid-bridge scale, and the inertialess solution will apply. We will show in chapter 6 that, while the viscous stresses dominate on the fluid-bridge scale, there is a larger scale on which inertia matters.

This asymptotic solution for inertialess drop coalescence in two dimensions holds while $r_b \ll a$. This is true while $t \ll a\mu/\gamma$. For these times, we have seen that the asymptotic solution is a good approximation to the exact solution found by Hopper and Richardson.

5.9 Three-dimensional asymptotic solution

We will now adapt the solution to the coalescence of three-dimensional drops. The structure is similar to the two-dimensional case; we will find a similarity solution on the fluid-bridge scale, and match this to Hopper's parabola solution on the radius-of-curvature scale at the edge of the fluid bridge.

The problem will be axisymmetric, and we will work with cylindrical co-ordinates (r, θ, z) so that z is along the line joining the drop centres, and r is the radial distance from that line. The co-ordinates are shown in figure 5.8.

5.9.1 Ring of Stokeslets

The edge of the fluid bridge is tightly curved in the (r, z) plane. In addition, the surface is curved azimuthally around the circle $r = r_b$ on $z = 0$. Since the curvature in the (r, z) plane is much larger than the azimuthal curvature (since $1/r_c \gg 1/r_b$), we can neglect the contribution to the surface stress from the azimuthal curvature.

We must solve for a flow driven by the force from surface tension at the edge of the fluid bridge, with no stress on the free surface, and no normal velocity or tangential stress on the fluid bridge. In two dimensions, we showed that the appropriate leading-order solution was a pair of outward-pointing Stokeslets. Here, we will show that the axisymmetric version is a ring of outward-pointing Stokeslets around the circle $r = r_b$ on $z = 0$.

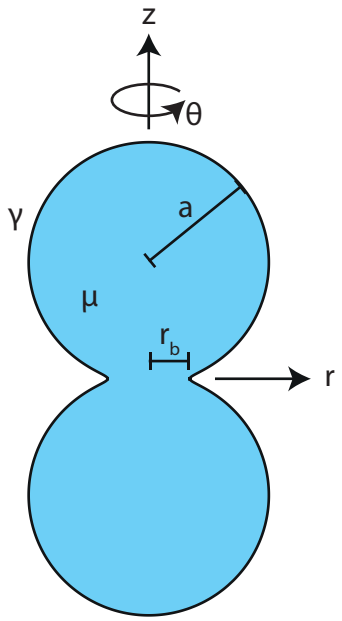

Fig. 5.8 Co-ordinates for the axisymmetric coalescence of three-dimensional drops. The z-axis is the line joining the drop centres, and r is the radial distance from that line.

In three dimensions, the Stokeslet flow due to a point force $\mathbf{F}$ at the origin has stress

$$\boldsymbol{\sigma} = -\frac{3}{4\pi}\frac{\mathbf{F}\cdot\mathbf{xxx}}{r^5}. \tag{5.61}$$

On any plane through the origin, we have $\mathbf{x}\cdot\mathbf{n} = 0$, and so $\boldsymbol{\sigma}\cdot\mathbf{n} = \mathbf{0}$. A three-dimensional Stokeslet therefore has no stress on any plane through its point of application.

On the fluid-bridge scale, the free surface lies near the plane $z = 0$, and we can linearise the stress-free boundary conditions to the plane. Then a ring of Stokeslets at $r = r_b$ on $z = 0$ will satisfy the linearised stress-free boundary conditions to leading order, since each part of the ring of Stokeslets has no stress on the plane $z = 0$. In addition, the ring of Stokeslets satisfies the stress condition on the fluid bridge.

Now we consider the velocity. Since the Stokeslet velocity for a point force F at the origin is

$$\mathbf{u} = \frac{\mathbf{F}}{8\pi\mu}\cdot\left(\frac{\mathbf{I}}{r} + \frac{\mathbf{xx}}{r^3}\right), \tag{5.62}$$

we note that if $\mathbf{F}\cdot\mathbf{n} = 0$ and $\mathbf{x}\cdot\mathbf{n} = 0$ then $\mathbf{u}\cdot\mathbf{n} = 0$. So our ring of radially-pointing Stokeslets has no normal velocity on the plane $z = 0$, including the fluid bridge $r < r_b$.

This Stokeslet ring is therefore the leading-order solution for the flow due to surface tension on the fluid-bridge scale, by essentially the same reasoning as above for a pair of Stokeslets in two dimensions.

Near the edge, we will need an expression for the velocity of the ring of Stokeslets. This requires integration to find the effect of the Stokeslet distribution. We expect to recover the two-dimensional Stokeslet, up to some solid-body motion, near the edge of the fluid bridge.

On the plane $z = 0$, we will find the radial component of the velocity on $\theta = 0$ without loss of generality. The ring of Stokeslets around $r = r_b$ has

$$u_r = \frac{1}{8\pi\mu}\int_0^{2\pi} 2\gamma \begin{pmatrix}\cos\theta\\ \sin\theta\end{pmatrix} \cdot \left\{ \frac{\mathbf{e}_r}{R(\theta)} + \begin{pmatrix} r - r_b\cos\theta \\ -r_b\sin\theta\end{pmatrix} \frac{(r - r_b\cos\theta)}{R(\theta)^3}\right\} r_b\,\mathrm{d}\theta, \tag{5.63}$$

where $R(\theta) = ((r - r_b\cos\theta)^2 + (r_b\sin\theta)^2)^{1/2}$. This can be integrated exactly for

$$u_r = \frac{\gamma}{2\pi\mu r(r - r_b)}\left((r^2 + r_b^2)K\left(\frac{-4rr_b}{(r - r_b)^2}\right) - (r - r_b)^2 E\left(\frac{-4rr_b}{(r - r_b)^2}\right)\right), \tag{5.64}$$

where K and E are the complete elliptic integrals of the first and second kind. Taking the limit near the edge, we have

$$u_r \sim \frac{\gamma}{2\pi\mu}\left(-\log\left(\frac{r - r_b}{r_b}\right) + 3\log 2 - 2\right) \quad \text{for } 0 < r - r_b \ll r_b,\ z = 0. \tag{5.65}$$

We have therefore recovered the velocity for a two-dimensional Stokeslet, together with a solid-body motion. This will be useful when we match the velocity to the radius-of-curvature scale.

5.9.2 Similarity solution on the fluid-bridge scale

Our leading-order solution on the fluid-bridge scale is a ring of Stokeslets. But this has no normal velocity on the free surface. As with two-dimensional coalescence, we must solve for the next-order velocity proportional to $r_b\dot{r}_b/a$, in order to find the motion of the surface from its far-field shape $h \sim r^2/2a$ down to $h = 0$ at $r = r_b$.

We must solve the Stokes equations

$$-\boldsymbol{\nabla} p + \mu\nabla^2\mathbf{u} = \mathbf{0}, \quad \boldsymbol{\nabla}\cdot\mathbf{u} = 0, \tag{5.66}$$

with stress-free boundary conditions on the free surface, and symmetry conditions on the fluid bridge. These are

$$-p + 2\mu\frac{\partial u_z}{\partial z} = 0 \quad \text{on } z = 0,\ r > r_b, \tag{5.67}$$

$$\mu\left(\frac{\partial u_r}{\partial z} + \frac{\partial u_z}{\partial r}\right) = 0 \quad \text{on } z = 0,\ r > r_b, \tag{5.68}$$

and

$$u_z = 0 \quad \text{on } z = 0,\ r < r_b, \tag{5.69}$$

$$\frac{\partial u_r}{\partial z} = 0 \quad \text{on } z = 0,\ r < r_b. \tag{5.70}$$

The kinematic boundary condition in cylindrical co-ordinates is

$$\frac{\partial h}{\partial t} - u_r\frac{\partial h}{\partial r} = u_z. \tag{5.71}$$

and the far-field displacement is

$$h \sim \frac{r^2}{2a} \quad \text{as } r \to \infty, \tag{5.72}$$

with $h(r_b) = 0$.

Now we scale the velocity, the pressure and the displacement according to scales based on the far-field shape, the kinematic boundary condition and the Stokes equations:

$$\mathbf{x} = r_b\bar{\mathbf{x}}, \quad h = \frac{r_b^2}{2a}\bar{h}(\bar{r}), \quad \mathbf{u} = \frac{r_b\dot{r}_b}{a}\bar{\mathbf{u}}, \quad p = \frac{\mu\dot{r}_b}{a}\bar{p}, \tag{5.73}$$

The Stokes equations become

$$-\bar{\boldsymbol{\nabla}}\bar{p} + \bar{\nabla}^2\bar{\mathbf{u}} = \mathbf{0}, \quad \bar{\boldsymbol{\nabla}}\cdot\bar{\mathbf{u}} = 0. \tag{5.74}$$

and we neglect the non-linear term in the kinematic boundary condition, leaving

$$\bar{h} - \frac{\bar{r}}{2}\frac{\partial\bar{h}}{\partial\bar{r}} = \bar{u}_y \quad \text{on } \bar{z} = 0,\ \bar{r} > 1. \tag{5.75}$$

We will use the streamfunction ψ such that

$$u_r = \frac{1}{r}\frac{\partial\psi}{\partial z}, \quad u_z = -\frac{1}{r}\frac{\partial\psi}{\partial r}. \tag{5.76}$$

We work with oblate spheroidal co-ordinates $\bar{z} + i\bar{r} = \sinh(\xi + i\eta)$. This is the axisymmetric analogue to the co-ordinates used above for the two-dimensional problem. The contours of ξ are confocal oblate ellipsoids, and the contours of η are the orthogonal hyperboloids of one sheet. In these co-ordinates, the streamfunction must satisfy $E^4\psi = 0$, where

$$E^2 = \frac{\lambda^2+1}{\lambda^2+\zeta^2}\frac{\partial^2}{\partial\lambda^2} + \frac{1-\zeta^2}{\lambda^2+\zeta^2}\frac{\partial^2}{\partial\zeta^2} \quad \text{with} \quad \lambda = \sinh\xi, \quad \zeta = \cos\eta. \tag{5.77}$$

We look for analogue solutions to ψ_1 and ψ_2 found above (5.28). After some trial and error, we can find two solutions which satisfy the Stokes equations and all the boundary and symmetry conditions. They are

$$\psi_3 = \frac{\lambda^3(1-\zeta^2)}{\lambda^2+\zeta^2} \quad \text{and} \quad \psi_4 = (1-\zeta^2)(\lambda - (1+\lambda^2)\arctan\lambda), \tag{5.78}$$

and the corresponding velocity fields are shown in figure (5.9).

In the far-field,

$$\psi_3 \sim \lambda(1-\zeta^2) \quad \text{as } \xi \to \infty, \tag{5.79}$$

$$\sim \frac{r^2}{(r^2+z^2)^{1/2}} \quad \text{as } r^2+z^2 \to \infty. \tag{5.80}$$

which gives

$$u_r \sim -\frac{rz}{(r^2+z^2)^{3/2}}, \quad u_z \sim -\frac{r^2+2z^2}{(r^2+z^2)^{3/2}}. \tag{5.81}$$

This is a three-dimensional Stokeslet flow.

The second streamfunction has the far-field behaviour

$$\psi_4 \sim (1-\zeta^2)\left(-\lambda^2\frac{\pi}{2} + 2\lambda\right) \quad \text{as } \xi \to \infty, \tag{5.82}$$

$$\sim -\frac{\pi}{2}r^2 + 2\frac{r^2}{(r^2+z^2)^{1/2}} \quad \text{as } r^2+z^2 \to \infty. \tag{5.83}$$

which gives a solid-body motion in addition to some Stokeslet:

$$u_r \sim 2\frac{rz}{(r^2+z^2)^{3/2}}, \quad u_z \sim \pi + 2\frac{r^2+2z^2}{(r^2+z^2)^{3/2}}. \tag{5.84}$$

We take a linear combination of the streamfunctions with $\psi = A\psi_3 + B\psi_4$. As above in two dimensions, we must have no net Stokeslet in the far-field, as the flow

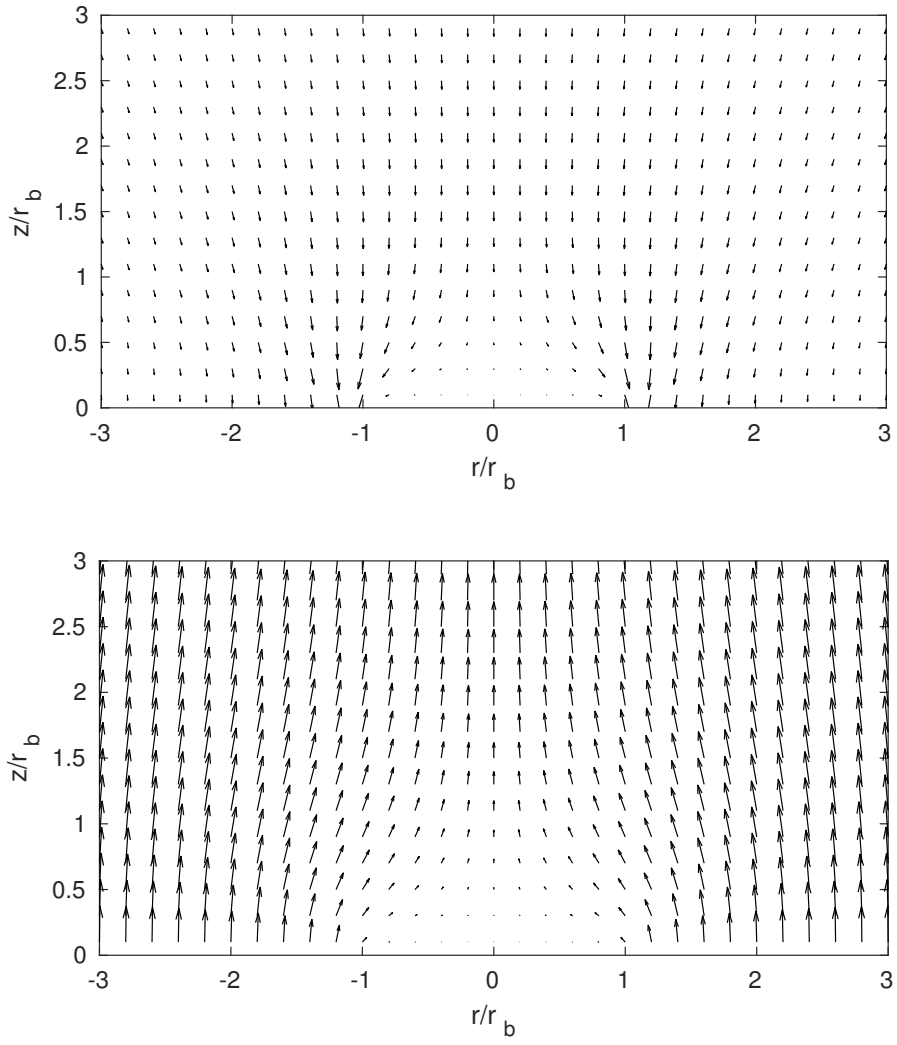

Fig. 5.9 The Stokes flows given by streamfunctions ψ_3 and ψ_4 (5.78).

on larger scales is a Stokes flow for which the forces must balance. In order for the net force in the far-field to vanish, we must have $A - 2B = 0$. With this condition, we can integrate the kinematic boundary condition (5.75) and apply the far-field shape to solve for A. The resulting shape is

$$h(r) = \frac{4}{3\pi a}\left(\arctan\left(\sqrt{\frac{r^2}{r_b^2}-1}\right)\left(\frac{3}{4}r^2 - \frac{r_b^2}{2}\right) + \frac{3r_b}{4}\sqrt{r^2 - r_b^2}\right). \tag{5.85}$$

This is the similarity solution for the shape of the surface on the fluid-bridge scale. Near the edge of the fluid bridge, the surface is curved as $h^2 = r_c(r - r_b)$, with $r_c = 32r_b^3/9\pi^2a^2$. This sets the radius of curvature of the surface.

5.9.3 Inner-inner scale

On the radius-of-curvature scale near the edge, we can neglect the azimuthal curvature since it is much smaller than the curvature of the surface in the (r, z)-plane, because $1/r_b \ll 1/r_c$. If we neglect the curvature of the fluid bridge, then we have a parabolically curved surface with no variation along the edge of the fluid bridge. The problem is therefore two-dimensional under these approximations.

The solution is therefore Hopper's parabola solution [31] again, suitably rescaled to agree with the parabolic shape set by the flow on the fluid-bridge scale.

Finally, we can match between the fluid-bridge scale and the radius-of-curvature scale to find $r_b(t)$.

5.9.4 Matching

The matching follows the same logic as above in the two-dimensional case. We know that the velocity on the fluid bridge scale is a ring of Stokeslets to leading order, and this gives one expression for the velocity on intermediate scales (5.65). We also know that the solution on the inner-inner scale is the parabola solution above, and the far-field of that flow gives another expression for the velocity on intermediate scales.

The radial velocity on $z = 0$ must agree, and this gives

$$\dot{r_b} - \frac{\gamma}{2\pi\mu}\log\frac{x - r_b}{r_c} - \frac{\gamma\log 4}{\pi\mu} = -\frac{\gamma}{2\pi\mu}\log\frac{x - r_b}{r_b} + \frac{\gamma}{2\pi\mu}\left(3\log 2 - 2\right), \tag{5.86}$$

where the expression on the left-hand side is the velocity from the rescaled parabola solution, and the expression on the right-hand side is from the Stokeslet ring. We can

solve this for $\dot{r}_b$ as

$$\dot{r}_b \sim \frac{\gamma}{\pi\mu} \log \frac{6\pi a}{e r_b}. \tag{5.87}$$

We integrate this at leading order for

$$r_b \sim \frac{\gamma t}{\pi\mu} \log \frac{6\pi^2 a\mu}{e\gamma t}. \tag{5.88}$$

This expression for r_b closes the problem, giving the rate of coalescence and the size of each scale.

5.9.5 Discussion

We have adapted our similarity solution for the initial stage of drop coalescence from two dimensions to three dimensions. This required new solutions of the Stokes equations in a particular cut geometry in three dimensions. On the radius-of-curvature scale near the edge of the fluid bridge, we used Hopper's solution for the retraction of a parabola [31].

Matching the flows together gave $r_b \propto (\gamma t/\mu)\log(1/t)$, as for two-dimensional coalescence without inertia. The velocity in the bulk of each drop is

$$\frac{2\gamma^2 t \log^2 t}{3\pi^2\mu^2} \tag{5.89}$$

for three-dimensional coalescence. This is comparable with the velocity above for two-dimensional coalescence, with a different numerical prefactor.

This solution neglected inertia. We will now adapt the asymptotic structure of the solution to include the effect of inertia.

Chapter 6

Drop coalescence with inertia

6.1 Introduction

6.1.1 Motivation

At the end of the previous chapter, we saw that the solution for inertialess drop coalescence involves some solid-body motion in the bulk of each drop given by (5.89). The velocity in the bulk of each drop is proportional to $t \log^2 t$, and we recall that the solution was asymptotically consistent for sufficiently early times.

Paulsen *et al.* [49] report experiments with pendant drops of radius roughly 1mm. By slowly bringing the drops together, Paulsen *et al.* initiate coalescence without much initial motion. Images taken from the side show the subsequent motion of the drops in the drops as they coalesce. For the experiments with a very viscous fluid, the photographs show that just after coalescence there is indeed some solid-body motion in the bulk of each drop. This is in agreement with the initial stage of the exact solution [28, 56]. However, for fluids with a more moderate viscosity, the experiments show that the bulk of each drop is stationary while the fluid bridge grows. Paulsen *et al.* attribute this to the inertia of the fluid, which acts to hold the drop stationary.

Paulsen *et al.* sketch an argument for how inertia should affect coalescence. By their reasoning, the vertical force from surface tension on each drop is $-2\pi\gamma r_b$, multiplying the force per unit length $-\gamma$ by the circumference of the fluid bridge $2\pi r_b$. But this neglects the effect of the viscous stress on the fluid bridge. Consider Hopper's solution for the retraction of a parabola, reviewed above in §4.8. Following the reasoning of Paulsen *et al.*, the vertical force on the upper half of the fluid $y > 0$ would be $-\gamma$ from surface tension. But this neglects the viscous stress along the boundary $\{y = 0, x < 0\}$ which exactly balances the force from surface tension; there is in fact no net vertical

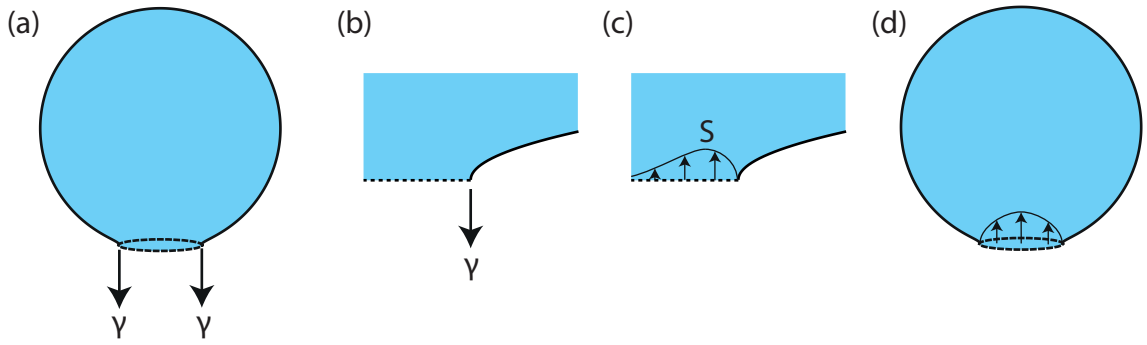

Fig. 6.1 The force argument due to Paulsen *et al.* [49], and a counterexample. (*a*) Paulsen *et al.* claim that the force on the upper drop is given by surface tension alone. (*b*) If this were true, the parabola solution of §4.8 would have a force $-\gamma$ on the upper-half-space. (*c*) In fact, the parabola solution has some viscous stress distribution S on the boundary $\{y = 0, x < 0\}$. (*d*) Analogously, there could be some viscous stress over the fluid bridge during coalescence.

force on the fluid in $y > 0$. For drop coalescence, there could be any amount of viscous stress over the fluid bridge, giving any force on the drop. This argument and counterexample are sketched in figure 6.1.

We will therefore seek a new theoretical description of drop coalescence that explains the roles of viscosity and inertia. We will use ideas from the previous chapters on wedge retraction and the coalescence of inertialess drops.

We saw in chapter 5 that the initial stage of inertialess drop coalescence can be explained with a similarity solution on the fluid-bridge scale, matching to an exact Stokes flow for the surface-tension–driven flow around the tightly-curved surface. The far-field condition on the fluid-bridge scale was given by the fact that the flow in the bulk of each drop was a Stokes flow, and so there could be no net force on each drop.

In chapter 4, we reviewed Billingham's asymptotic solution for the retraction of a fluid wedge with inertia and viscosity. That solution had two separate lengthscales; an inner lengthscale on which the Stokes equations described the flow, and an outer diffusive lengthscale $(\nu t)^{1/2}$ on which inertia balanced viscosity and the unsteady Stokes equations governed the flow. The unsteady Stokes flow on this diffusive outer scale provided a far-field condition for the inner Stokes flow through a solid-body motion Kb_∞.

We will now adapt these ideas to the problem of drop coalescence with inertia.

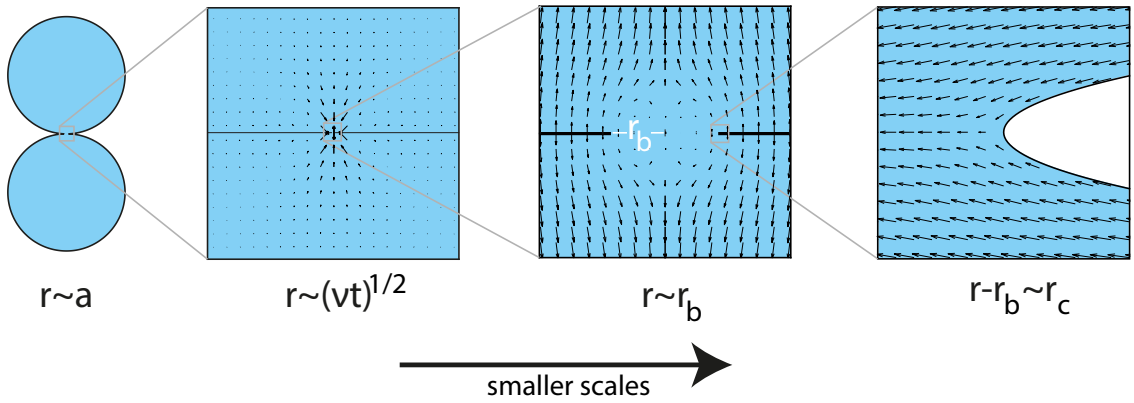

Fig. 6.2 Spatial scales for the initial stage of drop coalescence with inertia and viscosity. On the scale of the drops $r \sim a$, there is some irrotational flow, as vorticity has only diffused out from the point of contact by a distance proportional to $(\nu t)^{1/2}$. There is an unsteady Stokes flow on the $(\nu t)^{1/2}$ scale describing the diffusion of vorticity, and this flow sets the far-field condition for the flow on smaller scales. On the fluid-bridge scale, $r \sim r_b$, there is a Stokes flow that matches to the imposed far-field velocity from the outer diffusive scale. This matches to a particular surface-tension–driven flow around the tightly-curved edge of the fluid bridge, which has radius of curvature proportional to r_c.

6.1.2 Structure of the solution

We will consider an asymptotic solution with a variety of lengthscales which are asymptotically separated at early times. The scales are shown in figure 6.2. In general, the flow on smaller scales drives the motion on larger scales, while the resulting flow on larger scales sets boundary conditions on the solution on smaller scales.

As in the moving-plate problem in §1.5, and as in Billingham's solution for wedges, we will include a $(\nu t)^{1/2}$ lengthscale where inertia balances viscosity. On this diffusive outer scale, we will solve the unsteady Stokes equations, as Billingham does for wedge retraction. This will give the manner in which the velocity decays to zero, and explain how the bulk of each drop is essentially stationary during the initial stage of coalescence.

Then we will consider the flow on the fluid-bridge scale, as we did for inertialess coalescence in chapter 5. On this scale, the viscous stresses will dominate and the Stokes equations will describe the flow. There is a parallel between the fluid-bridge scale and Billingham's O(t) scale.

For inertialess coalescence, we used the fact that the far-field had no net force. Here, we will need to solve for the unsteady flow on the outer scale, and then use this as a matching condition for the fluid flow on the fluid-bridge scale. This is analogous to the way Billingham's solid-body motion Kb_∞ from the outer diffusive scale affects the

motion on the inner scale. However, where Billingham could simply add a corresponding solid-body motion to the solution on the inner scale, here we must satisfy symmetry conditions on the fluid bridge, and so the solution is more involved.

The flow on the fluid-bridge scale will give the similarity solution for the shape of the surface, and in particular the radius of curvature r_c of the edge. Surface tension acting on this tightly-curved surface drives the flow. As above with wide wedges and inertialess drop coalescence, we will apply Hopper's exact solution for the retraction of a parabola to the problem on the smallest 'inner-inner' scale.

The solution is asymptotic at early times, while $a \gg (\nu t)^{1/2} \gg r_b \gg r_c$. We will use asymptotic matching to match the flows together, and we will determine the growth of the fluid bridge, $r_b(t)$.

6.1.3 Context

We will show that the outer flow on the diffusive lengthscale $(\nu t)^{1/2}$ satisfies the unsteady Stokes equations above a free surface. We will consider the flows that are driven by a normal point force or a dipole at the origin, and show how these are relevant to the drop coalescence problem. Previous work has identified various fundamental solutions to the unsteady Stokes equations [13, 37, 38, 58, 61]. In particular, Chan and Chwang give an expression for the unsteady Stokes flow due to a point force in three dimensions [13]. However, their solution does not satisfy stress-free boundary conditions on our free surface. Work by Lu and Chwang gives the unsteady Stokes flow due to a point force near a free surface. However, this does not include the case of a normal force acting on the surface [37, 38].

Billingham's work on the unsteady Stokes flow in a cone with half-angle close to $\pi/2$ is closely related to the drop coalescence problem [5]. In that paper, Billingham considers the effect of a particular normal force distribution on a free surface. For drop coalescence, we will require the solution for a point dipole localised at the origin with some time-dependence, and this is not included in Billingham's work [5].

The Stokes solution on the inner scale is related to work by Eggers *et al.* [23]. The numerical solution in that paper on the fluid-bridge scale revealed the rate of coalescence for inertialess drops surrounded by another fluid. Our solution will neglect any effect of the outer fluid, but will include the effect of inertia through the inclusion of the outer diffusive scale. Our method is also different; whereas Eggers *et al.* solve for the motion numerically with the Stokes boundary integral, we will linearise the surface and find an analytical similarity solution to the Stokes equations in this simplified geometry.

6.2 Diffusive lengthscale

First, we must solve for the flow on the diffusive lengthscale, where inertia balances viscosity. This will give the way that the flow driven by surface tension decays on larger scales, as inertia holds the bulk of each drop stationary.

6.2.1 Problem set-up

The problem is axisymmetric, so we use cylindrical co-ordinates (r, θ, z) defined (as above) with the z-axis along the line joining the drop centres, and r the radial distance from that line. The velocity components are $(u_r, 0, u_z)$ where u_r and u_z are each independent of θ. We write the velocity in terms of the potential ϕ such that

$$u_r = \frac{\partial \phi}{\partial z} \quad \text{and} \quad u_z = -\frac{1}{r}\frac{\partial (r\phi)}{\partial r}, \tag{6.1}$$

so that $\psi = r\phi$ is the streamfunction.

The Navier–Stokes equations are

$$\rho\left(\frac{\partial \mathbf{u}}{\partial t} + \mathbf{u}\cdot\nabla\mathbf{u}\right) = -\boldsymbol{\nabla} p + \mu\nabla^2\mathbf{u}, \quad \text{and} \quad \boldsymbol{\nabla}\cdot\mathbf{u} = 0. \tag{6.2}$$

If we scale distances with some lengthscale L and times with the elapsed time t, then the inertial term of the Navier–Stokes equations balances the viscous term when

$$\frac{\rho}{t} \sim \frac{\mu}{L^2}, \tag{6.3}$$

which happens on the lengthscale $L \sim (\nu t)^{1/2}$. We will call this the 'diffusive lengthscale', and write r_ν for the length $(\nu t)^{1/2}$. On this scale, viscosity and inertia are in balance. If the velocity is sufficiently small, then we can neglect the non-linear term of the Navier–Stokes equations, and this gives the unsteady Stokes equations

$$\rho\frac{\partial \mathbf{u}}{\partial t} = -\boldsymbol{\nabla} p + \mu\nabla^2\mathbf{u}, \quad \boldsymbol{\nabla}\cdot\mathbf{u} = 0. \tag{6.4}$$

Now we consider the free-surface boundary conditions. These apply on the surfaces of the drops, but since $r_\nu \ll a$ during the initial stage, the drop surfaces are near to the plane $z = 0$. We will therefore linearise the boundary conditions to the plane $z = 0$. The forcing from smaller scales appears at the origin on this scale. As we argued above that we do not initially know the force distribution over the fluid bridge, we

will model the effect on the diffusive scale with a general time-dependent normal point force at the origin. As part of our solution, we will solve for the stress distribution on the fluid bridge and the time-dependent net force. We will model the leading-order effect of surface tension acting on the tightly-curved edge of the fluid bridge with an infinitesimally small ring of tangential stress at the origin. Since the unsteady Stokes equations are linear, we can consider the dipole and point force separately.

In this section, we will consider the effect of a point force or a point dipole acting on a fluid half-space, above an otherwise free surface, with the fluid initially at rest. For the point force, we will have no tangential stress on the free surface, and normal stress localised at the origin with Dirac's delta function. For the dipole, we will have no normal stress on the free surface, and we take the limit of a small ring of tangential stress.

6.2.2 Unsteady Stokeslet in three dimensions

We will solve the axisymmetric unsteady Stokes equations with a Hankel–Laplace transform. The boundary conditions on $z = 0$ for a point force at the origin are

$$-p + 2\mu\frac{\partial u_z}{\partial z} = -F(t)\frac{\delta(r)}{r} \quad \text{and} \quad \mu\left(\frac{\partial u_r}{\partial z} + \frac{\partial u_z}{\partial r}\right) = 0, \tag{6.5}$$

where the functional $\delta(r)/r$ is defined by $\int_0^\epsilon R(r)\,(\delta(r)/r)\;r\mathrm{d}r\mathrm{d}\theta = 2\pi R(0)$ for any function $R(r)$ and any $\epsilon > 0$. The upward force on the fluid is therefore $2\pi F(t)$. We take a Hankel–Laplace transform, and the inverse transform gives

$$p(t,r,z) = \frac{1}{2\pi i}\int_{c-i\infty}^{c+i\infty} \mathrm{e}^{st}\int_0^\infty \tilde{p}(s,k,z)J_0(kr)k\,\mathrm{d}k\,\mathrm{d}s, \tag{6.6}$$

$$\phi(t,r,z) = \frac{1}{2\pi i}\int_{c-i\infty}^{c+i\infty} \mathrm{e}^{st}\int_0^\infty \tilde{\phi}(s,k,z)J_1(kr)k\,\mathrm{d}k\,\mathrm{d}s, \tag{6.7}$$

$$h(t,r) = \frac{1}{2\pi i}\int_{c-i\infty}^{c+i\infty} e^{st}\int_0^\infty \tilde{h}(s,k)J_0(kr)k\,\mathrm{d}k\,\mathrm{d}s, \tag{6.8}$$

where c is a constant chosen so that the poles of $\tilde{p}$ and $\tilde{\phi}$ lie to the left of the integration contour. We note that the Hankel transforms for p and ϕ are of different orders. Now Laplace's equation for the pressure and the r-component of the momentum equation become

$$\rho s\tilde{\phi}_z = k\tilde{p} + \mu\left(\tilde{\phi}_{zzz} - k^2\tilde{\phi}_z\right) \quad \text{and} \quad -k^2\tilde{p} + \tilde{p}_{zz} = 0, \tag{6.9}$$

using subscripts for derivatives. The solution which decays in the far-field is

$$\tilde{p} = \rho s A(s,k) e^{-kz}, \quad \tilde{\phi} = -A(s,k)e^{-kz} + B(s,k)e^{-mz}, \tag{6.10}$$

for some functions $A(s,k)$ and $B(s,k)$ to be determined by the boundary conditions (6.5). Transforming each boundary condition gives

$$-\tilde{p} - 2\mu k \tilde{\phi}_z = -\hat{f}(s) \quad \text{and} \quad \tilde{\phi}_{zz} + k^2 \tilde{\phi} = 0, \tag{6.11}$$

where $\hat{f}(s) = \int_0^\infty \mathrm{e}^{-st} F(t)\,\mathrm{d}t$ is the Laplace transform of the forcing. We substitute the general solution into the boundary conditions and solve for the coefficients A and B:

$$\begin{pmatrix} A \\ B \end{pmatrix} = \frac{-\hat{f}(s)}{\mu(4k^3 m - (k^2+m^2)^2)} \begin{pmatrix} k^2+m^2 \\ 2k^2 \end{pmatrix}, \tag{6.12}$$

where $m = (k^2 + s/\nu)^{1/2}$. Meanwhile, the kinematic boundary condition becomes $s\tilde{h}(s,k) = -k\tilde{\phi}(s,k,0)$. Transforming back gives

$$p(t,r,z) = -\frac{1}{2\pi i \nu} \int_{c-i\infty}^{c+i\infty} e^{st} s\hat{f}(s) \int_0^\infty \frac{(k^2+m^2)e^{-kz}}{4k^3 m - (k^2+m^2)^2} J_0(kr) k\,\mathrm{d}k\,\mathrm{d}s \tag{6.13}$$

$$\phi(t,r,z) = \frac{1}{2\pi i \mu} \int_{c-i\infty}^{c+i\infty} e^{st} \hat{f}(s) \int_0^\infty \frac{(k^2+m^2)e^{-kz} - 2k^2 e^{-mz}}{4k^3 m - (k^2+m^2)^2} J_1(kr) k\,\mathrm{d}k\,\mathrm{d}s \tag{6.14}$$

$$h(t,r) = -\frac{1}{2\pi i \nu} \int_{c-i\infty}^{c+i\infty} e^{st} \hat{f}(s) \int_0^\infty \frac{k}{4k^3 m - (k^2+m^2)^{1/2}} J_0(kr) k\,\mathrm{d}k\,\mathrm{d}s. \tag{6.15}$$

which is a closed-form solution for the pressure, potential and surface displacement.

We can find the asymptotic behaviour for $x, y \ll r_\nu$ with a divide-and-conquer method for the k-integral. There are two contributions to the integral; a large-k contribution representing the local effect, and a small-k term describing the effect of the history of the unsteady flow. More details of the calculation are given in appendix B. We find

$$\phi \sim -\frac{F(t)r}{2\mu\sqrt{r^2+z^2}} + \frac{c_1 r}{2\pi^{1/2}\mu r_\nu} \int_0^t \frac{F'(\tau)}{\sqrt{1-\tau/t}}\,\mathrm{d}\tau, \tag{6.16}$$

where $c_1 \approx 0.6561$ is derived in the appendix. The first term is the potential for the expected Stokeslet at the origin. The other term represents a solid-body motion at the origin, with a magnitude which depends on the history of the forcing. This solid-body motion is present as a result of the far-field condition; in order for the velocity to decay in the far-field, there must be some additional solid-body motion at the origin.

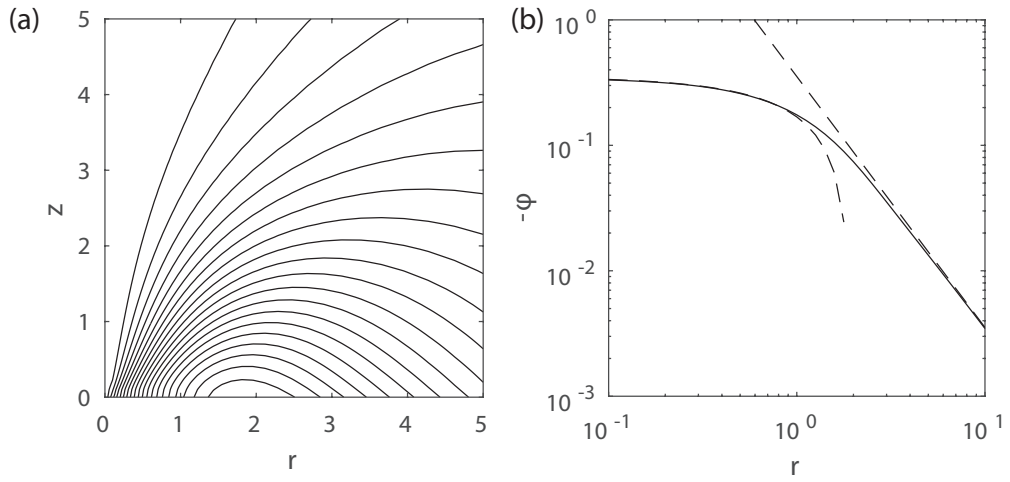

Fig. 6.3 Unsteady Stokeslet for $F(t) = \mathcal{H}(t)$. (a) Contours of $r\phi$. (b) Comparison along the cone $z = r$ of $-\phi$ (solid line) against the asymptotic expressions (dashed lines; (6.18))

In the far-field, a similar divide-and-conquer method for $r, z \gg r_\nu$ gives

$$\phi \sim -\frac{r}{\rho(r^2+z^2)^{3/2}} \int_0^t F(\tau)\,\mathrm{d}\tau. \tag{6.17}$$

The fluid is initially at rest, and vorticity has only diffused outwards by a distance proportional to r_ν, so the far-field is an irrotational flow. The magnitude of this far-field flow depends on the history of the forcing through the integral $\int_0^t F(\tau)\,\mathrm{d}\tau$.

We can calculate the streamfunction numerically for any $F(t)$. As an example, take $\mu = 1$, $\rho = 1$ and $F(t) = \mathcal{H}(t)$, the Heaviside step function. For $t > 0$, the asymptotic expressions (6.16) and (6.17) become

$$\phi \sim -\frac{r}{2\sqrt{r^2+z^2}} + \frac{c_1 r}{2\pi^{1/2} r_\nu} \quad \text{for } r, z \ll r_\nu \text{ and} \quad \phi \sim -\frac{rt}{(r^2+z^2)^{3/2}} \quad \text{for } r, z \gg r_\nu. \tag{6.18}$$

We calculate the inverse Hankel–Laplace transform (6.7) with seven-point Gaussian integration, taking $c = 1$ in the Laplace transform. The streamlines are contours of $r\phi$, and are shown at time $t = 1$ in figure 6.3(a). The numerically-calculated potential compares well with the asymptotic expressions on the cone $z = r$ (figure 6.3(b)).

6.2.3 Unsteady dipole in three dimensions

Now we solve for the flow due to an axisymmetric dipole at the origin. The stress boundary conditions are now

$$-p + 2\mu\frac{\partial u_z}{\partial z} = 0 \quad \text{and} \quad \mu\left(\frac{\partial u_r}{\partial z} + \frac{\partial u_z}{\partial r}\right) = G(t)\frac{\delta'(r)}{r}. \tag{6.19}$$

where the functional $\delta'(r)/r$ is defined by $\int_0^\epsilon R(r)\,(\delta'(r)/r)\;r\mathrm{d}r\mathrm{d}\theta = -2\pi R'(0)$ for any function $R(r)$ and any $\epsilon > 0$. The dipole strength is $G(t)$.

Taking the same Hankel–Laplace transform as above (6.6, 6.7), the boundary conditions (6.19) become

$$-\tilde{p} - 2\mu k\tilde{\phi}_z = 0 \quad \text{and} \quad \mu\left(\tilde{\phi}_{zz} + k^2\tilde{\phi}\right) = -\frac{k}{2}\hat{g}(s), \tag{6.20}$$

where $\hat{g}(s) = \int_0^\infty \mathrm{e}^{-st}G(t)\,\mathrm{d}t$ is the Laplace transform of the dipole strength. The pressure and potential are given by the same general solution to the unsteady Stokes equations above (6.10), and the boundary conditions become new algebraic equations for A and B.

We solve this matrix problem for A, B:

$$\begin{pmatrix} A \\ B \end{pmatrix} = \frac{k\hat{g}(s)}{2\mu\left(4k^3m - (2k^2 + \frac{s}{\nu})^2\right)}\begin{pmatrix} 2km \\ 2k^2 + \frac{s}{\nu} \end{pmatrix}. \tag{6.21}$$

The solution for the transformed pressure and potential is

$$\tilde{p} = s\hat{g}(s)\frac{k^2me^{-kz}}{\nu\left\{4k^3m - (k^2+m^2)^2\right\}}, \quad \text{and} \quad \tilde{\phi} = \hat{g}(s)\frac{k(k^2+m^2)e^{-mz} - 2k^2me^{-kz}}{2\mu\left\{4k^3m - (k^2+m^2)^2\right\}}. \tag{6.22}$$

and so

$$p(t,r,z) = \frac{1}{2\pi i\nu}\int_{c-i\infty}^{c+i\infty} e^{st}s\hat{g}(s)\int_0^\infty \frac{k^2(k^2+\frac{s}{\nu})^{1/2}e^{-kz}}{4k^3m - (2k^2+\frac{s}{\nu})^2}J_0(kr)k\,\mathrm{d}k\,\mathrm{d}s, \tag{6.23}$$

$$\phi(t,r,z) = \frac{1}{2\pi i\mu}\int_{c-i\infty}^{c+i\infty} e^{st}\hat{g}(s)\int_0^\infty \frac{k(k^2+\frac{s}{2\nu})e^{-mz} - k^2me^{-kz}}{4k^3m - (2k^2+\frac{s}{\nu})^2}J_1(kr)k\,\mathrm{d}k\,\mathrm{d}s, \tag{6.24}$$

$$h(t,r) = \frac{1}{2\pi i\mu}\int_{c-i\infty}^{c+i\infty} e^{st}\frac{\hat{g}(s)}{s}\int_0^\infty \frac{k^3m - k^2(k^2+\frac{s}{2\nu})}{4k^3m - (2k^2+\frac{s}{\nu})^2}J_0(kr)k\,\mathrm{d}k\,\mathrm{d}s. \tag{6.25}$$

We can use the same divide-and-conquer method again to find the asymptotic behaviour for $r, z \ll r_\nu$. This is more involved than before, as several terms are the

same order. We find that for $r, z \ll r_\nu$,

$$\phi \sim \frac{G(t)rz}{4\mu(r^2+z^2)^{3/2}} + \frac{G'(t)r}{32\mu\nu}\left\{\log\left(\frac{z+\sqrt{r^2+z^2}}{r_\nu}\right) + \frac{z}{r^2}\left(z - \frac{3r^2+z^2}{\sqrt{r^2+z^2}}\right)\right\} + \frac{r}{32\mu\nu}\left(G'(t)c_2 - \frac{1}{2}\int_0^t \log\left(1-\frac{\tau}{t}\right)G''(\tau)\,\mathrm{d}\tau\right), \tag{6.26}$$

where the constant $c_2 \approx -0.9111$ is derived in appendix B. The first term is the potential for the expected Stokes dipole at the origin. The other terms are the response from the inertia. The terms in braces are the Stokes flow driven by the inertia of the leading dipole. The remaining terms are a solid-body motion set by the history of the forcing. The corresponding surface displacement is

$$h(t,r) \sim -\frac{G(t)}{16\mu\nu}\left(c_2 + \frac{1}{2} + \log\left(\frac{r}{r_\nu}\right)\right) + \frac{\gamma}{32\mu\nu}\int_0^t \log\left(1-\frac{\tau}{t}\right)G'(\tau)\,\mathrm{d}\tau. \tag{6.27}$$

In the far-field, we can use a divide-and-conquer method to find the rate of decay for $r, z \gg r_\nu$. We find

$$\phi \sim \frac{6r_\nu r(4z^2-r^2)}{\pi^{1/2}\rho(r^2+z^2)^{7/2}}\int_0^t G(\tau)\sqrt{1-\frac{\tau}{t}}\,\mathrm{d}\tau. \tag{6.28}$$

We can calculate ϕ numerically for any given dipole strength $G(t)$. As an example, we take $\mu = 1$, $\rho = 1$ and the dipole strength $G(t) = \mathcal{H}(t)$. The contours of the streamfunction $r\phi$ at time $t = 1$ are shown in figure 6.4(a). For $t > 0$, the asymptotic expressions (6.26) and (6.28) become

$$\phi \sim \frac{rz}{4(r^2+z^2)^{3/2}} - \frac{r}{64t} \quad \text{for } r, z \ll r_\nu \text{ and} \quad \phi \sim \frac{4t^{3/2}r(4z^2-r^2)}{\pi^{1/2}(r^2+z^2)^{7/2}} \quad \text{for } r, z \gg r_\nu. \tag{6.29}$$

A comparison on the cone $z = r$ shows good agreement between the numerically-calculated potential and the asymptotic expressions (figure 6.4(b)).

For drop coalescence, the driving dipole is given by a ring of radial Stokeslets around the edge of the fluid bridge. A calculation in appendix C shows that this gives a dipole with strength $G(t) = \gamma r_b^2$.

6.3 Fluid-bridge scale

On the fluid-bridge scale, we have $r_b \ll (\nu t)^{1/2}$ and so viscosity dominates. As above with our fluid-bridge scale solution for inertialess coalescence, there is a leading-order

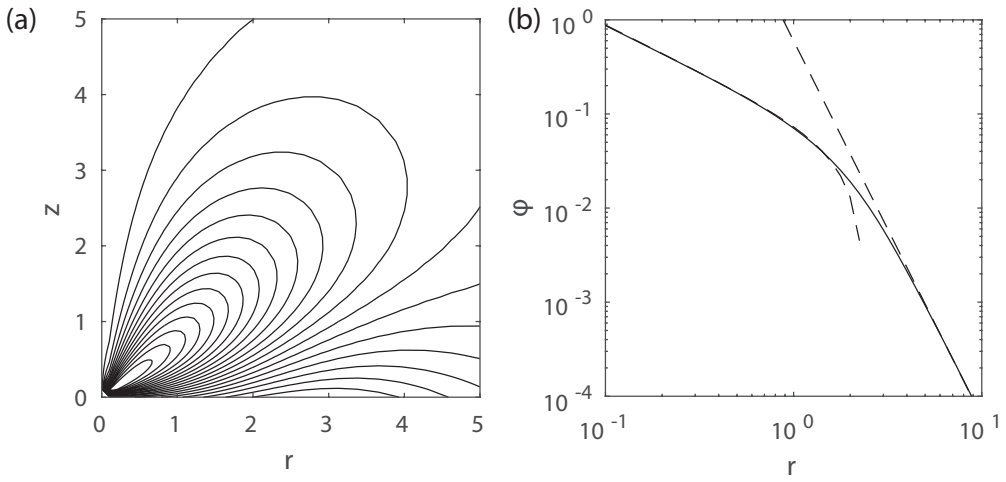

Fig. 6.4 Unsteady dipole for $G(t) = \mathcal{H}(t)$. (a) Contours of $r\phi$. (b) Comparison on the cone $z = r$ of ϕ (solid line) against the asymptotic expressions (dashed lines; (6.29))

Stokeslet flow driven by the ring of tightly-curved surface at the edge of the fluid bridge. We have see in section §5.9.1 that a ring of Stokeslets satisfies stress-free boundary conditions on the plane $z = 0$.

Now we will solve for the similarity solution on the fluid-bridge scale. The outer flow on the diffusive scale has set up a flow at the origin which our inner solution must match. On the fluid-bridge scale, the solution must describe the velocity which matches to the flow in each drop, but also have no normal velocity on the fluid bridge. This flow will give the displacement of the surface, from zero at the edge of the fluid bridge, out to its far-field displacement set up by the outer flow.

The surface stresses drive a further correction flow, as does the inertia of the Stokeslet ring. We will show below in §6.4 that these correction terms are asymptotically smaller than the flow driven by the velocity from the outer scale.

We write

$$u_\infty(t) = -\frac{\gamma r_b \dot{r}_b}{8\mu\nu}\left(\log\frac{r_b}{r_\nu} + c_2 + \frac{1}{2}\right) + \frac{\gamma}{16\mu\nu}\int_0^t \log\left(1 - \frac{\tau}{t}\right)\frac{\mathrm{d}r_b\dot{r}_b}{\mathrm{d}\tau}\,\mathrm{d}\tau \tag{6.30}$$

and

$$h_\infty = \int_0^t u_\infty(t')\,\mathrm{d}t' \sim -\frac{\gamma r_b^2}{16\mu\nu}\log\frac{r_b}{r_\nu} \tag{6.31}$$

for the largest term in the solid-body motion from the outer diffusive scale, and for the corresponding surface displacement.

As above for the coalescence of three-dimensional drops without inertia, we work with oblate spheroidal coordinates, $z + ir = r_b \sinh(\xi + i\eta)$. The two solutions with no stress on the boundaries are

$$\psi_3 = \frac{\lambda^3(1-\zeta^2)}{\lambda^2+\zeta^2} \quad \text{and} \quad \psi_4 = (1-\zeta^2)(\lambda - (1+\lambda^2)\arctan\lambda). \tag{6.32}$$

We use a linear combination of these Stokes solutions, writing $\psi = u_\infty r_b^2(A\psi_3 + B\psi_4)$. The velocity tends to the correct value, u_∞, if we take $B = 1/\pi$. Now we write the leading-order surface position as $h_1 = h_\infty H(\xi)$, and the kinematic boundary condition becomes

$$H - \frac{1}{2}\coth\xi\frac{\partial H}{\partial \xi} = -\frac{1}{\sinh\xi}\frac{\partial \psi}{\partial \xi}. \tag{6.33}$$

We integrate this for

$$H(\xi) = (A-B)\left(\cosh^2\xi \arctan\sinh\xi + \sinh\xi\right) + 2B\arctan\sinh\xi, \tag{6.34}$$

where we have applied $H(0) = 0$. The far-field shape does not grow as r^2 in the far-field at this order, so we take $A = B$ and this closes the problem. We have

$$\psi = \frac{u_\infty r_b^2}{\pi}\left(\psi_3 + \psi_4\right), \tag{6.35}$$

and the surface displacement is

$$h_1 = \frac{2h_\infty}{\pi}\arctan\sqrt{\left(\frac{r}{r_b}\right)^2 - 1}. \tag{6.36}$$

This tends to h_∞ for large r, matching the displacement in the far-field.

We can find the force over the fluid bridge by looking for the far-field Stokeslet present in ψ_3 and ψ_4. For the solution here, the force over the fluid bridge is

$$\boldsymbol{F} = -12\mu r_b u_\infty \boldsymbol{e}_z. \tag{6.37}$$

We note that this does not have magnitude $2\pi\gamma r_b$, as claimed by Paulsen *et al.* [49].

6.4 Corrections due to inertia and surface stresses

In finding this similarity solution, we have neglected the surface stresses from the Stokeslet ring and from surface tension acting on the curved shape (6.36). As before

with inertialess drop coalescence, these stresses appear at the next order and drive a correction flow. In this case, the correction velocity scales as

$$u \sim \frac{\gamma h_\infty}{\mu r_b}. \tag{6.38}$$

There is an additional source of correction terms; the inertia of the leading-order Stokeslet ring drives a flow. Considering the neglected terms of the Navier–Stokes equations, we see that the leading-order Stokeslet ring has

$$\rho \frac{\partial \mathbf{u}}{\partial t} \sim \rho \dot{r}_b \frac{\partial u}{\partial \bar{r}} \sim \frac{\dot{r}_b \rho \gamma}{r_b \mu}. \tag{6.39}$$

At the next order, we have the Stokes equations for the correction velocity driven by the inertia of the Stokeslet ring, which appears in the equations as a body force. The correction velocity is therefore proportional to $\dot{r}_b r_b \rho \gamma / \mu^2$. Once again, this is smaller than u_∞.

We can solve for these corrections due to inertia and surface stresses with Tranter's method. The details of the solution are given in appendix C. The solution driven by the surface stress matches to the single-cut solution found in §4.7 near the edge of the fluid bridge. The solution driven by inertia matches to the remaining far-field terms in (6.26) from the unsteady outer scale.

6.5 Matching

As before with inertialess coalescence, we can neglect the azimuthal curvature on the inner-inner scale, and this gives a local two-dimensional problem for the flow due to surface tension. We define local coordinates (x, y) with the origin on the edge of the fluid bridge, the x-axis in the local radial direction, and the y-axis in the axial direction. We will write (u_x, u_y) for the corresponding velocity components. The surface is at $y = h(x)$. On scales smaller than r_b near the edge of the fluid bridge, the surface is parabolically curved as $h^2 \sim r_c x$, with $r_c = 8h_\infty^2/\pi^2 r_b$. The Stokes flow solution is once again Hopper's exact solution for the retraction of a parabola, which we described above in §4.8.

We will now match the velocity fields between the Stokeslet ring and the rescaled parabola solution. The ring of Stokeslets has radial velocity which is locally

$$u_x \sim \frac{\gamma}{2\pi\mu} \left(-\log \frac{(x^2 + y^2)^{1/2}}{r_b} + 3\log 2 - 2 \right) \tag{6.40}$$

in these coordinates. The rescaled parabola solution has

$$u_x \sim \frac{\gamma}{2\pi\mu}\left(-\log\frac{(x^2+y^2)^{1/2}}{r_c}+\frac{x^2}{x^2+y^2}\right)-\frac{\gamma}{\pi\mu}\left(\log 4+\frac{1}{2}\right)+\dot{r}_b \tag{6.41}$$

in the far-field. These must agree, and setting the two expressions equal and solving for $\dot{r}_b$ gives

$$\dot{r}_b \sim \frac{\gamma}{\pi\mu}\log\frac{4\pi r_b}{eh_\infty}, \tag{6.42}$$

where we recall that

$$h_\infty \sim \frac{\gamma}{32\mu\nu}r_b^2\log\frac{\nu t}{r_b^2}. \tag{6.43}$$

We integrate this differential equation for r_b at leading order for

$$r_b \sim \frac{\gamma t}{\pi\mu}\log\frac{128\pi^2\mu^2\nu}{e\gamma^2 t\log\left(\pi^2\mu^2\nu/\gamma^2 t\right)}. \tag{6.44}$$

This gives the growth of the fluid bridge and the rate of coalescence. Neglecting $\mathrm{O}(t)$ constants, we can write $t=\mu^3\bar{t}/\rho\gamma^2$ for a simpler non-dimensional expression

$$\frac{r_b}{a}\sim\frac{\mathrm{Oh}^2\bar{t}}{\pi}\log\frac{1}{\bar{t}\log 1/\bar{t}}, \tag{6.45}$$

where $\mathrm{Oh}=\mu/\sqrt{\rho a\gamma}$ is the Ohnesorge number.

6.6 Drop scale

We have seen that the velocity decays on the diffusive scale, so the velocity in the bulk of each drop is small. We can now solve for the actual velocity in the drops, driven by the flow on the diffusive scale.

Since $a \gg r_\nu$, the inertial terms of the Navier–Stokes equations dominate on the drop scale, and we must solve for an inviscid flow. If we write $\mathbf{u}=\boldsymbol{\nabla}\Phi$ then the potential Φ must satisfy Laplace's equation $\nabla^2\Phi=0$.

We will use the far-field asymptotic expressions (6.17) and (6.28) to compare the decaying unsteady dipole and Stokeslet in order to find the largest contribution to the flow in the drops. The dipole velocity with $G\propto\gamma r_b^2$ decays proportional to

$$\frac{\gamma r_\nu r_b^2 t}{\rho r^5}, \tag{6.46}$$

while the unsteady Stokeslet velocity, with the $F \propto \mu u_\infty r_b$ by (6.37), decays proportional to

$$\frac{\mu r_b u_\infty t}{\rho r^3}. \tag{6.47}$$

On the drop radius scale, the unsteady Stokeslet therefore dominates as $r_\nu r_b^2 t \ll r_b u_\infty t$.

We must solve $\nabla^2 \Phi = 0$, finding the solution which matches to the far-field velocity of the unsteady Stokeslet, and which has a constant pressure on surface of the sphere, which has radius a. We can solve this analytically; the potential is simply

$$\Phi = -\frac{\int_0^t F(\tau)\,\mathrm{d}\tau}{\rho}\left(\frac{z}{(r^2+z^2)^{3/2}} - \frac{1}{2a(r^2+z^2)^{1/2}}\right). \tag{6.48}$$

This gives the flow in the bulk of the drop during the initial stage of drop coalescence.

6.7 Electrical problem

Recent experiments infer the size of the fluid bridge through measurements of the resistance of the electrical flow through the fluid bridge [12, 49]. If we neglect the curvature of the drops, then the leading-order resistance comes from the electrical flow on the fluid-bridge scale through the region of contact between the drops. Paulsen *et al.* [49] and Case and Nagel [12] try to solve for this electrical flow numerically, but there is a simple analytical solution that we can use, which we will find here.

The electrical potential ϕ satisfies $\nabla^2 \phi = 0$ and tends to $\pm \Delta V/2$ in the bulk of each drop, where ΔV is the potential drop over the coalescing drops. On the surface, we have

$$\frac{\partial \phi}{\partial z} = 0. \tag{6.49}$$

The current density $\mathbf{j}$ satisfies Ohm's law $\mathbf{j} = -\sigma \boldsymbol{\nabla} \phi$.

First, we non-dimensionalise with

$$\mathbf{x} = r_b \bar{\mathbf{x}}, \quad \phi = \Delta V \bar{\phi}, \quad \mathbf{j} = \frac{\sigma V}{r_b}\bar{\mathbf{j}}. \tag{6.50}$$

We will solve Laplace's equation with oblate spheroidal co-ordinates, looking for a potential $\phi(\xi)$, independent of η. Then we have

$$\bar{\nabla}^2 \bar{\phi} = \frac{2\left(\bar{\phi}''(\xi) + \bar{\phi}'(\xi)\tanh\xi\right)}{\cos 2\eta + \cosh 2\xi}, \tag{6.51}$$

and so

$$\bar{\phi}(\xi) = A \arctan\left(\tanh\frac{\xi}{2}\right) + B \tag{6.52}$$

for some constants A and B. As $\xi \to \pm\infty$, we want $\bar{\phi} \to \pm\frac{1}{2}$, so we must have $A = 2/\pi$ and $B = 0$.

The total current through the fluid bridge is

$$\int_{\theta=0}^{2\pi}\int_{r=0}^{1} \frac{\partial\phi}{\partial z}\, r\,\mathrm{d}r\,\mathrm{d}\theta = 2\int_0^1 \frac{r}{\sqrt{1-r^2}}\,\mathrm{d}r = 2. \tag{6.53}$$

In dimensional terms, we have a current $2\Delta V\sigma r_b$ associated with the potential drop ΔV, so the resistance is

$$R = \frac{1}{2\sigma r_b}. \tag{6.54}$$

Case and Nagel [12] solve numerically for the resistance of the fluid bridge, and arrive at the conclusion that the resistance is given by (6.54) exactly (no numerical results are given). That paper attributes this to the resistance of the hemisphere; our solution shows that the resistance arises from the electrical flow through the circle of contact, independent of the outer geometry (which contributes a smaller resistance). This next correction depends on the exact interface shape and the geometry of the drops (e.g. on the curvature and the connection with the electrical circuit).

The numerical pre-factor calculated by Paulsen et al. [48] is 2/3.62, which is wrong by 10%. Errors have probably entered from the use of a particular form for the next-order correction.

6.8 Discussion

This solution is asymptotic, and only valid at early times. To find out when the initial stage gives way to some further dynamics, we can consider the order of the scales. During the initial stage, we have

$$r_b \ll (\nu t)^{1/2} \ll a. \tag{6.55}$$

There are two ways that this asymptotic solution can break down. It may be the case that $r_b \sim (\nu t)^{1/2}$, which occurs when

$$\frac{\gamma t}{\mu} \sim (\nu t)^{1/2} \quad \text{which is when} \quad t \sim \frac{\mu^3}{\rho\gamma^2}. \tag{6.56}$$

The other possibility is that $(\nu t)^{1/2} \sim a$. This occurs at a time when

$$(\nu t)^{1/2} \sim a \quad \text{when} \quad t \sim \frac{a^2\rho}{\mu}. \tag{6.57}$$

We can also say which of these happens first. We note that

$$\frac{\mu^3}{\rho\gamma^2} < \frac{a^2\rho}{\mu} \quad \text{if} \quad \mathrm{Oh} < 1 \tag{6.58}$$

and vice versa, where $\mathrm{Oh} = \mu/(\rho a\gamma)^{1/2}$ is the Ohnesorge number. So for inviscid fluids with $\mathrm{Oh} \ll 1$, we expect the asymptotic solution to break down when the fluid bridge meets the diffusive scale. This happens when $t \sim \mu^3/\rho\gamma^2$ and the fluid bridge is of size $r_b \sim \mathrm{Oh}^2 a$. Since $\mathrm{Oh} \ll 1$, this happens before $r_E \sim a$, so the fluid bridge is still small when the initial stage ends.

For more viscous fluids with $\mathrm{Oh} \gg 1$, we expect the solution to break down when the diffusive scale meets the radius of the fluid bridge. This happens when $t \sim a^2\rho/\mu$, when the fluid bridge is of size $r_b \sim \mathrm{Oh}^{-2} a$. Since $\mathrm{Oh} \gg 1$, this happens before $r_E \sim a$, so once again the fluid bridge is small when the initial stage ends.

It is interesting to consider the motion of the drops after the initial stage. In the viscous case $\mathrm{Oh} \gg 1$, vorticity has now diffused out through the bulk of each drop, and in the subsequent motion, vorticity diffuses through the fluid on a timescale proportional to $a^2\rho/\mu$. In the subsequent motion, we therefore expect the Stokes equations to hold for the flow in the bulk of each drop. We could then use the inertialess solution of chapter 5 to describe the flow, at least while $r_b \ll a$.

For more inviscid fluids with $\mathrm{Oh} \ll 1$, it is less clear what subsequent flow we should expect. At the cross-over time, the fluid bridge is now comparable with the diffusive lengthscale, and so we should consider the possibility that inertia matters on a scale near the edge of the fluid bridge. Balancing the inertial and viscous terms of the Navier–Stokes equations, using the capillary velocity γ/μ, we see that

$$\rho\mathbf{u}\cdot\boldsymbol{\nabla}\mathbf{u} \sim \mu\nabla^2\mathbf{u} \quad \text{on the lengthscale} \quad L \sim \frac{\mu^2}{\rho\gamma}. \tag{6.59}$$

This is also the size of the fluid bridge at the cross-over time. It is no longer clear that the surface is tightly curved, as motion on this small scale could change the shape of the surface, or cause reconnection ahead of the fluid bridge.

The cross-over time $\mu^3/\rho^2\gamma$ is a much earlier time than that seen in experimental studies [48] for the crossover to the inviscid dynamics. We note that if the lengthscale

$\mu^2/\rho\gamma$ is important in the subsequent motion, then there will be another cross-over when this lengthscale becomes comparable with the typical gap between the drops r_b^2/a. If r_b is still proportional to $\gamma t/\mu$, then this would happen at a cross-over time proportional to $\mu^2(a/\rho\gamma^3)^{1/2}$. This is the cross-over time observed by Paulsen *et al.* [48].

We can therefore hypothesise the existence of an asymptotic solution for the intermediate stage of drop coalescence, with an irrotational motion on the scale of the fluid bridge, except possibly for a narrow wake behind the edge of the expanding fluid bridge. On scales proportional to $\mu^2/\rho\gamma$ near the edge of the fluid bridge, we expect an Oseen flow to govern the motion of the fluid surface, driven by surface tension on the interface.

Investigating the existence of this intermediate stage should be the focus of future work on the dynamics of drop coalescence. Asymptotic analysis may confirm the structure suggested above, and careful experimental or numerical work may reveal the lengthscales of the flow.

6.9 Two-dimensional asymptotic solution

For completeness, we will consider the remaining case of two dimensional drop coalescence with inertia. There is some suggestion in the literature that two-dimensional and three-dimensional flows should be comparable; Eggers et al. [23] solve for a two-dimensional flow, and Paulsen et al. [49] compare the two-dimensional solution for inertialess drop coalescence with the three-dimensional experiments. This section will serve as a cautionary tale; we will show that the leading-order time-dependence of r_b for two-dimensional coalescence is not the same as it is for the analogous three-dimensional problem.

6.9.1 Structure of the solution

The spatial structure of the solution is the same as the three-dimensional case above. As before, we must solve for the outer unsteady flow on the diffusive scale. We do this in two dimensions for a general Stokeslet and general dipole with a Fourier–Laplace transform. On the fluid bridge scale, we adapt our similarity solution from the inertialess case, taking different multiples of the free-surface eigenfunctions. As always, the flow on the scale of the radius of curvature of the surface is given by Hopper's

solution for the capillary flow around a parabola, and matching the velocity sets the rate of coalescence.

6.9.2 Unsteady Stokeslet in two dimensions

We will work with Cartesian coordinates (x, y) so that the fluid lies in the half-space $y > 0$. For the flow due to a point force, we have no tangential stress on $y = 0$, and we will represent the normal stress with a delta function. We will solve the unsteady Stokes equations in $y > 0$ subject to these boundary conditions, looking for the solution for which the velocity decays in the far-field. We take a streamfunction ψ such that

$$u_x = \frac{\partial \psi}{\partial y} \quad \text{and} \quad u_y = -\frac{\partial \psi}{\partial x}, \tag{6.60}$$

and take a Fourier–Laplace transform for the pressure and streamfunction. The inverse transform gives

$$p(t,x,y) = \frac{1}{2\pi^2 i}\int_{c-i\infty}^{c+i\infty} \mathrm{e}^{st}\int_0^\infty \cos(kx)\tilde{p}(s,k,y)\,\mathrm{d}k\,\mathrm{d}s, \tag{6.61}$$

$$\psi(t,x,y) = \frac{1}{2\pi^2 i}\int_{c-i\infty}^{c+i\infty} \mathrm{e}^{st}\int_0^\infty \sin(kx)\tilde{\psi}(s,k,y)\,\mathrm{d}k\,\mathrm{d}s, \tag{6.62}$$

$$h(t,x) = \frac{1}{2\pi^2 i}\int_{c-i\infty}^{c+i\infty} \mathrm{e}^{st}\int_0^\infty \cos(kx)\tilde{h}(s,k)\,\mathrm{d}k\,\mathrm{d}s, \tag{6.63}$$

where c is a real constant chosen so that poles of the integrand lie to the left of the s-contour. Now Laplace's equation for the pressure and the x-component of the momentum equation become

$$\rho s\tilde{\psi}_y = k\tilde{p} + \mu(\tilde{\psi}_{yyy} - k^2\tilde{\psi}_y) \quad \text{and} \quad -k^2\tilde{p} + \tilde{p}_{yy} = 0, \tag{6.64}$$

in which we use subscripts to denote derivatives. The solution that decays in the far-field is given by

$$\tilde{p} = \rho s A(s,k)e^{-ky} \quad \text{and} \quad \tilde{\psi} = -A(s,k)e^{-ky} + B(s,k)e^{-my} \tag{6.65}$$

for some functions $A(s,k)$ and $B(s,k)$ to be determined by the boundary conditions, where $m = (k^2 + s/\nu)^{1/2}$. The boundary conditions on $y = 0$ are

$$-p + 2\mu\frac{\partial u_y}{\partial y} = -F(t)\delta(x) \quad \text{and} \quad \mu\left(\frac{\partial u_x}{\partial y} + \frac{\partial u_y}{\partial x}\right) = 0, \tag{6.66}$$

where $F(t)$ is the time-dependent force on the fluid. These transform to

$$-\tilde{p} - 2\mu k\tilde{\psi}_y = -\hat{f}(s) \quad \text{and} \quad \tilde{\psi}_{yy} + k^2\tilde{\psi} = 0, \tag{6.67}$$

where $\hat{f}(s) = \int_0^\infty \mathrm{e}^{-st}F(t)\,\mathrm{d}t$ is the Laplace transform of the forcing. The boundary equations become algebraic equations for A and B, and the solution gives

$$\begin{pmatrix} A \\ B \end{pmatrix} = \frac{-\hat{f}(s)}{\mu(4|k|^3(k^2+s)^{1/2} - (2k^2+s)^2)} \begin{pmatrix} m^2+k^2 \\ -2ik|k| \end{pmatrix}, \tag{6.68}$$

and so

$$\tilde{p} = -s\hat{f}(s)\frac{(k^2+m^2)e^{-ky}}{\nu\left\{4k^3m - (k^2+m^2)^2\right\}}, \quad \tilde{\psi} = \hat{f}(s)\frac{(k^2+m^2)e^{-ky} - 2k^2e^{-my}}{\mu\left\{4k^3m - (k^2+m^2)^2\right\}}. \tag{6.69}$$

Using a divide-and-conquer method for the k-integral, we can find the asymptotic behaviour for $x, y \ll r_\nu$. There are two contributions to the integral; a large-k contribution representing the local effect, and a small-k term describing the effect of the history of the unsteady flow. More details of the calculation are given in appendix B. We find

$$\psi \sim \frac{x}{2\pi\mu}\left(F(t)\log\sqrt{\frac{x^2+y^2}{r_\nu^2}} + c_3F(t) - \frac{1}{2}\int_0^t F'(\tau)\log\left(1-\frac{\tau}{t}\right)\,\mathrm{d}\tau\right), \tag{6.70}$$

where $c_3 \approx -0.9367$ is derived in appendix B. The first term is the streamfunction for the expected Stokeslet at the origin. The other terms give a solid-body motion at the origin which depends on the history of the forcing. This solid-body motion is present as a result of the far-field condition; in order for the velocity to tend to zero in the far-field, there must be some additional solid-body motion at the origin.

We can use a similar divide-and-conquer method to find the behaviour for $x, y \gg r_\nu$. In this case, only the small-k contribution is significant, and it gives

$$\psi \sim -\frac{x}{\pi\rho(x^2+y^2)}\int_0^t F(\tau)\,\mathrm{d}\tau. \tag{6.71}$$

The fluid is initially at rest, and vorticity has only diffused to a distance proportional to r_ν, so the far-field is an irrotational flow, satisfying $\nabla^2\psi = 0$. The magnitude of this flow depends on the history of the forcing.

We can calculate the streamfunction numerically for any $F(t)$. As an example, take $\mu = \rho = 1$ and $F(t) = \mathcal{H}(t)$, the Heaviside step function. The Laplace transform

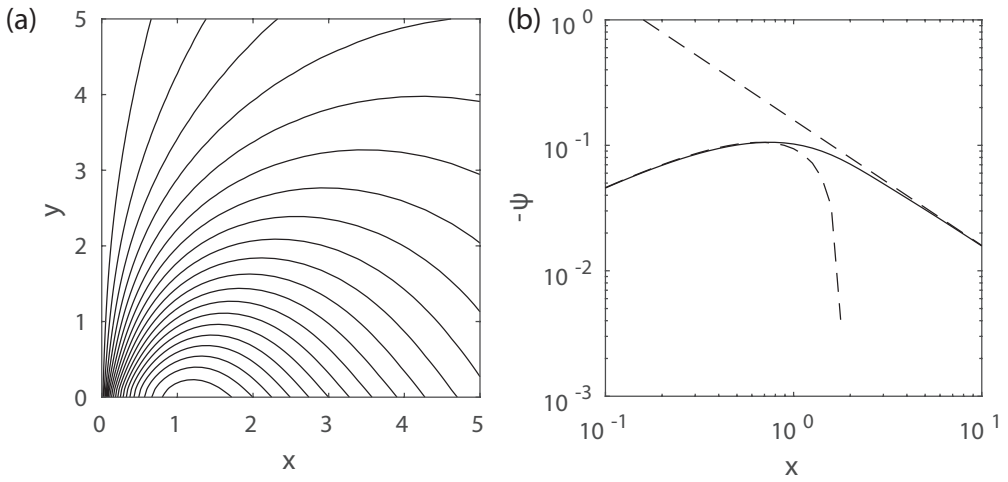

Fig. 6.5 Unsteady Stokeslet in two dimensions for $F(t) = \mathcal{H}(t)$. (a) Contours of ψ. (b) Comparison along the line $y = x$ of $-\psi$ (solid line) against the asymptotic expressions (dashed lines)

is $\hat{f}(s) = s^{-1}$, and we calculate the integral numerically with seven-point Gaussian integration. The streamlines at time $t = 1$ are shown in figure 6.5(a). For $t > 0$, the asymptotic expressions become

$$\psi \sim \frac{x}{2\pi} \log \sqrt{\frac{x^2+y^2}{r_\nu^2}} + \frac{c_3 x}{2\pi} \quad \text{for } x, y \ll r_\nu, \quad \psi \sim -\frac{tx}{\pi(x^2+y^2)} \quad \text{for } x, y \gg r_\nu, \tag{6.72}$$

and we note that $r_\nu = 1$ at time $t = 1$. Comparing ψ with the asymptotic expressions along the line $y = x$ in figure 6.5(b), we see that the numerically-calculated values agree well in the appropriate limits.

6.9.3 Unsteady Dipole in two dimensions

The stress on the interface is

$$-p + 2\mu \frac{\partial u_y}{\partial y} = 0 \quad \text{and} \quad \mu \left(\frac{\partial u_x}{\partial y} + \frac{\partial u_y}{\partial x} \right) = G(t)\delta'(x), \tag{6.73}$$

using subscripts for components. The dipole strength $G(t)$ would be $\frac{1}{2}F(t)d(t)$ for the dipole found by taking the limit as $d \to 0$ of a pair of point forces $\pm F(t)\boldsymbol{e}_x$ acting at $x = \pm\frac{1}{2}d(t)$, with half of the force carried by the upper half-space. The

kinematic boundary condition for the surface displacement h is $\frac{\partial h}{\partial t} = u_y$, neglecting terms quadratically small in u and h.

Differentiating the normal stress condition with respect to x before transforming each boundary condition gives

$$-\tilde{p} - 2\mu ik\tilde{\psi}_z = 0 \quad \text{and} \quad \mu\left(\tilde{\psi}_{yy} + k^2\tilde{\psi}\right) = ik\hat{g}(s), \tag{6.74}$$

where $\hat{g}(s)$ is the Laplace transform of $G(t)$. We substitute the general solution into the boundary equations and solve the resulting matrix problem for A and B:

$$\begin{pmatrix} A \\ B \end{pmatrix} = \frac{-ik\hat{g}(s)}{\mu(4|k|^3 m - (k^2+m^2)^2)} \begin{pmatrix} 2ikm \\ k^2+m^2 \end{pmatrix}. \tag{6.75}$$

Transforming back, we have

$$p(t,x,y) = \frac{1}{\pi^2 i\nu} \int_{c-i\infty}^{c+i\infty} s\hat{g}(s)e^{st} \int_0^\infty \cos kx \frac{k^2 m e^{-ky}}{4k^3 m - (k^2+m^2)^2} \,\mathrm{d}k\,\mathrm{d}s, \tag{6.76}$$

$$\psi(t,x,y) = \frac{i}{2\pi^2\mu} \int_{c-i\infty}^{c+i\infty} \hat{g}(s)e^{st} \int_0^\infty \sin kx \frac{2k^2 m e^{-ky} - k(k^2+m^2)e^{-my}}{4k^3 m - (k^2+m^2)^2} \,\mathrm{d}k\,\mathrm{d}s, \tag{6.77}$$

$$h(t,x) = \frac{i}{2\pi^2\mu} \int_{c-i\infty}^{c+i\infty} \frac{\hat{g}(s)}{s} e^{st} \int_0^\infty k\cos kx \frac{k(k^2+m^2) - 2k^2 m}{4k^3 m - (k^2+m^2)^2} \,\mathrm{d}k\,\mathrm{d}s. \tag{6.78}$$

Once again, a divide-and-conquer method for the integral gives the asymptotic behaviour near the origin, for $x, y \ll r_\nu$, as

$$\psi \sim \frac{G(t)xy}{2\pi\mu(x^2+y^2)} - \frac{c_4 x}{\pi^{3/2}\mu r_\nu} \int_0^t \frac{G'(\tau)}{\sqrt{1-\tau/t}} \,\mathrm{d}\tau, \tag{6.79}$$

where $c_4 \approx 0.1360$ is derived in the appendix. The first term is the streamfunction for the expected Stokes dipole. The second term is a solid-body motion at the origin. As before, this solid-body motion is necessary at the origin for the velocity to decay in the far-field, and this velocity depends on the history of the forcing.

In the far-field, the asymptotic behaviour is

$$\psi \sim \frac{8r_\nu x(3y^2 - x^2)}{\pi^{3/2}\rho(x^2+y^2)^3} \int_0^t G(\tau)\sqrt{1-\frac{\tau}{t}} \,\mathrm{d}\tau. \tag{6.80}$$

which is an irrotational flow as before.

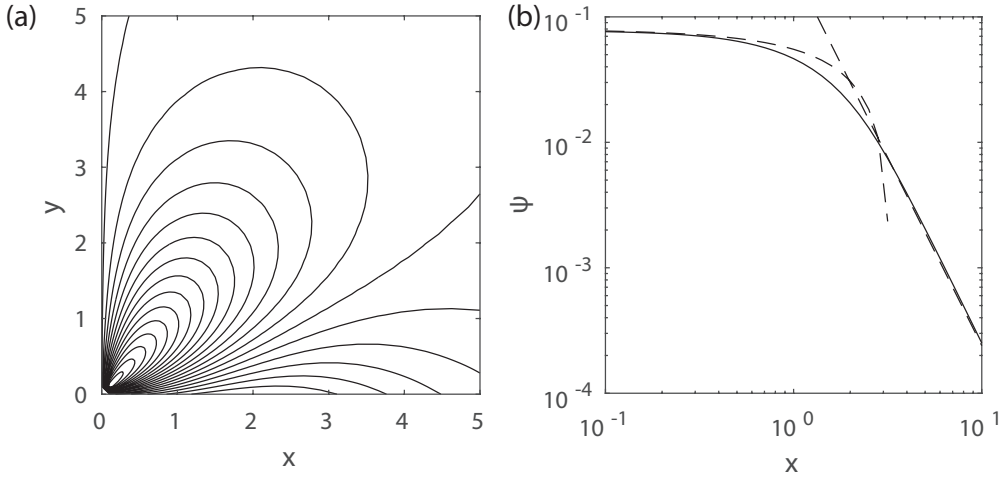

Fig. 6.6 Unsteady dipole in two dimensions for $G(t) = \mathcal{H}(t)$. (a) Contours of ψ. (b) Comparison along the line $y = x$ of ψ (solid line) against the asymptotic expressions (dashed lines)

As an example, we can take $\mu = 1$, $\rho = 1$ and $G(t) = \mathcal{H}(t)$. The streamlines at time $t = 1$ are shown in figure 6.6(a). For $t > 0$, the asymptotic expressions for ψ become

$$\psi \sim \frac{xy}{2\pi(x^2+y^2)} - \frac{c_4 x}{\pi^{3/2} r_\nu} \quad \text{for } x, y \ll r_\nu, \quad \psi \sim \frac{16 r_\nu t x(3y^2 - x^2)}{3\pi^{3/2}(x^2+y^2)^3} \quad \text{for } x, y \gg r_\nu. \tag{6.81}$$

This comparison is shown in figure 6.6(b) along the line $y = x$, and the numerically-calculated streamfunction agrees well with the asymptotic expressions.

6.9.4 Fluid-bridge scale

For two-dimensional drop coalescence, the effect of surface tension acting on the tightly-curved surface at the edges of the fluid bridge, on the fluid-bridge scale, is a pair of Stokeslets at $x = \pm r_b$ of strength $\pm 2\gamma$. We have shown before that this pair of Stokeslets satisfies no-stress boundary conditions on $y = 0$. We now consider the additional flow that is driven by the outer flow on the diffusive lengthscale.

On the diffusive scale, the pair of Stokeslets can be approximated as a dipole of strength $G(t) = 2\gamma r_b$. We have just seen that, as a result of inertia, this sets up a flow

at the origin with streamfunction

$$\psi \sim \frac{\gamma r_b x y}{\pi\mu(x^2+y^2)} - \frac{2\gamma c_4 x}{\pi^{3/2}\mu r_\nu}\int_0^t \frac{r_b'(\tau)}{\sqrt{1-\tau/t}}\,\mathrm{d}\tau, \tag{6.82}$$

which consists of the Stokes dipole together with a solid-body motion. We will show that $r_b \propto t\log\frac{1}{t}$ during the initial stage, so we expect the solid-body motion to have size proportional to $r_b/r_\nu \sim t^{1/2}$, up to factors of $\log t$. The surface displacement will therefore be proportional to $t^{3/2}$.

On the fluid-bridge scale, we will solve for a stress-free similarity solution with velocity of magnitude $t^{1/2}$ to match to the outer flow. We write

$$\mathbf{x} = r_b\bar{\mathbf{x}}, \quad \mathbf{u} = t^{1/2}\bar{\mathbf{u}}, \quad h = t^{3/2}H\left(\bar{x}\right), \quad \psi = t^{1/2}r_b\bar{\psi}. \tag{6.83}$$

We found two Stokes solutions in this doubly-cut geometry above (5.28); they are

$$\psi_1 = \frac{\sinh^3\xi\cos\eta}{\sinh^2\xi+\sin^2\eta} \quad \text{and} \quad \psi_2 = \cos\eta\left(\xi\cosh\xi - \sinh\xi\right). \tag{6.84}$$

We combine these with $\bar{\psi} = A\psi_1 + B\psi_2$. Now the kinematic boundary condition becomes

$$\frac{3}{2}H - \bar{x}H' = -\frac{3}{2}\frac{\partial\bar{\psi}}{\partial\bar{x}}. \tag{6.85}$$

We integrate the kinematic boundary condition and choose the solution which does not grow as $H \sim x^{3/2}$ for large x. This requires $3A+2B=0$. The surface shape is then

$$h = \frac{3At^{3/2}}{2}\operatorname{arccosh}\left(\frac{x}{r_b}\right). \tag{6.86}$$

Near the edge,

$$h^2 \sim \frac{9A^2t^3(x-r_b)}{2r_b}, \tag{6.87}$$

and this gives the curvature near the edge in terms of A. Now we can set A by requiring the far-field velocity to match to the flow from the outer unsteady scale. At leading order in t, we have

$$\frac{3At^{1/2}}{2}\log\left(\frac{r_\nu}{r_b}\right) = \frac{2\gamma c_4}{\pi^{3/2}\mu r_\nu t^{1/2}}\int_0^t \frac{r_b'(\tau)}{\sqrt{1-\tau/t}}\,\mathrm{d}\tau. \tag{6.88}$$

This sets A in terms of r_b. We will now determine r_b to leading order by matching to Hopper's parabola solution on the inner-inner solution.

6.9.5 Matching

As before, we rescale the parabola solution and match the velocity between the inner-inner scale and the fluid-bridge scale. Here, we have

$$\frac{\mathrm{d}r_b}{\mathrm{d}t} - \frac{\gamma}{2\pi\mu}\log\left(\frac{2r_b r}{9A^2t^3}\right) - \frac{\gamma}{\pi\mu}\left(\log 4 + \frac{1}{2}\right) \sim -\frac{\gamma}{2\pi\mu}\log\frac{r}{r_b} + \frac{\gamma}{2\pi\mu}\left(\log 2 - 1\right), \quad (6.89)$$

which we can rearrange for

$$\frac{\mathrm{d}r_b}{\mathrm{d}t} \sim \frac{\gamma}{2\pi\mu}\log\left(\frac{64r_b^2}{9A^2t^3}\right). \quad (6.90)$$

At leading order, we can integrate this for

$$r_b \sim \frac{\gamma t}{2\pi\mu}\log\left(\frac{16\gamma^2}{9A^2\pi^2\mu^2 t}\right). \quad (6.91)$$

This in turn gives a leading-order expression for A, as we can now approximate the integral in (6.88). We have

$$\frac{3At^{1/2}}{2}\log\left(\frac{(\nu t)^{1/2}}{\gamma t/\pi\mu}\right) \sim \frac{2\gamma c_4}{\pi^{3/2}\mu(\nu t)^{1/2}}\frac{\gamma}{2\pi\mu}2t\log\frac{1}{t}, \quad (6.92)$$

and so

$$A = \frac{8c_4}{3\pi^{5/2}}\frac{\gamma^2}{\mu^2\nu^{1/2}}, \quad (6.93)$$

which closes the problem. Our leading-order asymptotic for r_b is finally

$$r_b \sim \frac{\gamma t}{2\pi\mu}\log\left(\frac{\pi^3}{4c_4^2}\frac{\mu^3}{\gamma^2\rho t}\right). \quad (6.94)$$

6.9.6 Discussion

We saw above in chapter 5 that the two-dimensional and three-dimensional problems without inertia had the same leading-order behaviour

$$r_b \sim \frac{\gamma t}{\pi\mu}\log\frac{a\mu}{\gamma t}, \quad (6.95)$$

if we neglect $\mathrm{O}(t)$ terms. This supported the claim of Eggers *et al.* that two-dimensional and three-dimensional coalescence should have the same asymptotic behaviour [23].

However, we have now seen an example where the asymptotic expressions differ at leading order. Neglecting $O(t)$ terms, three-dimensional coalescence with inertia has the asymptotic behaviour

$$r_b \sim \frac{\gamma t}{\pi\mu} \log \frac{\mu^3}{\rho\gamma^2 t}, \tag{6.96}$$

whereas two-dimensional coalescence with inertia has the asymptotic behaviour

$$r_b \sim \frac{\gamma t}{2\pi\mu} \log \frac{\mu^3}{\rho\gamma^2 t}, \tag{6.97}$$

which is slower by a factor of 2.

The argument of Eggers *et al.* is therefore incorrect; two-dimensional analogue problems do not always have the same asymptotic behaviour as the three-dimensional versions. We can summarise the difference with a simple scaling argument based on the analysis above. For three-dimensional coalescence, surface tension acting on the tightly-curved surface drives a dipole which decays as

$$\mathbf{u} \sim \frac{\gamma r_b^2}{\mu r^2}, \tag{6.98}$$

and so, on the outer scale, this is proportional to $\gamma r_b^2/\mu\nu t$. The unsteady Stokes flow on the outer diffusive scale includes a solid-body motion at the origin of this order (and in fact, also a logarithmically larger term, which we will ignore for this simple scaling argument). We expect this flow to move the surfaces apart by a distance proportional to $\gamma r_b^2/\mu\nu$. The radius of curvature at the edge of the fluid bridge is therefore proportional to $\gamma^2 r_b^3/\mu^2\nu^2$. Slender body theory suggests that the motion of the edge will therefore be

$$\frac{\mathrm{d}r_b}{\mathrm{d}t} \sim \frac{\gamma t}{\pi\mu} \log\left(\frac{r_b}{\gamma^2 r_b^3/\mu^2\nu^2}\right). \tag{6.99}$$

The nature of the matching is also different between the two cases, and this is in part to the difference between the Stokeslet flow in two dimensions and three dimensions. For the three-dimensional problem, the force on the fluid bridge was unimportant for the matching since the Stokeslet flow decays in three dimensions. On the other hand, for the two-dimensional problem, the Stokeslet flow grows with distance, and matches to the far-field velocity driven by the unsteady outer flow.

Chapter 7

Conclusions

7.1 Summary of results

When two spheres of one fluid, surrounded by a second fluid, come close enough together to touch, a change of topology occurs, and the spheres are joined through a neck, with high curvature at the edge of the neck. Surface tension acts on this tightly-curved edge pulls the neck wider and the spheres closer together. This is coalescence.

We have solved for the fluid motion during the initial stage of coalescence in two extreme cases; firstly neglecting any effect of a fluid inside the spheres, and then neglecting any effect of a fluid outside the spheres. In these two cases, we have identified the lengthscales of the flow and solved appropriate forms of the Navier-Stokes equations analytically or numerically on each scale. Matching these solutions together gives an asymptotic solution, valid for sufficiently early times; we have identified the initial motion, while the neck is small.

7.1.1 Coalescence of bubbles

If the fluid inside the spheres has negligible viscosity and inertia, then we can apply the results of chapter 2, in which we called the spheres 'bubbles'. In that chapter, we found a similarity solution for the fluid velocity and the thickness of the sheet between the bubbles. This asymptotic solution holds while the hole joining the bubbles is sufficiently small. During this initial stage, we found that the radius of the hole, $r_{\scriptscriptstyle E}$, grows as

$$r_{\scriptscriptstyle E} \sim 0.8895 \left(\frac{a\gamma}{\mu}\right)^{1/2} t^{1/2} \text{ if } \mathrm{Oh} \gg 1 \quad \text{and} \quad r_{\scriptscriptstyle E} \sim 1.807 \left(\frac{a\gamma}{\rho}\right)^{1/4} t^{1/2} \text{ if } \mathrm{Oh} \ll 1, \quad (7.1)$$

where $\mathrm{Oh} = \mu/\sqrt{\rho a \gamma}$ is the Ohnesorge number with a the bubble radius, γ the coefficient of surface tension, and μ and ρ the dynamic viscosity and the density of the fluid outside the bubbles. For all Oh, the hole grows as $r_E \propto t^{1/2}$, with a prefactor which we found numerically.

We also found a similar result for the coalescence of circular bubbles in two dimensions; $r_E \propto t^{1/2}$ for all Oh in this case.

7.1.2 Coalescence of drops

If the fluid outside the spheres has negligible viscosity and inertia, then we can apply the results of chapter 6, in which we called the spheres 'drops'. In this case, there is an outer diffusive scale proportional to $(\nu t)^{1/2}$ over which vorticity diffuses out from the point of contact between the drops, where ν is the kinematic viscosity and t is the elapsed time. On the scale of the fluid bridge joining the drops, the effect of inertia is negligible. We solved for the Stokes flow on the scale of the fluid bridge joining the drops, and solved for the unsteady Stokes flow on the outer diffusive scale. We found that the radius of the fluid bridge, r_b, grows as

$$r_b \sim \frac{\gamma t}{\pi \mu} \log \frac{128 \pi^2 \mu^2 \nu}{e \gamma^2 t \log \pi^2 \mu^2 \nu / \gamma^2 t} \tag{7.2}$$

while the fluid bridge is sufficiently small.

7.2 Future work

7.2.1 General coalescence problems

We have solved for coalescence where one of the fluids has negligible viscosity and inertia. In general, fluids have some viscosity and inertia, and future work could address the case of coalescence of spherical drops of one fluid surrounded by a comparable second fluid.

Eggers *et al.* [23] give the solution for the coalescence of two dimensional drops in a fluid with the same viscosity, but neglect inertia. It would be interesting to know how inertia modifies this flow; we might expect that inertia would matter on a diffusive outer scale proportional to $t^{1/2}$, and that the unsteady Stokes equations would govern the flow on such a scale, as above. The solution would be affected by the thin viscous layer of fluid between the drops, which would perhaps impede the normal motion of the interface. If the outer flow cannot move the interface, then we might expect the

flow on the inner Stokes scale to be relatively unaffected by the presence of inertia, in contrast to the solution above.

In this general case, an initial stage in which inertia matters in both fluids will last only while $(\nu t)^{1/2} \ll a$, where ν is the larger kinematic viscosity of the fluids, before vorticity has diffused out to the scale of the drops. In fact, the initial stage might end much earlier, and there may be a complicated picture of crossover from a general initial stage to either the bubble coalescence solution above, the drop coalescence solution above, or to something like the matched-viscosity solution of Eggers *et al.* [23]. Only by solving for the flow would we know where these crossovers occur.

7.2.2 Next stages of coalescence

We have solved for the flow during the initial stage of coalescence, for sufficiently early times. Future work could identify the subsequent flows, after the initial stage has ended.

For example, in the work on drop coalescence, we identified a crossover time after which the radius of the fluid bridge is larger than $(\nu t)^{1/2}$. After this, the asymptotic structure above does not hold. But since the fluid bridge is still much smaller than the radius of the drops, we might expect some asymptotic solution to be possible, exploiting that separation of scales.

Such a solution might itself involve several distinct lengthscales, and there might be further crossovers and stages of coalescence before the radius of the fluid bridge is comparable to the radius of the drops. This potential for future work to identify further crossovers gives us hope that we could perhaps justify the crossover times observed experimentally, for example by Paulsen *et al.* [50].

This is an exciting time to work on coalescence problems, as advances in numerical and experimental techniques mean that there is likely to be new examination of the initial stages of coalescence, as smaller scales and quicker events can be imaged and simulated. Whatever the landscape of crossovers turns out to be, it is clear that there is more theoretical work to be done to explain all the possible flows that can arise.

References

[1] Aarts, D. G. A. L., Lekkerkerker, H. N. W., Guo, H., Wegdam, G. H., and Bonn, D. (2005). Hydrodynamics of droplet coalescence. *Phys. Rev. Lett.*, 95:164503.

[2] Anthony, C. R., Kamat, P. M., Thete, S. S., Munro, J. P., Lister, J. R., Harris, M. T., and Basaran, O. A. (2017). Scaling laws and dynamics of bubble coalescence. *Phys. Rev. Fluids*, 2:083601.

[3] Batchelor, G. K. (2000). *Expressions for some common vector differential quantities in orthogonal curvilinear co-ordinate systems*, page 598–603. Cambridge University Press.

[4] Beard, K. V. and Chuang, C. (1987). A new model for the equilibrium shape of raindrops. *J. Atmos. Sci.*, 44(11):1509–1524.

[5] Billingham, J. (1999). Surface-tension driven flows in fat wedges and cones. *J. Fluid Mech.*, 397:45–71.

[6] Billingham, J. (2005). The initial surface tension-driven flow of a wedge of viscous fluid. *SIAM J. Appl. Math*, 66:510–532.

[7] Blanchard, D. C. (1989). The ejection of drops from the sea and their enrichment with bacteria and other materials: A review. *Estuaries*, 12(3):127–137.

[8] Bourouiba, L. and Bush, J. W. M. (2013). Drops and bubbles in the environment. In Fernando, H. J. S., editor, *Handbook of Environmental Fluid Dynamics, Volume One*, chapter 32, pages 427–439. CRC Press.

[9] Brenner, M. P. and Gueyffier, D. (1999). On the bursting of viscous films. *Phys. Fluids*, 11(3):737–739.

[10] Burton, J. C., Rutledge, J. E., and Taborek, P. (2004). Fluid pinch-off dynamics at nanometer length scales. *Phys. Rev. Lett.*, 92:244505.

[11] Burton, J. C. and Taborek, P. (2007). Role of dimensionality and axisymmetry in fluid pinch-off and coalescence. *Phys. Rev. Lett.*, 98:224502.

[12] Case, S. C. and Nagel, S. R. (2008). Coalescence in low-viscosity liquids. *Phys. Rev. Lett.*, 100:084503.

[13] Chan, A. T. and Chwang, A. T. (2000). The unsteady Stokeslet and Oseenlet. *Proc. Inst. Mech. Eng. C*, 214(1):175–179.

[14] Christodoulou, K. and Scriven, L. (1992). Discretization of free surface flows and other moving boundary problems. *J. Comp. Phys.*, 99(1):39 – 55.

[15] Copson, E. (1961). On certain dual integral equations. *Proc. Glasgow Math. Assoc.*, 5:21–24.

[16] Culick, F. E. C. (1960). Comments on a ruptured soap film. *J. Appl. Phys.*, 31:1128–1129.

[17] de Maleprade, H., Clanet, C., and Quéré, D. (2016). Spreading of bubbles after contacting the lower side of an aerophilic slide immersed in water. *Phys. Rev. Lett.*, 117:094501.

[18] Debrégeas, G., de Gennes, P.-G., and Brochard-Wyart, F. (1998). The life and death of "bare" viscous bubbles. *Science*, 279(5357):1704–1707.

[19] Debrégeas, G., Martin, P., and Brochard-Wyart, F. (1995). Viscous bursting of suspended films. *Phys. Rev. Lett.*, 75:3886–3889.

[20] Duchemin, L., Eggers, J., and Josserand, C. (2003). Inviscid coalescence of drops. *J. Fluid Mech.*, 487:167–178.

[21] Dupré, A. and Dupré, P. (1869). *Théorie mécanique de la chaleur*. Gauthier-Villars.

[22] Eggers, J. (2014). Post-breakup solutions of Navier-Stokes and Stokes threads. *Phys. Fluids*, 26(7):072104.

[23] Eggers, J., Lister, J. R., and Stone, H. A. (1999). Coalescence of liquid drops. *J. Fluid Mech*, 401:293–310.

[24] Etoh, T. G., Poggemann, D., Kreider, G., Mutoh, H., Theuwissen, A., Ruckelshausen, A., Kondo, Y., Maruno, H., Takubo, K., Soya, H., Takehara, K., Okinaka, T., and Takano, Y. (2003). An image sensor which captures 100 consecutive frames at 1000000 frames/s. In *IEEE Transactions on Electron Devices*.

[25] Etoh, T. G., Poggemann, D., Ruckelshausen, A., Theuwissen, A., Kreider, G., Folkerts, H. O., Mutoh, H., Kondo, Y., Maruno, H., Takubo, K., Soya, H., Takehara, K., Okinaka, T., Takano, Y., Reisinger, T., and Lohmann, C. (2002). A CCD image sensor of 1 Mframes/s for continuous image capturing 103 frames. In *2002 IEEE International Solid-State Circuits Conference. Digest of Technical Papers*.

[26] Hopper, R. W. Coalescence of two viscous cylinders by capillarity: Part I, theory. *J. Am. Ceram. Soc.*, 76(12):2947–2952.

[27] Hopper, R. W. Coalescence of two viscous cylinders by capillarity: Part II, shape evolution. *J. Am. Ceram. Soc.*, 76(12):2953–2960.

[28] Hopper, R. W. (1984). Coalescence of two equal cylinders: Exact results for creeping viscous plane flow driven by capillarity. *J. Am. Ceram. Soc.*, 67(12):262–264.

[29] Hopper, R. W. (1990). Plane stokes flow driven by capillarity on a free surface. *J. Fluid Mech.*, 213:349–375.

[30] Hopper, R. W. (1991). Plane stokes flow driven by capillarity on a free surface. Part 2. Further developments. *J. Fluid Mech.*, 230:355–364.

[31] Hopper, R. W. (1993). Capillarity-driven plane Stokes flow exterior to a parabola. *Q. J. Mech. Appl. Maths*, 46(2):193–210.

[32] Hutchings, I. M. and Martin, G. D. (2013). *Inkjet Technology for digital fabrication*. Wiley.

[33] Keller, J. B. (1983). Breaking of liquid films and threads. *Phys. Fluids*, 26(12):3451–3453.

[34] Keller, J. B., King, A., and Ting, L. (1995). Blob formation. *Phys. Fluids*, 7:226–228.

[35] Keller, J. B. and Miksis, M. J. (1983). Surface tension driven flows. *SIAM J. Appl. Math.*, 43:268–277.

[36] Lowengrub, M. and Sneddon, I. (1963). The solution of a pair of dual integral equations. *Proc. Glasgow Math. Assoc.*, 6:14–18.

[37] Lu, D. and Chwang, A. T. (2005). Unsteady free-surface waves due to a submerged body moving in a viscous fluid. *Phys. Rev. E*, 71:066303.

[38] Lu, D. Q. (2008). Generation of free-surface gravity waves by an unsteady Stokeslet. *Arch. Appl. Mech.*, 79(4):311.

[39] Miksis, M. J. and Vanden-Broeck, J.-M. (1999). Self-similar dynamics of a viscous wedge of fluid. *Phys. Fluids*, 11(11):3227–3231.

[40] Moffatt, H. K. (1964). Viscous and resistive eddies near a sharp corner. *J. Fluid Mech.*, 18:1–18.

[41] Munro, J. P., Anthony, C. R., Basaran, O. A., and Lister, J. R. (2015). Thin-sheet flow between coalescing bubbles. *J. Fluid Mech.*, 773:R3.

[42] Munro, J. P. and Lister, J. R. (2018). Capillary retraction of the edge of a stretched viscous sheet. *J. Fluid Mech.*, 844:R1.

[43] Notz, P. K. and Basaran, O. A. (2004). Dynamics and breakup of a contracting liquid filament. *J. Fluid Mech.*, 512:223–256.

[44] Notz, P. K., Chen, A. U., and Basaran, O. A. (2001). Satellite drops: Unexpected dynamics and change of scaling during pinch-off. *Phys. Fluids*, 13(3):549–552.

[45] O'Kiely, D., Breward, C. J. W., Griffiths, I. M., Howell, P. D., and Lange, U. (2015). Edge behaviour in the glass sheet redraw process. *J. Fluid Mech.*, 785:248–269.

[46] O'Kiely, D., Breward, C. J. W., Griffiths, I. M., Howell, P. D., and Lange, U. (2018). Glass sheet redraw through a long heater zone. *IMA J. Appl. Math.*, 83:799–820.

[47] Paulsen, J. D. (2013). Approach and coalescence of liquid drops in air. *Phys. Rev. E*, 88:063010.

[48] Paulsen, J. D., Burton, J. C., and Nagel, S. R. (2011). Viscous to inertial crossover in liquid drop coalescence. *Phys. Rev. Lett.*, 106:114501.

[49] Paulsen, J. D., Burton, J. C., Nagel, S. R., Appathurai, S., Harris, M. T., and Basaran, O. A. (2012). The inexorable resistance of inertia determines the initial regime of drop coalescence. *Proc. Natl. Acad. Sci. U.S.A.*, 109(18):6857–6861.

[50] Paulsen, J. D., Carmigniani, R., Burton, A. K. J. C., and Nagel, S. R. (2014). Coalescence of bubbles and drops in an outer fluid. *Nat. Commun.*, 5(3182).

[51] Pegler, S. S. and Worster, M. G. (2012). Dynamics of a viscous layer flowing radially over an inviscid ocean. *J. Fluid Mech.*, 696:152–174.

[52] Pozrikidis, C. (1992). *Boundary Integral and Singularity Methods for Linearized Viscous Flow*. Cambridge Texts in Applied Mathematics. Cambridge University Press.

[53] Rallison, J. M. (1984). The deformation of small viscous drops and bubbles in shear flows. *Ann. Rev. Fluid Mech.*, 16:45–66.

[54] Ranz, W. E. (1959). Some experiments on the dynamics of liquid films. *J. Appl. Phys.*, 30(12):1950–1955.

[55] Rayleigh (1891). Some applications of photography. *Nature*, 44:249–254.

[56] Richardson, S. (1992). Two-dimensional slow viscous flows with time-dependent free boundaries driven by surface tension. *Eur. J. Appl. Math.*, 3:193–207.

[57] Savva, N. and Bush, J. W. M. (2009). Viscous sheet retraction. *J. Fluid Mech.*, 626:211– 240.

[58] Shu, J. and Chwang, A. T. (2001). Generalized fundamental solutions for unsteady viscous flows. *Phys. Rev. E*, 63:051201.

[59] Sierou, A. and Lister, J. R. (2003). Self-similar solutions for viscous capillary pinch-off. *J. Fluid Mech.*, 497:381–403.

[60] Sierou, A. and Lister, J. R. (2004). Self-similar recoil of inviscid drops. *Phys. Fluids*, 16(5):1379–1394.

[61] Smith, S. H. (1987). Unsteady Stokes' flow in two dimensions. *J. Eng. Math.*, 21(4):271–285.

[62] Sünderhauf, G., Raszillier, H., and Durst, F. (2002). The retraction of the edge of a planar liquid sheet. *Phys. Fluids*, 14(1):198–208.

[63] Sneddon, I. (1960). The elementary solution of dual integral equations. *Proc. Glasgow Math. Assoc.*, 4:108–110.

[64] Sparks, R. (1978). The dynamics of bubble formation and growth in magmas: A review and analysis. *J. Volcanol. Geotherm. Res.*, 3(1–2):1–37.

[65] Stover, R. L., Tobias, C. W., and Denn, M. M. (1997). Bubble coalescence dynamics. *AIChE J.*, 43(10):2385–2392.

[66] Taylor, G. I. (1959a). The dynamics of thin sheets of fluid. II. Waves on fluid sheets. In *Proc. Roy. Soc. A*, volume 253, pages 296–312.

[67] Taylor, G. I. (1959b). The dynamics of thin sheets of fluid. III. Disintegration of fluid sheets. In *Proc. Roy. Soc. A*, volume 253, pages 313–321.

[68] Taylor, G. I. and Howarth, L. (1959). The dynamics of thin sheets of fluid. I. Water bells. In *Proc. Roy. Soc. A*, volume 253, pages 289–295.

[69] Thompson, A. B. and Billingham, J. (2012). Inviscid coalescence in the presence of a surrounding fluid. *IMA J. Appl. Math.*, 77(5):678–696.

[70] Thoroddsen, S. T., Etoh, T. G., Takehara, K., and Ootsuka, N. (2005a). On the coalescence speed of bubbles. *Phys. Fluids*, 17(7):071703.

[71] Thoroddsen, S. T., Takehara, K., and Etoh, T. G. (2005b). The coalescence speed of a pendent and a sessile drop. *J. Fluid Mech.*, 527:85–114.

[72] Timoshenko, S. and Goodier, J. N. (1951). *Theory of elasticity*. McGraw-Hill Book Company, second edition.

[73] Ting, L. and Keller, J. B. (1990). Slender jets and thin sheets with surface tension. *SIAM J. Appl. Math.*, 50:1533–1546.

[74] Worthington, A. M. (1883). On impact with a liquid surface. *Proc. Roy. Soc. A*, 34:217–230.

Appendix A

Next-order correction for 2D coalescence without inertia

Our similarity solution on the fluid bridge scale neglects the surface stresses. As a result, we saw that the exact solution due to Hopper and Richardson only decayed to the similarity solution slowly, with the next term only slightly smaller. Here, we solve for the next correction due to the surface stresses.

There are two sources of surface stress; from the leading-order Stokeslets and from surface tension acting on the curved surface. These stresses of order $\gamma h/r_b^2$ drive a flow of size $\gamma h/\mu r_b \sim \gamma r_b/\mu a$. This is smaller than the leading-order velocity by a factor of $\dot{r}_b\mu/\gamma \sim \log(8a/r_b)/\pi$.

A.1 Solution with Tranter's method

Non-dimensionalise all distances with r_b, and the velocities with $\gamma r_b/\mu a$. We solve the Stokes equations in $y > 0$. The boundary conditions on $y = 0$ are known stress on $|x| > 1$ and symmetry on the fluid bridge (no tangential stress or normal velocity on $|x| < 1$). In non-dimensionalised variables, these are

$$-p + 2\frac{\partial v}{\partial y} = -h_{xx} + 1 \qquad \text{for } |x| > 1, \tag{A.1}$$

$$-\left(\frac{\partial u}{\partial y} + \frac{\partial v}{\partial x}\right) = \frac{2}{\pi}\left(\frac{(x-1)h_x - h}{(x-1)^2} - \frac{(x+1)h_x - h}{(x+1)^2}\right) \qquad \text{for } |x| > 1, \tag{A.2}$$

$$v = 0 \qquad \text{for } |x| < 1 \tag{A.3}$$

$$-\left(\frac{\partial u}{\partial y} + \frac{\partial v}{\partial x}\right) = 0 \qquad \text{for } |x| < 1, \tag{A.4}$$

where we have chosen the pressure so that $N(x) \to 0$. The shape h is given by the leading-order solution $h = x\sqrt{x^2-1}$.

We want to solve this with Tranter's method, but there is a technical problem; the stresses are divergent and so the integrals in Tranter's method do not converge. To work around this, we subtract a solution to the Stokes equations that diverges in the right way at the edge. In section §4.7, we solved for the Stokes flow around a single narrow parabolic cut with surface tension, and so here we employ a pair of the single-cut solutions at $x = \pm 1$, $y = 0$. The streamfunction for this is

$$\begin{aligned}\psi_{ABCD} =& \frac{r_1^{1/2}}{24\sqrt{2}\pi}\left(\cos\left(\frac{3\theta_1}{2}\right)(3\log r_1 - 4) + 3\cos\left(\frac{\theta_1}{2}\right)(4 + 3\log r_1) + 12(\pi-\theta_1)\sin^3\left(\frac{\theta_1}{2}\right)\right) \\ &- \frac{r_2^{1/2}}{24\sqrt{2}\pi}\left(\cos\left(\frac{3\theta_2}{2}\right)(3\log r_2 - 4) + 3\cos\left(\frac{\theta_2}{2}\right)(4 + 3\log r_2) + 12(\pi-\theta_2)\sin^3\left(\frac{\theta_2}{2}\right)\right),\end{aligned} \tag{A.5}$$

where $x = 1 + r_1\cos\theta_1 = -1 - r_2\cos\theta_2$ and $y = r_1\sin\theta_1 = -r_2\sin\theta_2$. This removes the largest singularities of the normal and tangential stresses. We also subtract a solid-body motion and a multiple of the stress-free solution ψ_1 above (5.28), given by

$$\psi_1 = \frac{\sinh^3\xi\cos\eta}{\sinh^2\xi + \sin^2\eta}. \tag{A.6}$$

With all these subtracted terms, we write

$$\psi = \psi_{ABCD} - k_{SBM}x + k_1\psi_1 + \bar{\psi} \tag{A.7}$$

for the streamfunction, and similarly for the pressure. The boundary conditions become

$$\begin{aligned}-\bar{p} + 2\frac{\partial\bar{v}}{\partial y} =& 2 + \frac{3x - 2x^3}{(x^2-1)^{3/2}} \\ &+ \sqrt{2}\left(-\frac{1}{4(x-1)^{3/2}} + \frac{1}{6\pi(x+1)^{3/2}} + \frac{\log(x+1)}{4\pi(x+1)^{3/2}}\right) \quad \text{for } |x| > 1,\end{aligned} \tag{A.8}$$

$$-\left(\frac{\partial\bar{u}}{\partial y} + \frac{\partial\bar{v}}{\partial y}\right) = -\frac{4}{\pi}\frac{1}{(x^2-1)^{3/2}} + \frac{\sqrt{2}}{\pi(x-1)^{3/2}} \quad \text{for } |x| > 1, \tag{A.9}$$

$$\bar{v} = -k_{SBM} \quad \text{for } |x| < 1, \tag{A.10}$$

$$-\left(\frac{\partial\bar{u}}{\partial y} + \frac{\partial\bar{v}}{\partial x}\right) = 0 \quad \text{for } |x| < 1. \tag{A.11}$$

We will write $N(x)$ and $T(x)$ for the applied stresses on the right-hand sides of (A.8) and (A.9) respectively.

We can take a Fourier transform for the pressure and streamfunction, and then the inverse gives

$$\bar{\psi} = \int_0^\infty \tilde{\psi} \sin kx \, \mathrm{d}k, \quad \bar{p} = \int_0^\infty \tilde{\psi} \cos kx \, \mathrm{d}k. \tag{A.12}$$

The solution to the transformed Stokes equations is

$$\tilde{p} = A\mathrm{e}^{-ky}, \quad \tilde{\psi} = -\frac{Ay}{2k}\mathrm{e}^{-ky} + B\mathrm{e}^{-ky}, \tag{A.13}$$

where $A(k)$ and $B(k)$ are set by the boundary conditions. These transform to

$$-\int_0^\infty \left(2k^2 B + A\right) \sin kx \, \mathrm{d}k = \begin{cases} T(x') & \text{for } |x| > 1 \\ 0 & \text{for } |x| < 1 \end{cases}, \tag{A.14}$$

$$\int_0^\infty Bk^2 \sin kx \, \mathrm{d}k = 0 \quad \text{for } |x| < 1, \tag{A.15}$$

$$\int_0^\infty Bk \sin kx \, \mathrm{d}k = -\frac{1}{2}\int_x^\infty N(x') \, \mathrm{d}x' \quad \text{for } |x| > 1, \tag{A.16}$$

where we have taken the x-derivative of the velocity condition to remove the constant k_{SBM}, and we have taken the x-integral of the normal stress condition, choosing the constant so that the integral decays in the far-field.

The tangential stress condition gives A in terms of B and the tangential stress T;

$$A = -\frac{2}{\pi}\int_1^\infty T(x') \sin kx' \, \mathrm{d}x' - 2k^2 B, \tag{A.17}$$

so we just need to solve for $B(k)$. We do this with Tranter's method.

We write $\sin kx$ as $(\pi/2)^{1/2} J_{1/2}(kx)\sqrt{kx}$ and the problem for B is in the form solved by Sneddon [63] with $\alpha = 1/2$, $\nu = 1/2$. The solution is

$$B = -\frac{1}{\pi k}\int_0^\infty J_1(k\rho)\rho \frac{\partial}{\partial \rho}\int_\rho^\infty \frac{-\int_t^\infty N(t') \, \mathrm{d}t'}{\sqrt{t^2 - \rho^2}} \, \mathrm{d}t \, \mathrm{d}\rho, \tag{A.18}$$

which we will calculate numerically, making use of asymptotic expressions for the integrals. First note that

$$-\int_x^\infty N(x') \, \mathrm{d}x' = \frac{1}{\sqrt{2}(x-1)^{1/2}} + 2x - \frac{4\sqrt{2}}{3\pi(x+1)^{1/2}} + \frac{1-2x^2}{(x^2-1)^{1/2}} - \frac{\log(x+1)}{\pi\sqrt{2}(x+1)^{1/2}}, \tag{A.19}$$

with asymptotic behaviour

$$-\int_x^\infty N(x')\,\mathrm{d}x' \sim \begin{cases} \dfrac{-8+12\pi-3\log 2}{6\pi} & \text{for } 0<x-1\ll 1 \\ \dfrac{-8+3\pi-3\log x}{3\pi\sqrt{2}x^{1/2}} & \text{for } x\gg 1, \end{cases} \tag{A.20}$$

and then integrate by parts, defining $C(\rho)$ by

$$C(\rho) = \frac{\partial}{\partial\rho}\int_\rho^\infty \frac{-\int_t^\infty N(t')\,\mathrm{d}t'}{\sqrt{t^2-\rho^2}}\,\mathrm{d}\rho = \frac{\partial}{\partial\rho}\left(-\int_\rho^\infty \frac{\mathrm{d}}{\mathrm{d}t}\left(\frac{-\int_t^\infty N(t')\,\mathrm{d}t'}{t}\right)\sqrt{t^2-\rho^2}\,\mathrm{d}\rho\right) \tag{A.21}$$

$$= \rho\int_0^\infty \frac{\mathrm{d}}{\mathrm{d}t}\left(\frac{-\int_t^\infty N(t')\,\mathrm{d}t'}{t}\right)\frac{\mathrm{d}t}{\sqrt{t^2-\rho^2}}. \tag{A.22}$$

The asymptotic behaviour of $N(x)$ gives

$$C(\rho) \sim \begin{cases} 0.4305 + 0.9375\log(\rho-1) & \text{for } 0<\rho-1\ll 1 \\ 0.2951\rho^{-3/2}\log\rho - 0.2668\rho^{-3/2} & \text{for } \rho\gg 1, \end{cases} \tag{A.23}$$

and then we calculate

$$B(k) = -\frac{1}{\pi}\int_0^\infty J_1(k\rho)\rho C(\rho)\,\mathrm{d}\rho, \tag{A.24}$$

replacing $C(\rho)$ with its asymptotic expressions for extreme values of ρ. We find

$$B \sim \begin{cases} 0.07791k^{-3/2} + 0.08979k^{-3/2}\log k & \text{for } k\ll 1 \\ (0.2381\log k + 0.02810)k^{-5/2}\sin\left(k+\dfrac{\pi}{4}\right) + 0.3740k^{-5/2}\sin\left(k-\dfrac{\pi}{4}\right) & \text{for } k\gg 1. \end{cases} \tag{A.25}$$

Now we need to find k_{SBM} to satisfy the normal velocity condition on the fluid bridge. The velocity at the origin is

$$-k_{SBM} = v(0,0) = \int_0^\infty Bk\,\mathrm{d}k = 0.1089, \tag{A.26}$$

where we have integrated numerically, using the asymptotics for extreme k.

The final coefficient k_1 is set by the kinematic boundary condition. Write

$$h_2 = H\left(\frac{x}{r_b}\right)\int_0^t \frac{\gamma r_b}{\mu a}\,\mathrm{d}t', \tag{A.27}$$

so that the kinematic boundary condition,

$$\frac{\partial h}{\partial t} = v - u\frac{\partial h}{\partial x}, \tag{A.28}$$

becomes

$$-\frac{xH'}{2} + H = h_1\frac{\partial v_S}{\partial y} + v - u_S h_1'. \tag{A.29}$$

Now recall that $v = v_{ABCD} + k_{SBM} + k_1 v_1 + \bar{v}$, where

$$v_{ABCD} = -\frac{8 + 3\log(x-1)}{12\pi(x-1)^{1/2}}, \quad v_1 = -\frac{x}{\sqrt{x^2-1}}, \tag{A.30}$$

and

$$\frac{\partial v_S}{\partial y} = \frac{\gamma}{2\pi\mu}\left(\frac{1}{x-1} - \frac{1}{x+1}\right), \quad u_S = -\frac{1}{2\pi}\log\left(\frac{x-1}{x+1}\right). \tag{A.31}$$

We integrate for H;

$$\frac{H}{x^2} = -2\int_x^\infty \frac{h\frac{\partial v_S}{\partial y} + v_{ABCD} + k_{SBM} + k_1 v_1 + \bar{v} - u_S h_1'}{x'^3}\,\mathrm{d}x'. \tag{A.32}$$

Since we do not want H to grow as x^2 in the far-field at this order, we must have

$$0 = -\frac{4.496}{2\pi} + \frac{2}{2\pi} - k_1 + 0.1841, \tag{A.33}$$

which sets

$$k_1 = -0.2131, \tag{A.34}$$

completing the solution.

A.2 Velocity on the centreline

To check the solution, we calculate v on $x = 0$. We need

$$v = v_{ABCD} + k_{SBM} + k_1 v_1 - \int_0^\infty \left(-\frac{Ay}{2k}\mathrm{e}^{-ky} + B\mathrm{e}^{-ky}\right) k\,\mathrm{d}k. \tag{A.35}$$

The first three terms are all known analytically, and we can substitute for A;

$$-\int_0^\infty \left(-\frac{Ay}{2k}\mathrm{e}^{-ky} + B\mathrm{e}^{-ky}\right) k\,\mathrm{d}k = \int_0^\infty -\frac{y}{\pi}\left(\int_1^\infty T(x')\sin kx'\,\mathrm{d}x'\right)\mathrm{e}^{-ky} - Bk(1+ky)\mathrm{e}^{-ky}\,\mathrm{d}k. \tag{A.36}$$

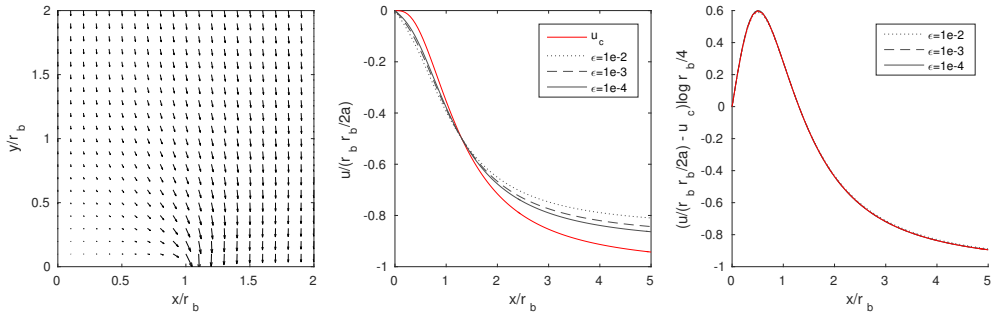

Fig. A.1 (a) Hopper and Richardson's solution on the fluid bridge scale with the Stokeslets subtracted. (b) The first correction scales with $r_b\dot{r}_b/2a$, with the next correction driven by the surface stress. (c) Subtract the first correction and the next term collapses when rescaled. The red line is the velocity calculated in this appendix.

If we swap the order of integration for the term involving $T(x')$, we get

$$-\frac{y}{\pi}\int_1^\infty T(x')\int_0^\infty \sin kx' \mathrm{e}^{-ky}\,\mathrm{d}k\,\mathrm{d}x' = -\frac{y}{\pi}\int_1^\infty T(x')\frac{x'}{x'^2+y^2}\,\mathrm{d}x', \tag{A.37}$$

and we recall that

$$T(x) = -\frac{4}{\pi}\frac{1}{(x^2-1)^{3/2}} + \frac{\sqrt{2}}{\pi(x-1)^{3/2}}. \tag{A.38}$$

This can be integrated analytically

$$\int_1^\infty T(x')\frac{x'}{x'^2+y^2}\,\mathrm{d}x' = \frac{2+\sqrt{2}(1+y^2)^{1/4}(y\sin\frac{\arctan y}{2} - \cos\frac{\arctan y}{2})}{(y^2+1)^{3/2}}. \tag{A.39}$$

We must still integrate the term involving B numerically, using the asymptotic behaviour for large k again. This gives the velocity shown with a red line in figure A.1(c). The exact solution, with the leading-order Stokeslet and similarity solution subtracted, collapses extremely well onto the curve for the next correction.

Appendix B

Asymptotics for unsteady flows

In section 6.2, we found Hankel–Laplace transforms for the pressure, potential and surface displacement. To match these flows to the solution on smaller scales, we need the asymptotic behaviour at the origin, and to find the flow on larger scales, we need the asymptotic behaviour in the far-field. In this appendix, we use a divide-and-conquer method to find the required asymptotic expressions from the transformed quantities.

We then repeat the calculation for the two-dimensional flows considered in section 6.9.

B.1 3D point force

The solution derived above (6.15) is

$$p(t,r,z) = -\frac{1}{2\pi i\nu}\int_{c-i\infty}^{c+i\infty} \mathrm{e}^{st} s\hat{f}(s) \int_0^\infty \frac{(k^2+m^2)\mathrm{e}^{-kz}}{4k^3m-(k^2+m^2)^2} J_0(kr)k\,\mathrm{d}k\,\mathrm{d}s \tag{B.1}$$

$$\phi(t,r,z) = \frac{1}{2\pi i\mu}\int_{c-i\infty}^{c+i\infty} \mathrm{e}^{st} \hat{f}(s) \int_0^\infty \frac{(k^2+m^2)\mathrm{e}^{-kz}-2k^2\mathrm{e}^{-mz}}{4k^3m-(k^2+m^2)^2} J_1(kr)k\,\mathrm{d}k\,\mathrm{d}s \tag{B.2}$$

$$h(t,r) = -\frac{1}{2\pi i\nu}\int_{c-i\infty}^{c+i\infty} \mathrm{e}^{st} \hat{f}(s) \int_0^\infty \frac{k}{4k^3m-(k^2+m^2)^{1/2}} J_0(kr)k\,\mathrm{d}k\,\mathrm{d}s. \tag{B.3}$$

B.1.1 Near the origin

Let

$$I_k = \int_0^\infty \frac{(k^2+m^2)\mathrm{e}^{-kz}-2k^2\mathrm{e}^{-mz}}{4k^3m-(k^2+m^2)^2} J_1(kr)k\,\mathrm{d}k. \tag{B.4}$$

We will make the substitution $k = \hat{k}/r$, $s = \hat{s}/t$, and write $\hat{\eta}^2 = \hat{s}r^2/\nu t$, $\beta = z/r$. Then

$$I_k = \int_0^\infty \frac{(2\hat{k}^2 + \hat{\eta}^2)\mathrm{e}^{-\hat{k}\beta} - 2\hat{k}^2\mathrm{e}^{-(\hat{k}^2+\hat{\eta}^2)^{1/2}\beta}}{4\hat{k}^3(\hat{k}^2+\hat{\eta}^2)^{1/2} - (2\hat{k}^2+\hat{\eta}^2)^2} J_1(\hat{k})\hat{k}\,\mathrm{d}\hat{k}. \tag{B.5}$$

For $r \ll (\nu t)^{1/2}$ and $|\hat{s}| = \mathrm{O}(1)$, we have $\hat{\eta} \ll 1$. So we can split the k-integral at some δ such that $\hat{\eta} \ll \delta \ll 1$. Then asymptotic expressions for the exponentials and the rational part of the integrand give

$$I_k \sim \frac{\hat{\eta}^2}{2}\int_0^\delta \frac{\hat{k}^2}{4\hat{k}^3(\hat{k}^2+\hat{\eta}^2)^{1/2} - (2\hat{k}^2+\hat{\eta}^2)^2}\,\mathrm{d}\hat{k} + \int_\delta^\infty \frac{\beta\hat{\eta}^2\hat{k} + \hat{\eta}^2}{-2\hat{k}^2\hat{\eta}^2}\mathrm{e}^{-\hat{k}\beta}J_1(\hat{k})\hat{k}\,\mathrm{d}\hat{k} \tag{B.6}$$

$$= \frac{\hat{\eta}}{2}\int_0^{\delta/\hat{\eta}} \frac{u^2}{4u^3(u^2+1)^{1/2} - (2u^2+1)^2}\,\mathrm{d}u - \frac{1}{2}\int_\delta^\infty \frac{(1+\hat{k}\beta)}{\hat{k}}\mathrm{e}^{-\hat{k}\beta}J_1(\hat{k})\,\mathrm{d}\hat{k} \tag{B.7}$$

$$= \frac{\hat{\eta}}{2}(c_1) - \frac{1}{2}\left(\frac{1}{\sqrt{1+\beta^2}}\right) + \mathrm{O}(\delta), \tag{B.8}$$

where

$$c_1 = \int_0^\infty \frac{u^2}{4u^3(u^2+1)^{1/2} - (2u^2+1)^2} + \frac{1}{2}\,\mathrm{d}u \approx 0.6561. \tag{B.9}$$

Then the inverse Laplace transform for the potential becomes

$$\phi \sim \frac{1}{2\pi i\mu}\int_{c-i\infty}^{c+i\infty} \mathrm{e}^{st}\hat{f}(s)\left(\frac{\sqrt{sr^2/\nu}}{2}(c_1) - \frac{1}{2}\left(\frac{1}{\sqrt{1+(z/r)^2}}\right)\right)\mathrm{d}s \tag{B.10}$$

$$= -\frac{1}{2\mu}\frac{r}{\sqrt{r^2+z^2}}F(t) + \frac{c_1 r}{2\mu\nu^{1/2}}\frac{1}{2\pi i}\int_{c-i\infty}^{c+i\infty}\mathrm{e}^{st}\hat{f}(s)s^{1/2}\,\mathrm{d}s \tag{B.11}$$

$$= -\frac{1}{2\mu}\frac{r}{\sqrt{r^2+z^2}}F(t) + \frac{c_1 r}{2\mu\nu^{1/2}}\int_0^t F'(\tau)\frac{1}{\pi^{1/2}}\frac{1}{\sqrt{t-\tau}}\,\mathrm{d}\tau, \tag{B.12}$$

so

$$\phi \sim -\frac{F(t)r}{2\mu\sqrt{r^2+z^2}} + \frac{c_1 r}{2\pi^{1/2}\mu r_\nu}\int_0^t \frac{F'(\tau)}{\sqrt{1-\tau/t}}\,\mathrm{d}\tau, \tag{B.13}$$

which is the asymptotic expression given above as equation (6.16).

B.1.2 Far-field

For $r, z \gg (\nu t)^{1/2}$, we split the k-integral at Δ with $1 \ll \Delta \ll \sqrt{|s|/\nu}$. Then we have

$$\phi \sim \frac{1}{2\pi i\mu} \int_{c-i\infty}^{c+i\infty} \mathrm{e}^{st} \hat{f}(s) \int_0^\infty \frac{(s/\nu)\mathrm{e}^{-kz}}{-(s/\nu)^2} J_1(kr) k \,\mathrm{d}k \,\mathrm{d}s \tag{B.14}$$

$$= \frac{1}{2\pi i\mu} \int_{c-i\infty}^{c+i\infty} \mathrm{e}^{st} \hat{f}(s) \left(-\frac{\nu}{s}\right) \frac{r}{(r^2+z^2)^{3/2}} \,\mathrm{d}s \tag{B.15}$$

$$= -\frac{r}{\rho(r^2+z^2)^{3/2}} \frac{1}{2\pi i} \int_{c-i\infty}^{c+i\infty} \mathrm{e}^{st} \hat{f}(s) s^{-1} \,\mathrm{d}s. \tag{B.16}$$

So we have

$$\phi \sim -\frac{r}{\rho(r^2+z^2)^{3/2}} \int_0^t F(\tau) \,\mathrm{d}\tau. \tag{B.17}$$

which is given above as equation (6.17). Similarly, the pressure becomes

$$p \sim -\frac{1}{2\pi i\nu} \int_{c-i\infty}^{c+i\infty} \mathrm{e}^{st} s\hat{f}(s) \int_0^\infty \frac{(s/\nu)\mathrm{e}^{-kz}}{-(s/\nu)^2} J_0(kr) k \,\mathrm{d}k \,\mathrm{d}s \tag{B.18}$$

$$= -\frac{1}{2\pi i\nu} \int_{c-i\infty}^{c+i\infty} \mathrm{e}^{st} s\hat{f}(s) \left(-\frac{\nu}{s}\right) \frac{z}{(r^2+z^2)^{3/2}} \,\mathrm{d}s \tag{B.19}$$

$$= \frac{z}{(r^2+z^2)^{3/2}} F(t). \tag{B.20}$$

B.2 3D dipole

For the three-dimensional dipole, we have the inverse transform (6.25)

$$p(t,r,z) = \frac{1}{2\pi i\nu} \int_{c-i\infty}^{c+i\infty} \mathrm{e}^{st} s\hat{g}(s) \int_0^\infty \frac{k^2 m \mathrm{e}^{-kz}}{4k^3 m - (k^2+m^2)^2} J_0(kr) k \,\mathrm{d}k \,\mathrm{d}s, \tag{B.21}$$

$$\phi(t,r,z) = \frac{1}{2\pi i\mu} \int_{c-i\infty}^{c+i\infty} \mathrm{e}^{st} \hat{g}(s) \int_0^\infty \frac{\frac{1}{2}k(k^2+m^2)\mathrm{e}^{-mz} - k^2 m \mathrm{e}^{-kz}}{4k^3 m - (k^2+m^2)^2} J_1(kr) k \,\mathrm{d}k \,\mathrm{d}s \tag{B.22}$$

$$h(t,r) = \frac{1}{2\pi i\mu} \int_{c-i\infty}^{c+i\infty} \mathrm{e}^{st} \frac{\hat{g}(s)}{s} \int_0^\infty \frac{k^3 m - \frac{1}{2}k^2(k^2+m^2)}{4k^3 m - (k^2+m^2)^2} J_0(kr) k \,\mathrm{d}k \,\mathrm{d}s. \tag{B.23}$$

B.2.1 Near the origin

Let

$$I_k = \int_0^\infty \frac{\frac{1}{2}k(k^2+m^2)\mathrm{e}^{-mz} - k^2 m \mathrm{e}^{-kz}}{4k^3 m - (k^2+m^2)^2} J_1(kr) k \,\mathrm{d}k. \tag{B.24}$$

As above, we make the substitution $k = \hat{k}/r$, $s = \hat{s}/t$, and write $\hat{\eta}^2 = \hat{s}r^2/\nu t$, $\beta = z/r$. Then

$$I_k = \frac{1}{r}\int_0^\infty \frac{\frac{1}{2}\hat{k}(2\hat{k}^2+\hat{\eta}^2)\mathrm{e}^{-(\hat{k}^2+\hat{\eta}^2)^{1/2}\beta} - \hat{k}^2(\hat{k}^2+\hat{\eta}^2)^{1/2}\mathrm{e}^{-\hat{k}\beta}}{4\hat{k}^3(\hat{k}^2+\hat{\eta}^2)^{1/2} - (2\hat{k}^2+\hat{\eta}^2)^2} J_1(\hat{k})\hat{k}\,\mathrm{d}\hat{k}. \tag{B.25}$$

For $r \ll (\nu t)^{1/2}$ and $|\hat{s}| = \mathrm{O}(1)$, we have $\hat{\eta} \ll 1$. So we can split the k-integral at δ such that $\hat{\eta} \ll \delta \ll 1$. Then

$$\begin{aligned}
I_k \sim & \frac{1}{r}\int_0^\delta \frac{\frac{1}{2}\hat{k}(2\hat{k}^2+\hat{\eta}^2) - \hat{k}^2(\hat{k}^2+\hat{\eta}^2)^{1/2}}{4\hat{k}^3(\hat{k}^2+\hat{\eta}^2)^{1/2} - (2\hat{k}^2+\hat{\eta}^2)^2}\left(\frac{\hat{k}^2}{2}\right)\mathrm{d}\hat{k} \\
& + \frac{1}{r}\int_\delta^\infty \left(\frac{\beta}{4} - \frac{\beta^2\hat{\eta}^2}{16\hat{k}} - \frac{\beta\hat{\eta}^2}{8\hat{k}^2} - \frac{\hat{\eta}^2}{16\hat{k}^3}\right)\mathrm{e}^{-\hat{k}\beta}J_1(\hat{k})\hat{k}\,\mathrm{d}\hat{k} \\
= & \frac{\hat{\eta}^2}{r}\int_0^{\delta/\hat{\eta}} \frac{\frac{1}{2}u(2u^2+1) - u^2(u^2+1)^{1/2}}{4u^3(u^2+1)^{1/2} - (2u^2+1)^2}\left(\frac{u^2}{2}\right)\mathrm{d}u \\
& + \frac{\beta}{4r}\frac{1}{(1+\beta^2)^{3/2}} - \frac{\beta^2\hat{\eta}^2}{16r}\left(1 - \frac{\beta}{\sqrt{1+\beta^2}}\right) - \frac{\beta\hat{\eta}^2}{8r}(\sqrt{1+\beta^2}-\beta) \\
& - \frac{\hat{\eta}^2}{32r}\left(\frac{1}{2} + \log 2 + \beta^2 - \beta\sqrt{1+\beta^2} - \log\left(\beta + \sqrt{1+\beta^2}\right) + (-E_\gamma - \log\delta)\right) \\
= & \frac{\hat{\eta}^2}{r}\left(A_2 + \frac{1}{32}\log\hat{\eta}\right) + \frac{\beta}{4r(1+\beta^2)^{3/2}} \\
& + \frac{\hat{\eta}^2}{32r}\left(-\frac{1}{2} - \log 2 + E_\gamma + \beta^2 - \frac{\beta(3+\beta^2)}{\sqrt{1+\beta^2}} + \log\left(\beta + \sqrt{1+\beta^2}\right)\right) \\
= & \frac{sr}{\nu}\left(A_2 + \frac{1}{64}\log\frac{sr^2}{\nu}\right) + \frac{rz}{4(r^2+z^2)^{3/2}} \\
& + \frac{sr}{32\nu}\left(-\frac{1}{2} - \log 2 + E_\gamma + \frac{z^2}{r^2} - \frac{z(3r^2+z^2)}{r^2\sqrt{r^2+z^2}} + \log\left(\frac{z+\sqrt{r^2+z^2}}{r}\right)\right),
\end{aligned}$$

where E_γ is the Euler–Mascheroni constant.

We note that

$$\frac{1}{2\pi i}\int_{c-i\infty}^{c+i\infty} \mathrm{e}^{st}\hat{g}(s)s\log s\,\mathrm{d}s = -\int_0^t G''(\tau)\left(E_\gamma + \log(t-\tau)\right)\mathrm{d}\tau \tag{B.26}$$

$$= -\int_0^t G''(\tau)\log\left(1-\frac{\tau}{t}\right)\mathrm{d}\tau - \left(E_\gamma + \log t\right)G'(t), \tag{B.27}$$

so

$$\phi \sim \frac{G(t)rz}{4\mu(r^2+z^2)^{3/2}} + \frac{G'(t)r}{32\mu\nu}\left\{\log\left(\frac{z+\sqrt{r^2+z^2}}{r_\nu}\right) + \frac{z}{r^2}\left(z - \frac{3r^2+z^2}{\sqrt{r^2+z^2}}\right)\right\} + \frac{r}{32\mu\nu}\left(G'(t)c_2 - \frac{1}{2}\int_0^t \log\left(1-\frac{\tau}{t}\right)G''(\tau)\,\mathrm{d}\tau\right), \tag{B.28}$$

which is presented above as (6.26) with

$$c_2 = \int_0^\infty 16u^2\left(\frac{\frac{1}{2}u(2u^2+1) - u^2(u^2+1)^{1/2}}{4u^3(u^2+1)^{1/2} - (2u^2+1)^2}\right) + \frac{u}{1+u^2}\,\mathrm{d}u - \frac{1}{2} - \log 2 + \frac{1}{2}E_\gamma \tag{B.29}$$

$$\approx -0.6947. \tag{B.30}$$

B.2.2 Far-field

In the far-field, we have

$$\phi \sim \frac{1}{2\pi i\mu}\int_{c-i\infty}^{c+i\infty} \mathrm{e}^{st}\hat{g}(s)\int_0^\infty \frac{-k^2(s/\nu)^{1/2}\mathrm{e}^{-kz}}{-(s/\nu)^2}J_1(kr)k\,\mathrm{d}k\,\mathrm{d}s \tag{B.31}$$

$$= \frac{1}{2\pi i\mu}\int_{c-i\infty}^{c+i\infty} \mathrm{e}^{st}\hat{g}(s)\left(\frac{\nu}{s}\right)^{3/2}\frac{3r(4z^2-r^2)}{(r^2+z^2)^{7/2}}\,\mathrm{d}s \tag{B.32}$$

$$= \frac{3\nu^{1/2}r(4z^2-r^2)}{\rho(r^2+z^2)^{7/2}}\frac{1}{2\pi i}\int_{c-i\infty}^{c+i\infty} \mathrm{e}^{st}\hat{g}(s)s^{-3/2}\,\mathrm{d}s \tag{B.33}$$

$$= \frac{3\nu^{1/2}r(4z^2-r^2)}{\rho(r^2+z^2)^{7/2}}\int_0^t G(\tau)\frac{2}{\pi^{1/2}}\sqrt{t-\tau}\,\mathrm{d}\tau, \tag{B.34}$$

so

$$\phi \sim \frac{6r_\nu r(4z^2-r^2)}{\pi^{1/2}\rho(r^2+z^2)^{7/2}}\int_0^t G(\tau)\sqrt{1-\frac{\tau}{t}}\,\mathrm{d}\tau, \tag{B.35}$$

which is given above as equation (6.28).

Similarly, the pressure

$$p(t,r,z) \sim \frac{1}{2\pi i\nu}\int_{c-i\infty}^{c+i\infty} \mathrm{e}^{st}s\hat{g}(s)\int_0^\infty \frac{k^2(s/\nu)^{1/2}\mathrm{e}^{-kz}}{-(s/\nu)^2}J_0(kr)k\,\mathrm{d}k\,\mathrm{d}s, \tag{B.36}$$

$$= \frac{1}{2\pi i\nu}\int_{c-i\infty}^{c+i\infty} \mathrm{e}^{st}s\hat{g}(s)\left(\frac{\nu}{s}\right)^{3/2}\frac{z(9r^2-6z^2)}{(r^2+z^2)^{7/2}}\,\mathrm{d}s \tag{B.37}$$

$$= \frac{\nu^{1/2}z(9r^2-6z^2)}{(r^2+z^2)^{7/2}}\frac{1}{2\pi i}\int_{c-i\infty}^{c+i\infty} \mathrm{e}^{st}\hat{g}(s)s^{-1/2}\,\mathrm{d}s \tag{B.38}$$

$$= \frac{\nu^{1/2}z(9r^2-6z^2)}{(r^2+z^2)^{7/2}}\int_0^t G(\tau)\frac{1}{\pi^{1/2}\sqrt{t-\tau}}\,\mathrm{d}\tau, \tag{B.39}$$

so

$$p \sim \frac{3\nu^{1/2} z(3r^2 - 2z^2)}{\pi^{1/2}(r^2+z^2)^{7/2}} \int_0^t G(\tau) \frac{1}{\sqrt{1-\tau/t}} \,\mathrm{d}\tau. \tag{B.40}$$

B.3 2D point force

We have

$$p(t,x,y) = -\frac{1}{2\pi^2 i\nu} \int_{c-i\infty}^{c+i\infty} \mathrm{e}^{st} s\hat{f}(s) \int_0^\infty \cos kx \frac{(k^2+m^2)\mathrm{e}^{-ky}}{4k^3 m - (k^2+m^2)^2} \,\mathrm{d}k \,\mathrm{d}s, \tag{B.41}$$

$$\psi(t,x,y) = \frac{1}{2\pi^2 i\mu} \int_{c-i\infty}^{c+i\infty} \mathrm{e}^{st} \hat{f}(s) \int_0^\infty \sin kx \frac{(k^2+m^2)\mathrm{e}^{-ky} - 2k^2\mathrm{e}^{-my}}{4k^3 m - (k^2+m^2)^2} \,\mathrm{d}k \,\mathrm{d}s. \tag{B.42}$$

B.3.1 Near the origin

Let

$$I_k = \int_0^\infty \sin kx \frac{(k^2+m^2)\mathrm{e}^{-ky} - 2k^2\mathrm{e}^{-my}}{4k^3 m - (k^2+m^2)^2} \,\mathrm{d}k. \tag{B.43}$$

Make the substitution $k = \hat{k}/x$, $s = \hat{s}/t$, and write $\hat{\eta}^2 = \hat{s}x^2/\nu t$, $\beta = y/x$. Then

$$I_k = x \int_0^\infty \sin \hat{k} \frac{(2\hat{k}^2+\hat{\eta}^2)\mathrm{e}^{-\hat{k}\beta} - 2\hat{k}^2\mathrm{e}^{-(\hat{k}^2+\hat{\eta}^2)^{1/2}\beta}}{4\hat{k}^3(\hat{k}^2+\hat{\eta}^2)^{1/2} - (2\hat{k}^2+\hat{\eta}^2)^2} \,\mathrm{d}\hat{k}. \tag{B.44}$$

For $x \ll (\nu t)^{1/2}$ and $|\hat{s}| = \mathrm{O}(1)$, we have $\hat{\eta} \ll 1$. We can split the k-integral at δ such that $\hat{\eta} \ll \delta \ll 1$. Then

$$I_k \sim x \int_0^\delta \hat{k} \frac{\hat{\eta}^2}{4\hat{k}^3(\hat{k}^2+\hat{\eta}^2)^{1/2} - (2\hat{k}^2+\hat{\eta}^2)^2} \,\mathrm{d}\hat{k} + x \int_\delta^\infty \left(-\frac{\beta}{2\hat{k}} - \frac{1}{2\hat{k}^2}\right) \mathrm{e}^{-\hat{k}\beta} \sin \hat{k} \,\mathrm{d}\hat{k} \tag{B.45}$$

$$= x \int_0^{\delta/\hat{\eta}} \frac{u}{4u^3(u^2+1)^{1/2} - (2u^2+1)^2} \,\mathrm{d}u - \frac{x}{2}\left(1 - \frac{1}{2}\log(1+\beta^2) - E_\gamma - \log\delta\right) \tag{B.46}$$

$$= x\left(A_3 + \frac{1}{4}\log\frac{sx^2}{\nu}\right) - \frac{x}{2}\left(1 - \frac{1}{2}\log\left(\frac{x^2+y^2}{x^2}\right) - E_\gamma\right). \tag{B.47}$$

Now let $B_3 = A_3 - 1/2 + E_\gamma/2$

$$\psi \sim \frac{x}{2\pi^2 i\mu}\int_{c-i\infty}^{c+i\infty} \mathrm{e}^{st}\hat{f}(s)\left(B_3 + \frac{1}{4}\log s + \frac{1}{4}\log\left(\frac{x^2+y^2}{\nu}\right)\right) \tag{B.48}$$

$$= \frac{x}{\pi\mu}F(t)\left(B_3 + \frac{1}{4}\log\left(\frac{x^2+y^2}{\nu}\right)\right) + \frac{x}{4\pi\mu}\frac{1}{2\pi i}\int_{c-i\infty}^{c+i\infty}\mathrm{e}^{st}\hat{f}(s)\log s\,\mathrm{d}s. \tag{B.49}$$

We note that

$$\frac{1}{2\pi i}\int_{c-i\infty}^{c+i\infty}\mathrm{e}^{st}\hat{f}(s)\log s\,\mathrm{d}s = -\int_0^t F'(\tau)\left(\log(t-\tau)+E_\gamma\right)\,\mathrm{d}\tau \tag{B.50}$$

$$= -\int_0^t F'(t)\log\left(1-\frac{\tau}{t}\right)\,\mathrm{d}\tau - F(t)\left(\log t + E_\gamma\right), \tag{B.51}$$

so

$$\psi \sim \frac{x}{2\pi\mu}\left(F(t)\log\sqrt{\frac{x^2+y^2}{r_\nu^2}} + c_3F(t) - \frac{1}{2}\int_0^t F'(\tau)\log\left(1-\frac{\tau}{t}\right)\,\mathrm{d}\tau\right), \tag{B.52}$$

where $c_3 = 2B_3 - E_\gamma/2 \approx -0.9367$.

B.3.2 Far-field

In the far-field,

$$\psi \sim \frac{1}{2\pi^2 i\mu}\int_{c-i\infty}^{c+i\infty}\mathrm{e}^{st}\hat{f}(s)\int_0^\infty \sin(kx)\frac{(s/\nu)\mathrm{e}^{-ky}}{-(s/\nu)^2}\,\mathrm{d}k\,\mathrm{d}s \tag{B.53}$$

$$= \frac{1}{2\pi^2 i\mu}\int_{c-i\infty}^{c+i\infty}\mathrm{e}^{st}\hat{f}(s)\left(-\frac{\nu}{s}\right)\frac{x}{x^2+y^2}\,\mathrm{d}s \tag{B.54}$$

$$= -\frac{1}{\pi\rho}\frac{x}{x^2+y^2}\frac{1}{2\pi i}\int_{c-i\infty}^{c+i\infty}\mathrm{e}^{st}\frac{\hat{f}(s)}{s}\,\mathrm{d}s, \tag{B.55}$$

so

$$\psi \sim -\frac{x}{\pi\rho(x^2+y^2)}\int_0^t F(\tau)\,\mathrm{d}\tau. \tag{B.56}$$

Similarly, the pressure

$$p \sim -\frac{1}{2\pi^2 i\nu}\int_{c-i\infty}^{c+i\infty}\mathrm{e}^{st}s\hat{f}(s)\int_0^\infty \cos(kx)\frac{(s/\nu)\mathrm{e}^{-ky}}{-(s/\nu)^2}\,\mathrm{d}k\,\mathrm{d}s \tag{B.57}$$

$$= \frac{1}{2\pi^2 i}\int_{c-i\infty}^{c+i\infty}\mathrm{e}^{st}\hat{f}(s)\frac{y}{x^2+y^2}\,\mathrm{d}s, \tag{B.58}$$

and so

$$p \sim \frac{y}{\pi(x^2+y^2)} F(t). \tag{B.59}$$

B.4 2D dipole

We have

$$p(t,x,y) = \frac{1}{\pi^2 i\nu} \int_{c-i\infty}^{c+i\infty} \mathrm{e}^{st} s\hat{g}(s) \int_0^\infty \cos kx \frac{k^2 m \mathrm{e}^{-ky}}{4k^3 m - (k^2+m^2)^2} \,\mathrm{d}k \,\mathrm{d}s, \tag{B.60}$$

$$\psi(t,x,y) = \frac{i}{2\pi^2\mu} \int_{c-i\infty}^{c+i\infty} \mathrm{e}^{st} \hat{g}(s) \int_0^\infty \sin kx \frac{2k^2 m \mathrm{e}^{-ky} - k(k^2+m^2)\mathrm{e}^{-my}}{4k^3 m - (k^2+m^2)^2} \,\mathrm{d}k \,\mathrm{d}s, \tag{B.61}$$

$$h(t,x) = \frac{i}{2\pi^2\mu} \int_{c-i\infty}^{c+i\infty} \mathrm{e}^{st} \frac{\hat{g}(s)}{s} \int_0^\infty k \cos kx \frac{k(k^2+m^2) - 2k^2 m}{4k^3 m - (k^2+m^2)^2} \,\mathrm{d}k \,\mathrm{d}s. \tag{B.62}$$

B.4.1 Near the origin

Let

$$I_k = \int_0^\infty \sin kx \frac{2k^2 m \mathrm{e}^{-ky} - k(k^2+m^2)\mathrm{e}^{-my}}{4k^3 m - (k^2+m^2)^2} \,\mathrm{d}k. \tag{B.63}$$

Make the substitution $k = \hat{k}/x$, $s = \hat{s}/t$, and write $\hat{\eta}^2 = \hat{s}x^2/\nu t$, $\beta = y/x$. Then

$$I_k = \int_0^\infty \sin \hat{k} \frac{2\hat{k}^2(\hat{k}^2+\hat{\eta}^2)^{1/2}\mathrm{e}^{-\hat{k}\beta} - \hat{k}(2\hat{k}^2+\hat{\eta}^2)\mathrm{e}^{-(\hat{k}^2+\hat{\eta}^2)^{1/2}\beta}}{4\hat{k}^3(\hat{k}^2+\hat{\eta}^2)^{1/2} - (2\hat{k}^2+\hat{\eta}^2)^2} \,\mathrm{d}\hat{k}. \tag{B.64}$$

For $x \ll (\nu t)^{1/2}$ and $|\hat{s}| = \mathrm{O}(1)$, we have $\hat{\eta} \ll 1$. So we can split the k-integral at δ such that $\hat{\eta} \ll \delta \ll 1$. Then

$$I_k \sim \int_0^\delta \hat{k} \frac{2\hat{k}^2(\hat{k}^2+\hat{\eta}^2)^{1/2} - \hat{k}(2\hat{k}^2+\hat{\eta}^2)}{4\hat{k}^3(\hat{k}^2+\hat{\eta}^2)^{1/2} - (2\hat{k}^2+\hat{\eta}^2)^2} \,\mathrm{d}\hat{k} + \int_\delta^\infty \left(-\frac{\beta}{2}\right) \mathrm{e}^{-\hat{k}\beta} \sin \hat{k} \,\mathrm{d}\hat{k} \tag{B.65}$$

$$= \hat{\eta} \int_0^{\delta/\hat{\eta}} u \frac{2u^2(u^2+1)^{1/2} - u(2u^2+1)}{4u^3(u^2+1)^{1/2} - (2u^+1)^2} \,\mathrm{d}u - \frac{\beta}{2} \frac{1}{1+\beta^2} \tag{B.66}$$

$$= x \left(\frac{s}{\nu}\right)^{1/2} (A_4) - \frac{xy}{2(x^2+y^2)}. \tag{B.67}$$

Now

$$\psi \sim \frac{i}{2\pi^2\mu}\int_{c-i\infty}^{c+i\infty} \mathrm{e}^{st}\hat{g}(s)\left(-\frac{xy}{2(x^2+y^2)} + x\left(\frac{s}{\nu}\right)^{1/2}(A_4)\right) \tag{B.68}$$

$$= \frac{G(t)xy}{2\pi\mu(x^2+y^2)} - \frac{A_4 x}{\pi\mu\nu^{1/2}}\frac{1}{2\pi i}\int_{c-i\infty}^{c+i\infty} \mathrm{e}^{st}\hat{g}(s)s^{1/2}\,\mathrm{d}s \tag{B.69}$$

$$= \frac{G(t)xy}{2\pi\mu(x^2+y^2)} - \frac{A_4 x}{\pi\mu\nu^{1/2}}\int_0^t G'(\tau)\frac{1}{\pi^{1/2}}\frac{1}{\sqrt{t-\tau}}\,\mathrm{d}\tau, \tag{B.70}$$

so

$$\psi \sim \frac{G(t)xy}{2\pi\mu(x^2+y^2)} - \frac{c_2 x}{\pi^{3/2}\mu r_\nu}\int_0^t \frac{G'(\tau)}{\sqrt{1-\tau/t}}\,\mathrm{d}\tau, \tag{B.71}$$

where $c_2 \approx 0.1360$

B.4.2 Far-field

In the far-field,

$$\psi \sim \frac{i}{2\pi^2\mu}\int_{c-i\infty}^{c+i\infty} \mathrm{e}^{st}\hat{g}(s)\int_0^\infty \sin kx \frac{2k^2(s/\nu)^{1/2}\mathrm{e}^{-ky}}{-(s/\nu)^2}\,\mathrm{d}k\,\mathrm{d}s \tag{B.72}$$

$$= \frac{i}{2\pi^2\mu}\int_{c-i\infty}^{c+i\infty} \mathrm{e}^{st}\hat{g}(s)\left(\frac{\nu}{s}\right)^{3/2}\left(\frac{4(x^3-3xy^2)}{(x^2+y^2)^3}\right)\mathrm{d}s \tag{B.73}$$

$$= \frac{\nu^{1/2}}{\pi\rho}\left(\frac{4x(3y^2-x^2)}{(x^2+y^2)^3}\right)\frac{1}{2\pi i}\int_{c-i\infty}^{c+i\infty} \mathrm{e}^{st}\hat{g}(s)s^{-3/2}\,\mathrm{d}s \tag{B.74}$$

$$= \frac{\nu^{1/2}}{\pi\rho}\left(\frac{4x(3y^2-x^2)}{(x^2+y^2)^3}\right)\int_0^t G(\tau)\frac{2}{\pi^{1/2}}\sqrt{t-\tau}\,\mathrm{d}\tau, \tag{B.75}$$

so

$$\psi \sim \frac{8r_\nu x(3y^2-x^2)}{\pi^{3/2}\rho(x^2+y^2)^3}\int_0^t G(\tau)\sqrt{1-\frac{\tau}{t}}\,\mathrm{d}\tau. \tag{B.76}$$

Similarly,

$$p \sim \frac{1}{\pi^2 i\nu}\int_{c-i\infty}^{c+i\infty} \mathrm{e}^{st}s\hat{g}(s)\int_0^\infty \cos kx \frac{k^2(s/\nu)^{1/2}\mathrm{e}^{-ky}}{-(s/\nu)^2}\,\mathrm{d}k\,\mathrm{d}s \tag{B.77}$$

$$= \frac{1}{\pi^2 i\nu}\int_{c-i\infty}^{c+i\infty} \mathrm{e}^{st}s\hat{g}(s)\left(\frac{\nu}{s}\right)^{3/2}\left(\frac{2y(3x^2-y^2)}{(x^2+y^2)^3}\right)\mathrm{d}s \tag{B.78}$$

$$= \frac{4\nu^{1/2}y(3x^2-y^2)}{\pi(x^2+y^2)^3}\int_{c-i\infty}^{c+i\infty} \mathrm{e}^{st}\hat{g}(s)s^{-1/2}\,\mathrm{d}s \tag{B.79}$$

$$= \frac{4\nu^{1/2}y(3x^2-y^2)}{\pi(x^2+y^2)^3}\int_0^t G(\tau)\frac{1}{\pi^{1/2}\sqrt{t-\tau}}\,\mathrm{d}\tau \tag{B.80}$$

so

$$p \sim \frac{4\nu y(3x^2 - y^2)}{\pi r_\nu (x^2 + y^2)^3} \int_0^t G(\tau) \frac{1}{\sqrt{1 - \tau/t}} \, \mathrm{d}\tau. \tag{B.81}$$

Appendix C

Next-order corrections for 3D coalescence with inertia

C.1 Stokeslet ring

First, we will need an expression for a ring of radial Stokeslets around the circle of radius r_b. It will be convenient to have the result in the form of a Hankel transform. First, write

$$p_0 = \int_0^\infty \tilde{p}_0(k,z) J_0(kr) k \,\mathrm{d}k, \quad \phi_0 = \int_0^\infty \tilde{\phi}_0(k,z) J_1(kr) k \,\mathrm{d}k \tag{C.1}$$

for the pressure p_0 and potential ϕ_0, where

$$u_r = \frac{\partial \phi}{\partial z}, \quad u_z = -\frac{1}{r}\frac{\partial (r\phi)}{\partial r}. \tag{C.2}$$

Now the Stokes equations become

$$-k^2 \tilde{p}_0 + \frac{\partial^2 \tilde{p}_0}{\partial z^2} = 0, \quad \text{and} \quad k\tilde{p}_0 + \mu\left(\frac{\partial^3 \tilde{\phi}_0}{\partial z^3} - k^2 \frac{\partial \tilde{\phi}_0}{\partial z}\right) = 0, \tag{C.3}$$

with solution

$$\tilde{p}_0 = -2\mu k A_0(k) \mathrm{e}^{-kz}, \quad \tilde{\phi}_0 = B_0(k)\mathrm{e}^{-kz} + A_0(k) z \mathrm{e}^{-kz}. \tag{C.4}$$

Now we apply the boundary conditions. We have no normal stress, and tangential stress set by the ring of Stokeslets;

$$-p + 2\mu\frac{\partial u_z}{\partial z} = 0, \quad \mu\left(\frac{\partial u_r}{\partial z} + \frac{\partial u_z}{\partial r}\right) = -\gamma\delta(r - r_b), \tag{C.5}$$

and these transform to

$$-2\mu k^2 B_0 = 0, \quad -k^2 B_0 - 2kA_0 = -\frac{\gamma}{\mu} J_1(kr_b) r_b, \tag{C.6}$$

with solution

$$A_0 = \frac{\gamma r_b J_1(kr_b)}{2\mu k}, \quad B_0 = 0, \tag{C.7}$$

and so

$$p_0 = -\gamma r_b \int_0^\infty J_0(kr) J_1(kr_b) e^{-kz} k \,\mathrm{d}k, \quad \phi_0 = \frac{\gamma r_b}{2\mu} \int_0^\infty J_1(kr) J_1(kr_b) z e^{-kz} \,\mathrm{d}k. \tag{C.8}$$

Note that this has no vertical velocity on the fluid bridge. In the far-field, where $x, z \gg r_b$, split the integral at $1/r_b \ll \delta \ll 1/x, 1/z$ and approximate ϕ_0 as

$$\phi_0 \sim \frac{\gamma r_b}{2\mu} \int_0^\delta J_1(kr) \frac{kr_b}{2} z \mathrm{e}^{-kz} \,\mathrm{d}k = \frac{\gamma r_b^2}{4\mu} \frac{rz}{(r^2 + z^2)^{3/2}}, \tag{C.9}$$

which is the potential for a Stokeslet dipole used above.

We will use this Hankel representation of the Stokeslet ring as a neat form for the body force from inertia.

C.2 Forcing from inertia

The inertia of this ring of Stokeslets drives a correction flow, with the fluid acceleration acting as a body force in the Stokes equations. The radial component of the force is

$$\rho\frac{\partial^2 \phi_0}{\partial t \partial z} = \frac{\gamma}{2\nu} \int_0^\infty J_1(kr) \left\{ J_1'(kr_b) k r_b \dot{r}_b + J_1(kr_b) \dot{r}_b \right\} e^{-kz} (1 - kz) \,\mathrm{d}k. \tag{C.10}$$

We write ϕ_1 and p_1 for the potential and pressure of the flow due to this body force. We non-dimensionalise with $r = r_b \bar{r}$, $z = r_b \bar{z}$ and write

$$\phi_1 = \frac{\gamma r_b^2 \dot{r}_b}{\mu\nu} \left(\phi^* + \bar{\phi}_1\right) \quad \text{where} \quad \phi^* = \frac{\bar{r}}{16} \log\left(\bar{z} + \sqrt{\bar{r}^2 + \bar{z}^2}\right). \tag{C.11}$$

Here, we have subtracted the large growing flow in the far-field.

Taking a Hankel transform, we write $\bar{p}_1 = \int_0^\infty \tilde{p}_1 J_0(k\bar{r})k\,\mathrm{d}k$, and $\bar{\phi}_1 = \int_0^\infty \tilde{\phi}_1 J_1(k\bar{r})k\,\mathrm{d}k$ and the Stokes equations become

$$-k^2\tilde{p}_1 + \tilde{p}_{1\bar{z}\bar{z}} = 0 \quad \text{and} \quad k\tilde{p}_1 + (\tilde{\phi}_{1\bar{z}\bar{z}\bar{z}} - k^2\tilde{\phi}_{1\bar{z}}) = T(k)e^{-k\bar{z}}(1-k\bar{z}), \tag{C.12}$$

where $T(u) = \frac{1}{2}(J_1'(u) + J_1(u)/u)$, with solution

$$\tilde{p}_1 = -2kA_1(k)e^{-k\bar{z}}, \quad \tilde{\phi}_1 = B_1(k)e^{-k\bar{z}} + A_1(k)\bar{z}e^{-k\bar{z}} - \frac{T(k)}{4k^2}\bar{z}e^{-k\bar{z}}\left(1+k\bar{z}\right), \tag{C.13}$$

where A_1 and B_1 are functions of k to be determined by the boundary conditions. We take the radial derivative of the normal velocity condition in order to transform it. As a result, our solution will have some constant normal velocity on the fluid bridge, which we will later remove. The boundary conditions become

$$\int_0^\infty \left(\tilde{\phi}_{1zz} + k^2\tilde{\phi}_1\right) J_1(k\bar{r})k\,\mathrm{d}k = \frac{1}{8\bar{r}} \qquad \text{for } \bar{r} > 0, \tag{C.14}$$

$$\int_0^\infty k^3\tilde{\phi}_1 J_1(k\bar{r})\,\mathrm{d}k = \frac{1}{8\bar{r}} \qquad \text{for } 0 < \bar{r} < 1, \tag{C.15}$$

$$\int_0^\infty \left(k\tilde{p}_1 + 2k^2\tilde{\phi}_{1z}\right) J_1(k\bar{r})k\,\mathrm{d}k = -\frac{1}{4\bar{r}^2} \qquad \text{for } \bar{r} > 1. \tag{C.16}$$

The tangential stress condition gives $A_1 = kB_1 - 1/16k^2$. We use this to eliminate A_1, which gives

$$\int_0^\infty k^3 B_1(k) J_1(k\bar{r})\,\mathrm{d}k = \frac{1}{8\bar{r}} \quad \text{for } 0 < \bar{r} < 1, \tag{C.17}$$

$$\int_0^\infty k^4 B_1(k) J_1(k\bar{r})\,\mathrm{d}k = \frac{1}{8}\left(\frac{1}{\bar{r}^2} + \frac{2E(1/\bar{r}^2)}{\pi(1-\bar{r}^2)}\right) \quad \text{for } \bar{r} > 1, \tag{C.18}$$

where $E(m)$ is the complete elliptic integral. This is a dual integral equation for $B_1(k)$, with the forcing partly in the form solved by [15] and partly in the form solved by [36]. Taking a linear combination, the solution is

$$B_1(k) = \frac{1}{4\pi k^3}\left(\int_1^\infty \tau C(\tau)\sin k\tau\,\mathrm{d}\tau + \int_0^1 \frac{\sin k\tau}{\tau}\,\mathrm{d}\tau\right), \tag{C.19}$$

where

$$C(\tau) = \int_\tau^\infty \left(\frac{2E(\chi^{-2})}{\pi\left(1-\chi^2\right)} + \frac{1}{\chi^2}\right)\frac{\mathrm{d}\chi}{(\chi^2-\tau^2)^{1/2}}, \tag{C.20}$$

which we use in

$$\bar{\phi}_1(\bar{r},\bar{z}) = \int_0^\infty \left(B_1(k)(1+k\bar{z}) - \frac{\bar{z}}{16k^2} - \frac{T(k)}{4k^2}\bar{z}(1+k\bar{z}) \right) e^{-k\bar{z}} J_1(k\bar{r}) k \,\mathrm{d}k. \quad \text{(C.21)}$$

Expanding $C(\tau)$ and $B_1(k)$ gives the velocity on the fluid bridge and the far-field behaviour. In the far-field, we find

$$\bar{\phi}_1(\bar{r},\bar{z}) \sim \frac{\bar{z}}{16\bar{r}} \left(\bar{z} - \frac{3\bar{r}^2+\bar{z}^2}{\sqrt{\bar{r}^2+\bar{z}^2}} \right), \quad \text{(C.22)}$$

which agrees with the far-field solution. On the fluid bridge, we find

$$\bar{\phi}_1(\bar{r},0) \sim c_6\bar{r} - \frac{1}{16}\bar{r}\log\bar{r}, \quad \text{(C.23)}$$

where the constant is approximately $c_6 \approx 0.0312$. Adding ϕ^* removes the logarithmic term, leaving a solid body motion $u_z = -2c_6$ on the fluid bridge. We add the streamfunction

$$c_6 r_b \left(\frac{2}{\pi}(\psi_3 - \psi_4) - \bar{r}^2 \right), \quad \text{(C.24)}$$

to remove this solid-body motion without introducing a solid-body motion in the far-field. This gives a solution that satisfies all the boundary conditions.

C.3 Forcing from surfaces

The stress on the surface drives a Stokes flow of size $u = O(u_\infty/\log r_b)$. The stresses are all known functions of r; the boundary conditions are

$$\mu\left(\frac{\partial u_r}{\partial z} + \frac{\partial u_z}{\partial r}\right) = -\frac{2\gamma}{\pi}\frac{\partial}{\partial r}\left(\frac{h_1}{r+r_b} E\left(\frac{-4rr_b}{(r-r_b)^2}\right) - \frac{h_1}{r-r_b} K\left(\frac{-4rr_b}{(r-r_b)^2}\right)\right) \quad \text{for } r > r_b, \quad \text{(C.25)}$$

$$-p + 2\mu\frac{\partial u_z}{\partial z} = -\gamma\left(\frac{\partial^2 h_1}{\partial r^2} + \frac{1}{r}\frac{\partial h_1}{\partial r}\right) \quad \text{for } r > r_b, \quad \text{(C.26)}$$

$$\left(\frac{\partial u_r}{\partial z} + \frac{\partial u_z}{\partial r}\right) = 0 \quad \text{for } 0 < r < r_b, \quad \text{(C.27)}$$

$$u_z = 0 \quad \text{for } 0 < r < r_b, \quad \text{(C.28)}$$

where h_1 is the leading-order surface displacement given by equation (6.36), and where $E(m)$ and $K(m)$ are complete elliptic integrals. Near the edge we know that

$h_1^2 \sim r_c(r - r_b)$ with $r_c = 8h_\infty^2/\pi^2 r_b$. The stresses diverge at $r = r_b$ so we subtract a solution that diverges in the same way, with the streamfunction

$$\psi_6 = \frac{\gamma(r_c r_b)^{1/2}}{\sqrt{2}\pi\mu}\left\{-\arctan\lambda + \frac{\zeta^3(1+\lambda^2)}{\lambda^2+\zeta^2}\arctan\frac{\lambda}{\zeta}\right. \tag{C.29}$$

$$\left. + \frac{1-\zeta^2}{\lambda^2+\zeta^2}\lambda\left(\zeta^2 + \lambda^2\left(\frac{1}{3} - \frac{1}{2}\log 2 - \frac{1}{2}\log\left(\frac{1+\lambda^2}{\zeta^2+\lambda^2}\right)\right)\right)\right\}. \tag{C.30}$$

In particular, we have chosen a streamfunction which satisfies the normal stress boundary condition for all $r > r_b$. The remaining flow therefore has no normal stress outside $r > r_b$ and no vertical velocity inside $r < r_b$, and so we take a Hankel transform and use Tranter's method for the remainder;

$$p_2 = -\frac{2\gamma}{\pi}\int_0^\infty A_2(k)e^{-kz}J_1(kr)k^2\,\mathrm{d}k, \quad \phi_2 = \frac{\gamma}{\pi\mu}\int_0^\infty A_2(k)ze^{-kz}J_1(kr)k\,\mathrm{d}k, \tag{C.31}$$

where $A_2(k)$ is known in terms of the tangential stress boundary condition. This correction term has no normal velocity outside the $r > r_b$, and so does not affect the surface shape.

C.4 Surface shape

The leading-order surface shape is given by h_1 above (equation (6.36)). Here we integrate for the $O(h_\infty/\log r_b)$ correction. The kinematic boundary condition becomes

$$u_{0z} - u_{0r}\frac{\partial h_1}{\partial r} - \frac{1}{r}\frac{\partial}{\partial r}(r\phi_1 + \psi_6 + K\psi_3) = \frac{\partial h_2}{\partial t}, \tag{C.32}$$

where u_0 is the Stokeslet ring, ϕ_1 is the flow driven by the inertia of the Stokeslet ring, ψ_6 is the flow driven by the surface stresses and ψ_3 is the stress-free solution which decays in the far-field. The leading-order surface displacement is h_1, and we write the correction as $h_2 = (r_b^2/a)H_2(\bar{r})$ where a is the initial radius of the drops and $\bar{r} = r/r_b$.

We apply the boundary conditions $H_2(1) = 0$ and $H_2(\bar{r}) \sim \frac{1}{2}\bar{r}^2$ as $r \to \infty$, determining the constant of integration and the free parameter K. Writing $f(\bar{r})$ for the velocity on the left-hand side of equation (C.32), we can integrate up for

$$H_2(\bar{r}) = -\bar{r}^2\frac{a}{r_b\dot{r}_b}\int_1^{\bar{r}}\frac{f(r')}{r'^3}\,\mathrm{d}r', \tag{C.33}$$

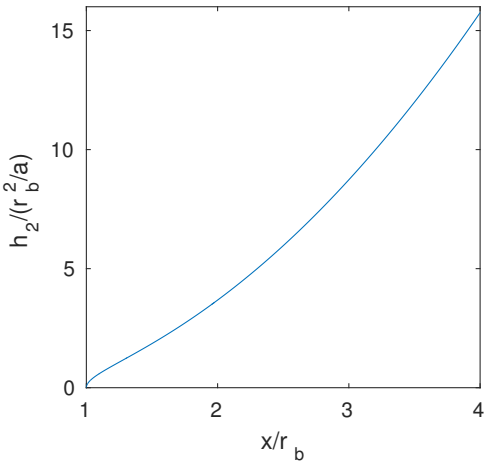

Fig. C.1 Next-order surface shape h_2 at $\mathrm{Oh} = 1$.

which we calculate numerically. Matching to the far-field shape gives

$$\frac{a\gamma}{\mu\nu}\left(6.23\times10^{-2}\right)+\frac{a\gamma h_\infty}{\mu r_b^2\dot{r}_b}\left(-3.10\times10^{-2}+2K\right)=\frac{1}{2}. \tag{C.34}$$

The dimensionless quantity $\nu h_\infty/r_b^2\dot{r}_b$ depends on the size of r_b. Using our asymptotic for r_b, this number is $\pi/32$. Then $K = 8\mathrm{Oh}^2/\pi - 0.302$ where $\mathrm{Oh} = \mu/\sqrt{\rho a\gamma}$ is the Ohnesorge number. This determines the last constant, and we have the surface shape correct to order r_b^2/a. As an example, the second-order shape with $\mathrm{Oh} = 1$ is shown in figure C.1.